

INVESTIGATION OF THE PROCESSES OF RETENTION AND RELEASE OF IMPLANTED DEUTERIUM AND HELIUM IONS FOR TUNGSTEN AND TANTALUM COATINGS

 M.O. Azarenkov^b,  V.V. Bobkov^{a,*},  L.P. Tishchenko^a, Yu.I. Kovtunenکو^a,  A.O. Skrypnyk^a,
 D.I. Shevchenko^a,  L.O. Gamayunova^a

^a V. N. Karazin Kharkiv National University, 4, Svobody Sq., Kharkiv, 61022, Ukraine

^b National Science Center "Kharkov Institute of Physics and Technology", 1, Akademichna St., Kharkiv, 61108, Ukraine

*Corresponding Author e-mail: bobkov@karazin.ua

Received November 1, 2023; revised December 6, 2023; accepted December 15, 2023

The analysis of main published results of studies of retention and migration of ion-implanted hydrogen isotopes and helium in tungsten and tantalum coatings, formation of radiation damages of the crystal lattice and their interaction with implanted gases, as well as the influence of helium and deuterium on various properties and surface morphology of coatings was carried out. The irradiation of samples was performed by beams of accelerated ions of hydrogen isotopes or He⁺, and in a plasma containing these ions, at various fluences and energies of incident ions, and at various temperatures of targets during implantation. Special attention was paid to the research results obtained at simultaneous irradiation of W both in bulk and in thin-film form. The used methods were electron microscopy, reemission mass spectrometry, thermal desorption spectrometry, X-ray photoelectron spectroscopy, X-ray diffraction, nuclear reaction analysis and Rutherford ion scattering.

Keywords: Deuterium; Helium; Ion implantation; Thermal desorption; Retention; Damage; W and Ta coatings

PACS: 61.80.-x, 61.80.Jh

INTRODUCTION

At present, most of the world's electricity demands are satisfied by fossil fuels, mainly oil, natural gas and coal. According to the conclusions of the Intergovernmental Panel on Climate Change, a noticeable increase in temperature in the last century is a result of a significant increase in greenhouse gas emissions, including CO₂, due to the use of these sources. To prevent dangerous climate change, the current energy supply system must change significantly. We need new sources of energy with renewable resources. These are the energies of the sun, wind, biomass, hydropower, which are fully mastered or in the process of development. However, they are not always available, are unstable, subject to sudden climate change, and require additional equipment for concomitant energy storage. Precisely for this reason energy sources based on nuclear fission have been adopted by many developed countries. Existing nuclear power plants are long-term sources of energy, and the used fuel has little impact on the environment. However, natural cataclysms led to the destruction of station blocks and the release of radioactive products of nuclear reactions.

Recent researches of controlled fusion have shown that this new energy source can produce environmentally safe electricity, has rich fuel resources that will satisfy the needs of the growing population of a world. In a fusion reaction, the released amount of energy is about four million times higher than the amount of energy released when burning coal. However, as Pranevičius et al. noted [1], the successful operation of fusion power plants requires the use of plasma-facing materials (PFM) with certain parameters. First, they must withstand high temperatures. The surface temperature can reach 1073 K, but in some areas and during transients, this temperature can exceed 2273 K. The material must work under intense X-rays and gamma radiation, be resistant to bombardment by produced in the fusion reaction high-intensity accelerated neutrons with energy of ~ 14 MeV, and to the impact during plasma disruption of intense flows of hydrogen isotopes and helium with a density of 10²² m⁻²·s⁻¹ – 10²⁴ m⁻²·s⁻¹ and the energies from several eV to tens of keV. The mechanical and physical properties of PFM are changed including erosion and subsequent impurities transfer, which leads to mixing of the materials of these devices. At this, the plasma becomes contaminated with eroded particles of impurities. Getting into the plasma, they cause its radiation losses, which are proportional to the atomic number Z of the impurity. This additionally leads to the plasma cooling and disruption of the fusion reaction. High-energy neutrons and tritium, interacting with the walls of the plasma chamber and internal vessels, activate materials. Retention of great amounts of tritium in the PFM increases the cost of fuel in the reactor and presents a safety problem. It is possible to reduce the level of radioactivity and resist the deterioration of mechanical and physical properties, as well as erosion, by developing radiation-resistant structural materials. The main requirements for PFM are as follows: good mechanical and physical properties, excellent resistance to high temperature cyclic loads, low sputtering ratio, insensitivity to chemical sputtering, low tritium retention, low activation by neutron irradiation, and low Z.

The processes in a solid as a result of irradiation with accelerated ions of hydrogen isotopes (H⁺, D⁺, T⁺) and He⁺ or as a result of exposure to containing the listed ions plasma, can be both inelastic and elastic. At the inelastic interaction, electron radiation, X-ray and light radiation, and heating of a solid are observed. Their influence on the properties of the

irradiated layers is negligible. The elastic interaction of ions with a solid causes desorption of atoms adsorbed on the surface, emission of neutrals, excited atoms and ions, formation of crystal lattice defects, and retention of bombarding ions in the bulk. The energy of elastic interaction of H^+ , D^+ , T^+ , and He^+ ions with tungsten, for example, should exceed ~ 2050 eV, ~ 960 eV, ~ 700 eV, and ~ 480 eV respectively, as it is shown in [2] and [3]. The adsorption and desorption processes are determined mainly by the properties of the upper monolayer of the solid. Ion-photon emission and secondary ion emission are very sensitive to the composition, structure and morphology of the target surface. The emission of sputtered atoms occurs from depths of 2–3 monolayers and in many cases can be considered as a surface process. The formation of radiation defects in the crystal lattice and the retention of bombarding ions in the volume (implantation) depend on the energy of the ions. Schematic representation of the dominant processes during irradiation with ions of different energies is shown in Figure 1 [1].

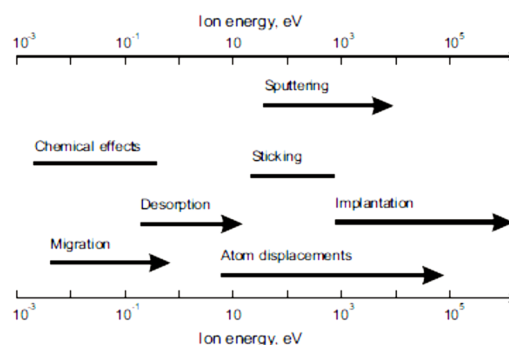


Figure 1. Schematic presentation of the dominant processes under irradiation by ions of different energies [1].

The dominant processes are determined by the type of ions, their energy, mass, charge state, intensity of ion irradiation, and properties of the target material. In plasma, due to very high ion flux densities, even at low energy, radiation damages of the target can occur in the result of the local supersaturating with particles.

For ITER, according to estimation of Yoshida [4], hydrogen ions, that bombarded divertor plates, have a flux and average energy not high than $10^{24} \text{ m}^{-2} \text{ s}^{-1}$ and 100 eV, respectively. Therefore, one of the main problem for the divertor material is erosion due to sputtering with these high-density ions. The situation for the first wall is significantly different then for the divertor plate. The flux and the energy of hydrogen particles bombarding the first wall of ITER estimate as do not exceed $10^{20} \text{ m}^{-2} \cdot \text{s}^{-1}$ and 100–500 eV, respectively. These particles are hydrogen ions and neutrals produced in the edge plasma. In addition to these low energy particles, high energy neutrals coming out from the high temperature core will also hit the first wall. Their flux and energy as predicted are respectively $\sim 10^{18} \text{ m}^{-2} \cdot \text{s}^{-1}$ and 10 keV. Although the number of neutrals on the first wall is much smaller than the number of ions on the divertor plates, they can result in significant erosion due to sputtering, as well as striking damage of materials. One of the main problems for PFM is penetration and retention of implanted hydrogen isotopes. Retention helium ion with the energy of several tens keV in the PFM [5] is also dangerous because of their intense interaction with lattice defects. Helium greatly accelerates the formation of bubbles, blisters and fuzz. As a result, local swelling and deterioration of the mechanical properties of materials occur.

Tungsten was chosen as a radiation-resistant structural material in the protective coatings of ITER devices because of its good resistance to erosion by ions and recharged particles in comparison with other materials and because of its heat resistance [6]. Tungsten has high energy threshold for physical sputtering, low tritium retention, and does not form hydrides or compounds with deposited tritium [7]. In addition, it has the highest melting point of all metals, low vapor pressure, high recrystallization temperature (1720 K), good thermal conductivity and retains strength at high temperature. This combination of physical and mechanical properties makes it suitable for use as a coating for high heat flux components. However, Jiang at al. in [8] pointed out that the disadvantages of tungsten, such as brittleness at low temperatures (the transition temperature from plastic to brittle state is ranging from 370 K to 670 K) and high weight, make difficult its processing and welding. The operating temperature of the plasma-facing (PFC) tungsten components must be above the temperature of transition.

Brossa at al. considered Ta as a radiation-resistant structural material in the protective coatings of ITER components [9]. Tantalum has a very low sputtering coefficient, low tritium retention, high melting point, low vapor pressure and good mechanical properties at low and high temperatures. Like other refractory metals, Ta does not form an arc. Significant resistance to thermal fatigue, high recrystallization temperature (1620 K), low brittle-ductile transition temperature and resistance to thermal shock permit to use tantalum in such structural components as the first wall and blanket in a tokamak, despite the high Z.

Manufacturing of products of complex shape from pure and massive tungsten or tantalum is a technologically complex and, as a result, expensive task. The promising solution for their use as PFM is to coat a functional or heat-removing PFC with a layer of these materials. Recent studies [5, 10] have shown that the most promising candidates for PFM will be nanocrystalline coatings for PFC. For such PFMs, it is possible to adapt their radiation resistance by creating a high density of grain boundaries, which are considered to be defect absorbers.

For practical use of W and Ta coatings in ITER devices, at present the study of the processes of retention and release of ion-implanted hydrogen isotopes and helium in them is very important. Analysis of the formation of matrix radiation defects, their interaction with deuterium and helium, and the influence on their behavior permits to study many fundamental parameters and regularities and determine the radiation resistance of coatings to the influence of flows of hydrogen isotope and helium ions under real ITER conditions. The development of methods for obtaining W or Ta coatings of various thicknesses with high adhesion rates, good structure and properties is also an important task.

EXPERIMENTAL PROCEDURE

In practice promising PFM for ITER tungsten or tantalum can be used as coatings deposited on PFCs. The following technologies of metal coating deposition could be used: vacuum plasma spray (VPS), plasma deposition in inert gas (IPS), chemical vapor deposition (CVD), physical vapor deposition or materials vapor deposition (PVD), magnetron sputtering of material (MS), combination of magnetron sputtering of material with ion implantation (CMSII). PFCs most often are structures from carbon based materials - CFC (carbon-fiber composite), copper, stainless steel, etc. At that, the thermal conductivity of W and Ta coatings on the PFC should be high [11]. Boir-Lavigne et al. showed relation of the thermal conductivity of W coating on its microstructure [12]. Tungsten coatings deposited on graphite by the VPS, CPS and PVD methods were investigated and tested at high thermal loads [13, 14]. Smid et al. compared tungsten coatings deposited by PVD, CVD, and VPS methods on a copper substrate [15]. According to [12, 15], the VPS method was recommended for objects in areas with a lower heat flux (below 5 MW/m²), its advantages were high metal deposition rates and a high recovery probability. CVD coatings demonstrated heat flux resistance up to 20 MW/m² [15]. However, high thermal conductivity of coatings deposited by CVD as well as PVD methods did not necessarily mean good thermal shock resistance. In addition, the disadvantages of both the latter methods were low deposition rates and high costs. In tests with a very high heat flux, W coatings with thicknesses of 0.5 μm, 1–3 μm, and 10 μm deposited by the CMSII on a CFC substrate displayed the best result [16, 17]. In [7, 18], W coatings deposited on a CFC substrate by the same method withstood tests up to 23 MW/m² (1.5 s) and a cyclic load with 200 pulses of 10.5 MW/m² (5 s) without delaminating. The surface temperature during the tests was above 2273 K. The following factors determined the obtained results: nanostructure of W coatings and a Mo interlayer, which was introduced between the coating and the substrate, removed the stresses induced in the coatings by high-energy ion bombardment. Detailed characteristics of W coatings deposited on a CFC substrate by the CMSII method were given in [7, 19, 20]. TEM (transmission electron microscopy) studies [19, 20] showed the formation of extremely dense nanostructure with crystallites less than 10 nm in size and without any pores. Ruset et al. in [7] showed that the introduction of Mo interlayer with a thickness from 2 μm to 3 μm reduced the arising at the interface stress by ~ 40%. Removing the stress at the Mo/W interface and inside the W coating permitted to fabricate coatings with a thickness of 10–30 μm. The successful use of molybdenum as an intermediate layer was also noted in [19]. This seemed to be due to the correction of the thermal expansion mismatch between CFC and W. Re also was successfully used as an intermediate layer [21, 22]. It did not form carbides, had a high melting temperature and could act as a diffusion barrier between carbon and tungsten.

In [23–26] the results of studies with optical microscopy, SEM (scanning electron microscopy), TEM, X-ray diffraction, etc. of adhesion, structure, and resistance to high thermal loads of W coatings, deposited by various methods on CFC, stainless steel, and copper substrates, were presented. Pranevičius in [23] described the preparation of W coatings on stainless steel and graphite substrates changing the deposition parameters in the MS method for obtaining coatings with improved properties. W films less than 2 μm thick on stainless steel and graphite substrates showed good adhesion in a wide range of deposition parameters: working gas pressure Ar from 0.4 Pa to 2 Pa, negative bias from 50 V to 150 V, substrate temperature from 320 K to 470 K and a distance to the substrate of 0.05–0.07 m. Adhesion to the same substrates of W films with the thickness of more than 5 μm worsened. SEM studies showed a columnar microstructure of the W films. The electrical resistance ρ of the films measured with a four-point probe scheme was 0.058 μΩ · m, and less than ρ of the bulk W. Mechanical properties, such as Vicker micro hardness, erosion resistance, and wear of the W films depended on their deposition parameters. W films obtained under intense low-energy ion irradiation with a high flux density demonstrated an improvement in mechanical properties.

Tungsten coatings VPS deposited on a copper substrate were studied by Niu et al. [24]. For improving the adhesion between the coating and the substrate, an additional intermediate layer of tungsten - copper composite was deposited. The microstructure and composition of W coatings were analyzed using SEM, TEM, XRD, and EDX methods. The structures of the coatings were mainly lamellar and contained columnar crystalline grains. Pores of irregular and linear shape were observed, they were formed as a result of unmelted or semi-molten splashes of W and the gases trapping. The porosity reached ~ 4%. Distinguished interfaces were found, consisting of tungsten oxide or micro pores between layers. The imperfect microstructure of the tungsten coatings resulted in their low thermal and electrical conductivity.

Nanostructured W coatings of thicknesses from 9 μm to 12 μm were CMSII method deposited on CFC substrates [25, 26]. The grain size was less than 10 nm with the preferred orientation of {200} planes parallel to the surface and {110} planes perpendicular to the surface. W coatings of 10 μm thick showed excellent thermal resistance at high heat fluxes compared to similar coatings deposited by traditional PVD or CVD methods.

Alimov and Scherzer also reported about pores in W coatings [27], several types of coatings were studied:

– CVD-W coating 15 μm thick on a copper substrate, which had a textured structure with a grain size of 2–3 μm, a porosity not exceeding 0.04%, and a surface roughness of about 1 μm;

– IPS-W coating 200 μm thick on a graphite substrate, having a lamellar structure, porosity 15–20% and surface roughness $\sim 18 \mu\text{m}$;

– VPS-W coating 500 μm thick on a graphite substrate with an intermediate layer of rhenium from 10 μm to 20 μm thick. The last coating after the deposition process was heated for 1 h at a temperature of 1700 K; that resulted in the structure recrystallization with a porosity of ~ 8 –9% and a surface roughness of about 4 μm .

Bizyukov et al. [28] in MS-W films on substrates of polished pyrolytic graphite studied their mechanical and thermal properties, surface erosion, and retention of hydrogen isotopes. For reducing mechanical stresses occurred on the coating-substrate interface, an intermediate layer of copper was deposited.

The result of studies of Ta coatings deposited by CVD and VPS methods on Al, Cu, AISI 316L, and Inconel 600 substrates were represented in [9]. The mechanical properties of Ta coatings and the conditions that improve their adhesion to the substrates were studied. The authors showed that tantalum coatings could be used to reduce the erosion of components subjected to short-term but intense thermal loads. CVD and VPS were good methods for their deposition with good adhesion on various metals. Under powerful heat fluxes CVD-Ta coatings were destroyed only after the melting of the base material of the substrate. Powerful mechanical deformation led to the formation of cracks in the VPS-Ta coatings, but without detachment from the substrate. The presence of porosity of VPS-Ta coatings enhanced the process of hydrogen isotopes and helium release into vacuum. Taylor and Green considered the possibility of using Ta coatings of 1 mm thick, VPS deposited on ferritic steel pipes for the first wall of the ICF reactor chamber [29]. The coatings demonstrated good mechanical properties that completely remained under low-cyclic high-temperature loads concerned with the reactor work.

The dependence of mechanical properties of Ta coatings on their structure was showed in [30]. The authors studied the evolution of the structure of deposited tantalum films to select the parameters of MS deposition of high-quality single-phase Ta coatings with thicknesses from 1 μm to hundreds μm on steel. Bulk tantalum had a crystallographic bcc structure, also known as the α -phase, hard and ductile, with a Knoop hardness of 300–400 and a relatively low electrical resistivity ($0.135 \mu\Omega \cdot \text{m}$). In deposited tantalum films ([31, 32]) tetragonal structure, also known as the β phase, was identified. This metastable phase was hard (Knoop hardness greater than 900), brittle and had an electrical resistivity of an order of magnitude higher than the α -phase. The deposition of high-quality thick tantalum films was problematic because the β -phase dominated in the coatings on most substrates at different processing parameters. To stimulate the predominant growth of the α -phase, the choice of special deposition conditions, substrates or the deposition of interfacial layers were required [33, 34]. In [21, 30], the growth of the pure α -phase of tantalum was achieved by heating steel substrates during the deposition to the temperature of $\sim 670 \text{ K}$, at which the properties of steel did not deteriorate.

The authors of this work studied tungsten and tantalum coatings deposited by the MS method on stainless steel. The deposition technique was described in details in [35–37]. Coatings were prepared by sputtering W or Ta targets in Ar atmosphere at the pressure of 1.0 Pa. The coatings were deposited on a 0.8 mm thick substrate with a Ti layer of less than 10 nm thick predeposited on it at the temperature $T = 600 \text{ K}$ and at the rate of $0.6 \text{ nm} \cdot \text{s}^{-1}$. In some cases, stainless steel with Ti sublayer up to 10 nm thick was additionally coated with 3 μm thick Cu layer, then a Ti sublayer less than 10 nm thick, and then W layer. The thicknesses of the W coatings were in the range 0.1–1.0 μm or 2.2 μm . The Ta coatings were 1.5 μm thick. The W and Ta coatings had a polycrystalline bcc structure with an average grain size from 20 nm to 60 nm and were considered as nanocrystalline.

RESULTS AND DISCUSSION

Hydrogen (deuterium) implantation, retention and release from tungsten coatings

Proper design of a fusion reactor is not possible without understanding the hydrogen isotopes (protium, deuterium, and tritium) retention and recycling for plasma-facing components [38]. Recycling is the return of cold hydrogen into plasma. As a result, the plasma temperature decreases. Hydrogen isotopes trapping is especially important for tritium. The retention of great amounts of tritium in components facing the reactor plasma increases the cost of fuel in the reactor and offers a safety problem. Initial defects existing in the PFM and defects produced by thermonuclear neutrons and energetic ions of hydrogen isotopes can trapped atoms of these gases in the implantation zone. The traps eventually become saturated, and entrapped hydrogen isotope atoms disperse from the implantation zone, going either deeper into the material or toward the front surface. Atoms reaching any surface are not guaranteed to be released immediately. On a plasma-facing surface, except at extremely high temperatures, recombination of atoms into molecules should occur before their release is possible. A high recombination rate factor results in a rapid release of atoms reaching the surface, effectively reducing the concentration of hydrogen isotopes on the surface to zero. For hydrogen in bulk tungsten at 500 K, the recombination rate coefficients 10^{-29} – $10^{-31} \text{ m}^4/\text{s}$ have been determined by many researchers. In the described below works [10, 14, 27, 28, 36, 37, 39–51] much attention has been paid to the processes of retention and release of hydrogen isotopes in tungsten coatings proposed as protect for components facing the plasma (the first wall, divertor, antenna mirrors).

W plate 1.5 mm thick and nanocrystalline tungsten film 10 μm thick, exposed to low-energy (78 eV) deuterium plasma with $\text{D}^+ > 85\%$ at the fluence of $3.9 \times 10^{24} \text{ m}^{-2}$, were analyzed in [10]. The polycrystalline W plate with purity 99.95% and density 99% from Advanced Technology & Materials Company, Ltd. was prepared by powder sintering. The tungsten film was deposited on the polycrystalline W plate (which was preliminarily kept heated to 750 K for the first 2 h

and then the temperature was lowered to 520 K for the next 8 h) by magnetron sputtering the W target in argon atmosphere (99.99% purity) at the pressure of 1 Pa on the device KYKY MP 650-A. The deposition rate was about 1 $\mu\text{m}/\text{h}$.

The W films had a grain size of less than 100 nm, a preferred (211) plane orientation, and a columnar structure perpendicular to the substrate. Samples from a polycrystalline W plate had the average grain size of about 5 μm . They were prepared by powder sintering. The samples were subjected to heat treatment at 1273 K for 1 h to relieve stress and degassing. They were polished to a mirror surface. Then, all samples were subjected to ultrasonic cleaning with acetone, alcohol, and boiled water for 15 min. The samples prepared in this way were used for irradiation in deuterium plasma as well as a substrate for the deposition of W films,.

For comparison the results for the W plate and the deposited W film, both types of samples were irradiated simultaneously. Changes in surface morphology and deuterium retention in both samples were determined using SEM and TDS, respectively. After exposure to deuterium plasma, several blisters with a size of several micrometers were observed on the surface of the W plate. The surface morphology of the tungsten film after exposure to deuterium plasma did not change (see Figure 2).

The trapping of deuterium in both samples was determined with a special installation, in a chamber evacuated to a pressure of less than 5×10^{-6} Pa. The sample was heated to 1373 K at the rate $\alpha = 1$ K/s. The desorbed gases components, including H_2O , O_2 , HDO, HD, and D_2 , were analyzed by a quadrupole mass spectrometer. The amounts of D_2 and HD were measured using a calibrated leak. The yield of HD relative to D_2 was below 4%. Absolute values of the HDO and D_2O signals were very low. Thermal desorption spectra of D_2 from both samples were compared. The total retention of deuterium was estimated by integrating the D_2 and HD thermal desorption spectra.

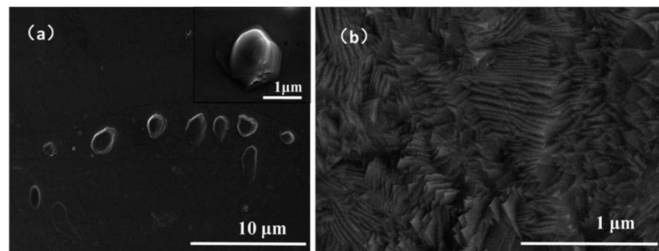


Figure 2. Surface morphologies of two different samples exposed to deuterium plasma: (a) polycrystalline tungsten plate and (b) nanocrystalline tungsten film [10].

The deuterium thermal desorption spectra for the tungsten plate and for the tungsten film differed significantly (see Figure 3). For polycrystalline tungsten the D_2 spectrum had two peaks with a maximum at the temperatures $T_{\text{max}} = 490$ K and 670 K, respectively. They could be associated with deuterium trapping by grain boundaries (GBs) and by dislocations and vacancies. Noise peaks in the vicinity of 490 K could be attributed to the explosive release of deuterium due to the rupture of gas-filled blisters during thermal desorption. The total amount of trapped D_2 was $2.4 \times 10^{20} \text{ m}^{-2}$.

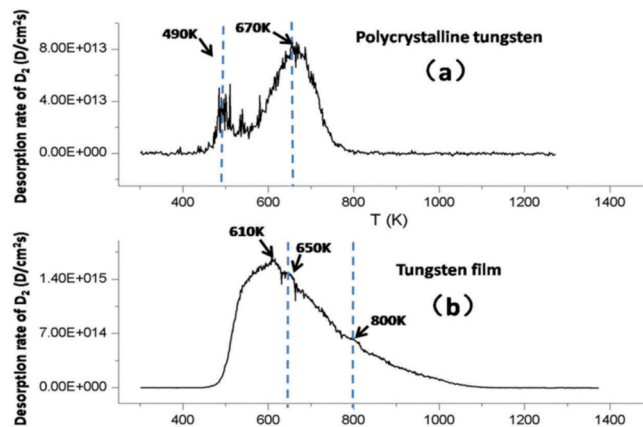


Figure 3. TDS spectra of deuterium from: (a) polycrystalline W plate, (b) nanocrystalline W film (sample heating rate $\alpha = 1$ K/s) [10].

TDS spectrum for the tungsten film had no main emission peak with a maximum at the temperature $T_{\text{max}} = 670$ K. It was characterized by a wide temperature range of D_2 release from 500 K to 1100 K and two weak peaks at temperatures of ~ 650 K and ~ 800 K. The main peak with $T_{\text{max}} = 610$ K and a peak near 650 K could be related to deuterium trapping on GBs and by dislocations and vacancies, respectively. For the higher temperature peak at 800 K deuterium trapping sites could be pores or the inner side of the vacancy cluster. The long desorption tail after 820 K, extending up to 1100 K, was attributed to the deuterium release from defects at different distances from the surface, since a large number of GBs acted as preferred diffusion channels for deuterium. The total amount of retained deuterium in the tungsten film was $6.9 \times 10^{21} \text{ m}^{-2}$, which was 30 times higher than for the W plate. So the form of the deuterium thermal desorption spectra

and the amount of trapping deuterium for the tungsten film and the tungsten plate differed significantly. The tungsten film had a nanocrystalline structure. The behavior of deuterium during irradiation was largely affected by the high density of grain boundaries. The W film showed a typical columnar structure perpendicular to the substrate, which could be the reason for the diffusion of deuterium into the material. Many intrinsic defects and a high density of grain boundaries could significantly increase the deuterium saturation threshold and deuterium retention. In addition, compressive stresses in MS-deposited tungsten film could be unfavorable for the formation of blisters and suppressed their formation to some extent.

Garcia-Rosales et al. studied trapping and thermal desorption of deuterium implanted in rolled tungsten and in two types of W coatings [14]. Both coatings were deposited on fine grain graphite substrates by the plasma spray method. The first, PVS-W coating 500 μm thick, provided by Plansee AG, was deposited in a vacuum. The second, CPS-W sample 200 μm thick was provided by CEN Cadarache (France) and was deposited in an Ar atmosphere. 10 μm thick intermediate layer of rhenium was deposited on the graphite substrate before chemical vapor deposition of the PVS-W coating to prevent the diffusion of graphite into a tungsten coating and the formation of tungsten carbide. After the coating deposition, the first sample was annealed at high-temperature (for 1 h at 1670 K). At that the coating recrystallized. No intermediate rhenium layer was in the CPS-W coating, and the sample was not high-temperature annealed. The studied samples had different porosity: rolled W at the level of 1%, PVS-W of 8–9%, CPS-W of 19–20%. Since the deposition and subsequent cooling of the deposited layer in a vacuum with an inert gas as the main component of the residual gas, no tungsten oxides were formed on the inner surfaces of the cavities.

The samples were irradiated with D_3^+ ions (300 eV) at a room temperature. Fluences were from $1 \times 10^{21} \text{ m}^{-2}$ to $1 \times 10^{22} \text{ m}^{-2}$. The flux density of D^+ ions (100 eV) was $4.4 \times 10^{19} \text{ m}^{-2} \cdot \text{s}^{-1}$. The thermal desorption spectra of deuterium for rolled W was got at a heating from room temperature to 1400 K with the rate $\alpha = (5 \pm 0.5) \text{ K/s}$ and had two peaks with $T_{\text{max}} = 475 \text{ K}$ and 850 K, while the concentration of trapped deuterium was $C = 1.6 \times 10^{20} \text{ m}^{-2}$. TDS spectra of deuterium from PVS-W also had two peaks with $T_{\text{max}} = 525 \text{ K}$ and $T_{\text{max}} = 670 \text{ K}$ and $C = 2.6 \times 10^{20} \text{ m}^{-2}$; for CPS-W in spectra there was one peak with $T_{\text{max}} = 612 \text{ K}$, and $C = 4.4 \times 10^{20} \text{ m}^{-2}$. The authors related the higher concentrations of trapped deuterium to higher porosity of the samples. Numerous gas-metal interfaces were in the volume of the porous material. The release of hydrogen from such a material could include multi-stage adsorption and desorption processes, thereby slowing down the release of deuterium from the sample. Deuterium was trapped mainly in pores and at grain boundaries.

Alimov and Scherzer studied the deuterium retention in tungsten materials with various structures at temperatures from 300 K up to 900 K using re-emission mass spectrometry (RMS), thermal desorption spectrometry (TDS), and nuclear reaction analysis (NRA). Five types of tungsten samples were investigated [27].

(i) W single crystal, 1.5 mm thick, made in State Institute of Rare Metals (Moscow) by double electron-beam zone melting. The surface was parallel to the (112) plane and was mechanically and electrochemically polished.

(ii) Hot-rolled tungsten (powder-metallurgy product, 95 at. % W, 3 at. % C, 2 at. % O, porosity $\leq 1\%$), 0.5 mm thick. The surface was also mechanically and electrochemically polished.

(iii) Chemical vapor deposited tungsten coating, CVD-W (99 at. % W, 1 at. % O), 15 μm thick, on copper substrate (from Institute of Physical Chemistry Moscow). The coating was deposited from a mixture of tungsten fluoride and hydrogen at the temperature of $\sim 900 \text{ K}$ and had a textured structure with grain size of 2–3 μm . The porosity did not exceed 0.04% and the surface roughness was about 1 μm .

(iv) Inert gas plasma sprayed tungsten coating, IPS-W (85 at. % W, 10 at. % C, 5 at. % O), 200 μm thick, on graphite substrate (from CEN Cadarache, France). The IPS coating was produced in Ar atmosphere at pressures up to atmospheric one and had a lamellar structure typical for a quick cool down of the molten droplets after spraying. Large macro-pores were present between the individual lamellae, and the porosity was 15–20%. Surface roughness was 18 μm .

(v) Vacuum plasma sprayed tungsten coating, VPS-W (99 at. % W, 1 at. % O), 500 μm thick, deposited on graphite substrate with an intermediate rhenium layer of thickness from 10 to 20 μm (from Plansee AG, Austria). As a result of the thermal treatment after the spray process (1600–1700 K for 1 h), the VPS coatings had a very homogeneous, recrystallized structure, which did not show the characteristic lamellar structure. The surface roughness of these coatings was low (about 4 μm) and the porosity was of the order 8–9%. In experiments the carbon substrate was partly removed.

Before implantation the samples were annealed at 1200 K for 10 min. The implantation was done with 4.5 keV D_3^+ ions. The flux density of 1.5 keV D-ions was $6.4 \times 10^{18} \text{ m}^{-2} \cdot \text{s}^{-1}$. Re-emission experiments were realized at temperatures of target 300, 600, and 900 K at fluences did not exceed $3.0 \times 10^{21} \text{ m}^{-2}$. TDS was carried out on samples implanted at target temperature of 300 K and at fluences equal to Φ^{sat} . The Φ^{sat} values were $0.35 \times 10^{20} \text{ m}^{-2}$ for W single crystal, $500.0 \times 10^{20} \text{ m}^{-2}$ for hot-rolled W, $0.20 \times 10^{20} \text{ m}^{-2}$ for CVD-W, $0.45 \times 10^{20} \text{ m}^{-2}$ for IPS-W, and $0.22 \times 10^{20} \text{ m}^{-2}$ for VSP-W. The samples were heated to 1200 K 5–10 min after the end of ion implantation and measurement of re-emission. In the temperature range 300–1100 K the heating rate was $4.6 \pm 0.4 \text{ K/s}$. Desorbed HD and D_2 particles were detected with a quadrupole mass spectrometer. 1–2 days after the re-emission measurements, the areas implanted at 300 K were analyzed using the D (^3He , p) α nuclear reaction (NRA) with 790 keV ^3He ion beam to determine the amount of retained deuterium within the limit of sensitivity of the NRA method which was approximately 0.7 μm . The fraction of deuterium emitted as HD molecules depended mainly on the target temperature and did not exceed 0.10–0.12 at 300 K, 0.15–0.20 at 600 K, and 0.21–0.24 at 900 K.

Deuterium retention varied from a low of $2 \times 10^{19} \text{ m}^{-2}$ for the CVD and single crystal samples at 900 K up to a high of $4.5 \times 10^{21} \text{ m}^{-2}$ for the hot-rolled material at 300 K. The re-emission approached unity most rapidly for the higher

temperatures and for the single crystals. The thermal desorption spectra for the different materials were very different. TDS spectra of deuterium from W samples implanted at 300 K at fluences Φ^{sat} for single crystal W, CVD-W and IPS-W samples were characterized by a broad temperature range of release, which could be explained by the superposition of two peaks with $T_{\text{max}} \approx 400$ K and $T_{\text{max}} \approx 690$ K respectively in the W crystal and with $T_{\text{max}} \approx 400$ K and $T_{\text{max}} \approx 590$ K for CVD-W and IPS-W. The thermal release from hot-rolled W showed a broad distribution, with maximum at $T_{\text{max}} \approx 530$ K and gradual decrease between 700 K and 1000 K. VPS-W had a sharp thermal release peak at $T_{\text{max}} \approx 350$ K, small desorption steps occurred at $T_{\text{max}} \approx 500$ K and $T_{\text{max}} \approx 600$ K and a small additional peak at $T_{\text{max}} \approx 950$ K.

Most of the implanted D seemed to be strongly trapped by defects such as vacancies or cavities that already exist initially or were created during implantation. The average concentration of D atoms in the radiation induced defects was estimated to be ≤ 0.1 D/W atomic ratio. However, most of the deuterium trapped in W samples during implantation was located far beyond the ion range. The authors suggested that some of the implanted D trapped in experiments in ion-induced vacancy type defects. Apparently, another part of the implanted D diffused into the bulk and was trapped by lattice imperfections (small cavities, impurity inclusions, etc.). The TDS spectrum peak at $T_{\text{max}} \approx 950$ K observed for VPS-W could be attributed to the release of chemisorbed atomic deuterium inside the cavities.

Bizyukov et al. investigated the influence of D^+ ion irradiation on erosion, mechanical stress, and deuterium retention in tungsten films by weight loss measurements and using ion-beam methods of analysis such as Rutherford back scattering (RBS) and nuclear reaction analysis (NRA) [28]. Tungsten films 200 nm thick were deposited on polished pyrolytic graphite with an intermediate 400 nm thick copper layer. The Cu/W interface with a sharp transition between the two materials provided good depth resolution for the RBS analysis. Copper did not form carbides and did not form an alloy with W. The metal films were MS deposited in an argon atmosphere. To minimize oxygen contamination of the deposited films, the residual pressure in the chamber was $\sim 10^{-5}$ Pa. The influence of irradiation with 9 keV D_3^+ ions at the flux density of $5 \times 10^{19} \text{ m}^{-2} \cdot \text{s}^{-1}$ was studied. Erosion of W coatings was studied at fluences in the range $(0.25-7) \times 10^{23} \text{ m}^{-2}$, measuring the decrease of the W layer thickness by RBS with ^4He ions. The authors analyzed trapping of deuterium in W films measuring the depth profile of the deuterium atomic concentration. The concentration D increased to $C \approx 10$ at. % just under the surface, D enriched zone extended to a depth of 70 nm, after that the concentration slowly decreased towards the W/Cu interface. After fluences above $2.2 \times 10^{23} \text{ m}^{-2}$ the SEM studies showed on the surface of the W films the formation and growth of blisters with a diameter from 5 μm to 50 μm . The blisters formed as a result of the detachment of the W layer at the W/Cu interface. At fluences well below $2 \times 10^{22} \text{ m}^{-2}$, the bubbles covered the main part of the irradiation spot. The authors concluded that W films represented an acceptable replacement of bulk tungsten in plasma-wall interaction experiments with significantly better diagnostic accessibility.

Oya et al. consider VPS-W on an F82H (Fe-8Cr-2W) substrate as a promising plasma-facing material [39]. The F82H substrate, developed by JAEA, had low activation. Tungsten powder was melted and sprayed on the substrate by an argon and hydrogen plasma jet in a vacuum chamber. The 1 mm thick VPS-W coating was produced by TOCALO Co. Ltd. in Japan at 873 K to prevent the F82H phase transition. The density of the VPS-W coatings reached 88% of pure tungsten. Sample surfaces were mechanically polished to a mirror finish and cleaned in an ultrasonic bath. The accumulation of deuterium in the VPS-W/F82H samples was realized by two different methods: by exposure to primary D^+ ions of plasma and by implantation of accelerated D_2^+ ions. During the exposure to D-plasma, the energy and flux of D^+ ions were respectively ~ 100 eV and $\sim 1 \times 10^{22} \text{ m}^{-2} \cdot \text{s}^{-1}$. The fluence was $6 \times 10^{25} \text{ m}^{-2}$. The sample temperature was 453 K. Then the sample was cooled to room temperature during 30 min. In a few minutes after the sample was transferred to the thermal desorption spectrometry device. TDS was done from room temperature to 773 K at the heating rate of 10 K/min.

3.0 keV D_2^+ was implanted into VPS-W/F82H with the flux of $1 \times 10^{18} \text{ m}^{-2} \cdot \text{s}^{-1}$ up to the fluence $\sim 1 \times 10^{22} \text{ m}^{-2}$ at room temperature in Shizuoka University. After D_2^+ ions implantation, the sample was transferred to the TDS chamber without exposure to air. TDS was done at a heating rate of $\alpha = 0.5$ K/s to 1173 K. Surface morphology was observed with an optical microscope before and after exposure to D-plasma and after TDS. The cross section of the near-surface region of the sample was observed by scanning electron microscopy and transmission electron microscopy with the focused ion beam (FIB). The cross-sectional image of VPS-W/F82H showed that most of the tungsten grains were columnar with dimensions of 1 $\mu\text{m} \times 0.5 \mu\text{m}$. In addition, a porous structure was found around the grain boundaries and on the interface of the VPS-W layers. It was ascertained that the retention of deuterium for polished VPS-W/F82H after exposure to plasma was lower than for polycrystalline tungsten (see Figure 4).

SEM/TEM observation indicated that porous structure around the grain boundaries and interface between VPS-W layers would be a potential D desorption path, leading to the low D retention. In the case of D_2^+ ion implantation, the shape of D_2 TDS spectra was nearly identical to that for plasma-exposed VPS-W/F82H, but the amount of D_2 was quite higher for unpolished VPS-W/F82H, indicating that most of D was trapped by the oxide layer produced during VPS. Reduction of surface area via the polishing process also reduces D retention for VPS-W/F82H. Controlling the chemical states of the surface was important in reducing tritium retention for materials used in future fusion devices.

Niu et al. studied the chemical states and deuterium retention behavior in VPS-W coatings and elucidate the mechanism of interaction between deuterium and tungsten coatings [40]. Tungsten coatings about 300 μm thickness were prepared on copper alloy substrates using a vacuum plasma spraying system (A-2000, Sulzer Metco, Switzerland). Argon and hydrogen were used as plasma source gases. Tungsten coatings had the original (un-polished) or polished surface.

The test setup consisted of two vacuum chambers. One of them was equipped with thermal desorption spectroscopy and a deuterium ion gun, and the other was equipped with X-ray photoelectron spectroscopy (XPS) (ESCA 1800 series, manufactured by ULVAC PHI Inc.). The Al K α was used for X-ray source. Both chambers were connected to each other via a gate valve. The sample was mounted on the holder with a ceramic heater. To remove gaseous impurities such as H₂O, O₂, and H₂, both chambers were evacuated to a vacuum of less than 10⁻⁷ Pa using ion pumps, and then the sample was preheated at 1173 K for 10 min under ultrahigh vacuum. The XPS measurements were carried out after the heat-treatment.

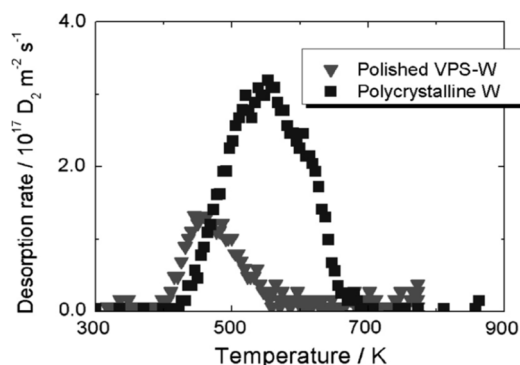


Figure 4. TDS spectra of deuterium for the D plasma-exposed VPS-W/F82H and polycrystalline W: $\alpha = 0.5$ K/s [39]

One keV D₂⁺ ions were implanted into samples at room temperature with the flux of $1.0 \times 10^{18} \text{ m}^{-2} \cdot \text{s}^{-1}$ and fluence up to $1.0 \times 10^{22} \text{ m}^{-2}$. To study the thermal desorption behavior of implanted deuterium, TDS experiments were carried out after the implantation by heating the samples up to 1150 K at the heating rate of 0.5 K/s. The desorbed gases were analyzed with a quadrupole mass spectrometer. The XPS measurements were also carried out after D₂⁺ implantation to characterize the chemical structure change. The XPS results of the original samples showed that both chemisorbed oxygen (in the O-O bond configuration) and chemical reacted oxygen (in the W-O bond configuration) existed on the surface and inside the tungsten coatings. The amount of chemisorbed oxygen inside the coating was much less compared to its amount on the surface of the coating. The chemical states of oxygen in tungsten coatings did not change after D₂⁺ implantation. But the implantation process reduced the oxygen content in the coatings due to chemical sputtering. The results of TDS of D₂ for tungsten coatings with the original and polished surfaces showed that gas was mainly desorbed in two temperature intervals ranging from 300 to 700 K and from 800 to 1150 K, respectively. For bulk W irradiated with 3 keV D₂⁺, the deuterium desorption peak located at 300–700 K, was also observed, which corresponded to the deuterium thermodesorption from intrinsic and ion-induced defects, and there was no desorption peak at higher temperatures of 800–1150 K (see Figure 5a)).

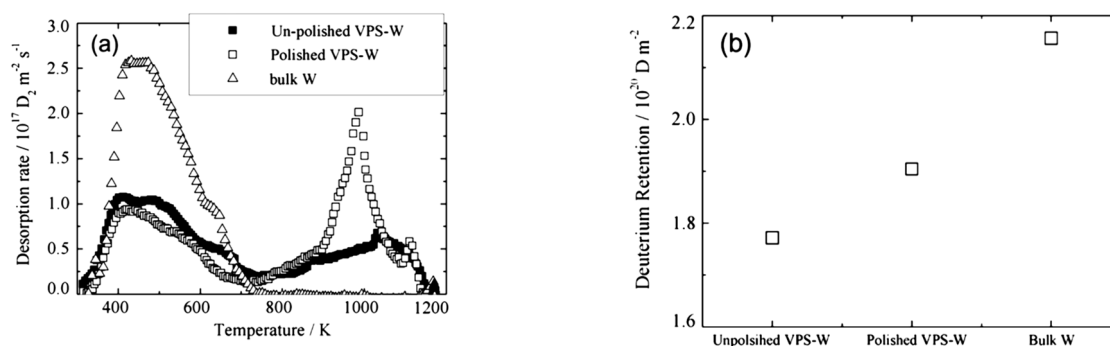


Figure 5. (a) TDS spectra of deuterium for D₂⁺ implanted W coating and bulk W and (b) comparison of deuterium retention data obtained from current TDS experiments: $\alpha = 0.5$ K/s [40]

It was considered that the deuterium desorption peak at higher temperature of 800–1150 K was due to the deuterium interaction with an oxygen impurity. The concentration C of deuterium trapping in W coatings was lower than in bulk tungsten, for which $C = 2.15 \times 10^{20} \text{ m}^{-2}$ and the trapping coefficient $\eta = 0.022$. The C and η values were: for the polished sample $C = 1.9 \times 10^{20} \text{ m}^{-2}$ and $\eta = 0.019$, and for unpolished one $C = 1.8 \times 10^{20} \text{ m}^{-2}$ and $\eta = 0.018$. The authors explained this difference in the results by the presence of oxygen in the W coatings (see Figure 5b)).

Zhang et al. analyzed 99.95% pure W films about 800–900 nm thick, deposited by magnetron sputtering on various substrates, including quartz, silicon, graphite and copper [41]. The effect of hydrogen plasma irradiation of the thin films was investigated. The samples were exposed to 50 keV hydrogen ion beam for different fluences from $2 \times 10^{21} \text{ m}^{-2}$ to $2 \times 10^{23} \text{ m}^{-2}$. The surface structure and morphology of post-irradiated samples were studied by XRD and SEM. W films, deposited on copper, crystallized after annealing at 1100 K for 1 h. When the hydrogen fluence reached $2 \times 10^{23} \text{ m}^{-2}$, on the surface of W films on copper substrates bubbles were observed, which could be caused by diffusion and retention of hydrogen at the interface between the film and substrate.

Anderl et al. reported studies of hydrogen penetration in samples of bulk tungsten and tungsten coatings on copper substrates both irradiated with a beam of 3 keV D^+ ions at a flux density of $(4-5) \times 10^{19} \text{ m}^{-2} \cdot \text{s}^{-1}$ [42]. The experiments included measurements of the re-emission and penetration rates of deuterium at temperatures from 638 K to 825 K. The time dependences of re-emission and penetration of deuterium into the sample were measured using a quadrupole mass spectrometer calibrated with deuterium standard leaks. Twenty-five-mm diameter discs of copper, tungsten, and copper with a tungsten coating were investigated in this work. Copper specimens were machined to a thickness of 0.5 mm from high-purity OFHC copper rod, and they were polished to a mirror finish using conventional metallurgical techniques. Tungsten specimens were punched from high-purity foil material (99.95% W, reduction-rolled, powder-metallurgy product) with thicknesses of 25 μm and 50 μm . The tungsten-coated copper specimen was made by sputter-deposition of a 0.5 μm thick tungsten layer onto a polished 0.5 mm thick copper disk heated to 773 K during the coating process.

From measurements, diffusion constants and surface recombination coefficients were obtained. The authors draw the following conclusions. A coating of a low solubility material (W) deposited on a higher solubility material (Cu) should result in a step increase in the deuterium concentration across the interface and lead to higher permeation than in samples of comparable thickness with uniformly high solubility. Therefore, coatings of materials with high rather than low solubility could be effective in reducing permeability.

Ogorodnikova et al. studied deuterium retention in different tungsten coatings on carbon substrates for various incident ion energies ranging from 20 eV to 200 eV per deuterium atom and fluences in the range from $1 \times 10^{23} \text{ m}^{-2}$ to $2 \times 10^{25} \text{ m}^{-2}$ [43]. The targets were irradiated with deuterium ions at the IPP laboratory by the mass-separated beam with the flux of $10^{15} \text{ m}^{-2} \cdot \text{s}^{-1}$ as well as with deuterium plasma providing the flux of $10^{16} \text{ m}^{-2} \cdot \text{s}^{-1}$. Irradiation was done at various sample temperatures from 320 K to 650 K. The depth profiles of deuterium in the W coatings were measured up to the depth of 6 μm using nuclear reaction analysis (NRA), and the total amounts of retained deuterium were determined by thermal desorption spectroscopy. It was shown that deuterium retention significantly depended on the microstructure of each W coating. The retention of deuterium in the 7 μm thick W coating produced by the CMSII method was higher compared to the 4–5 μm thick PVD-W coating and the 200 μm thick VPS-W coating for all investigated energies and sample temperatures up to 650 K.

Katayama et al. prepared tungsten coatings on W substrates at 294 K and 773 K by hydrogen radio-frequency (RF) plasma sputtering of W targets [44]. The thickness and density of the W coatings were 970 nm and 10 kg/m^3 on average, respectively. The porosity of the coatings was 0.45. In EDX analysis, no oxygen signal was detected from them. Samples were irradiated with 1 keV D^+ (2 keV D_2^+) ions to the fluence of $2 \times 10^{21} \text{ m}^{-2}$ at 294 K or 773 K. Two samples (W coatings on W substrates) and the W substrate for comparison were picked out for irradiation. Each sample was cut in half together with substrates. One of them was irradiated with deuterium ions and then analyzed by TDS. Another one was tested by TDS without exposure to deuterium ions. In both experiments, the temperature increased to 1273 K at a rate of 1 K/s. The D_2 thermal desorption rate was calibrated by a standard helium leak, taking into account the relative ionization cross section. The temperature dependences of deuterium retention in different types of samples were studied.

On the surface of W coatings deposited at substrate temperatures of 294 K and 773 K, blisters of the size from 5 μm to 15 μm were observed both before and after irradiation with 1 keV D^+ ions to the fluence of $2.0 \times 10^{21} \text{ m}^{-2}$. The cross section observation showed that the formation of blisters took place not at the boundary between the W coating and the substrate, but inside the coating. Blister formation suggested that hydrogen was implanted into the growing surface with high flux and migrated into the deeper region and gathered in voids. The blisters were ruptured after TDS of D_2 from samples.

The results of HD and D_2 release from W coatings irradiated with D^+ ions were as follows. From the W coating irradiated at 294 K D_2 release started at 320 K, while the release of HD started at 340 K, and a large peak of D_2 release was observed at 330 K. For W coating irradiated at 573 K deuterium release started at 420 K and continued up to 1130 K with the peak at the temperature of about 570 K, that corresponded to the irradiation temperature. A small peak at 1090 K was due to the release of deuterium from broken blisters. From the W coating irradiated at 773 K, deuterium released in the temperature range from 540 K to 970 K, and the peak had maximum at $T_{\text{max}} = 840 \text{ K}$. The tiny peak at 1120 K was supposed to be the result of the deuterium release from broken blisters. The deuterium retention (D/W ratio) was 0.0031 for 294 K, 0.0021 for 573 K, and 0.0004 for 773 K, i.e. decreased with increasing sample temperature during irradiation. The decrease in D/W with T increasing from 294 K to 573 K was lower than at increasing from 573 K to 773 K, although the deuterium trapping capacity at 294 K was greater than at 573 K. This was because deuterium, implanted at 294 K, was trapped only in a narrow region near the surface. It was considered that deuterium implanted at 573 K and 773 K penetrated deeper into the coatings and remained in the trap sites at both temperatures.

At heating the W coatings, both non-irradiated and irradiated at 294 K with deuterium ions, hydrogen release was observed. The ratio H/W was 0.073 for the unirradiated coating and H/W = 0.11 for the irradiated coating. During irradiation of the W coating at 773 K, part of hydrogen was released, and the H/W value was 0.05 instead of H/W = 0.11. The peak of release at the temperature of about 1100 K was explained by the rupture of blisters. The amount of hydrogen released at the temperature of about 1100 K from the irradiated sample was greater than from the unirradiated one. This indicated that hydrogen migrated in the coating during irradiation or during TDS measurement, and part of the hydrogen entered into the blister. The D/W ratio at ion irradiation under existing conditions was significantly less than H/W during the sputtering-deposition of W coating. Authors considered that this was due to the fact that the fluence of hydrogen ions in the process of sputtering-deposition was much greater than the fluence of deuterium ions in the process of D^+ ions irradiation.

The results of the HD and D₂ release from the W foil (substrate) irradiated with D⁺ ions were as follows. The deuterium signals (HD and D₂) from the W foil irradiated at 773 K were below the detection limit. From the W foil irradiated at 294 K, relatively large HD and D₂ peaks were observed at 470 K and 480 K, respectively. From the W foil irradiated at 573 K, the release of HD began at 460 K and two peaks were observed at 1020 K and 1150 K. The trapping of deuterium in the W coating irradiated at 294 K was 2.8 times greater than in the W foil. The deuterium retention in the W coating irradiated at 573 K was 17.3 times greater than in the W foil.

This work authors Bobkov et al. studied tungsten coatings of different thicknesses deposited on stainless steel substrates [36, 37, 45–49]. The stainless steel substrate 0.8 mm thick had the following composition (at%): 20 Cr, 70 Fe, 8.5 Ni, and 1.5 Ti. W coatings were irradiated with D⁺ ions to different fluences and at different temperatures of the bombarded target. Coatings were MS deposited by sputtering W target in Ar atmosphere at the pressure of 1.0 Pa on substrate at $T = 600$ K at the rate of $0.6 \text{ nm}\cdot\text{s}^{-1}$ with Ti layer less than 10 nm thick pre-deposited on it. In some cases, stainless steel substrate with Ti sublayer up to 10 nm thick was additionally coated with 3 μm thick Cu sublayer, then again Ti sublayer less than 10 nm thick, and then W layer. The thicknesses of the W coatings were or in the range of 0.1–1.0 μm or 2.2 μm . The deposition technique was described in detail in [35]. The structure, surface morphology, macrostresses of W coatings and radiation damages formed in them were studied with electron microscopy, X-ray diffractometry and thermal desorption spectrometry. The W coatings had a polycrystalline bcc structure with an average grain size from 20 nm to 60 nm. This was the nanocrystalline grain size for W, as it did not exceed 100 nm. The W coatings had different internal macrostresses depending on the thicknesses of the tungsten coatings and the multilayer nature of the substrates. They could be compressive as well as tensile. There was tensile macro stress $\sigma = +0.64$ GPa in the compositions (SSt. + Cu + W (2.2 μm)). Compressive macrostress $\sigma = -4.5$ GPa was in (SSt. + Cu + W (0.5 μm)). In the compositions (SSt. + W (2.2 μm)) and (SSt. + W (0.5 μm)) there were macrostresses $\sigma = -8.0$ GPa and $\sigma = -10.0$ GPa respectively. The copper sublayer reduced internal compressive stresses. In the listed works [36, 37, 45–49], the authors studied the types of formed radiation defects, their relationship with defects in the tungsten crystal lattice, mechanisms of their migration and annealing, including release of implanted deuterium from the sample into vacuum. Spectra of deuterium thermal desorption were analyzed and temperature intervals for the release of D₂ from the coatings into vacuum were cleared. Concentrations and trapping coefficients of implanted deuterium in coatings were determined. Changes in the microstructure of the W coatings and the morphology of their surface in the result of ion irradiation and subsequent heating were observed. To clarify the radiation stability of the system “W-film-implanted deuterium”, we studied the influence of coating thickness [45, 46, 48], the type of composite system (determined by the multilayer nature of the substrate) [45, 46], fluences of D⁺ ions irradiation [46, 47, 49] and sample temperature during bombardment [36, 37] on the above parameters, characteristics, physical and structural properties of the coatings.

The processes of implanted deuterium trapping, retention and thermal desorption, formation and annealing of radiation defects in the crystal lattice of W coatings irradiated with 5.0 keV and 10 keV D⁺ ions at flux densities of $3.0 \times 10^{16} \text{ m}^{-2}\cdot\text{s}^{-1}$ and $3.0 \times 10^{17} \text{ m}^{-2}\cdot\text{s}^{-1}$ were studied [45–49]. Fluences of ions irradiation Φ were from $0.05 \times 10^{22} \text{ m}^{-2}$ to $1.65 \times 10^{22} \text{ m}^{-2}$ and the samples were at room temperature ($T_0 = 290$ K) during the bombardment. Tungsten coatings with thicknesses from 0.1 μm to 2.2 μm were deposited on stainless steel substrates both with an intermediate copper layer (SSt. + Cu + W) and without it (SSt. + W). The influence of the W coating thickness, the type of composite system, and the fluence of D⁺ ions irradiation on the behavior of spectra of D₂ thermal desorption into vacuum were investigated. The influence of these parameters on the concentration C [m^{-2}] or C [at. %] and the deuterium trapping coefficient $\eta = C/\Phi$ was also analyzed. For low fluences $\Phi \leq 0.5 \times 10^{22} \text{ m}^{-2}$, thermal desorption of deuterium from W coatings of compositions (SSt. + Cu + W (μm , nm)) and (SSt. + W (μm)) had mainly the peak with $T_{\text{max}} \approx 640$ K (see Figure 6, curves 1–6). For high fluences $0.7 \times 10^{22} < \Phi \leq 1.65 \times 10^{22} \text{ m}^{-2}$ thermal desorption of deuterium occurred with the peak with $T_{\text{max}} \approx 640$ K (80–85% D₂ was released) as well as at $T > 1000$ K with the peak with $T_{\text{max}} \approx 1400$ K (see Figure 6, curves 7, 8).

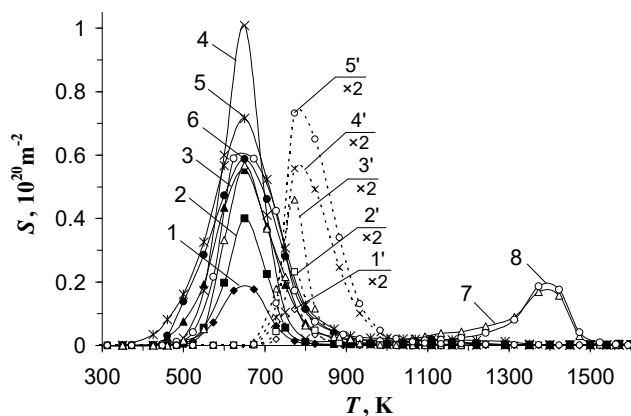


Figure 6. Thermal desorption spectra of deuterium from W (1–8) and Ta (1'–5') coatings deposited on SSt. and irradiated with 10 keV D⁺ ions to fluences $\Phi, 10^{22} \text{ m}^{-2}$: 0.1 (1, 1'), 0.2 (2, 2'), 0.3 (3), 0.4 (4, 3'), 0.5 (5), 0.7 (6), 0.8 (4'), 1.0 (7), 1.1 (5'), 1.65 (8); $T_0 = 290$ K, $\alpha = 0.8$ K/s [36, 49].

The spectra of deuterium thermal desorption from the thin W coating (SSt. + W (nm)) also had peaks of gas release in the temperature range $700 < T < 1000$ K. This was probably due to the release of deuterium into vacuum from the transition region of tungsten – stainless steel. For thin tungsten coatings with a thickness of ~ 500 nm, in both compositions (with an intermediate copper layer and without it) as the fluence increased, the concentration C of trapping deuterium increased from 0.02 at. % up to ~ 4 at. % and the deuterium trapping coefficient η increased from 0.004 to ~ 0.03 respectively. For thick tungsten coatings (with thicknesses from $1.5 \mu\text{m}$ to $2.2 \mu\text{m}$) in both compositions, with the fluence increase the concentration C increased from 0.5 at. % up to 3–4 at. %, and η decreased from (0.09–0.10) to 0.03 respectively. The authors found that at $\Phi < 1.3 \times 10^{22} \text{ m}^{-2}$ deuterium retained in higher concentrations in W (μm) coatings as compared to W (nm) coatings. With a further increase of the fluence, $1.3 \times 10^{22} < \Phi \leq 1.65 \times 10^{22} \text{ m}^{-2}$, the deuterium trapping coefficient in W (μm) coatings decreased from ~ 0.04 to 0.03, while in W(nm) coatings it increased from ~ 0.02 to 0.03.

X-ray diffraction studies of this work authors [46] showed that the initial compressive stresses in the W condensates of the studied compositions were due to the formation in W lattice its own interstitial atoms during the deposition with the used method. D^+ ions irradiation created an additional amount of defects and contributed for their radiation-stimulated migration forming clusters and complexes such as interstitial dislocation loops. Radiation defects of the vacancy type trapped and retained implanted deuterium with its subsequent release at heating from the solid solution into vacuum or into bubbles. Electron microscopic studies of W coatings [49] did not show the formation of deuterium bubbles in them at room temperature after D^+ ions irradiation up to fluences $\Phi \leq 6 \times 10^{22} \text{ m}^{-2}$. The formation of interstitial dislocation loops with average size more than 5 nm and the density $3.2 \times 10^{16} \text{ m}^{-2}$ was found out at $\Phi = 6 \times 10^{22} \text{ m}^{-2}$.

In [36, 37], effects of the samples temperature T_0 during D^+ ions irradiation on the trapping, retention, and thermal desorption of ion-implanted deuterium in vacuum, and on the formation and annealing of radiation defects in the crystal lattice of tungsten coatings were represented. The samples were irradiated with 20 keV (10 keV D^+) D_2^+ ions at the flux density of $3.0 \times 10^{17} \text{ m}^{-2} \cdot \text{s}^{-1}$. The fluences were $1.0 \times 10^{21} \text{ m}^{-2}$ and $2.0 \times 10^{21} \text{ m}^{-2}$. The temperatures T_0 were 290, 370, 440, 470, and 500 K. The thickness W of the coatings was $\sim 1.0 \mu\text{m}$. They were prepared by magnetron sputtering of a W target and deposited on a stainless steel substrate with an intermediate Ti layer pre-deposited on it. The deposition parameters and substrate temperature were the same as in [35, 45–49]. The authors noted for W coatings the influence of the samples temperature T_0 during irradiation on the behavior of the spectra of deuterium thermal desorption into vacuum, concentration C and trapping coefficient η of deuterium. The character of deuterium thermal desorption spectra retained with T_0 increasing. They had one peak of deuterium thermal desorption for all irradiated samples with the temperature T_{max} close to 640 K (see Figure 7, curves 1–5). But with the increase in temperature T_0 , the intensities of thermal desorption peaks decreased, and the start of noticeable deuterium thermal desorption from coatings shifted to the higher temperatures of post-implantation heating. As T_0 increased, the deuterium concentration and trapping coefficient η in W coatings decreased. For example, η changed from 0.06 to 0.02.

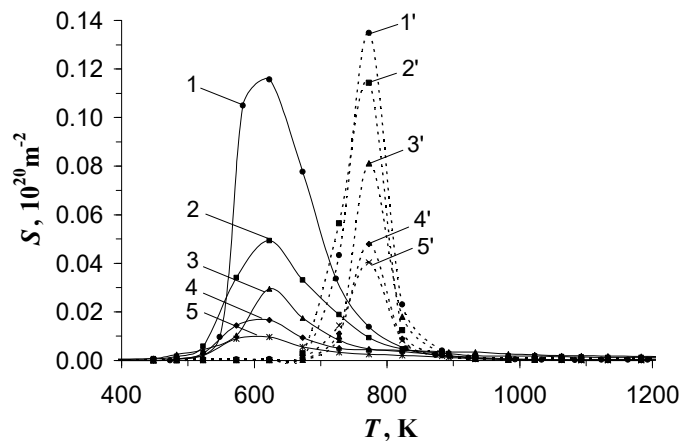


Figure 7. Thermal desorption spectra of deuterium from W (1–5) and Ta (1'–5') coatings deposited on SSt. and irradiated with 10 keV D^+ ions at different temperatures T_0 , K: 290 (1, 1'), 370 (2, 2'), 440 (3), 470 (4, 3'), 500 (5) 570 (4'), 670 (5'); $\Phi = 0.2 \times 10^{22} \text{ m}^{-2}$, $\alpha = 0.8 \text{ K/s}$ [37]

Based on the invariance of the behavior (one peak) of deuterium thermal desorption spectra for the studied temperatures T_0 of the samples and low fluences of irradiation with D^+ ions, it could be assumed that the nature of the formed radiation damages and the mechanisms of their annealing were the same. According to the results of [49], the peak of deuterium release with $T_{\text{max}} = 640$ K and with the activation energy of thermal desorption $E_a = 1.4 \text{ eV}$ was due to the dissociation of deuterium–vacancy complexes DV_n ($n = 4–10$), migration of deuterium atoms along the interstices to the surface with a migration energy $E_{\text{D}_i}^{\text{m}} \approx 0.39 \text{ eV}$, recombination into a D_2 molecule, and subsequent desorption of D_2 into vacuum. The high-temperature peak ($T_{\text{max}} \approx 1400$ K) of deuterium desorption from the W coating, observed for fluences $\Phi \geq 8.0 \times 10^{21} \text{ m}^{-2}$, was most likely due to the formation of deuterium bubbles during heating and the release of deuterium from them. Gas bubbles at such Φ were usually formed in metals at $T > 0.4 T_m$. For tungsten $0.4 T_m = 1470$ K.

It could be supposed that this peak of deuterium release was the result of the dislocations movement during the recrystallization of heated tungsten. In this experiment, it proceeded on the tail of the thermal desorption spectrum ($T > 1700$ K) and, therefore, had low effect on the release of D_2 into vacuum.

So, in tungsten coatings, D^+ ions irradiated at $T_0 = 290$ – 500 K, the following radiation damages, being traps for implanted deuterium, were formed: vacancy-type defects, interstitial dislocation loops, and gas-vacancy complexes. With the temperature T_0 of the samples at ion irradiation increase, as well as during subsequent post-implantation heating, thermal desorption of deuterium increased. This was due to the acceleration of the gas-vacancy complexes dissociation processes, the gas particles migration to the surface and released into vacuum.

In [10, 14, 27, 28, 36, 37, 39–49] the results of studies of the processes of trapping and retention of hydrogen isotopes in tungsten coatings were presented. The results were obtained at the implantation of accelerated D^+ , H^+ ions or plasma implantation of primary D^+ or H^+ ions. The study of the same processes in films of co-deposited hydrogen isotopes and tungsten required a separate analysis [50, 51]. These results could differ significantly from the ion implantation. Eroded particles from the plasma-facing W components (PFCs) migrated through the plasma and re-deposited on the surface in some other area of the facility while the same surface was bombarded with hydrogen isotopes from the plasma. The result of these two processes was a continuously growing co-deposited layer enriched with hydrogen isotopes. Since hydrogen accumulated in it as it grew rather than when was implanted into an already formed layer, the co-deposited films had a high hydrogen content throughout their depth. Such layers, in principle, could become rather thick, increasing with the discharge time, and could form in hard-to-reach places. All of this meant that co-deposited layers in fusion devices could store arbitrarily high amounts of hydrogen, including radioactive tritium. In tungsten layers deposited on laboratory facilities [50] the relative content D/W was 5–10 at.%. The content of hydrogen isotopes in the co-deposited layers depended on the deposition conditions: 1) – the temperature of the substrate of co-deposition, 2) – the flows of hydrogen and the re-deposited material, 3) – the energy of hydrogen particles implanting in the co-deposited layers.

Deposition conditions could vary greatly from reactor to reactor and even within the same plant. This made it important to be able to predict the content of hydrogen isotopes in co-deposited layers in the dependence on the deposition conditions, identifying areas of rapid hydrogen retention and estimating the rate of tritium retention in fusion devices.

Experimental results of tungsten and deuterium co-deposition in a wide range of substrate temperatures (from room temperature to 800 K) were presented in [50]. A simple analytical model of co-deposition based on a one-dimensional equation of diffusion with trapping was proposed. The MD-2 installation using to study the co-deposition of tungsten and deuterium had two separately evacuated chambers, a deposition chamber and a chamber for analytical thermal desorption spectrometry. A tungsten plate was sputtered by planar DC magnetron in an Ar- D_2 atmosphere. In the deposition chamber the residual pressure was less than 10^{-4} Pa, the operating pressure was 1.9 ± 0.1 Pa, and the Ar partial pressure was 0.8 Pa. The voltage, current, and discharge power were ≈ 640 V, ≈ 0.3 A, and 200 W, respectively. In the TDS chamber the residual pressure was $\sim 10^{-7}$ Pa. Tungsten-deuterium films were deposited on a molybdenum substrates. The deposition rate was ~ 0.4 nm/s. The thickness of the films deposited in each experiment was ~ 100 nm. Before placing in a vacuum, the substrate was cleaned in an ultrasonic bath with acetone and alcohol, and was annealed at ~ 1500 K for 7 h in vacuum before to the first experiment. The substrate temperatures during and after deposition were 290, 525, 600, 685, and 800 K. The substrate heating was started before deposition and turned off at the end of it. Then the substrate was cooled to room temperature in a deuterium atmosphere at a pressure of ~ 1 Pa. After that, the supply of deuterium gas was stopped, and the substrate with the co-deposited film was moved into the TDS chamber without being exposed to air. In studying the spectra of deuterium thermal desorption, the samples were linearly heated from 290 K to ~ 1450 K at the rate of 2 K/s. The release of deuterium was registered with a quadrupole mass spectrometer. The TDS spectra for D-W films, deposited at room temperature, 560 K and 800 K, included mass signals of 2, 3, 4, and 40 amu related to H_2 , HD, D_2 , and Ar. If the substrate during the deposition was at 290 K, for mass 4 the signal peaks with maxima at ~ 500 K, ~ 700 K, and ~ 1000 K were observed. If the substrates at deposition were at 290 K and 560 K, deuterium released mainly as D_2 molecules but for the films deposited at 800 K, the contributions of HD and D_2 molecules were comparable. The total deuterium concentration was ~ 5 at.% for deposition at 290 K, 2.2 at.% for 570 K, and 0.37 at.% for 800 K. When calculating the deuterium content, both D_2 and HD were taken into account. A simple analytical approach was proposed based on the assumption of a quasi-stationary equilibrium between mobile and trapping deuterium during a slow film growth. The model described the experimental data very well, supposing three types of traps for deuterium in a W-D film: D trapping on dislocations with the energy 0.74 ± 0.08 eV; trapping of several D atoms into one vacancy with the energy 1.18 ± 0.12 eV; D trapped into a vacancy with the energy 1.56 ± 0.16 eV. Trap concentrations were 2.3 at.%, 1.8 at.% and 1.0 at.% respectively.

Gasparyan et al. represented the dependence of deuterium concentration in co-deposited W-D, Mo-D, and Al-D films on the substrate temperature (from room temperature to 800 K) during the deposition (see Figure 8) [51]. The maximum D retention was in W-D films, the retention in Mo-D films was slightly lower, and the minimum value was for Al-D films. This trend contradicted the well-known tendency for solubility: W had the lowest solubility of deuterium. The decrease in the solubility of D (from Mo to W) and the increase in the total content of D in the films could be due to a higher binding energy of D with defects. Experiments with high temperature resolution revealed a characteristic step structure of the temperature dependence curve, where each step corresponded to one separate type of traps.

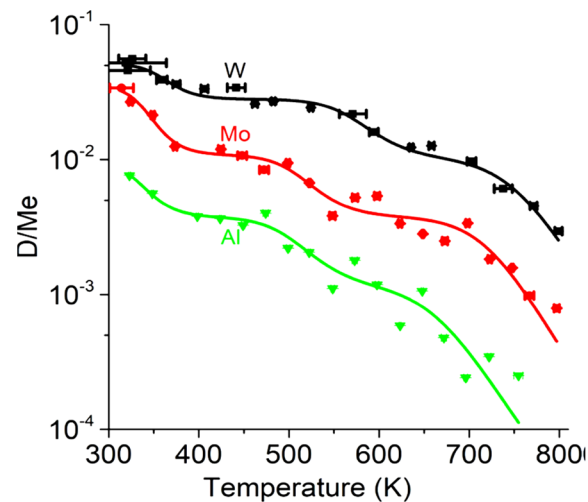


Figure 8. Dependences of deuterium concentration in atomic fractions in co-deposited W-D, Mo-D and Al-D films on the substrate temperature during deposition [51]

Helium implantation, retention and release from tungsten coatings

In the course of a nuclear fusion reaction, one of the products is helium with the energy varies from a few eV to tens of keV [52]. In fusion devices, tungsten is simultaneously or sequentially irradiated with ions of hydrogen isotopes and helium. The recent studies described above have shown that the microstructure of tungsten coatings is changed at irradiation with hydrogen isotope ions. Irradiation with He^+ ions also causes various changes in the microstructure of W, such as voids or bubbles, blisters and fluff. Yu et al. simultaneously irradiated 10 μm thick nanocrystalline tungsten films and 1.5 mm thick W plates at room temperature with 60 keV He^+ ions to the fluence of $1.0 \times 10^{22} \text{ m}^{-2}$ [5]. The average ion flux density was about $2.44 \times 10^{17} \text{ m}^{-2} \cdot \text{s}^{-1}$. The residual pressure in the irradiation chamber was $5 \times 10^{-4} \text{ Pa}$. A piece of W plate of the purity 99.95% and the density 99% purchased from Advanced Technology & Materials Co., Ltd (AT&M) was prepared by powder sintering, and then heat treatment at 1273 K for 1 h for stress relieve. The average grain size in it was about 1–5 μm , there was no preferred grain orientation. The W plate was cut into several samples of 4 mm \times 4 mm. One side was mirror polished by mechanical and electrochemical polishing. Then they were used as samples for He^+ ions irradiation and as the substrates for tungsten films.

Before irradiation and deposition of the W film, all cut plates were sequentially ultrasonic cleaned with acetone, alcohol, and deionized water for 15 min. Tungsten films with the average grain size of about 50 nm were deposited on the aforementioned W substrate by magnetron sputtering in argon atmosphere at a pressure $\sim 1 \text{ Pa}$, the residual pressure was less than $5 \times 10^{-4} \text{ Pa}$. Before the deposition of tungsten films, W substrates (purity 99.95%) were bombarded by argon plasma for 10 min to remove oxides and impurities on their surface. For enhancing adhesion and preventing the delamination of W film, the substrate during deposition was heated up to 770 K and then the temperature was kept constant for the first 2 h, and reduced to 520 K for the next 8 h. The film deposition rate was about 1 $\mu\text{m}/\text{h}$. Research methods were SEM and X-ray diffraction.

The irradiation experiments were performed at 320 keV multi-discipline research platform for Highly Charged Ions equipped with an Electron Cyclotron Resonance (ECR) plasma source in the Institute of Modern Physics, Chinese Academy of Sciences (IMP, CAS), in Lanzhou

Numerous blisters were observed after He^+ ions irradiation on the surface of both types of samples. Blisters with sizes from a few micrometers to about 20 μm were formed on the entire surface of the bulk W (see Figure 9).

On the surface of the W film, blisters of several micrometers were formed (see Figure 10). The authors noted that at the same parameters of He^+ ions irradiation, the density and average size of blisters in the bulk W were greater than in the W film. This indicated that the structure of nano-crystalline tungsten film affected the formation of blisters. In W nanostructured films, besides the ion-induced defects, the presence of initial defects, trapping implanted helium particles, was more characteristic. The latter included point defects, dislocations, vacancies, voids, and a high density of grain boundaries (GBs) which could be absorbers of implanted helium particles and displaced matrix atoms along the He^+ ion range. These facts resulted in a delay of the formation of helium bubbles with excess pressure, as well as blisters formation and W film detachment or layering.

Accounting the structural difference between bulk W and W film, the authors suggested that the formation of blisters, their rupture and detachment on the surface of bulk W should begin earlier than that in the film. As the amount of GBs in the nanocrystalline W film was greater than in the bulk W, the critical fluence of blister formation should be higher; therefore, the density of blisters on its surface was lower. In addition, in the magnetron deposited W film, there were compressive stresses that should prevent the formation of blisters caused by He^+ ions irradiation. Therefore, the blisters on the W film surface were smaller than on the surface of bulk W.

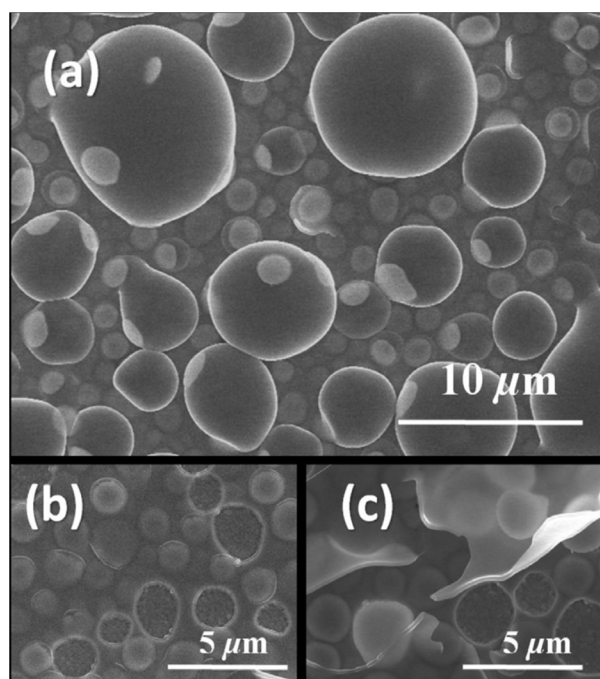


Figure 9. Blistering of the surface of bulk W: (a) big blisters with size from several to tens micrometers, (b) small blisters with size of no more than 2 μm and (c) blisters under the ruptured blisters [5]

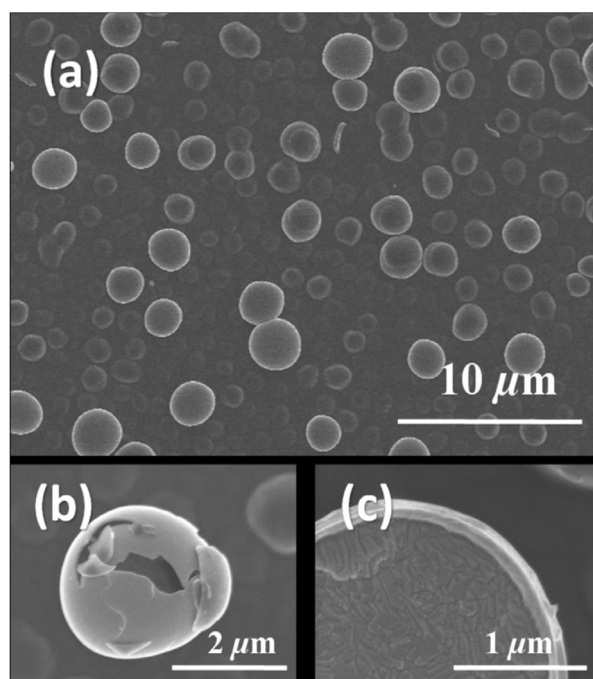


Figure 10. Blistering of the surface of W film: (a) blisters with size of several micrometers, (b) ruptured blisters and (c) surface morphology under a ruptured blister [5]

Jiang at al. proposed tungsten coatings on V-4Cr-4Ti alloy substrates [8], considering it as a promising structural material because of alloy good creep resistance, high thermal stress coefficient, and excellent corrosion resistance. Such tungsten coatings with a thickness of 500 μm were prepared by electrodeposition in a molten salt with vanadium based alloy plate (V-4Cr-4Ti, 30 mm \times 25 mm \times 5 mm, self-provided) as the cathode and pure tungsten plate (purity: 99.95%, 30 mm \times 25 mm \times 5 mm, TLWM Co., Ltd) as the anode. Na_2WO_4 and WO_3 (99.5%, Tianjin Fu Chen Chemical Reagents Factory) were dried in a furnace at 773 K for 24 h. The dried chemicals were well mixed into a eutectic composition ($\text{Na}_2\text{WO}_4:\text{WO}_3 = 0.6:0.2$, by mole ratio) and then melt in an electric furnace at 1173 K. Prior to electrodeposition, the electrode surfaces were mechanically polished to obtain high quality surfaces and then cleaned in acetone and distilled water by ultrasonic cleaning. Tungsten coating was electrodeposited on V-4Cr-4Ti alloy substrate from the molten salt in an open bath at the temperature of 1173 K.

Surface SEM micrographs of tungsten coatings were obtained after irradiation with 10 keV He^+ or 65 keV He^+ ions at different fluence. At the fluence of $2.67 \times 10^{20} \text{ m}^{-2}$, the change in the surface morphology of the W coatings was relatively small, while at the fluence of $2.67 \times 10^{22} \text{ m}^{-2}$, small folded defects were visible. At the fluence of $2.67 \times 10^{20} \text{ m}^{-2}$ of 65 keV He^+ ions needle-like pores were noticeable on the surface of W coatings, and at the fluence of $2.67 \times 10^{22} \text{ m}^{-2}$ broken helium bubbles were observed.

This work authors in [37, 47, 49, 53, 54] studied effects of He^+ ions irradiation on tungsten coatings deposited on stainless steel substrates. The substrate 0.5 mm thick had the following composition: 20 Cr, 70 Fe, 8.5 Ni, and 1.5 Ti at %. The W coatings were irradiated with He^+ ions to different fluences [47, 49, 54] and at different temperatures of bombarded target [37, 53]. Processes of trapping, retention, and thermal desorption of implanted helium, as well as the formation and annealing of radiation defects in the crystal lattice of W coatings irradiated with 10 keV He^+ ions at the flux density of $3.0 \times 10^{17} \text{ m}^{-2} \cdot \text{s}^{-1}$, were studied [47, 49]. Fluences of ions irradiation Φ were from $0.05 \times 10^{22} \text{ m}^{-2}$ to $5.2 \times 10^{22} \text{ m}^{-2}$. The samples were at room temperature during the bombardment. Tungsten coatings were deposited by magnetron sputtering of a W target in an Ar atmosphere at the pressure ~ 1.0 Pa. The deposition rate and substrate temperature were the same as in [35–37, 45–46, 48]. The W deposition was done according to two schemes: 1) on stainless steel (SSt.) substrate coated with Ti less than 10 nm thick (SSt. + W); 2) on SSt. with Ti sublayer, then coated with 3 μm thick Cu layer, Ti sublayer and W deposition after that (SSt. + Cu + W). The tungsten coatings thickness was 2.2 μm . They had a polycrystalline structure with an average grain size of about 60 nm. Tungsten coating in composition (SSt. + Cu + W) had a small tensile macrostress $\sigma = +0.64$ GPa, while in (SSt. + W) the macrostress of the tungsten coating was compressive with $\sigma = -8.0$ GPa. For studying the helium retention and the formation of radiation damages in the crystal lattice of tungsten coatings, TDS, electron microscopy, and X-ray diffractometry, described in detail in [37, 45–47, 49, 54], were used. We studied the influence of He^+ ions fluence on the character of spectra of the helium thermal desorption from W coatings of the named composite systems. It was shown that the type of the composite system under study practically had no effect on the form of helium thermal desorption spectra. For W coatings at low fluences $\Phi \leq 0.4 \times 10^{22} \text{ m}^{-2}$, helium released into vacuum in the temperature range $700 \leq \Delta T \leq 1750$ K. In He TDS spectra from

coatings, the authors observed one predominant helium thermal desorption peak with $T_{\max} \approx 1520$ K and 100% helium release into a vacuum. When coatings were irradiated to high fluences of $0.47 \times 10^{22} \leq \Phi \leq 5.2 \times 10^{22} \text{ m}^{-2}$, helium TDS spectra in addition had also another region of He release, located in the temperature range 450–1300 K. With the Φ increase the fraction of helium in it grew to (65–70) % (see Figure 11a).

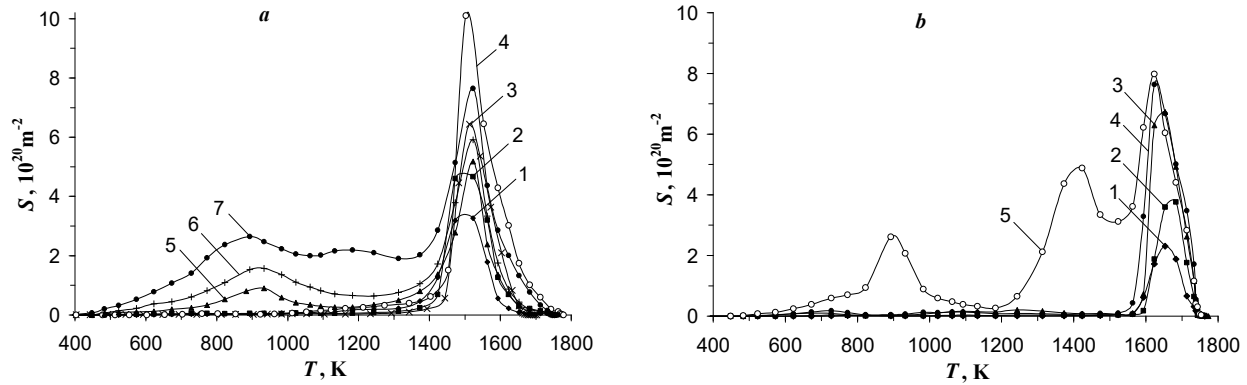


Figure 11. Thermal desorption spectra of helium from W (a) and Ta (b) coatings deposited on SSt. substrates and irradiated with 20 keV He^+ ions. Fluences Φ , 10^{22} m^{-2} : 0.1 (1), 0.2 (2), 0.31 (3), 0.4 (4), 0.47 (5), 0.61 (6), 0.83 (7) for W; 0.1 (1), 0.2 (2), 0.4 (3), 0.6 (4), 1.0 (5) for Ta; $T_0 = 290$ K, $\alpha = 0.8$ K/s [53]

The studies of microstructure of W coatings with helium implanted at the temperature $T_0 \approx 290$ K [37, 47, 49, 54] showed that at fluences of He^+ ions irradiation $\Phi < 7.0 \times 10^{21} \text{ m}^{-2}$, the interstitial dislocation loops with the density of $3.2 \times 10^{16} \text{ m}^{-2}$ and the average size more than 5 nm and dislocation networks formed. At this, the formation of helium bubbles was not observed. The formation of helium bubbles was detected after He^+ ions irradiation up to fluences $\Phi \geq 7 \times 10^{21} \text{ m}^{-2}$. They had the average diameter of about 2.5 nm and the density of $\sim 5 \times 10^{16} \text{ m}^{-2}$ at $\Phi = 7 \times 10^{21} \text{ m}^{-2}$.

The influence of the samples temperature T_0 during He^+ ions irradiation to various fluences on the trapping, retention, and thermal desorption of ion-implanted helium in vacuum, and the formation and annealing of radiation defects in the crystal lattice of tungsten coatings was shown in [37, 53]. The thickness of W coatings was $\sim 1.0 \mu\text{m}$. They were prepared by magnetron sputtering of a W target in an Ar atmosphere at a pressure ~ 1.0 Pa and deposited on a stainless steel substrate 0.8 mm thick with pre-deposited the intermediate Ti layer less than 10 nm thick. The way of preparation, deposition rate and substrate temperature were the same as in works [35–37, 45–49]. The samples were irradiated by 20 keV He^+ ions at the flux density of $3.0 \times 10^{17} \text{ m}^{-2} \cdot \text{s}^{-1}$. Fluences varied in the range $0.1 \times 10^{22} < \Phi \leq 1.0 \times 10^{22} \text{ m}^{-2}$. The samples temperatures T_0 were 290, 370, 470, 540, 570, 670, and 870 K. The effect of temperature T_0 on the helium retention and thermal desorption from the W coating into vacuum was studied for low Φ , not exceeding $0.4 \times 10^{22} \text{ m}^{-2}$, as well as for high Φ from the interval $0.47 \times 10^{22} \leq \Phi \leq 1.0 \times 10^{22} \text{ m}^{-2}$.

The character of the spectra of helium thermal desorption from tungsten coatings, He^+ ions irradiated to the same fluence from the low Φ values at different temperatures T_0 , did not changed with T_0 increasing. The spectra had one peak with the maximum at $T_{\max} \approx 1520$ K. However, with T_0 increasing, the intensity of these peaks decreased. Besides, with T_0 increase, the start of noticeable helium thermal desorption from the coatings shifted to the higher temperatures of post-implantation heating.

When W coatings irradiated with He^+ ions to a fluence $\Phi \sim 7.0 \times 10^{21} \text{ m}^{-2}$ from the high values, the thermal desorption spectra changes significantly with temperature T_0 increasing. Two temperatures were compared: room temperature $T_0 = 290$ K and elevated $T_0 = 570$ K. As noted above [47, 49], at room temperature helium TDS spectra from the coating had both the main region of helium release in the peak with $T_{\max} \approx 1520$ K and another region of its release in the temperature range 450–1300 K. At the elevated temperature, the thermal desorption spectra contained only one main peak at $T_{\max} \approx 1520$ K. No change in the peak height with increasing temperature T_0 was observed.

The regularities of helium retention in tungsten coatings of two types of composite systems at room temperature [47, 49] were analyzed based on the dependences of helium concentration C and trapping coefficient η on the fluence of He^+ ion irradiation of the samples. The increase of Φ resulted in C increase and η decrease. For example, the value of η ($\pm 10\%$) decreased from 0.8 to 0.2 with Φ increasing in the range $0.1 \times 10^{22} \leq \Phi \leq 3.55 \times 10^{22} \text{ m}^{-2}$. Dependences $C, \eta = f(\Phi)$ at $\Phi \geq 1.5 \times 10^{22} \text{ m}^{-2}$ tended to saturation, which could be associated with increasing the amount of implanted He^+ that released from the samples during ion bombardment. The values of helium C and η for the W coating in the composite system SSt. + W(μm) was slightly higher than the analogous C and η values for the composite system SSt. + Cu + W(μm). Early the difference between the type of macrostresses in the tungsten coating of these two composite systems was noted. Perhaps this fact could explain the observed discrepancy between the C and η values for helium. For the elevated temperature of tungsten coatings $T_0 = 570$ K, with an increase in the fluence of He^+ ions irradiation, C increased, and η ($\pm 10\%$) decreases slightly. In the range $0.1 \times 10^{22} < \Phi \leq 0.7 \times 10^{22} \text{ m}^{-2}$, η decreased from 0.82 to 0.68 at $T_0 = 290$ K and from ~ 0.60 to ~ 0.58 at $T_0 = 570$ K.

Thus, when T_0 of tungsten coatings during helium implantation increased, C decreased for both low and high values of Φ fluences. For T_0 in the interval of 290–570 K, C decreased approximately 1.6 times for low fluences and 1.2 times for high fluences; η ($\pm 10\%$) decreased from 0.82 to 0.50 for low Φ and from 0.7 to 0.6 for high Φ .

According to [49] calculations, the activation energy of helium thermal desorption peak with $T_{\max} \approx 1520$ K was $E_a \approx 4.2$ eV, which was close to the dissociation energy 4.42 eV for a helium-vacancy complex of the HeV type. The dissociation of the HeV complex included the release of He from a vacancy with the binding energy of 3.9 eV, the migration of a helium atom along interstices to the surface with the migration energy of 0.28 eV, and He desorption into vacuum. Helium thermal desorption into vacuum at $T \leq 1400$ K from the W coating, He⁺ irradiated at room temperature to high $\Phi \geq 0.47 \times 10^{22}$ m⁻², occurred as a result of gas release from other defects in the coating structure after the formation of helium bubbles, which were observed by the authors of this paper [47, 49].

When W coatings were high-temperature irradiated by He⁺ ions to low fluences, no effect of the temperature T_0 on the behavior of the helium TDS spectra was found. Based on the unchanging of the spectra nature (one peak with $T_{\max} \approx 1520$ K), it could be assumed that the formed radiation damage and the mechanisms of their annealing were the same. In W coatings for the studied temperature T_0 range, the following radiation damages were formed: defects of the vacancy type, helium-vacancy complexes, and interstitial dislocation loops. Thermal desorption of helium, due to the dissociation of helium-vacancy complexes, helium migration along interstices to the surface, and release into vacuum was enhanced for samples irradiated at elevated temperatures T_0 . Part of the implanted helium was released during irradiation with He⁺ ions.

The influence of temperature T_0 on the helium retention and thermal desorption from the coating was found at W coatings irradiation by He⁺ ions at high temperatures to high fluences. It should be noted in particular that the behavior of the spectra of helium thermal desorption into vacuum changed. For samples irradiated He⁺ at room temperature up to high fluences, TDS spectra had a multi-peak temperature region with $T \geq 450$ K of release. For samples irradiated at elevated temperature $T_0 = 570$ K and high fluence $\Phi \approx 7.0 \times 10^{21}$ m⁻² helium TDS spectra had one peak. The peak maximum temperature was $T_{\max} \approx 1520$ K. The concentration and helium trapping coefficient decreased with temperature T_0 increasing. Based on the single-peak character of the spectra of TDS helium at elevated T_0 , it could be supposed that the nature of the formed radiation damage and the mechanisms of their annealing were the same for both high and low fluences of ion irradiation. The following radiation defects also were formed: defects of the vacancy type and helium-vacancy complexes. Upon subsequent heating after implantation, helium thermal desorption from W coatings occurred as a result of dissociation of helium-vacancy complexes, migration of gas atoms along interstices to the sample surface, and release into vacuum.

Sequential and simultaneous implantations of deuterium and helium ions into tungsten coatings

The results of sequential irradiation with D⁺ and He⁺ ions of tungsten coatings deposited on a stainless steel substrate were shown by the authors of this work in [49, 55]. We studied the effect of preliminary implantation of He⁺ (or D⁺) ions on the retention of deuterium (or helium) and their thermal desorption into vacuum. Tungsten coatings with a thickness of ~ 1 μm were MS deposited on a stainless steel substrate 0.5 mm thick with an intermediate layer of Ti less than 10 nm thick pre-sputtered onto it. The method of their preparation, deposition rate, substrate temperature, substrate composition, and other parameters of the MS method were the same as in [35–37, 45–49, 53, 54]. The tungsten coatings had a polycrystalline structure with an average grain size of about 60 nm. The samples were irradiated at room temperature sequentially with beams of 10 keV D⁺ (20 keV D₂⁺) and 20 keV He⁺ ions at the flux density of 3.0×10^{17} m⁻²·s⁻¹ to fluences of $\Phi_{D^+} \leq 4.6 \times 10^{21}$ m⁻² and $\Phi_{He^+} \leq 4.0 \times 10^{21}$ m⁻² in order: He⁺, D⁺ or D⁺, He⁺. The average projective and total ranges of D⁺ (10 keV) and He⁺ (20 keV) ions in the W coating were about 60 nm and 160 nm, respectively, comparable for these ions and significantly less than the coatings thickness. The radiation damage profiles of the W crystal lattice, created by D⁺ and He⁺ ions, were identical and were located in the zone of the ions implantation.

For sequential irradiations with the named ions implanted in different order at the above fluences, the thermal desorption spectra of both gases were a superposition of the thermal desorption spectra of these ions implanted separately at the same fluences. The temperature intervals for the release of deuterium and helium were the same. The temperatures of the maxima of gas-release peaks in the spectra $T_{\max} = 640$ K (D₂) and $T_{\max} = 1520$ K (He) were the same for both sequential and separate implantations of D⁺ and He⁺ ions. Pre-implantation of helium up to different fluences in the range of 1.0×10^{21} m⁻² $\leq \Phi_{He^+} \leq 4.0 \times 10^{21}$ m⁻² did not change deuterium concentration C_D and trapping coefficient η_D . Preliminary implantation of deuterium to various fluences in the range 1.0×10^{21} m⁻² $\leq \Phi_{D^+} \leq 4.6 \times 10^{21}$ m⁻² also did not change C_{He} and η_{He} . Based on these facts, the authors suggested that in tungsten coatings irradiated with D⁺ and He⁺ ions both separately and sequentially, the types of formed radiation damages and the mechanisms of their annealing were the same. According to [45–49, 54, 55], in the tungsten coating irradiated with D⁺ or He⁺ ions at room temperature, radiation defects of the vacancy type were formed, which trapped deuterium or helium into gas–vacancy complexes D_mV_n or He_mV_n . The complexes transformed into gas bubbles with the increase of concentrations of implanted gases (for example, the helium bubbles formed at fluences $\Phi_{He^+} \geq 7 \times 10^{21}$ m⁻² [49, 54]). According to [46, 49, 54], at irradiations with D⁺ and He⁺ ions, intrinsic interstitial atoms of W lattice were formed, and their radiation-stimulated migration with the formation of clusters and complexes such as interstitial dislocation loops was observed. The main peak with $T_{\max} = 640$ K of deuterium release was due to the dissociation of deuterium–vacancy complexes, migration of deuterium atoms along interstitials to the

surface, their recombination into a molecule, and subsequent D₂ desorption into vacuum. The main peak with $T_{\max} = 1520$ K of helium thermal desorption as well resulted from the dissociation of helium-vacancy complexes, helium atoms migration along interstitials to the surface, and their subsequent desorption into vacuum. When analyzing separate and sequential implantations of D⁺ and He⁺ ions into tungsten coatings, general regularities were established: the concentration of retained deuterium in the coatings was lower compared to helium and its trapping coefficient was approximately an order of magnitude lower. The main release into vacuum of deuterium occurred at lower temperatures as compared to helium.

Ogorodnikova et al. [56] irradiated tungsten-based materials—polycrystalline PC-W and nanostructured CMSII-W coating—simultaneously with D⁺ and He⁺ ions both in the stationary mode and in a QSPA-T quasi-stationary high-current plasma gun, in which the pulse duration was 1 ms, the number of pulses varied from one to thirty. In stationary plasma impacts, the ion energy varied from 20 eV to 3 keV, and the ion fluxes were from 10^{17} to 10^{21} m⁻² s⁻¹. The ion fluencies were 10^{20} – 10^{25} m⁻² and the target temperatures were in the range 300–1200 K. Deuterium and helium retention in the irradiated samples was measured by thermal desorption spectroscopy using a high resolution quadrupole mass spectrometer to separate the He and D₂ signals. The amount of trapping D (ion energy 20 eV, fluence 2×10^{25} m⁻²) in the CMSII-W coatings decreased from 4.5×10^{21} to 2.0×10^{21} m⁻² with the temperature increase from 290 K to 650 K. The retention of D in PC-W decreased with temperature increasing at low $\Phi \leq 10^{22}$ m⁻². The retention of D in PC-W at the high fluence $\Phi = 10^{25}$ m⁻² with temperature increasing firstly increased and then decreased. The amount of trapping He (ion energy 60 eV, fluence 2×10^{24} m⁻²) in the CMSII-W coating increased from 0.6×10^{20} to 4.0×10^{20} m⁻² with the increase in temperature from 290 K to 1100 K. The He retention in PC-W did not significantly depend on the sample temperature at He⁺ ion energies above 400 eV and low fluences of $\Phi \leq 10^{22}$ m⁻², whereas it increased at He⁺ ion energies below 80 eV and high fluences of 2×10^{24} m⁻².

The results of helium influence on deuterium retention in co-deposited tungsten films were shown in [57]. For co-deposition W films a tungsten target was sputtered in a magnetron discharge in an Ar-D₂-He mixture. $P_{\text{Ar}} = P_{\text{D}_2} = 2.8$ Pa, $P_{\text{He}} = 0\text{--}20\%$ P_{D_2} . The residual pressure was 3×10^{-5} Pa, deposition rate was 0.2 nm/s, thickness of the deposited films was 100 nm. The sample temperature at the deposition was varied from 300 K to 800 K, the temperature jump was 50 K. The prepared films were analyzed by thermal desorption spectroscopy; the samples were linearly heated at the rate of 2 K/s to 1250 K. He and D₂ flows in TDS analysis were separated by two quadrupole mass spectrometers. In co-deposited films, the content of D₂ increased when 5% He was in the working gas and decreased with the presence of 20% He in the working gas as compared to films deposited without helium addition. The highest content of deuterium was D/W = 0.5 at.% for 5% He at the sample temperature of 800 K. The addition of 5–20% He to the working gas suppressed D₂ desorption at high temperatures $900 < T < 1100$ K, possibly due to competition between D₂ and He for the same places of trapping. For He/D > 0, D₂ desorption at high temperatures increased with increasing the deposition temperature: the peak at 800–900 K for He/D = 5%, the peak at 700–800 K for He/D = 20%.

Implantation of deuterium and helium ions into composite structure with tantalum coating

This work authors studied the processes accompanying the implantation of D⁺ or He⁺ ions into tantalum coatings deposited on stainless steel substrates [36, 37, 53]. The trapping and retention of deuterium or helium and their thermal desorption into vacuum, formation and annealing of radiation damages in the crystal lattice were studied. The types of radiation defects were determined and their interaction with ion-implanted gases was analyzed studying gases influence on the structural and physical properties of the coatings. The radiation stability of the samples at changing both their temperature during bombardment and the fluence of ions irradiation was studied. Tantalum coatings of ~ 1.5 μm thick were prepared by magnetron sputtering of a Ta target in an Ar atmosphere at a pressure ~ 1.0 Pa. Coatings were deposited at the rate of 0.6 nm/s on the 0.8 mm thick stainless steel substrates at the temperature of 600 K. An intermediate Ti layer of less than 10 nm thickness was pre-deposited on the substrate. The deposition rate, substrate temperature, substrate composition, and parameters of the MS method were the same as in [35, 45–49, 55] for tungsten coatings. The samples were irradiated with 20 keV D₂⁺ (10 keV D⁺) or 20 keV He⁺ ions at the flux density of 3.0×10^{17} m⁻²·s⁻¹ to fluences Φ in the range $(0.1 - 1.0) \times 10^{22}$ m⁻². Ions were implanted at several sample temperatures: deuterium at $T_0 = 290, 370, 470, 570,$ and 670 K, and helium at $T_0 = 290, 370, 670, 770,$ and 870 K. The average projective and total ranges of D⁺ and He⁺ ions in the Ta coating were about 60 nm and 160 nm, respectively, were comparable for these ions and significantly less than the coating thickness. Distribution profiles of radiation damages in the Ta crystal lattice created by D⁺ and He⁺ ions were located in the zone of the ions implantation.

Thermal desorption of deuterium from tantalum coatings irradiated with D⁺ ions to different fluences in the range of $0.1 \times 10^{22} \leq \Phi \leq 1.1 \times 10^{22}$ m⁻² was studied in [36]. During the bombardment the samples were at room temperature ($T_0 = 290$ K). A noticeable release of deuterium from coatings started at temperatures $T \geq 500$ K and ended at $T \approx 1100$ K. The deuterium thermal desorption spectra had one peak, the maximum of which was at a temperature $T_{\max} \approx 770$ K (see Figure 6, curves 1'–5').

The influence of samples temperature T_0 in the range of 290–670 K during D⁺ ions irradiation up to $\Phi = 2.0 \times 10^{21}$ m⁻² on the trapping, retention, and thermal desorption of deuterium from Ta coatings into vacuum was shown in [36, 37]. The character of the deuterium TDS spectra retained with T_0 increasing. The spectra had one peak and the temperature at the peak maximum $T_{\max} \approx 770$ K (see Figure 7, curves 1'–5'). As the temperature T_0 increased, the

intensity of the D₂ thermal desorption peak decreases. In addition, the deuterium noticeable release from coatings starts at higher temperatures of post-implantation heating shifting from 500 K to 690 K.

With T_0 increase, concentration C and trapping coefficient η of deuterium decreased. For example, η changed from 0.02 to 0.005 at $\Phi = 2.0 \times 10^{21} \text{ m}^{-2}$. With an increase of the D⁺ ions fluence at a constant temperature T_0 of coatings, the concentration C of deuterium decreased. The deuterium trapping coefficient η did not change in this case, whereas in W coatings deuterium trapping coefficient decreased in similar experiments (see [36]). This could be due to the different type of deuterium solubility: endothermic (W) or exothermic (Ta) and the ability to form hydrides in tantalum. The release of deuterium with the peak maximum at $T_{\text{max}} \approx 770 \text{ K}$ and the activation energy of thermal desorption $E_a = 1.7 \text{ eV}$ [37] was explained by the dissociation of deuterium-vacancy complexes, migration of deuterium atoms along the interstitials to the surface with the migration energy $E_{D,i}^m \approx 0.39 \text{ eV}$, recombination into a D₂ molecule and subsequent desorption into vacuum.

Helium thermal desorption from tantalum coating irradiated at $T_0 = 290 \text{ K}$ with He⁺ ions to different fluences in the range $0.1 \times 10^{22} \leq \Phi \leq 1.0 \times 10^{22} \text{ m}^{-2}$ was studied in [53]. The He TDS spectra were shown in Figure 11b. For low fluences $\Phi \leq 6.0 \times 10^{21} \text{ m}^{-2}$, helium released from the coatings into vacuum in the temperature range $500 \leq \Delta T \leq 1750 \text{ K}$, with the main peak having maximum at $T_{\text{max}} \approx 1670 \text{ K}$. For the highest fluence $\Phi = 1.0 \times 10^{22} \text{ m}^{-2}$ in the helium TDS spectra another temperature range of 480–1550 K of its release appeared. According [37], the spectra of helium thermal desorption into vacuum from Ta coatings, irradiated with He⁺ ions to the same fluence $\Phi = 2.0 \times 10^{21} \text{ m}^{-2}$ from the range of low Φ , at different temperatures T_0 of the samples in the range of 290–870 K, kept their behavior with T_0 increasing. The spectra had one peak with the temperature of peak maximum $T_{\text{max}} \approx 1670 \text{ K}$.

With T_0 increase, the concentration C and the helium trapping coefficient η of Ta coatings decreased. For example, η changed from 0.8 to 0.6 at $\Phi = 2.0 \times 10^{21} \text{ m}^{-2}$. With the fluence of He⁺ ions irradiation increase for Ta coatings at $T_0 = 290 \text{ K}$, the concentration C and the helium trapping coefficient η also decreased (see [36]). In [37, 53] the authors explained the release of helium with the main peak at $T_{\text{max}} = 1670 \text{ K}$ in its thermal desorption spectra by dissociation of helium-vacancy complexes, migration of helium atoms along interstices to the surface, and their subsequent desorption into vacuum. The mechanism of thermal desorption was described in detail in [37, 49].

The authors of [36, 37, 53] for Ta or W coatings established general regularities of the processes of D₂ and He retention and thermal desorption, the formation and annealing of radiation defects in the crystal lattice, and some differences in the values of their parameters. The concentration C and trapping coefficients η_D , η_{He} of implanted gases, temperature intervals of release into vacuum, and temperature T_{max} of deuterium (helium) thermal desorption peaks for these coatings had different values.

From the above it can be concluded the following:

1. TDS spectra of deuterium (helium), whose ions are implanted in Ta or W coatings at room temperature ($T_0 = 290 \text{ K}$) and low fluences no more than $1.1 \times 10^{22} \text{ m}^{-2}$ ($0.6 \times 10^{22} \text{ m}^{-2}$) for Ta and $0.7 \times 10^{22} \text{ m}^{-2}$ ($0.4 \times 10^{22} \text{ m}^{-2}$) for W, consist of one peak. Temperatures of peak maxima are for deuterium $T_{\text{max}} \approx 770 \text{ K}$ (Ta) and $T_{\text{max}} \approx 640 \text{ K}$ (W), and for helium $T_{\text{max}} \approx 1670 \text{ K}$ (Ta) and $T_{\text{max}} \approx 1520 \text{ K}$ (W). Temperatures of peak maximum T_{max} of the deuterium (helium) release from the Ta coating are higher compared to W one. TDS spectra of deuterium (Figure 6) and helium (Figure 11) for Ta and W coatings see above.

2. TDS spectra of deuterium (helium), whose ions are implanted in Ta or W coatings at low fluences $(0.1 - 0.2) \times 10^{22} \text{ m}^{-2}$, and elevated sample temperatures $T_0 = 290 - 870 \text{ K}$, contain one peak. The temperatures of peak maxima remain for all T_0 as for deuterium ($T_{\text{max}} \approx 770 \text{ K}$ (Ta) and $T_{\text{max}} \approx 640 \text{ K}$ (W)) as for helium ($T_{\text{max}} \approx 1670 \text{ K}$ (Ta) and $T_{\text{max}} \approx 1520 \text{ K}$ (W)). TDS spectra of deuterium (Figure 7) for Ta and W coatings see above.

3. For low fluences of D⁺ and He⁺ ions, deuterium releases into vacuum at lower temperatures as comparable with helium release.

4. At high fluences $\Phi = 1.0 \times 10^{22} \text{ m}^{-2}$ (Ta) and $0.47 \times 10^{22} \leq \Phi \leq 1.0 \times 10^{22} \text{ m}^{-2}$ (W) and $T_0 = 290 \text{ K}$ in the spectra of helium thermal desorption for coatings of both metals, besides the peaks of release with $T_{\text{max}} \approx 1670 \text{ K}$ (Ta) or $T_{\text{max}} \approx 1520 \text{ K}$ (W), there are also regions of He thermal desorption at $T = 480 - 1550 \text{ K}$ for the Ta coatings and at $T = 450 - 1300 \text{ K}$ for the W coatings. For the Ta coatings, the transformation of helium thermal desorption spectra from a single-peak to a more complex dependence occurs at higher fluences of He⁺ ions irradiation ($\Phi = 1.0 \times 10^{22} \text{ m}^{-2}$ for Ta and $\Phi = 0.47 \times 10^{22} \text{ m}^{-2}$ for W).

5. At all studied D⁺ or He⁺ ions fluences and T_0 for both tantalum and tungsten coatings, the concentration C_{He} and helium trapping coefficient η_{He} are much higher than the C_D and η_D for deuterium. Deuterium retains with a trapping coefficient approximately an order of magnitude lower than helium (see Figure 12 and Figure 13).

6. When the fluence of He⁺ ions irradiation increases, η_{He} decreases in the coatings of both materials. η_D decrease with the Φ increase for D⁺ ions is observed only for tungsten coatings. For tantalum coatings η_D does not change with Φ increasing. Dependences η_D , $\eta_{He} = f(\Phi)$ for coatings of both materials irradiated with D⁺ or He⁺ ions are shown in Figure 12.

7. When the temperature T_0 of tantalum and tungsten coatings during irradiation with D⁺ (He⁺) ions increases, the trapping coefficient η_D (η_{He}) of deuterium (helium) decreases. Figure 13 shows the dependences η_D , $\eta_{He} = f(T_0)$ for coatings of both irradiated materials. Comparing the same intervals of T_0 changing, a more significant η_D decrease is observed for the tungsten coatings compared to the tantalum coatings (by about 15 times and 2 times, respectively). The η_{He} decrease for the tungsten coating is insignificant (approximately 2 times and 1.5 times, respectively) comparing to the tantalum coating.

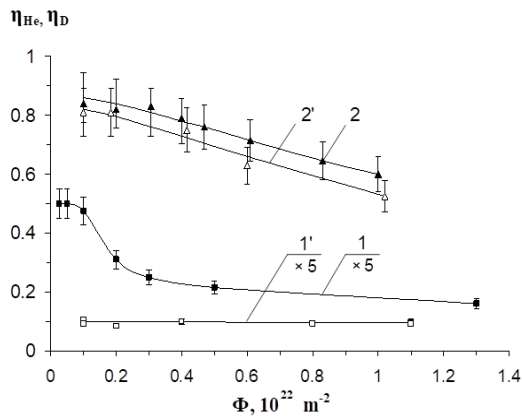


Figure 12. Deuterium (1, 1') and helium (2, 2') trapping coefficients versus the fluence of D⁺ and He⁺ ions for the W coating, curves 1, 2 and for the Ta coating, curves 1', 2'; ion energy: D⁺ – 10 keV, He⁺ – 20 keV; T₀ = 290 K [36]

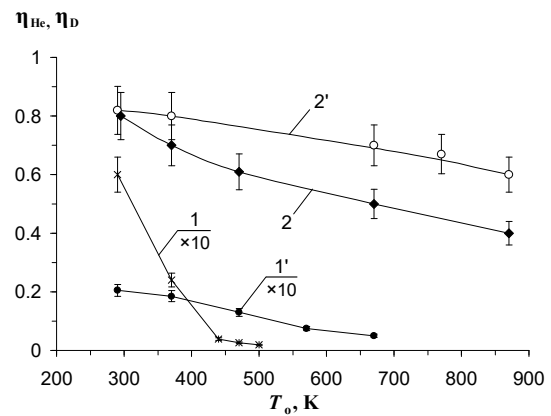


Figure 13. Deuterium (1, 1') and helium (2, 2') trapping coefficients versus temperature T₀ of the W coatings—curves 1, 2 and of the Ta coatings—curves 1', 2'. Ion energy: D⁺ – 10 keV, He⁺ – 20 keV; fluence 0.2×10²² m⁻² [37]

CONCLUSIONS

The analysis of published works about the influence of implanted hydrogen isotopes and helium on changes in the microstructure, morphology, and physical properties of tungsten and tantalum coatings, irradiated with D⁺, H⁺, and He⁺ ions, was made. The samples that irradiated both with beams of accelerated ions of hydrogen isotopes or He⁺, and in plasma containing the above-named ions were under consideration. The implantation of the above mentioned gases was performed in various modes of irradiation: individual, sequential in different order of the selected types of ions, and simultaneously with several given types of ions. Various fluences and energies of the bombarded ions were applied. The target temperature during implantation was chosen in a wide range. Modern highly sensitive research methods were used in analyzed works: electron microscopy, re-emission mass spectrometry, thermal desorption spectrometry, X-ray photoelectron spectroscopy, X-ray diffraction, analysis of nuclear reaction and Rutherford ion scattering. Simultaneous irradiation of W in bulk and in thin-film forms permitted to obtain data on the retention and migration of ion-implanted hydrogen isotopes in various types of W samples. In addition, the information about the formation of radiation damages in the crystal lattice and their interaction with the implanted gases was got. Studies of the processes of retention and release of D₂ and He, the formation and annealing of radiation defects in the crystal lattice of W and Ta coatings, carried out under similar conditions, established the common regularities of these processes in different metal coatings, as well as some differences in the parameters characterizing them. The influence of the metal choice for coatings on the concentrations and trapping coefficients of implanted gases, temperature intervals of gas release into vacuum, and temperatures of maxima T_{max} of thermal desorption peaks for deuterium (helium) into vacuum were shown.

It can be seen from this review that each presented paper contains useful information regarding the retention and release of hydrogen isotopes or helium from W and Ta coatings of plasma-facing structures for fusion reactors that needs for the efficient operation of a fusion reactor. It is necessary to take into account the radiation stability of the structural, physical and mechanical properties of promising PFM to the influence of implanted hydrogen isotopes and helium.

In the analyzed works the authors considered ways to solve one of the main problems of ITER and future tokamaks – the retention of H and He isotopes in PFC. The authors of this article, based on an analysis of the reviewed works, believe that one of the best solutions to this problem is nanocrystalline tungsten coatings deposited on reactor devices contacting with plasma.

Funding. This research did not receive any specific grant from funding agencies in the public, commercial, or not-for-profit sectors.

Conflict of Interest. Authors declared that there is no conflict of interest. The authors declare that they have no known competing financial interests or personal relationships that could have appeared to influence the work reported in this paper.

ORCID

Mykola Azarenkov, <https://orcid.org/0000-0002-4019-4933>; Lyudmila Tishchenko, <https://orcid.org/0000-0002-6300-6448>
 Valentyn V. Bobkov, <https://orcid.org/0000-0002-6772-624X>; Dmytro Shevchenko, <https://orcid.org/0000-0002-4556-039X>
 Lyubov Gamayunova, <https://orcid.org/0000-0001-7220-9944>; Anatolij Skrypnyk, <https://orcid.org/0000-0003-3691-2477>

REFERENCES

- [1] L. Pranevicius, L. Pranevicius, and D. Milcius, *Tungsten Coatings for Fusion Applications*, (Vytauto Didžiojo universitetas, Kaunas, 2009), pp. 262.
- [2] Z. Tian, J.W. Davis, and A.A. Haasz, *J. Nucl. Mater.* **399**, 101 (2010). <http://doi.org/10.1016/j.jnucmat.2010.01.007>
- [3] E.V. Kornelsen, *Canad. J. Phys.* **48**, 2812 (1970). <https://cdnsiencepub.com/doi/abs/10.1139/p70-350>
- [4] N. Yoshida, *J. Nucl. Mater.* **266-269**, 197 (1999). [https://doi.org/10.1016/s0022-3115\(98\)00817-4](https://doi.org/10.1016/s0022-3115(98)00817-4)
- [5] J. Yu, W. Han, Z. Chen, and K. Zhu, *Nucl. Mater. Energy.* **12**, 588 (2017). <https://doi.org/10.1016/j.nme.2016.10.001>

- [6] R. Behrisch, J. Surf. Invest.: X-Ray, Synchrotron Neutron Tech. **4**(4), 549 (2010). <https://doi.org/10.1134/S1027451010040014>
- [7] C. Ruset, E. Grigore, H. Maier, R. Neu, H. Greuner, M. Mayer, and G. Matthews, Fusion Eng. Des. **86**, 1677 (2011). <https://doi.org/10.1016/j.fusengdes.2011.04.031>
- [8] F. Jiang, Y. Zhang, and X. Li, Fusion Eng. Des. **93**, 30 (2015). <http://doi.org/10.1016/j.fusengdes.2015.02.020>
- [9] F. Brossa, G. Piatti, and M. Bardy, J. Nucl. Mater. **103**, 261 (1981). [https://doi.org/10.1016/0022-3115\(82\)90608-0](https://doi.org/10.1016/0022-3115(82)90608-0)
- [10] J. Yu, W. Han, Z. Lian, and K. Zhu, Fusion Sci. Technol. **73**, 5 (2018). <http://doi.org/10.1080/15361055.2017.1372680>
- [11] R. A. Neiser, G. R. Smolik, K. J. Hollis, and R. D. Watson, J. Thermal Spray Technol. **2**(4), 393 (1993). <http://doi.org/10.1007/bf02645870>
- [12] S. Boir-Lavigne, C. Moreau, and R. G. Saint-Jacques, J. Thermal Spray Technol. **4**(3), 261 (1995). <http://doi.org/10.1007/bf02646969>
- [13] S. Deschka, C. Garcia-Rosales, W. Hohenauer, R. Duwe, E. Gauthier, J. Linke, M. Lochter, W. Mallener, L. Plöchl, P. Rödhhammer, and A. Salito, J. Nucl. Mater. **233-237**, 645 (1996). [https://doi.org/10.1016/S0022-3115\(96\)00090-6](https://doi.org/10.1016/S0022-3115(96)00090-6)
- [14] C. Garcia-Rosales, P. Franzen, H. Plank, J. Roth, and E. Gauthier, J. Nucl. Mater. **233-237**, 803 (1996). [https://doi.org/10.1016/s0022-3115\(96\)00185-7](https://doi.org/10.1016/s0022-3115(96)00185-7)
- [15] I. Smid, M. Akiba, G. Vieider, and L. Plöchl, J. Nucl. Mater. **258-263**, 160 (1998). [https://doi.org/10.1016/s0022-3115\(98\)00358-4](https://doi.org/10.1016/s0022-3115(98)00358-4)
- [16] C. Ruset, E. Grigore, I. Munteanu, H. Maier, H. Greuner, C. Hopf, V. Phylipps, and G. Matthews, Fusion Eng. Des. **84**, 1662 (2009). <https://doi.org/10.1016/j.fusengdes.2008.11.053>
- [17] C. Ruset, E. Grigore, D. Falie, M. Gherendi, H. Maier, M. Rasinski, G. F. Matthews, and V. Zoita, Fusion Eng. Des. **88**, 1690 (2013). <https://doi.org/10.1016/j.fusengdes.2013.02.017>
- [18] H. Greuner, B. Boeswirth, J. Boscary, and P. McNeely, J. Nucl. Mater. **367**, 1444 (2007). <https://doi.org/10.1016/j.jnucmat.2007.04.004>
- [19] C. Ruset, E. Grigore, H. Maier, R. Neu, X. Li, H. Dong, R. Mitteau, and X. Courtois, Phys. Scr. **T128**, 171 (2007). <https://doi.org/10.1088/0031-8949/2007/t128/033>
- [20] E. Grigore, C. Ruset, K. Short, D. Hoefft, H. Dong, X. Y. Li, and T. Bell, Surf. Coat. Technol. **200**, 744 (2005). <https://sci-hub.st/10.1016/j.surfcoat.2005.02.118>
- [21] A. Cambe, E. Gauthier, J. M. Layet, and S. Bentivegna, Fusion Eng. Des. **56-57**, 331 (2001). [https://doi.org/10.1016/s0920-3796\(01\)00350-7](https://doi.org/10.1016/s0920-3796(01)00350-7)
- [22] K. Tokunaga, T. Matsubara, Y. Miyamoto, Y. Takao, N. Yoshida, N. Noda, Y. Kubota, T. Sogabe, T. Kato, and L. Plöchl, J. Nucl. Mater. **283-287**, 1121 (2000). [https://doi.org/10.1016/s0022-3115\(00\)00384-6](https://doi.org/10.1016/s0022-3115(00)00384-6)
- [23] L. Pranevičius, Mater. Sci. (Medžiagotyra). **15**(3), 212 (2009). <https://matsc.ktu.lt/index.php/MatSc/article/view/26151>
- [24] Y. Niu, X. Zheng, H. Ji, L. Qi, C. Ding, J. Chen, and G. Luo, Fusion Eng. Des. **85**, 1521 (2010). <https://doi.org/10.1016/j.fusengdes.2010.04.032>
- [25] S. Tamura, K. Tokunaga, and N. Yoshida, J. Nucl. Mater. **313-316**, 250 (2003). [https://doi.org/10.1016/S0022-3115\(02\)01336-3](https://doi.org/10.1016/S0022-3115(02)01336-3)
- [26] D. Jihong, L. Zhengxiang, L. Gaojian, Z. Hui, and H. Chunliang, Surf. Coat. Technol. **198**, 169 (2005). <https://doi.org/10.1016/j.surfcoat.2004.10.130>
- [27] V. K. Alimov, and B. M. U. Scherzer, J. Nucl. Mater. **240**(1), 75 (1996). [https://doi.org/10.1016/S0022-3115\(96\)00442-4](https://doi.org/10.1016/S0022-3115(96)00442-4)
- [28] I. Bizyukov, K. Krieger, N. Azarenkov, S. Levchuk, and Ch. Linsmeier, J. Nucl. Mater. **337-339**, 965 (2005). <https://doi.org/10.1016/j.jnucmat.2004.09.048>
- [29] L. H. Taylor, and L. Green, Fusion Eng. Des. **32-33**, 105 (1996). [https://doi.org/10.1016/S0920-3796\(96\)00457-7](https://doi.org/10.1016/S0920-3796(96)00457-7)
- [30] L. Gladczuk, A. Patel, Ch. S. Paur, and M. Sosnowski, Thin Solid Films. **467**(1-2), 150 (2004). <https://doi.org/10.1016/j.tsf.2004.04.041>
- [31] K. Hieber, and N. M. Mayer, Thin Solid Films. **90**(1), 43 (1982). [https://doi.org/10.1016/0040-6090\(82\)90069-4](https://doi.org/10.1016/0040-6090(82)90069-4)
- [32] S. Sato, Thin Solid Films. **94**(4), 321 (1982). [https://doi.org/10.1016/0040-6090\(82\)90493-X](https://doi.org/10.1016/0040-6090(82)90493-X)
- [33] D. W. Face, and D. E. Prober, J. Vac. Sci. Technol. A, **5**, 3408 (1987). <http://doi.org/10.1116/1.574203>
- [34] G. S. Chen, P. Y. Lee, and S. T. Chen, Thin Solid Films. **353**, 264 (1999). [https://doi.org/10.1016/S0040-6090\(99\)00431-9](https://doi.org/10.1016/S0040-6090(99)00431-9)
- [35] S. S. Alimov, N. A. Azarenkov, V. V. Bobkov, I. I. Okseniuk, A. A. Skrypnyk, R. I. Starovoytov, and L. P. Tishchenko, J. Kharkiv National University, (1041), 116 (2013). <https://periodicals.karazin.ua/eejp/article/view/13520>
- [36] V. V. Bobkov, L. P. Tishchenko, Yu. I. Kovtunenکو, O. B. Tsapenko, A. O. Skrypnyk, Yu. E. Logachev, and L. A. Gamayunova, PAST, Series: «Plasma Physics», (6), 63 (2018). https://vant.kipt.kharkov.ua/ARTICLE/VANT_2018_6/article_2018_6_63.pdf
- [37] V. V. Bobkov, L. P. Tishchenko, Yu. I. Kovtunenکو, A. B. Tsapenko, A. A. Skrypnyk, and L. A. Gamayunova, J. Surf. Invest. X-ray, Synchrotron Neutron Tech. **14**(5), 899 (2020). <http://link.springer.com/article/10.1134/S1027451020050031>
- [38] R. A. Causey, J. Nucl. Mater. **300**(2-3), 91 (2002). [https://doi.org/10.1016/S0022-3115\(01\)00732-2](https://doi.org/10.1016/S0022-3115(01)00732-2)
- [39] Y. Oya, M. Shimada, T. Tokunaga, H. Watanabe, N. Yoshida, Y. Hatano, R. Kasada, T. Nagasaka, A. Kimura, and K. Okuno, J. Nucl. Mater. **442**, S242 (2013). <http://doi.org/10.1016/j.jnucmat.2013.01.321>
- [40] Y. Niu, S. Suzuki, X. Zheng, Ch. Ding, J. Chen, W. Wang, Y. Oya, and K. Okuno, J. Nucl. Mater. **417**, 551 (2011). <http://doi.org/10.1016/j.jnucmat.2010.12.108>
- [41] Y. Zhang, W. Wang, H. Ren, W. Han, F. Liu, J. Yu, Sh. Peng, and K. Zhu, Nucl. Instrum. and Methods B. **307**, 357 (2013). <https://doi.org/10.1016/j.nimb.2013.04.026>
- [42] R. A. Anderl, D. F. Holland, and G. R. Longhurst, J. Nucl. Mater. **176-177**, 683 (1990). [https://doi.org/10.1016/0022-3115\(90\)90127-9](https://doi.org/10.1016/0022-3115(90)90127-9)
- [43] O. V. Ogorodnikova, K. Sugiyama, T. Schwarz-Selinger, T. Dürbeck, and M. Balden, J. Nucl. Mater. **419**, 194 (2011). <https://doi.org/10.1016/j.jnucmat.2011.07.023>
- [44] K. Katayama, K. Uehara, H. Date, S. Fukada, and H. Watanabe, J. Nucl. Mater. **463**, 1033 (2015). <https://doi.org/10.1016/j.jnucmat.2014.11.103>

- [45] L.P. Tishchenko, T.I. Peregon, Yu.I. Kovtunenکو, V.V. Bobkov, A.V. Onishchenko, and R.I. Starovoitov, *Bulletin of the Russian Academy of Sciences: Physics*, **70**(8), 1372 (2006). <https://www.elibrary.ru/item.asp?id=14370770>.
- [46] V.V. Bobkov, A.V. Onishchenko, O.V. Sobol, R.I. Starovoitov, Yu.I. Kovtunenکو, Yu.E. Logachev, and L.P. Tishchenko, *J. Surf. Invest. X-ray, Synchrotron Neutron Tech.* **4**(5), 852 (2010). <http://link.springer.com/article/10.1134/S1027451010050289>
- [47] V.V. Bobkov, L.P. Tishchenko, A.V. Onishchenko, E.N. Zubarev, R.I. Starovoitov, Yu.I. Kovtunenکو, Yu.E. Logachev, and L.A. Gamayunova, *J. Surf. Invest.: X-ray, Synchrotron and Neutron Tech.* **5**(4), 806 (2011). <http://link.springer.com/article/10.1134/S1027451011080052>
- [48] V.V. Bobkov, R.I. Starovoitov, L.P. Tishchenko, Yu.I. Kovtunenکو, and L.A. Gamayunova, *J. Surf. Invest.: X-ray, Synchrotron and Neutron Tech.* **8**(5), 853 (2014). <https://doi.org/10.1134/S1027451014030264>
- [49] V.V. Bobkov, L.P. Tishchenko, Yu.I. Kovtunenکو, R.I. Starovoitov, Yu.E. Logachev, A.B. Tsapenko, and L.A. Gamayunova, *Ukr. J. Phys.* **65**(1), 61 (2020). <https://doi.org/10.15407/ujpe65.1.61>
- [50] S. Krat, Yu. Gasparyan, Ya. Vasina, A. Davletiyarova, A. Pisarev, *Vacuum*. **149**, 23 (2018). <https://doi.org/10.1016/j.vacuum.2017.12.004>
- [51] Yu. Gasparyan, S. Krat, A. Davletiyarova, Ya. Vasina, and A. Pisarev, *Fusion Eng. Des.* **146**, 1043 (2019). <https://doi.org/10.1016/j.fusengdes.2019.01.154>
- [52] B.B. Cipiti, and G.L. Kulcinski, *J. Nucl. Mater.* **347**(3), 298 (2005). <https://doi.org/10.1016/j.jnucmat.2005.08.009>
- [53] V.V. Bobkov, L.P. Tishchenko, Yu.I. Kovtunenکو, A.O. Skrypnyk, and L.A. Gamayunova, *PAST, Series: «Plasma Physics»*, (6), 93 (2020). https://vant.kipt.kharkov.ua/ARTICLE/VANT_2020_6/article_2020_6_93.pdf
- [54] V.V. Bobkov, R.I. Starovoitov, L.P. Tishchenko, E.N. Zubarev, Yu.I. Kovtunenکو, Yu.E. Logachev, in: *Proceedings of the 20th International Conference on Ion-Surface Interactions*, (ISI-2011, Zvenigorod, 2011), Vol. **2**, pp. 61–64. (in Russian)
- [55] N.A. Azarenkov, V.V. Bobkov, L.P. Tishchenko, R.I. Starovoitov, Yu.I. Kovtunenکو, Yu.E. Logachev, and L.A. Gamayunova, *PAST, Series: «Plasma Physics»*, (6), 73 (2016). https://vant.kipt.kharkov.ua/ARTICLE/VANT_2016_6/article_2016_6_73.pdf
- [56] O.V. Ogorodnikova, N.S. Klimov, Yu.M. Gasparyan, Z.R. Harutyunyan, V.S. Efimov, D. Kovalenko, K. Gutarov, A.G. Poskakalov, M.M. Kharkov, and A.V. Kaziev, in: *Proceedings of the 25th International Conference on Ion-Surface Interactions*, (ISI-2021 Moscow, Russia, 2021), Vol. **1**, pp. 65–67.
- [57] S.A. Krat, E.A. Fefelova, A.S. Prishvitsyn, Yu.M. Gasparyan, and A.A. Pisarev, in: *Proceedings of the 25th International Conference on Ion-Surface Interactions*, (ISI-2021 Moscow, Russia, 2021), Vol. **1**, pp. 108–110. (in Russian)

ДОСЛІДЖЕННЯ ПРОЦЕСІВ ЗАХОПЛЮВАННЯ ТА ВИДІЛЕННЯ ІМПЛАНТОВАНИХ ІОНІВ ДЕЙТЕРІЮ ТА ГЕЛІЮ ДЛЯ ПЛІВОК ВОЛЬФРАМУ І ТАНТАЛУ

Микола Азаренков^b, Валентин Бобков^a, Людмила Тищенко^a, Юрій Ковтуненко^a, Анатолій Скрипник^a, Дмитро Шевченко^a, Любов Гамаюнова^a

^aХарківський національний університет імені В.Н. Каразіна, Харків, м. Свободи, 4, 61022, Україна

^bНаціональний науковий центр «Харківський фізико-технічний інститут», вул. Академічна, 1, Харків, 61108, Україна

Проведено аналіз основних наявних в літературі результатів досліджень накопичення та міграції іонно-імплантованих ізотопів водню та гелію у вольфрамівих і танталових покриттях, утворення радіаційних пошкоджень кристалічної решітки та їх взаємодії з імплантованими газами. Показано вплив гелію та дейтерію на різні властивості і морфологію поверхні покриттів. Опромінення зразків проводили як пучками прискорених іонів ізотопів водню або He⁺, так і у плазмі, яка містить перелічені іони, при різних дозах та енергіях падаючих іонів, різних температурах мішені при імплантації. Особливу увагу приділено результатам досліджень, отриманим при одночасному опроміненні W, як у масивному вигляді, так і в тонкоплівковому. Використовувалися методи електронної мікроскопії, ре-емісійної мас-спектрометрії, термодесорбційної спектрометрії, рентгенівської фотоелектронної спектроскопії, рентгенівської дифракції, аналізу ядерної реакції та резерфордівського розсіювання іонів.

Ключові слова: дейтерій; гелій; іонна імплантація; термодесорбція; дефекти; W і Ta плівки

THERMALLY ACTIVATED DELAYED FLUORESCENCE IN ORGANIC SEMICONDUCTORS AND ITS APPLICATION IN LIGHT EMITTING DIODES

 Serhii Melnykov,  Igor Helzhynskyy,  Tetiana Bulavinets,  Pavlo Stakhira

National University "Lviv Polytechnic", Department of Electronic Engineering, 1 St. Yura sq., Lviv, Ukraine

Corresponding Author e-mail: serhii.o.melnykov@lpnu.ua

Received October 31, 2023; revised December 26, 2023; accepted December 30, 2023

The presence of the effect of thermally activated delayed fluorescence (TADF) in organic light-emitting materials (emitters), manifested in the "collecting" of triplet excitons in organic semiconductor complexes that do not contain noble metals, creates excellent prerequisites for the application of TADF materials in the technology of manufacturing organic light-emitting diodes (OLED). The significant progress in solving theoretical and technical problems, achieved in the process of development of highly efficient TADF materials, paves the way for the formation of the future of organic electronics. This review presents the analyses of the nature of the long-term fluorescence generation mechanism at the molecular level and the up-to-date strategies for designing TADF donor-acceptor materials, as well as exciplex intermolecular complexes. Special attention is focused on the analysis of TADF emitter ambipolar materials with a highly twisted, rigid molecular structure, which reveal a tendency towards the multi-channel emission mechanisms and their implementation in a variety of OLED structure architectures.

Key words: Organic light-emitting diodes; Thermally activated delayed fluorescence; Emitter; Multilayer structure; Exciton; Singlet-triplet energy splitting

PACS: 78.55.Kz

INTRODUCTION

The current state of the OLED technologies development largely determines the commercial attractiveness of lighting systems based on organic LEDs and OLED displays, which have a number of advantages over the liquid crystal displays. In particular, the OLED displays are thinner and weigh less. In addition, they are characterized by a wide viewing angle (up to 180°) and higher color contrast. A significant argument that opens up new design possibilities for the production of OLED displays and their implementation on the electronic equipment market is the technological capability of forming OLED displays on flexible substrates with the functional possibility to bend and unfold the screen. Regarding the expediency of using organic LEDs in light-emitting devices, here, first of all, the low energy consumption of OLEDs and the absence of toxic substances in their design should be noted, which creates prerequisites for both global energy saving and reducing the industrial burden on the environment [1].

The organic light-emitting diodes (OLEDs) are electroluminescent devices with a multilayer structure of organic semiconductor materials sandwiched between a transparent anode and a metal cathode (Fig. 1). When an external voltage is applied to the OLED electrodes (cathode and anode), the charge carriers (electrons and holes) enter the electron and hole injection layers, respectively, with further injection into the electron and hole transport films, from where they drift into the emissive (light-emitting) layer in which, under the influence of the Coulomb interactions form excitons [2-4].

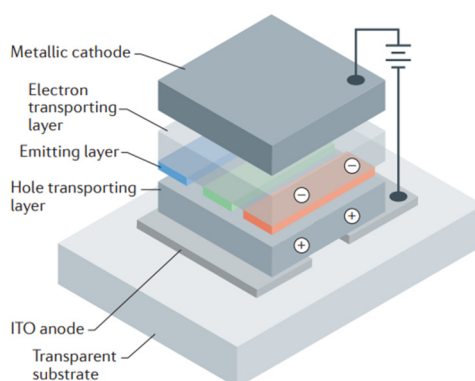


Figure 1. Schematic representation of the multilayer structure of the device based on an organic light-emitting diode (OLED)

Inherently, the excitons represent an emitter molecule in an excited state (Fig. 2). The molecular excited states can be classified as electrically balanced states formed by the exchange of energy and charge between neighboring molecules of singlet or triplet character. In the emitter molecule, there exist simultaneously two systems of electronic levels: singlet S_n and triplet T_n .

The triplet excitons have a rather long lifetime, since the radiative transition to the ground state is forbidden. This is equivalent to the indirect transitions in crystals. The triplet excitons can diffuse over long distances (up to 100 nm), while the singlet ones cannot diffuse more than 10 nm.

A definite set of vibrational states corresponds to each energy level. Both radiative and non-radiative transitions can occur during the transition of an excited molecule to an equilibrium state. In this context, internal conversion (IC) and Intersystem crossing (ISC) are distinguished. The internal conversion is characterized by intramolecular transitions between different electronic states of the same multiplicity, for example, $S_2 \rightarrow S_1$ (singlet-singlet) and $T_2 \rightarrow T_1$ (triplet-triplet). It should be noted that the probability of such transitions is the greater, the smaller is the difference between the energy levels of the initial and final state.

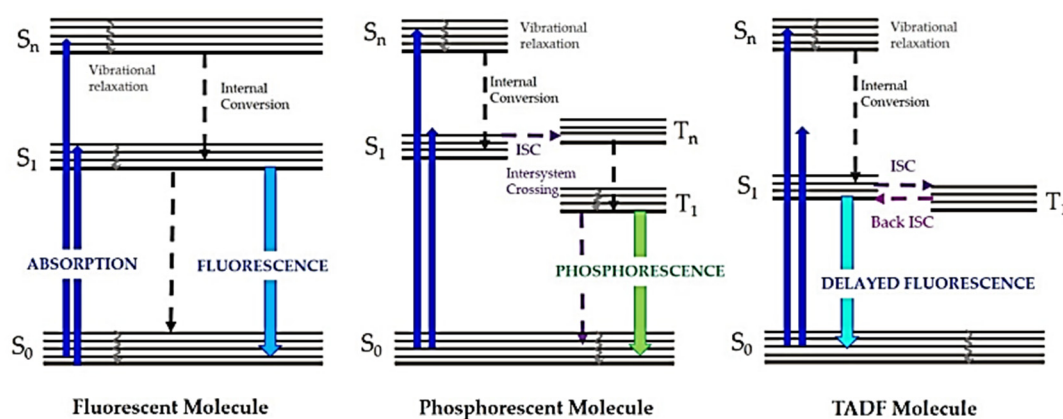


Figure 2. Energy level diagram that shows the main luminescence processes in an emitter molecule (left: fluorescent molecule; center: phosphorescent molecule; right: TADF molecule). Continuous arrows indicate radiative processes. Dotted arrows represent non-radiative relaxation

The total electron spin for the singlet state is zero, because the electrons are paired. For the triplet state, the total spin is equal to two, and the multiplicity, as opposed to one, for the singlet state corresponds to three, respectively. Generally, the basic unexcited state (state S_0) of organic molecules is singlet, and therefore, theoretically, a radiative transition from the lower singlet excited state - S_1 to the basic S_0 state is allowed. Such a radiative transition with short relaxation time in the nanosecond range is called fluorescence.

Unlike the phosphorescence, which is a theoretically forbidden radiative transition of triplet excitons from the lower triplet excited state T_1 to the main S_0 , the recombination time is in the microsecond or millisecond range. Note, that the relaxation time for triplet transitions is significantly reduced under the influence of such external factors, as heat or oxygen, on the emitter molecule [5, 6]. The intercombination conversion, that is, transitions between two isoenergetic vibrational levels, refers to the states of different multiplicity. For example, a molecule from the zero vibrational level of the S_1 state can move to the isoenergetic vibrational level of the triplet state T_2 , and then, as a result of vibrational relaxation, to the T_1 level. The transitions between the states of different multiplicities are, in principle, forbidden, however, the spin-orbit overlap may be sufficient to partially remove the prohibition [7-9].

It should be noted, that the presence of rare-earth metals (eg, Ir and Pt) increases the probability of spin-orbit overlap and, thus, increases the probability of intercombination conversion resulting in phosphorescence at the room temperature. Thus, this approach makes it possible to involve both triplet and singlet excitons in the process of light recombination, which theoretically allows obtaining a value of the external quantum efficiency (EQE) of the device close to 100%. Today, the maximum EQE value of the organic phosphorescent OLEDs, based on the latest phosphorescent metal complexes, shows a very high value, more than 50% [10-13].

SINGLET-TRIPLET ENERGY SPLITTING (ΔE_{ST}) AND TADF MECHANISM

The TADF-based organic LEDs use molecular systems with a small energy split between singlet and triplet states. This can be realized either in intramolecular charge transfer states of molecules with nearly orthogonal donor and acceptor parts, or in intermolecular exciplex states formed between an appropriate combination of individual donor and acceptor materials. These processes are described in more detail in our previous works [14-16,5,6,7]. Another method of using triplet excitons in OLEDs is the use of emitters that exhibit thermally activated delayed fluorescence. In fact, this type of molecule has a narrow energy gap between the triplet and singlet excited states, so that the thermal energy, inherent at the room temperature, is sufficient to activate the reverse Intersystem crossing (ISC (reverse ISC)), promoting the complete conversion of the triplet state to the singlet one, thus triggering the collection of singlets. When the gap is close to zero, the reverse intersystem crossing (RISC) is possible [17-19]. The most promising and effective approach to the collection of triplet excitons involving the RISC process is the use of TADF emitters. In the RISC TADF emitter, the thermal motion of the molecule at sufficiently high temperatures (more than 300 K) can easily activate the conversion. The efficiency of TADF is mainly determined by the temperature sensitive RISC process. The functional dependence of the RISC rate constant (k_{RISC}) on the temperature can be expressed by the Boltzmann equation:

$$k_{\text{RISC}} \propto \exp(\Delta E_{\text{ST}}/k_{\text{B}}T) \quad (1)$$

where T is the temperature and k_{B} is the Boltzmann constant.

It is well known that the presence of a narrow energy gap ΔE_{ST} of less than 0.2 eV in the emitter molecules enables an effective RISC process [20]. ΔE_{ST} can be defined as the energy difference of the lowest singlet (E_{S}) and triplet (E_{T}) excited states:

$$E_{\text{S}} = E + K + J, \quad (2)$$

$$E_{\text{T}} = E + K - J, \quad (3)$$

$$\Delta E_{\text{ST}} = E_{\text{S}} - E_{\text{T}} = 2J, \quad (4)$$

where E is the orbital energy, K is the electron repulsion energy, J is the exchange energy or the exchange integral [21].

$$J = \int_{-\infty}^{\infty} F_{\text{D}}(\lambda) \epsilon_{\text{A}}(\lambda) \lambda^4 d\lambda, \quad (5)$$

where $F_{\text{D}}(\lambda)$ is the normalized emission spectrum of the donor, ϵ_{A} is the standard for the molar absorption coefficient of the acceptor, and λ is the wavelength.

We remind that as a result of a conjugated bond formation in organic semiconductors, bonding π - and excited π^* molecular orbitals are formed. These orbitals form narrow energy levels that split into zones. The filled π -orbital is called the highest occupied molecular orbital (HOMO), and the excited π^* -orbital is called the lowest vacant molecular orbital LUMO (lowest unoccupied molecular orbital).

Thus, the value of the energy gap ΔE_{ST} is two times greater than that of J . Equation (4) shows that a small value of ΔE_{ST} can be obtained using a small overlap integral (5), i.e. by separating the HOMO and LUMO spatial wave functions. Note, that the molecular TADF emitters are the structures consisting of donor-acceptor (D-A) or donor-acceptor-donor (D-A-D) components, which are characterized by intramolecular charge transfer states between the acceptor and donor components. These emitter TADF components are so far apart in the orthogonal orbitals, that the spin-orbit interaction between them is very small, what makes the RISC scenario unlikely. From the molecular point of view, a spatially twisted structure can ensure a small value of ΔE_{ST} , since with an effective distribution of HOMO and LUMO, the value of the exchange integral can be small. A value of ΔE_{ST} close to zero can be obtained by spatial separation of the electron densities of the frontier orbitals, as shown in Fig. 3a. The spatial separation of the electron densities of HOMO and LUMO levels in the molecule with a twisted D-A structure is shown in Fig. 3 b. The right-angle rotation between the D and A components is important for the formation of the TADF molecule. These two key factors between the ^1CT singlet state and the ^3CT triplet state with a small energy gap provide TADF emission.

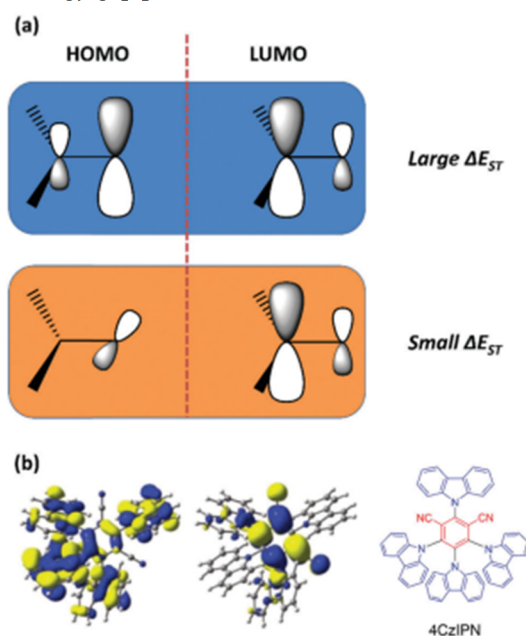


Figure 3. (a) Strategy for realizing small ΔE_{ST} values in the organic TADF molecules. HOMO: the highest occupied molecular orbital, LUMO: the lowest unoccupied molecular orbital, ΔE_{ST} : the energy gap between the S_1 and T_1 states. (b) Electron density in the HOMO and LUMO of the typical example (4CzIPN) of the organic TADF molecules with a twisted molecule of the D–A structure type. The inset shows the molecular structure. [22].

Besides the optimal values of ΔE_{ST} and k_{RISC} , a relatively large value of the radiation rate constant k_{r} , which is the rate of transition of a singlet exciton from the S_1 state to the S_0 one, is also important for obtaining effective TADF emission. However, the large value of k_{r} and close to zero ΔE_{ST} conflict with each other, what requires careful design of molecular structures for simultaneous implementation of the proper parameters. For example, some ketone derivatives

have a relatively small value of ΔE_{ST} , but exhibit phosphorescence only at low temperature due to the large value of k_r for the triplet excitons [23-25]. On the other hand, due to the special conjugation combination, resulting from the twisted central group $-CQ=$ in several diphenyl-ketones with different donor groups attached to the phenolic ring, there is a specific double TADF emission of white colour. Unlike the typical fluorescent emitters with rather narrow emission spectra, the TADF emitters usually exhibit poorer monochromeness. To improve the purity emission, steric hindrances are introduced into the TADF emitter core or intensify the stiffness of the acceptor fragment and, thus, suppress the molecular rotation between the donor and acceptor components [22, 26]. Another key direction that allows overcoming the limitations on the use of fluorescent dyes in the electroluminescent devices' technology is the study of promising TADF emitters with the aggregation induced effect. The fact is that under the influence of the $\pi-\pi$ interaction the TADF molecules are easily aggregated, what causes the aggregation-caused luminescence quenching (ACQ). This effect seriously limits the use of TADF emitters in optoelectronic devices. To overcome the occurrence of ACQ, numerous organic dyes with aggregation-induced emission (AIE) properties have been developed in the last decade. In fact, solutions of AIE luminophor are characterized by extremely low photoluminescence quantum efficiency, while their luminescence is sharply enhanced in the solid state. Such a phenomenon of enhanced emission is usually interpreted as a limitation of intermolecular rotations and the twisted Intramolecular Charge Transfer (TICT). Therefore, the charge transfer mechanisms and twisted molecular structures have a crucial effect on the photophysical properties of the TADF emitters, which are important for the high-performance OLED devices.

Besides the TADF exciplexes in this paper, i.e. the TADF emitter molecules with the AIE effect, attention is paid to highly twisted TADF molecules of the D-A type, subject to their molecular configurations. We also focus on developing the design and photophysical processes commonly used to optimize the TADF technology of the OLED device.

TADF EMITTERS BASED ON A DONOR-ACCEPTOR PAIR

Relative simplicity of the synthesis as well as the high quality of light emission of the TADF emitters, based on a donor-acceptor pair, determines their wide use in organic optoelectronic devices. However, the presence of a large twist angle between the D and A fragments can promote the significant steric hindrances. In this context, the use of ortho-D-A-compounds is a simple and effective strategy for the formation of an almost vertically twisted molecular configuration to obtain the smallest possible value of ΔE_{ST} , as well as an efficient TADF process. Su and colleagues [27] developed a series of D-A molecules based on TRZ groups acting as the acceptors and the dibenzothiophene or thianthrene (TE) derivatives as the donors. The presence of the influence of heavy sulfur atoms promoted an increase in the SOC coefficient and, as a result, enabled the passage of ISC. In the singlet state of oTE-DRZ (Fig. 4), the rigid molecular environment prevented the occurrence of a non-radiative transition, while the available permitted phosphorescent transitions promote further cascade conversion and the increase of the long-lived triplet excitons lifetime.

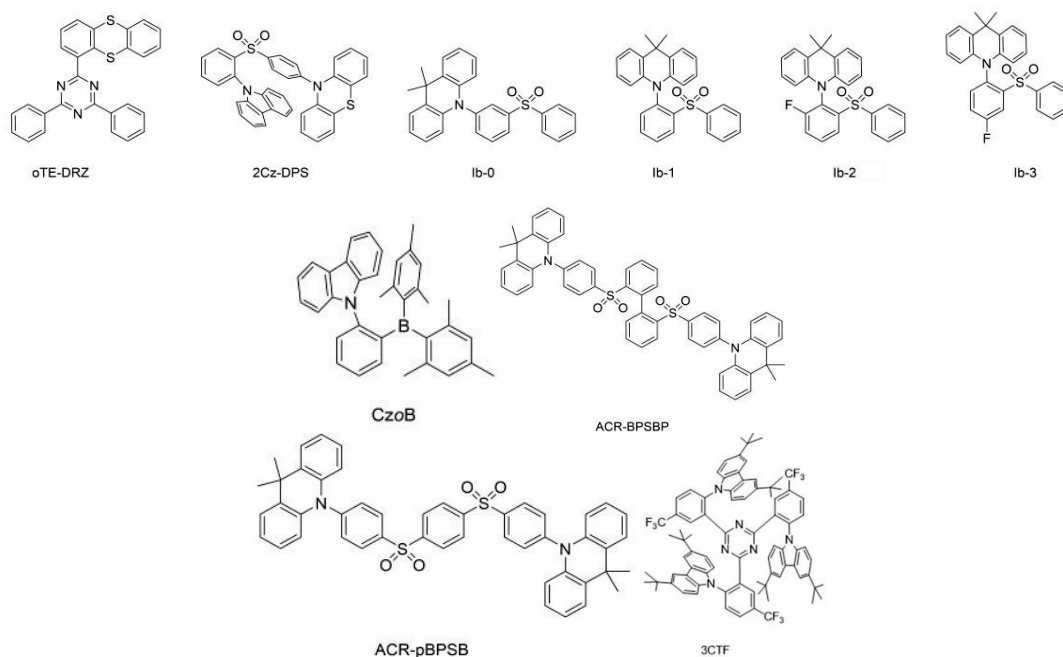


Figure 4. Molecular structure of TADF emitters based on a donor-acceptor pair.

It was found that the oTE-DRZ crystal (Fig. 4) exhibited the dual channel properties (TADF and the room temperature phosphor luminescence (RTP) with greenish-blue luminescence of photoluminescence quantum yield (PLQY 87%) (Fig. 5) due to the limitation of intermolecular and intramolecular degrees of motion freedom. Owing to the presence of strong $\pi-\pi$ intermolecular bonds, the OLEDs based on oTE-DRZ thin films showed the EQE of up to 20.6%. To achieve a high IQE for the simple TADF emitters Chi and colleagues [28] reported about the development of a new

molecular design and the synthesis of twisted molecular TADF emitters by introducing an ortho-bonded carbazole donor link, which forms an asymmetric D–A–D' structure. The close spatial proximity of the donor and acceptor in the asymmetric structure can intensify through-space charge transfer (TSCT), thereby suppressing molecular vibrations, thus preventing the energy loss. The X-ray diffraction data indicate a substantial bond between phenothiazine (D') and diphenylsulfone (A). Due to the two-channel mechanism of the charge transfer (CT), the molecular compound 2Cz-DPS (Fig. 4(42)) shows a high value (91.9%) of solid-state PLQ and the maximum quantum yield of electroluminescence = 28.7%. The same team [29] developed and synthesized two twisted D-A molecules characterized by ultra-long RTP and TADF relaxation time, namely o-Cz and p-Cz, in which the carbazole donor and the benzophenone acceptor were involved as they were combined by ortho- and the pair-method. Such molecules have been shown to exhibit a small ΔE_{ST} , that contributes to ISC and RISC under the dual-channel CT conditions, which in turn increases the number of triplet excitons involved to increase the TADF efficiency. Ultimately, o-Cz demonstrated the ultralong lifetime of 0.84 s and the quantum efficiency of 16.6%. To balance the lifetime and the emitter PLQY, Wang and colleagues [30] designed and synthesized three TADF molecules with a twisted structure based on diphenylsulfone and 9,9-dimethyl acridine groups. By removing the phenyl group from lb-Ph to reduce the distance between the D and A fragments, the through-space charge transfer TSCT can be achieved. The materials were characterized by multifunctional emissive properties, including TADF, the room temperature phosphorescence, aggregation, and triboluminescence (TL), which can be induced by a mechanical irritant action. The molecules exhibiting TSCT were found to show the PLQY value of nearly 100%. lb-1 (Fig. 4 (44)) and lb-3 (Fig. 4(46)) show obvious TL properties (Fig. 5). The both crystals showed good crystal clarity after grinding, which indicated good mechanical stability of the materials.

Although the effective TADF blue emitter materials are necessary for the commercialization of organic light-emitting diodes, there are a number of unsolved problems when implementing them into the technological route of the OLED fabrication. In particular: the high frequency of their emission negatively affects the effective life of blue OLEDs due to the rapid degradation of the emitting material [31-33]. Besides, a typical problem for such devices is a rapid performance degradation in the mode of high brightness. Therefore, the development of stable blue emitters for OLEDs is one of the most difficult tasks. Kido and colleagues [34] proposed a new strategy to obtain the blue TADF using 9,9-dimethyl-9,10-dihydroacridine (ACR) groups as the donor and double sulfonyl groups as the acceptor. ACR-BPSBP (Fig. 4) and ACR-pBPSB (Fig. 4) molecules had the same donors and the acceptors, but were characterized by different bonds. Compared to the ACR-pBPSB (Fig. 4), the ACR-BPSBP molecule (Fig. 4) has a more twisted structure and exhibits a higher PLQY due to the limitation of the conjugation length. Since the ACRBPSBP material (Fig. 4) showed steric difficulties on the part of the ortho-phenylsulfonyl group, the orthogonal configuration with a large twist angle of 85° was chosen. This molecule exhibited blue emission with the emission maximum in the region of 460 nm and with PLQY = 82%. However, the elongated ACR-pBPSB (Fig. 4) exhibited green emission with the maximum of 490 nm and the PLQY of 76%.

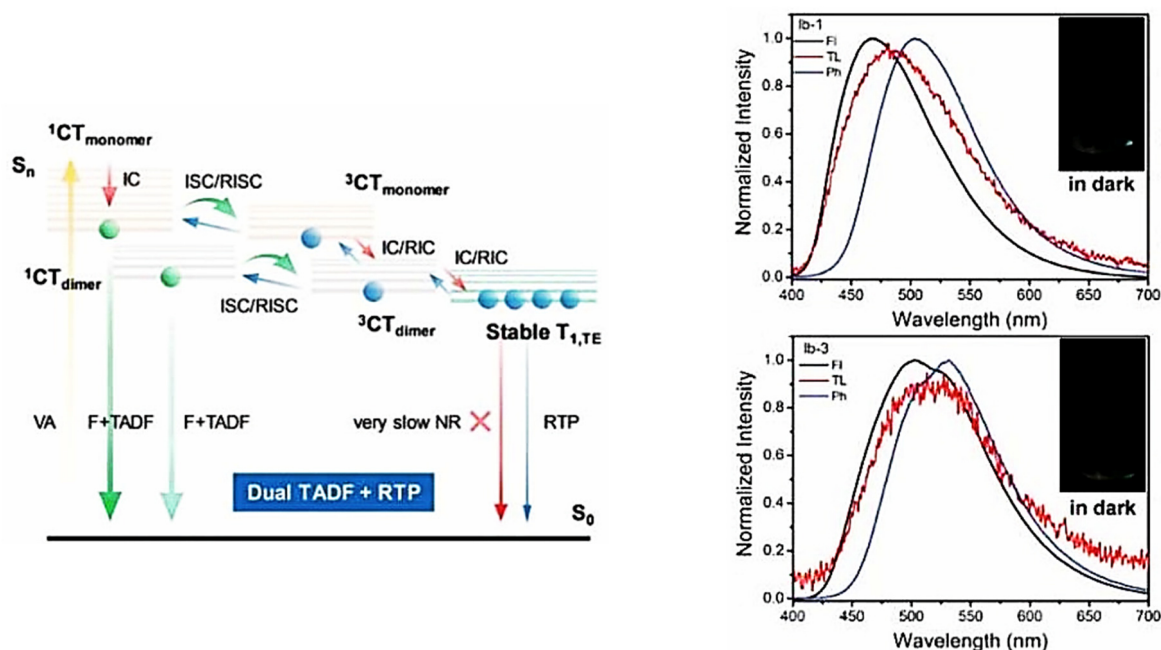


Figure 5. Diagram of the energy excited levels of 1CTF , 2CTF and 3CTF (a). Fluorescence (FI), triboluminescence (TL), and phosphorescence (Ph) spectra of lb-1 (44) and lb-3 (46) in the solid state (b)

ORGANIC LEDs BASED ON NON-DOPED TADF EMITTERS

The non-doped emitter layers in the OLED structure have a number of advantages as to the "doped" systems (guest-host): in particular, the manufacturing process is simplified, also most of the non-doped devices are characterized

by a lower supply voltage, higher brightness and a smaller drop in their efficiency than the doped devices. Besides, the inhomogeneities arising during the phase separation in the guest-host system, which are absent in the non-doped emitter, are harmful to the color stability and efficiency of the device. However, in terms of the quantity, the OLEDs based on the non-doped emitter layers are significantly inferior to the doped ones. The proper thermal and photochemical stability of TADF non-doped emitters is an important condition for their use in the OLED technology. Such a stability can be judged from the dissociation energy of the molecular bonds. The example of the presence of a relatively high bond dissociation energy, which promotes the increase in the effective life of TADF - OLED, is observed in the emitter molecule based on the combination of a stable acceptor (triazine) and a donor fragment (carbazole) [35-37]. Also, the key OLED parameter is the value of the external quantum efficiency (η_{EQE}), which can be represented as $\eta_{EQE} = IQE \times \eta_{out}$, where IQE and η_{out} are the internal quantum efficiency of the device and the light output coefficient, respectively. For the TADF-based OLEDs, the formula for determining IQE is written down as:

$$IQE = \left[0.25\phi_p + \{0.75 + 0.25(1 - \phi_p)\} \frac{\phi_d}{1 - \phi_p} \right] \gamma, \quad (6)$$

where γ is the charge balance coefficient, Φ_p and Φ_d are the contribution of instantaneous fluorescence and delayed fluorescence to the quantum yield of photoluminescence (Φ_{PL}) respectively: $\Phi_{PL} = \Phi_p + \Phi_d$. The γ value makes virtually 1.0 for most of modern multilayer OLEDs.

The non-doped OLEDs based on the green emitting molecule DMAC-BP show the EQE value and the maximum brightness of 18.9% and $\sim 50,000 \text{ cdm}^{-2}$, respectively [38]. DBT-BZ-DMAC-based organic LEDs showing combined emission, which is caused by aggregation and TADF, have the maximum EQE of 14.2% and the slight drop in the current efficiency of 0.46% from the peak values to the values at 1000 cdm^{-2} [39]. Also, in a non-doped green OLED with the CP-BP-PXZ-based emitter, whose peculiarity is the presence of the long-term aggregation-induced fluorescence, showed the EQE value of 18.4% with a slight drop in the current efficiency of 1.2% at 1000 cdm^{-2} [40]. Exciplex TADF OLEDs are another type of the non-doped devices (Fig. 6.).

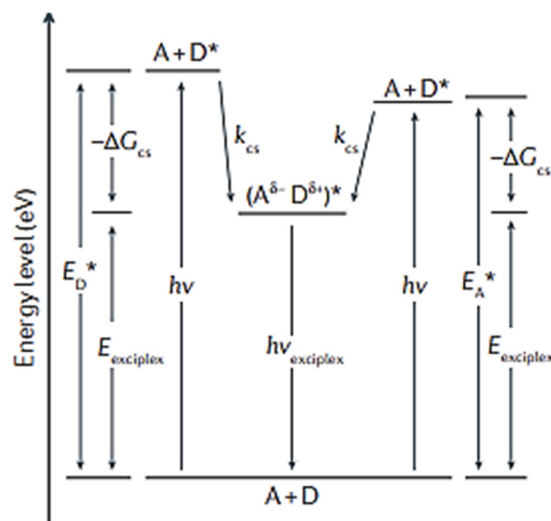


Figure 6. Electronic energy diagram demonstrating the process of exciplex formation and interconnection at the energy levels. First, the donors and acceptors form the excited ground-state donors and acceptors or form the excited ground-state acceptors and donors upon the high-energy excitation. Then, the donor excitons and acceptor excitons combine into an exciplex. And finally, the exciplex splits into a donor and an acceptor component. In this case, a transition to the ground state with emission occurs.

The exciplexes are the complexes in the excited state (CT), which are formed as a result of the interfacial interaction of an excited molecule (for example, an acceptor) with the other unexcited molecule (for example, a donor) ($1A^* + D \rightarrow 1(A D)^*$). Then, the complex disintegrates into a positive hole and a negative electron with the transition to the S_0 ground state with light emission. The electrostatic interaction of a positively charged donor with a negatively charged acceptor, which are located at a short distance from each other, enables exciplex stabilization. Similar to the intramolecular TADF in the TADF exciplex compounds, the spatial orientation of the HOMO and LUMO positions for D and A components and the intermolecular distance between them determine the formation of the RISC mechanism. It was found that the exciplexes, which emitted relatively high-energy light, were characterized by a relatively small CT energy from molecule to molecule and vice versa. Simulation of the emission energy in the solid phase showed the CT state to depend on the intermolecular distance between D and A molecules and their spatial orientation. To confirm this fact, the experimental observations were performed. An exciplex layer was formed with the 1:1 molar ratio of tris(4-carbazol-9-ylphenyl) amine (TCTA) and 4,6-bis(3,5-di(pyridin-4-yl)phenyl)-2-methylpyrimidine (B4Py-MPM) on the glass substrate [41]. The chemical structures and energy levels of TCTA and B4Py-MPM are shown in Fig. 7 a. The positions of the HOMO level were determined by UV photoelectron spectroscopy, and the LUMO levels were calculated from the HOMO level and

the absorption edge of the UV absorption spectrum. The film absorption spectrum corresponds to the absorption spectra of TCTA and B4PyMPM, indicating that no aggregation or formation of the ST complex has occurred in the solid state. Fig. 7 b shows the spectral time dependence of the exciplex emission. The change in the time parameter of the intense light pulse was recorded by a high-speed photo-recording camera. The photoluminescent excitation of the samples was carried out using a pulsed nitrogen laser with the generation wavelength of 337 nm. The presence of different time spectral distributions indicates fast and slow mechanisms of the exciplex fluorescence decay. The integrated emission spectrum is dominated by exciplex emission. A gradual spectral shift into the low-energy area was observed, so, with the radiation shift from $\lambda = 493$ nm at the beginning of the area, a fast emission region ($t = 0-10$ ns) to $\lambda = 535$ nm, and in the long-wave area a slowed-down emitting band ($t = 10-70$ μ s) was observed. The spectral red shift with the delayed emission is a feature of the exciplex caused by the effect of polarization under the influence of the host medium [42,43].

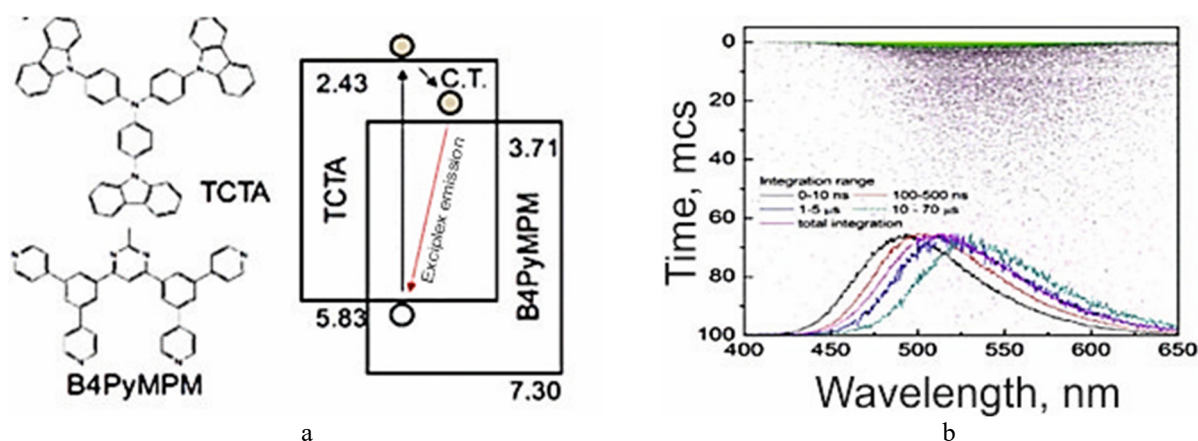


Figure 7. a) Chemical structures of tris(4-carbazol-9-ylphenyl)-amine (TCTA) and 4,6-bis(3,5-di(pyridin-4-yl)phenyl)-2-methylpyrimidine (B4PyMPM) with the energy levels, b) time dependences of photoluminescence amplitude spectra of the exciplexes

To increase further the efficiency of using the exciplex approach in the technology of organic light-emitting devices, it is advisable to develop molecules with a high PLQY level for the use of D and A, while in order to minimize the quenching of triplet states in the TADF process, the donor and acceptor molecules should contain high-energy triplet energy levels [44, 45].

OLED BASED ON THE DOPED TADF EMITTER

To prevent the excitons annihilation in the organic LEDs, based on the doped TADF systems (guest-host), the emitter is usually dispersed into a solid-state matrix film (into the host component). A number of requirements are imposed on the host material, in particular: the triplet energy of the matrix molecule must be higher than that of the TADF emitter, the HOMO and LUMO levels must be correctly oriented, the organic matrix semiconductor must be characterized by a wide band gap and bipolar mobility of the charge carriers to maximize the formation of excitons in the emitter layer. Besides, the matrix should be morphologically stable and have good film-forming properties. In most cases, in the production of organic LEDs with TADF emitters traditional starting materials were used, which had been originally developed for the phosphorescent metal-organic complexes based on heavy metals [46]. The typical matrix molecules with high triplet energies are: DPEPO (T1: 3.3 eV) [47], PPF (T1: 3.1 eV) [48], mCPCN (T1: 3.03 eV) [49], CzSi (T1 3.0 eV) [49], mCBP (T1: 2.9 eV) [50], TPBi (T1: 2.7 eV) [51]. For the highly efficient green emitter 4CzIPN, several materials with the host function were synthesized [52-54], with which the quantum efficiency of up to 31.2% was observed for OLEDs (Table 1). Many matrix materials have been developed for the DMAC-DPS blue emitter. In particular, the OLED with the maximum EQE of 23.0% was obtained using DPETPO as the host component [55]. It should be noted that due to the local dipole interaction, the polar matrix films can stabilize the CT excited state of the guest emitter. In this case, the emission of TADF OLED shifts to the red region of the spectrum. Thus, for the blue TADF-emitter DDMA-TXO2 due to combining the emitter with the matrix of the correct polarity, the energy of the 1 CT state decreases, and ΔE_{ST} is minimized, as a result of which EQE reaches the values of 22.4% for the device with CIE coordinates (0.16, 0, 24) [56].

Table 1. Photoluminescence and electroluminescence characteristics of representative low-molecular TADF materials

Molecule		λ_{PL} (nm)	ΔE_{ST} (eV)	Φ_{PL} Host/ toluene (%)	τ_{PF} (ns)/ τ_{DF} (μ s)	CE (cdA^{-1})	PE (lmW^{-1})	EQE _{max} (%)
DMAC-DPS	PL:mCP film (10wt%)	464	0.09	90/80	2.1/3.1	-	-	19.5
	EL:DPEPO film (10wt%)							
	mCP film (10wt%)							
	PL:mCP film (10wt%)							
	EL:DPEPO film (10wt%)					39.7	44.4	23.0

Molecule		ΔE_{ST} (eV)	Φ_{PL} Host/ toluene (%)	τ_{PF} (ns)/ τ_{DF} (μ s)	CE (cdA^{-1})	PE (lmW^{-1})	EQE_{max} (%)	
DMAC-TRZ	mCPCN film (8wt%)	495	0.05	90/83	20.3/1.9	66.8	65.6	26.5
	PL: mCPCN film (10wt%) EL: neat film					61.1	45.7	20
4CzIPN	CBP film (6wt%)	507	0.08	93.8/-	17.8/5.1	-	-	19.3
	3CzPFP (1%)					-	-	31.2
PXZ-TRZ	CBP film (6wt%)	545	0.08	66/43	20/1.1	-	-	12.5
DACT-II	CBP film (9wt%)	529	0.009	63.7/100	-/-	-	-	29.6
TPA-DCPP	Neat film	708	0.13	14/84	20.8/0.76	4.0	-	9.8
HAP-3TPA	26mCPy film (6 \pm 1wt%)	610	0.17	91/-	-/100	25.9	22.1	17.5

White TADF OLEDs have found wide application in the up-to-date display devices and lighting systems, what created the prerequisites for further investment in their research area. White TADF OLEDs are usually obtained by mixing the three primary red, green, blue (RGB) emitting colors, for example: green (4CzPN), red (4CzTPN-Ph) and blue (3CzTRZ) emitters from the matrix (mCBP and PPT) [57-59]. With the optimized hetero structure consisting of 4CzPN:mCBP(3 nm)/4CzTPN-Ph:mCBP (2 nm)/3CzTRZ:PPT (10 nm), the TADF OLED device achieved the maximum EQE value of 17.6% and CIE_{x,y} (0.26, 0.38). The application of hybrid "warm-white" WOLEDs, obtained using the TADF emitter of blue color (2CzPN) and yellow phosphor PO-01 in separate emitting layers (Fig. 8), made it possible to achieve the EQE_{max} values of 22.6% and (CIE_{x,y} = (0.45, 0.48)) [34]. By combining the yellow TADF emitter PXZDSO2 with the dark blue fluorescent emitter NI-1-PhTPA, the warm white LEDs were fabricated achieving the EQE_{max} of 15.8% (CIE_{x,y} = (0.401, 0.476)). Furthermore, when the dark-red fluorescent component was inserted, the three-color white OLEDs were obtained with EQE_{max} = 19.2% (CIE_{x,y}=(0.348, 0.577)), with a very high color rendering index of 95 [59,60].

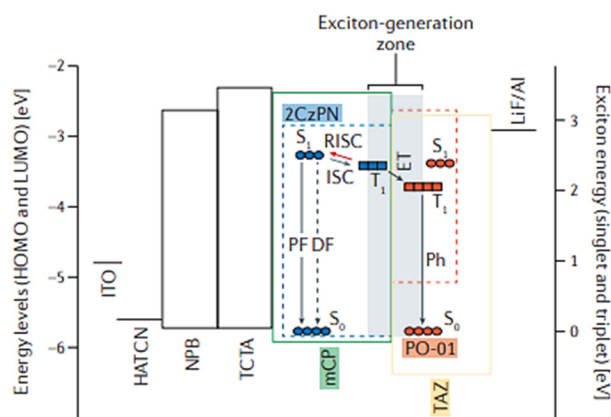


Figure 8. Energy levels, exciton energies and light emission mechanism of materials used in the hybrid white organic LEDs. The hybrid white OLED has two emissive layers (EML). The first EML, close to the hole transport layer (NPB), contains 2CzPN in the mCP matrix. In the second EML, located next to the electron transport layer, PO-01 is doped into the matrix. The emissive layers are located between the TAZ electron transport layer and the TCTA electron/exciton blocking layer. HATCN is used as a hole injection layer. The large energy shift of the highest occupied molecular orbitals (HOMO) of TAZ and the HOMO of mCP prevents the hole transport between adjacent hole-transporting layers. In the zone of exciton generation (gray color), a hole and an electron can combine due to the Coulomb forces with the excitons formation.

The correct orientation of the molecule can increase the efficiency of the doped OLEDs. The emitter with the horizontal dipole transition moment provides a much higher output coupling efficiency than the vertically oriented dipole, due to which the EQE increases [61]. Theoretically, the EQE can be increased up to 46% for the perfect horizontal orientation of emitters without using the external output structures with $\Phi_{PL} = 1$ and $\Theta = 1$, where Φ_{PL} is the photoluminescence quantum yield, Θ is the percentage of horizontal dipoles among all the emitting dipoles. For example, due to the high percentage of all the emitting dipoles ($\Theta=92\%$), the combination of the host component DPEPO and TADF of the CC2TA emitter as the emitting layer, provided $\text{EQE}_{\text{max}} = 11\pm 1\%$ [62] (Fig. 9). The efficiency of the horizontal orientation of the emitters was higher (31.3%) than that of the isotropic emitters (20.6%).

TADF OLED based on aggregation-induced emission.

The non-doped OLED using bis[3-(9,9-dimethyl-9,10-dihydroacridine) phenyl] sulfone (mSOAD) exhibits excellent blue electroluminescence performance with the emission maximum of 488 nm and EQE =14.0%. Besides, the turn-on voltage of this OLED is 3.1 V with the maximum output of 31.7 cd/A. The AIDF OLED based on DMAC-DPS emitter demonstrates high performance characteristics. Yang and colleagues later reported about highly efficient OLEDs using two isomers as emitters: the bis-[3-(9,9-dimethyl-9,10-dihydroacridine) phenyl] sulfone isomer (mSOAD) and the bis

compound [2-(9,9-dimethyl-9,10-dihydroacridine) phenyl] of sulfone (o-ACSO₂). Both of these molecules have good TADF properties with excellent solubility and AIE effect due to the large twist angles between the donor and acceptor fragments (Table 2) [63, 64].

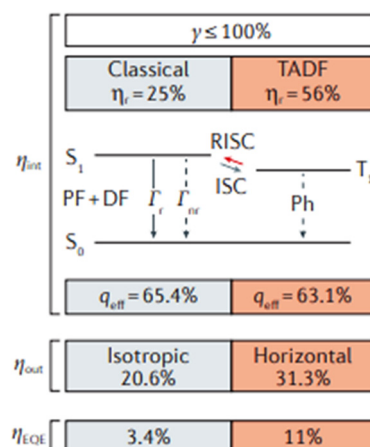


Figure 9. Individual contribution of isotropic and horizontal singlets to the external quantum efficiency (EQE or η_{EQE}) in the oriented EML. The left column lists the typical values for the isotropic singlet emitter, and the right column lists the typical values for the oriented TADF emitter, allowing the EQE to acquire values higher than the possible ones of the classical limit. The TADF increases the percentage of the emitting excitons η_r due to the reverse conversion of the triplet excitons to the singlet state, which, in turn, increases the internal quantum efficiency (η_{int}). The horizontal orientation of the dipole transition moments in the EML increases the output efficiency (η_{out}). The radiative quantum efficiency is assumed to be the same in both scenarios. However, since the Purcell factors depend on the orientation, different values of the emission quantum efficiency η_{EQE} are used in the calculation.

Table 2. Production performance of non-doped AIDF OLEDs

Compound	λ _{EL} nm	V _{on} V	L _{max} cd m ⁻²	CE _{max} cd A ⁻¹	PE _{max} lm W ⁻¹	EQE %
m-DTPACO	480	3.9	10005	4.8	2.8	2.4
m-ACSO ₂	486	4.1	-	37.9	23.8	17.2
mSOAD	488	3.1	-	31.7	28.4	14.0
o-ACSO ₂	492	4.4	-	14.1	7.8	5.9
ECPTT	494	5.6	10090	3.437	-	-
G2B	500 ^a	4.3 ^a	-	11.3	7.1	4.8
	500 ^b	3.4 ^b		14.0	11.5	5.7
CP-BP-DMAC	502	2.7	37680	41.6	37.9	15.0
DBT-BZ-DMAC	508	2.7	27270	43.3	35.7	14.2
G3B	513 ^a	3.6 ^a	-	8.7	6.6	3.6
	516 ^b	2.9 ^b		7.7	5.7	2.9
p-DTPACO	517	3.9	7354	10.8	8.2	3.7
ECPTT	517	5.8	7561	2.478	-	-
DCPDAPM	521	3.2	123371	26.88	15.63	8.2
SBDBQ-DMAC	544	2.8	14578	35.4	32.7	10.1

A bit higher efficiency than that of the AIDF OLED, which is based on the DMAC-DPS emitter, is demonstrated by a light-emitting organic device, which is made using mACSO₂ with electroluminescence in the blue-green region with the maximum in the region of 486 nm, the turn-on voltage of 4.1 V, the maximum current efficiency of 37.9 cd/A, with the energy efficiency of 23.8 lm/W and EQE of 17.2%. When using another isomer o-ACSO₂ in the OLED technology, the emission is slightly shifted to the red region of the spectrum with the maximum of 492 nm and EQE = 5.9%, the OLED turn-on voltage corresponds to the value of 4.4 V with the maximum current efficiency of 14.1 cd/A and with the maximum power output of 7.8 lm/W [63]. Also, a blue-green OLED was produced by Tang and colleagues using triphenylethylene as the AIE block, the carbazole, and thianthrene-9,9,10,10-tetraoxide (ECPTT) as the donor and acceptor, respectively [65]. The potential application of such a dye as an emitting layer in the non-doped OLED showed the maximum emission of 494 nm. The device turn-on voltage was 5.6V at the maximum brightness of 10090 cd/m² and with the maximum current efficiency of 3.437 cd/A. Li and colleagues [66] analyzed the application of AIE emitters, with the TADF effect inherent in them, in the non-doped green organic LEDs, which had been previously reported by Xu Zhang and colleagues [67,68]. By comparing the symmetric and asymmetric configuration of the donor and acceptor groups, i.e. using one (phenothiazine) or two different donors (phenothiazine and phenoxazine) in combination with one central acceptor component (bis-phenylsulfone), the authors concluded that the asymmetric structure of the emitters is a key condition to achieve high values of characteristics in the devices under study. Indeed, the non-doped film in the organic LEDs of the asymmetric PTSOPO provided higher current density, higher brightness, and higher EQE than of

the symmetric PTSOPT. In particular, the non-doped PTSOPO device can achieve maximum EQE= 17.0% of green electroluminescence. It should be noted, that a very low drop (0.2%) indicates to high performance of the non-doped blue-green OLED [40]. The asymmetric triple structure was also successfully investigated by Tan and colleagues [40] to obtain the organic LEDs emitting different colors. The emitter based on the D-A-D' configuration, where the D-A fragment is formed by 9-phenyl-9H-carbazole, which is bonded in the third position with the benzoyl unit (CP-BP) and uses 9,9-dimethyl-9,10.-dihydroacridine (DMAC) as the third substituent, provides the blue-green OLED generation. It takes interest that the HOMO orbitals are localized on the electron-donor part D (DMAC), and the LUMO – on the benzophenone (BP) core and they are extended to the second half of the carbazole fragment, and as a result, the emitter is characterized by a lower ΔE_{ST} value, as compared to the similar molecules containing phenoxazine (PXZ) or phenothiazine (PTZ) instead of DMAC (0.33, 0.45, and 0.11 eV for CP-BP-PXZ, CP-BP PTZ, and CP-BP-DMAC, respectively). Besides, the twisted phenyl ring in the 9th position of carbazole prevents close packing between the molecules and weakens the intermolecular interactions, thereby reducing the effect of ACQ on the film. The maximum spectral length of the emission of the OLED, based on this emitter, is 502 nm. The device is characterized by low turn on voltage (2.7 V), maximum brightness of 37,680 cd/m², maximum energy efficiency of 37.9 lm/W and EQE = 15.0%. It should be noted that the very low drop (0.2%) indicates to the high performance of the non-doped blue-green OLED [40].

CONCLUSIONS

The utilisation of the TADF materials as the emitters or as a host component matrix for other emitters in the OLEDs has progressed rapidly in the past few years and is considered to be the next-generation OLED technology. Nowadays, the TADF OLEDs demonstrate a high efficiency commensurate with the OLED devices based on the phosphorescent materials with organometallic complexes, which contain noble metals. The development of the molecular structures that resolve the contradiction between the large value of the emission rate constant from the excited state S_1 and the small value of ΔE_{ST} has become a notable achievement. A lot of new materials with TADF properties have also shown a promising potential for other applications in particular: in organic UV photodetectors, fluorescent sensors, and sensors based on mechanoluminescence, which really take advantage of small ΔE_{ST} values and efficient RISC process in the TADF molecules. However, the research and development of TADF materials is still under the development stage. And so, there is a need for the development of novel molecular design strategies and detailed theoretical approaches for the development of materials on the TADF effect, which inherent some other photophysical properties. Some new conceptual solutions of the model providing the utilization and control of excitons by the TADF process should appear to expand the TADF-type materials to some other research areas.

ORCID

✉ Serhii Melnykov, <https://orcid.org/0000-0002-1093-9869>; ✉ Igor Helzhynskyy, <https://orcid.org/0000-0001-5397-4595>
✉ Pavlo Stakhira, <https://orcid.org/0000-0001-5210-415X>; ✉ Tetiana Bulavinets, <https://orcid.org/0000-0001-6898-3363>

REFERENCES

- [1] S.R. Forrest, D.D.C. Bradley, and M.E. Thompson, *Advanced Materials*, **15**(13), 1043 (2003). <https://doi.org/10.1002/adma.200302151>
- [2] Fröbel, M.; Schwab, T.; Kliem, M.; Hofmann, S.; Leo, K.; Gather, M. C. *Light: Sci. Appl.* **4**, e247 (2015). <https://doi.org/10.1038/lsa.2015.20>
- [3] N. Ohon, T. Bulavinets, I. Yaremchuk, and R. Lesyuk, *East European Journal of Physics*, **4**, 6-22 (2022). <https://doi.org/10.26565/2312-4334-2022-4-01>
- [4] F. Dumur, *Org. Electron.* **21**, 27 (2015). <https://doi.org/10.1016/j.orgel.2015.02.026>
- [5] M.A. Baldo, D.F. O'Brien, M.E. Thompson, and S.R. Forrest, *Physical Review B*, **60**(20), 14422 (1999). <https://doi.org/10.1103/PhysRevB.60.14422>
- [6] M.A. Baldo, D.F. O'Brien, Y. You, A. Shoustikov, S. Sibley, M.E. Thompson, and S.R. Forrest, *Nature*, **395**, 151 (1998). <https://doi.org/10.1038/25954>
- [7] H. Uoyama, K. Goushi, K. Shizu, H. Nomura, and C. Adachi, *Nature*, **492**, 234 (2012). <https://doi.org/10.1038/nature11687>
- [8] Y. Tao, C. Yang, J. Qin, *Chem. Soc. Rev.* **40**, 2943 (2011). <https://doi.org/10.1039/c0cs00160k>
- [9] M. Godumala, S. Choi, M.J. Cho, and D.H.J. Choi, *Mater. Chem. C*, **4**, 11355 (2016). <https://doi.org/10.1039/C6TC04377A>
- [10] H. Yersin, A.F. Rausch, R. Czerwieniec, T. Hofbeck, and T. Fischer, *Coordination Chemistry Reviews*, **255**(21), 2622 (2011). <https://doi.org/10.1016/j.ccr.2011.01.042>
- [11] M.Y. Wong, and E. Zysman-Colman, *Adv. Mater.* **29**, 1605444 (2017). <https://doi.org/10.1002/adma.201605444>
- [12] Y. Li, J.-Y. Liu, Y.-D. Zhao, and Y.-C. Cao, *Mater. Today*, **20**, 258 (2017). <https://doi.org/10.1016/j.mattod.2016.12.003>
- [13] Z. Yang, Z. Mao, Z. Xie, Y. Zhang, S. Liu, J. Zhao, J. Xu, et al., *Chem. Soc. Rev.* **46**, 915 (2017). <https://doi.org/10.1039/C6CS00368K>
- [14] X. Tan, D. Volyniuk, T. Matulaitis, J. Keruckas, K. Ivaniuk, I. Helzhynskyy, P. Stakhira, and J.V.s Grazulevicius, *Dyes and Pigments*, **177**, 108259 (2020). <https://doi.org/10.1016/j.dyepig.2020.108259>
- [15] A. Bucinskas, K. Ivaniuk, G. Baryshnikov, O. Bezvikonnyi, P. Stakhira, D. Volyniuk, B. Minaev, et al., *Organic Electronics*, **86**, 105894 (2020). <https://doi.org/10.1016/j.orgel.2020.105894>
- [16] N. Bunzmann, B. Krugmann, S. Weissenseel, L. Kudriashova, K. Ivaniuk, and P. Stakhira, *Advanced Electronic Materials*, **7**, 2000702 (2021). <https://doi.org/doi.org/10.1002/aelm.202000702>
- [17] H. Uoyama, K. Goushi, K. Shizu, H. Nomura, and C. Adachi, *Nature*, **492**, 234 (2012). <https://doi.org/10.1038/nature11687>

- [18] Q.S. Zhang, B. Li, S.P. Huang, H. Nomura, H. Tanaka, and C. Adachi, *Nat. Photonics*, **8**, 326 (2014). <https://doi.org/10.1038/nphoton.2014.12>
- [19] S.Y. Lee, T. Yasuda, Y.S. Yang, Q. Zhang, and C. Adachi, *Angew. Chem., Int. Ed.* **126**, 6520 (2014). <https://doi.org/10.1002/ange.201402992>
- [20] J. Miller, *Phys. Today*, **66**, 10 (2013). <https://doi.org/10.1063/PT.3.2166>
- [21] Y. Tao, K. Yuan, T. Chen, P. Xu, H. Li, R. Chen, C. Zheng, et al., *Adv. Mater.* **26**, 7931 (2014). <https://doi.org/10.1002/adma.201402532>
- [22] D.R. Lee, B.S. Kim, C.W. Lee, Y. Im, K.S. Yook, S.H. Hwang, and J.Y. Lee, *ACS Appl. Mater. Interfaces*, **7**, 9625 (2015). <https://doi.org/10.1021/acsami.5b01220>
- [23] J.W. Sun, J.H. Lee, C.K. Moon, K.H. Kim, H. Shin, and J.J. Kim, *Adv. Mater.* **26**, 5684 (2014). <https://doi.org/10.1039/C9RA02875G>
- [24] Y. Im, M. Kim, Y.J. Cho, J.-A. Seo, K.S. Yook, and J.Y. Lee, *Chem. Mater.* **29**, 1946 (2017). <https://doi.org/10.1021/acs.chemmater.6b05324>
- [25] L. Yao, B. Yang, and Y. Ma, *Science China Chemistry*, **57**, 335 (2014). <https://doi.org/10.1007/s11426-013-5046-y>
- [26] Y. Im, S.Y. Byun, J.H. Kim, D.R. Lee, C.S. Oh, K.S. Yook, J.Y. Lee, *Adv. Funct. Mater.* **27**, 1603007 (2017). <https://doi.org/10.1002/adfm.201603007>
- [27] X. Cai, Z. Qiao, M. Li, X. Wu, Y. He, X. Jiang, Y. Cao, and S.J. Su, *Angew. Chem. Int. Ed.* **58**, 13522 (2019). <https://doi.org/10.1002/anie.201906371>
- [28] Z. Mao, Z. Yang, C. Xu, Z. Xie, L. Jiang, F.L. Gu, J. Zhao, et al., *Chem. Sci.* **10**, 7352 (2019). <https://doi.org/10.1039/C9SC02282A>
- [29] H. Fu, Y.-M. Cheng, P.-T. Chou, and Y. Chi, *Mater. Today*, **14**, 472 (2011). [https://doi.org/10.1016/S1369-7021\(11\)70211-5](https://doi.org/10.1016/S1369-7021(11)70211-5)
- [30] B. Li, Z. Yang, W. Gong, X. Chen, D.W. Bruce, S. Wang, H. Ma, et al., *Adv. Opt. Mater.* **9**, (2021). <https://doi.org/10.1002/anie.202301896>
- [31] W.-C. Chen, C.-S. Lee, and Q.-X. Tong, *J. Mater. Chem. C*, **3**, 10957 (2015). <https://doi.org/10.1039/C5TC02420J>
- [32] M. Zhu, and C. Yang, *Chem. Soc. Rev.* **42**, 4963 (2013). <https://doi.org/10.1039/c3cs35440g>
- [33] S. Winter, S. Reineke, K. Walzer, and K. Leo, *Proc. SPIE*, **6999**, 69992N (2008). <https://doi.org/10.1117/12.782784>
- [34] M. Liu, R. Komatsu, X. Cai, H. Sasabe, T. Kamata, K. Nakao, K. Liu, et al., *Adv. Opt. Mater.* **5**, (2017). <https://doi.org/10.1002/adom.201700334>
- [35] W.L. Tsai, et al. *Chem. Commun.* **51**, 13662 (2015). <https://doi.org/10.1039/C5CC05022G>
- [36] F.B. Dias, K.N. Bourdakos, V. Jankus, K.C. Moss, K.T. Kamtekar, V. Bhalla, J. Santos, et al., *Adv. Mater.* **25**, 3707 (2013). <https://doi.org/10.1002/adma.201300753>
- [37] S. Hirata, Y. Sakai, K. Masui, H. Tanaka, S.Y. Lee, H. Nomura, N. Nakamura, et al., *Nature Materials*, **14**, 330 (2015). <https://doi.org/10.1038/nmat4154>
- [38] Q. Zhang, et al., *Adv. Mater.* **27**, 2096 (2015). <https://doi.org/10.1002/adma.201405474>
- [39] J. Guo, et al., *Adv. Funct. Mater.* **27**, 1606458 (2017). <https://doi.org/10.1002/adfm.201606458>
- [40] J. Huang, et al., *Angew. Chem. Int. Ed.* **129**, 13151 (2017). <https://doi.org/10.1002/anie.201706752>
- [41] X. Hu, N. Aizawa, M. Kim, M. Huang, Z. Li, G. Liu, H. Gao, et al., *Chemical Engineering Journal*, **434**, 134728, (2022). <https://doi.org/10.1016/j.cej.2022.134728>
- [42] S. Kesari, B.K. Mishra, and A.N. Panda, *Chemical Physics Letters*, **791**, 139383 (2022). <https://doi.org/10.1016/j.cplett.2022.139383>
- [43] F.B. Dias, T.J. Penfold, and A. P. Monkman, *Methods Appl Fluoresc.* **5**, 012001 (2017). <https://doi.org/10.1088/2050-6120/aa537e>
- [44] S.-C. Ji, T. Zhao, Z. Wei, L. Meng, X.-D. Tao, M. Yang, X.-L. Chen, and C.-Z. Lu, *Chemical Engineering Journal*, **435**, 134868 (2022). <https://doi.org/10.1016/j.cej.2022.134868>
- [45] K. Suzuki, S. Kubo, K. Shizu, T. Fukushima, A. Wakamiya, Y. Murata, C. Adachi, and H. Kaji, *Angew. Chem. Int. Ed.* **54**, 15231 (2015). <https://doi.org/10.1002/anie.201508270>
- [46] M.-S. Lin, et al. *Mater. Chem.* **22**, 16114 (2012). <https://doi.org/10.1039/C2JM32717A>
- [47] Q. Zhang, et al. *Nat. Photon.* **8**, 326 (2014). <https://doi.org/10.1038/nphoton.2014.12>
- [48] I.S. Park, S.Y. Lee, C. Adachi, and T. Yasuda, *Adv. Funct. Mater.* **26**, 1813 (2016). <https://doi.org/10.1002/adfm.201505106>
- [49] Y.J. Cho, K.S. Yook, and J.Y. Lee, *Adv. Mater.* **26**, 6642 (2014). <https://doi.org/10.1002/adma.201402188>
- [50] S. Hirata, et al., *Nat. Mater.* **14**, 330 (2015). <https://doi.org/10.1038/nmat4154>
- [51] A. Senes, et al., *J. Mater. Chem. C*, **5**, 6555 (2017). <https://doi.org/10.1039/C7TC01568B>
- [52] B.S. Kim, and J.Y. Lee, *ACS Appl. Mater. Interfaces*, **6**, 8396 (2014). <https://doi.org/10.1021/am501301g>
- [53] Y. Seino, S. Inomata, H. Sasabe, Y.J. Pu, and J. Kido, *Adv. Mater.* **28**, 2638 (2016). <https://doi.org/10.1002/adma.201503782>
- [54] M.P. Gaj, C. Fuentes-Hernandez, Y. Zhang, S.R. Marder, and B. Kippelen, *Org. Electron.* **16**, 109 (2015). <https://doi.org/10.1007/s00894-016-3047-4>
- [55] J. Zhang, et al., *Adv. Mater.* **28**, 479 (2016). <https://doi.org/10.1002/adma.201502772>
- [56] P. Dos Santos, et al., *J. Phys. Chem. Lett.* **7**, 3341 (2016). <https://doi.org/10.1021/acs.jpcclett.6b01542>
- [57] J. Nishide, H. Nakanotani, Y. Hiraga, and C. Adachi, *Appl. Phys. Lett.* **104**, 233304 (2014). <https://doi.org/10.1063/1.4882456>
- [58] D. Zhang, L. Duan, Y. Li, D. Zhang, and Y. Qiu, *J. Mater. Chem. C*, **2**, 8191 (2014). <https://doi.org/10.1039/C4TC01289E>
- [59] X.L. Li, et al., *Adv. Mater.* **28**, 4614 (2016). <https://doi.org/10.1002/adma.201505963>
- [60] E. Angioni, M. Chapran, K. Ivaniuk, N. Kostiv, V. Cherpak, P. Stakhira, A. Lazauskas, et al., *J. Mater. Chem. C*, **4**, 3851 (2016). <https://doi.org/10.1039/C6TC00750C>
- [61] S. Nowy, B.C. Krummacher, J. Frischeisen, N.A. Reinke, and W. Brütting, *J. Appl. Phys.* **104**, 123109 (2008). <https://doi.org/10.1063/1.3043800>
- [62] C. Mayr, et al., *Adv. Funct. Mater.* **24**, 5232 (2014). <https://doi.org/10.1002/adfm.201400495>
- [63] J. Li, R. Zhang, Z. Wang, B. Zhao, J. Xie, F. Zhang, H. Wang, and K. Guo, *Adv. Opt. Mater.* **6**(6), 1701256 (2018). <https://doi.org/10.1002/adom.201701256>
- [64] K. Wu, Z. Wang, L. Zhan, C. Zhong, S. Gong, G. Xie, and C. Yang, *J. Phys. Chem. Lett.* **9**, 1547 (2018). <https://doi.org/10.1021/acs.jpcclett.8b00344>

- [65] X. Dong, S. Wang, C. Gui, H. Shi, F. Cheng, and B. Z. Tang, *Tetrahedron*, **74**, 497 (2018). <https://doi.org/10.1016/j.tet.2017.12.022>
- [66] I.H. Lee, W. Song, and J.Y. Lee, *Org. Electron.* **29**, 22 (2016). <https://doi.org/10.1002/adma.201605444>
- [67] S. Xu, T. Liu, Y. Mu, Y.-F. Wang, Z. Chi, C.-C. Lo, S. Liu, et al., *Angew. Chem. Int. Ed.* **54**, 874 (2015). <https://doi.org/10.1002/anie.201409767>
- [68] Z. Xie, C. Chen, S. Xu, J. Li, Y. Zhang, S. Liu, J. Xu, and Z. Chi, *Angew. Chem. Int. Ed.* **54**, 7181 (2015). <https://doi.org/10.1002/anie.201502180>

ТЕРМІЧНО АКТИВОВАНА УПОВІЛЬНЕНА ФЛУОРЕСЦЕНЦІЯ В ОРГАНІЧНИХ НАПІВПРОВІДНИКАХ ТА ЇЇ ЗАСТОСУВАННЯ У СВІТЛОВИПРОМІНЮЮЧИХ ДІОДАХ





Сергій Мельников, Ігор Гельжинський, Тетяна Булавінець, Павло Стахіра

Національний університет «Львівська політехніка», кафедра електронної інженерії, пл. Св. Юра 1, Львів, Україна

Наявність ефекту термічно активованої уповільненої флуоресценції (TADF) в органічних світловипромінюючих матеріалах (емітерах), що проявляється в «збиранні» триплетних екситонів в органічних напівпровідникових комплексах, які не містять благородних металів, створює чудові передумови до застосування TADF матеріалів у технології виготовлення органічних світловипромінюючих діодів (OLED). Значущий прогрес у вирішенні теоретичних та технічних завдань, що досягається в процесі розроблення вискоелективних TADF матеріалів, прокладає шлях до формування майбутнього органічної електроніки. У даному огляді розглянута природа механізму генерації довготривалої флуоресценції на молекулярному рівні та сучасні стратегії проектування TADF донорно-акцепторних матеріалів, а також ексиплексних міжмолекулярних комплексів. Особлива увага акцентується на аналізі TADF емітерних амбіполярних матеріалів з сильно закрученою, жорсткою молекулярною структурою, які виявляють тенденцію до багатоканальних механізмів випромінювання та їхньої імплементації в різноманітну архітектуру OLED структур.

Ключові слова: *органічні світловипромінюючі діоди; термічно активована уповільнена флуоресценція; емітер; багатощарова структура; екситон; синглет-триплетне енергетичне розщеплення*

COSMOLOGICAL EVOLUTION OF BIANCHI TYPE- VI_0 KANIADAKIS HOLOGRAPHIC DARK ENERGY MODEL

 B. Ganeswara Rao^{a,b},  Dipana Jyoti Mohanty^b,  Y. Aditya^{c,*},  U.Y. Divya Prasanthi^d

^aDepartment of Mathematics, Sri G.C.S.R. College, Rajam-532127, India

^bDepartment of Mathematics, GIET University, Gunupur-765002, India

^cDepartment of Mathematics, GMR Institute of Technology, Rajam-532127, India

^dDepartment of Statistics & Mathematics, College of Horticulture, Dr. Y.S.R. Horticultural University, Parvathipuram-535502, India

*Corresponding Author e-mail: aditya.y@gmrit.edu.in; yaditya2@gmail.com

Received December 5, 2023; revised December 19, 2023; accepted January 10, 2024

The purpose of this paper is to construct an anisotropic and spatially homogeneous Bianchi type- VI_0 Kaniadakis holographic dark energy model in general relativity. For this purpose, we consider Hubble horizons as the IR cutoff. To obtain a deterministic solution of the model's field equations, we assume a relationship between the metric potentials which leads to an exponential solution and accelerated expansion. To investigate the physical behaviour of our dark energy model, we obtain some important cosmological parameters like Hubble, deceleration, equation of state and statefinder as well as $\omega_{khde} - \omega'_{khde}$, $r - s$ and $r - q$ planes. We also included the stability analysis for the dark energy model through the squared speed of sound. It is observed that the equation of state parameter shows Λ CDM model at late times. Also, the squared speed of sound gives the stability of the Kaniadakis holographic dark energy model at the initial epoch and the model is unstable at late times. Statefinder diagnostic and deceleration parameters exhibit a smooth transition of the universe from the decelerating phase to the current accelerated expansion of the universe and also correspond to the Λ CDM model at late times. All these cosmological parameters support recent observational data.

Keywords: *Bianchi type- VI_0 model; Dark energy model; General theory of relativity; Cosmology; Kaniadakis holographic dark energy*

PACS: 98.80.-k, 95.36.+x

1. INTRODUCTION

Einstein's general relativity (GR) is regarded as a key theory for comprehending the concealed features of gravitational dynamics, which provide a fundamental comprehension of astrophysical events and the universe. Recent observations have provided compelling evidence that the universe undergoes both early inflation and late-time rapid expansion [1]-[3]. The phenomenon is attributed to the existence of an enigmatic force called dark energy (DE), which exhibits repulsive gravitational effects. There are primarily two methods to addressing the enigmatic characteristics of dark energy and cosmic acceleration problems. Modified theories of gravity are different attempts to integrate dark energy by modifying the action principle in general relativity. In an alternative approach, many dynamical dark energy candidates are offered in order to comprehend the essence of dark energy. Both updated theories of gravity and dynamical DE models have received quite positive evaluations [4]-[7]. Of the several dynamical dark energy theories, the primary contender is the cosmological constant. However, it is plagued by issues of cosmic coincidence and fine-tuning. Due to this rationale, many alternative dynamical differential equation (DE) models have been proposed, including a range of scalar field models such as K-essence, phantom, quintessence, ghost, etc., as well as Chaplygin gas and holographic DE models [8]-[14].

Among the several dynamical DE models, the holographic dark energy model has gained popularity as a preferred method to investigate the riddle of dark energy. The proposal is based on the quantum characteristics of black holes, which have been thoroughly studied in the literature to research quantum gravity [13, 14]. As per the holographic principle, the vacuum energy Λ of a system of size L must not exceed the mass of a black hole of the same size, since this would result in the development of a black hole in quantum field theory. The energy density of HDE is determined according to the formulation provided by Cohen et al. [15]

$$\rho_{khde} = 3d^2 m_p^2 L^{-2}. \quad (1)$$

where m_p represents the reduced Planck mass, $3d^2$ denotes a numerical constant, and L represents the IR-cutoff. Various forms of IR-cutoff have been examined in the scholarly literature, such as the Hubble horizon H^{-1} , event

Cite as: B.G. Rao, D.J. Mohanty, Y. Aditya, U.Y.D. Prasanthi, East Eur. J. Phys. 1, 43 (2024), <https://doi.org/10.26565/2312-4334-2024-1-03>

© B.G. Rao, D.J. Mohanty, Y. Aditya, U.Y.D. Prasanthi, 2024; CC BY 4.0 license

horizon, particle horizon, conformal universe age, Ricci scalar radius, and Granda–Oliveros cutoff [16]- [18]. The HDE models, with different IR cutoffs, provide a contemporary understanding of the universe’s acceleration. They also demonstrate that the transition redshift value, which marks the move from an earlier deceleration phase ($q>0$) to the present acceleration phase ($q<0$), aligns with modern observational evidence. Nojiri and Odintsov [19] introduced a method for combining the early and late stages of the universe using generalized HDE and phantom cosmology. They have recently extended this concept to what they call Hinflation [20] In recent times, many formulations of entropy have been used to create and examine cosmological models. Several novel models of holographic dark energy (HDE) have been developed, including the Tsallis HDE [21, 22], Sharma-Mittal HDE [23], and Renyi HDE model [24]. Several writers have examined several cosmological models of new HDE models [25]- [33]. Recently, the Kaniadakis statistics, which serves as a generalized measure of entropy [34]- [36], has been used to investigate various gravitational and cosmological implications. The generalized \mathcal{K} -entropy (Kaniadakis), which represents the entropy of a black hole, may be determined using a single free parameter [37]

$$S_{\mathcal{K}} = \frac{1}{\mathcal{K}} \sinh(\mathcal{K}S_{BH}) \tag{2}$$

where \mathcal{K} is an unknown parameter. Thus, by using the concept of entropy and the notion of holographic dark energy, a novel model of dark energy called Kaniadakis holographic dark energy (KHDE) is proposed [37], which exhibits significant characteristics. Jawad and Sultan [38], Sharma [39], and Drepanou et al. [40] have examined KHDE models inside various gravitational theories. The dynamic structures of HDE, as investigated by Sadeghi et al. [41], have been analyzed within the context of Brans-Dicke’s theory of gravity, using the Tsallis and Kaniadakis approaches.

Theoretical cosmology has shown increasing interest in anisotropic and spatially homogeneous worlds in recent decades. The primary empirical data from CMBR (Bennett et al. [42]) has been deemed as evidence in favor of a shift from a non-uniform phase of the universe to a uniform phase (Akarsu and Kilinc [43]). Furthermore, there is a belief that during the first stages of the universe, the isotropic FRW model may not provide a comprehensive and accurate depiction of matter. To conduct a realistic analysis of cosmological models and determine whether they can reach the observed level of homogeneity and isotropy, it is necessary to consider space-times that are both spatially homogeneous and anisotropic. Bianchi type (BT) cosmological models, which are homogeneous but not necessarily isotropic, have garnered significant attention from academics because to their anisotropic nature. Recently, several academics have developed intriguing cosmological models that include dark energy in the context of anisotropic Bianchi space-times. Various scholars have examined anisotropic cosmological models in diverse contexts [44]- [60].

Motivated by the above investigations and discussion, in this work, we consider BT- VI_0 space-time filled with matter and KHDE in the framework of GR. The work in this paper is configured as follows: In Sec. 2, the BT- VI_0 metric is given and the field equations in the presence of anisotropic KHDE fluid and matter are derived. Also, we obtained the solution of the field equations and constructed the KHDE model. Sec. 3 contains several cosmological parameters of our model. The results are summarised with conclusions in the last section.

2. FIELD EQUATIONS AND KANIADAKIS HDE MODEL

Einstein’s general theory of relativity is usually regarded as one of the most accomplished theories of gravity in contemporary physics. The salient feature of GR is its enduring constancy, which has been unaltered for over a century. The equations governing the field in this theory are expressed as

$$R_{ij} - \frac{1}{2}Rg_{ij} = -\frac{8\pi G}{c^4}T_{ij} \tag{3}$$

where R_{ij} is the Ricci tensor, T_{ij} is the energy–momentum tensor of matter distribution, G is Newton’s gravitational constant, R is Ricci scalar, g_{ij} is metric potential, and c is the speed of light. Here we assume the gravitational constants $8\pi G=c=1$. We consider the geometry of the universe as spatially homogeneous and anisotropic BT- VI_0 line element which can be written as

$$ds^2 = dt^2 - A^2 dx^2 - B^2 e^{2x} dy^2 - C^2 e^{-2x} dz^2, \tag{4}$$

where A , B and C are functions of cosmic time t only. The following are the some of physical parameters which are useful in finding the solution of field equations for the BT- VI_0 space-time given by Eq. (4).

The average scale factor $a(t)$ and volume V of the BT- VI_0 space-time are defined as

$$V = [a(t)]^3 = ABC. \tag{5}$$

Anisotropic parameter A_h is given by

$$A_h = \frac{1}{3} \sum_{i=1}^3 \left(\frac{H_i - H}{H} \right)^2 \tag{6}$$

where $H_1 = \frac{\dot{A}}{A}$, $H_2 = \frac{\dot{B}}{B}$, $H_3 = \frac{\dot{C}}{C}$ are directional Hubble's parameters and $H = \frac{1}{3} \left(\frac{\dot{A}}{A} + \frac{\dot{B}}{B} + \frac{\dot{C}}{C} \right)$ is mean Hubble's parameter. Here and after an overhead dot denotes differentiation concerning cosmic time t . Expansion scalar (θ) and shear scalar (σ^2) are defined as

$$\theta = u_{;i}^i = \frac{\dot{A}}{A} + \frac{\dot{B}}{B} + \frac{\dot{C}}{C} \quad (7)$$

$$\sigma^2 = \frac{1}{2} \sigma^{ij} \sigma_{ij} = \frac{1}{3} \left(\frac{\dot{A}^2}{A^2} + \frac{\dot{B}^2}{B^2} + \frac{\dot{C}^2}{C^2} - \frac{\dot{A}\dot{B}}{AB} - \frac{\dot{A}\dot{C}}{AC} - \frac{\dot{B}\dot{C}}{BC} \right) \quad (8)$$

where

$$\sigma_{ij} = \frac{1}{2} (u_{i;\mu} h_j^\mu + u_{j;\mu} h_i^\mu) - \frac{1}{3} \theta h_{ij}, \quad (9)$$

with $h_{ij} = g_{ij} - u_i u_j$ is the projection tensor while $u_i = (1, 0, 0, 0)$ is the four-velocity in the comoving coordinates. The deceleration parameter is given by

$$q = \frac{d}{dt} \left(\frac{1}{H} \right) - 1. \quad (10)$$

The matter distribution is assumed to be the combination of pressure-less matter and anisotropic DE which are, respectively, given as

$$T'_{ij} = \rho_m u_i u_j \quad (11)$$

$$\bar{T}_{ij} = (\rho_{khde} + p_{khde}) u_i u_j - p_{khde} g_{ij}. \quad (12)$$

where p_{khde} and ρ_{khde} are the pressure and energy density of DE fluid whereas ρ_m is the energy density of matter. The EoS parameter ω_{khde} of DE is defined as $\omega_{khde} = \frac{p_{khde}}{\rho_{khde}}$. To ensure the present acceleration of the universe, here, we consider the anisotropic distribution of DE. After parameterizing the energy-momentum tensor of DE \bar{T}_{ij} , it can be expressed as follows:

$$\begin{aligned} \bar{T}_{ij} &= [1, -\omega_x, -\omega_y, -\omega_z] \rho_{khde} \\ &= [1, -\omega_{khde}, -(\omega_{khde} + \alpha), -(\omega_{khde} + \beta)] \rho_{khde} \end{aligned} \quad (13)$$

where $\omega_x = \omega_{khde}$, $\omega_y = \omega_{khde} + \alpha$ and $\omega_z = \omega_{khde} + \beta$ are the directional equation of state (EoS) parameters on x , y and z respectively. Here, α and γ are the deviations from EoS parameter ω_{khde} in y and z directions respectively.

In the comoving coordinate system, with the help of (13), the field equations (3) for the metric (4) can be written as

$$\frac{\ddot{B}}{B} + \frac{\ddot{C}}{C} + \frac{\dot{B}\dot{C}}{BC} + \frac{1}{A^2} = -\omega_{khde} \rho_{khde} \quad (14)$$

$$\frac{\ddot{A}}{A} + \frac{\ddot{C}}{C} + \frac{\dot{A}\dot{C}}{AC} - \frac{1}{A^2} = -(\omega_{khde} + \alpha) \rho_{khde} \quad (15)$$

$$\frac{\ddot{A}}{A} + \frac{\ddot{B}}{B} + \frac{\dot{A}\dot{B}}{AB} - \frac{1}{A^2} = -(\omega_{khde} + \beta) \rho_{khde} \quad (16)$$

$$\frac{\dot{A}\dot{B}}{AB} + \frac{\dot{B}\dot{C}}{BC} + \frac{\dot{A}\dot{C}}{AC} - \frac{1}{A^2} = \rho_{khde} + \rho_m \quad (17)$$

$$\frac{\dot{B}}{B} - \frac{\dot{C}}{C} = 0 \quad (18)$$

and, also, the energy conservation equation $(T'_{ij} + \bar{T}_{ij})_{;j} = 0$ is obtained as

$$\dot{\rho}_m + \dot{\rho}_{khde} + \left(\frac{\dot{A}}{A} + \frac{\dot{B}}{B} + \frac{\dot{C}}{C} \right) (\rho_m + (1 + \omega_{khde}) \rho_{khde}) + \left(\alpha \frac{\dot{B}}{B} + \beta \frac{\dot{C}}{C} \right) \rho_{khde} = 0. \quad (19)$$

On integration, Eq. (18) yields $B = k_1 C$, where k_1 is an integration constant. It can be taken as unity, without loss of any generality, so that we have

$$B = C. \quad (20)$$

Given the Eq. (20), the field equations (14) to (17) reduce to

$$2 \frac{\ddot{B}}{B} + \frac{\dot{B}^2}{B^2} + \frac{1}{A^2} = -\omega_{khde} \rho_{khde} \quad (21)$$

$$\frac{\ddot{A}}{A} + \frac{\ddot{B}}{B} + \frac{\dot{A}\dot{B}}{AB} - \frac{1}{A^2} = -(\omega_{khde} + \alpha) \rho_{khde} \tag{22}$$

$$\frac{\ddot{A}}{A} + \frac{\ddot{B}}{B} + \frac{\dot{A}\dot{B}}{AB} - \frac{1}{A^2} = -(\omega_{khde} + \beta) \rho_{khde} \tag{23}$$

$$2\frac{\dot{A}\dot{B}}{AB} + \frac{\dot{B}^2}{B^2} - \frac{1}{A^2} = (\rho_{khde} + \rho_m). \tag{24}$$

From Eqs. (22) and (23), we obtain

$$\alpha = \beta. \tag{25}$$

The reason for this is that the model exhibits isotropy in the y and z directions, resulting in the elimination of any deviations from the equation of state of dark energy. Based on Equation (25), the field equations (21)-(24) form a set of three distinct equations involving six variables: $A, B, \rho_{khde}, \omega_{khde}, \rho_m$, and α . To get a predictable outcome for the complex and nonlinear field equations in our model, we impose the following reasonable physical constraints:

Here, we consider the fact that expansion scalar θ is directly proportional to shear scalar σ which leads to a relation between the metric potentials as follows:

$$B = A^k \tag{26}$$

k represents a positive constant that accounts for the anisotropy of space-time. Collins et al. [61] have determined that in a spatially homogeneous space-time, the normal congruence to the homogeneous expansion adheres to the constraint that the ratio of the shear stress (σ) to the Hubble parameter (H) remains constant.

Using the relation (26) in Eqs. (21) and (22), we obtain

$$\dot{A}A^{2k} = A_0 \exp \int \left\{ \frac{A}{(k-1)\dot{A}} \left(\frac{-2}{A^2} + \alpha \rho_{khde} \right) \right\} dt. \tag{27}$$

Recently, it has been common to assume that the skewness parameter is a function of the energy density of dark energy, in order to obtain a more comprehensive and specific solution. This assumption has been made by Akarsu and Kilinc [62], as well as Sharif and Zubair [63]. To get the explicit solution for Eq. (27), we use the assumption that there is a relationship between the skewness parameter $\alpha(t)$ and the energy density of dark energy (DE), denoted as ρ_{khde}

$$\alpha(t) = \frac{1}{\rho_{khde}} \left(\frac{2}{A^2} + \alpha_0(k-1) \frac{\dot{A}}{A} \right) \tag{28}$$

where α_0 is an arbitrary constant. These kinds of assumptions have been taken by several authors in literature [64]-[66]. Hence, from Eqs. (27) and (28) we find the metric potentials as

$$A = \left(\frac{A_0(2k+1)}{\alpha_0} \exp(\alpha_0 t) + (2k+1)A_1 \right)^{\frac{1}{2k+1}}$$

$$B = C = \left(\frac{A_0(2k+1)}{\alpha_0} \exp(\alpha_0 t) + (2k+1)A_1 \right)^{\frac{k}{2k+1}}. \tag{29}$$

Here A_0 and A_1 integrating constants. Now metric (4), with the help of metric potentials in Eq. (29), can be written as

$$ds^2 = dt^2 - \left(\frac{A_0(2k+1)}{\alpha_0} \exp(\alpha_0 t) + (2k+1)A_1 \right)^{\frac{2}{2k+1}} dx^2$$

$$- \left(\frac{A_0(2k+1)}{\alpha_0} \exp(\alpha_0 t) + (2k+1)A_1 \right)^{\frac{2k}{2k+1}} (e^{2x} dy^2 + e^{-2x} dz^2). \tag{30}$$

Eq. (29) represents a spatially homogeneous and anisotropic BT- VI_0 KHDE model within the framework of GR with the following properties along with the physical parameters given in the next sections. The average scale factor and volume of the model are, respectively, given by

$$a(t) = \left(\frac{A_0(2k+1)}{\alpha_0} \exp(\alpha_0 t) + (2k+1)A_1 \right)^{\frac{1}{3}} \tag{31}$$

$$V = \left(\frac{A_0(2k+1)}{\alpha_0} \exp(\alpha_0 t) + (2k+1)A_1 \right) \quad (32)$$

The average Hubble's parameter H and expansion scalar θ are obtained as

$$H = 3\theta = \frac{(2k+1)A_0 \exp(\alpha_0 t)}{3 \left(\frac{A_0(2k+1)}{\alpha_0} \exp(\alpha_0 t) + (2k+1)A_1 \right)} \quad (33)$$

The shear scalar σ^2 and average anisotropic parameter A_h are given by

$$\sigma^2 = \frac{A_1^2(k-1)^2 e^{2(\alpha_0 t)}}{3 \left(\frac{A_0(2k+1)}{\alpha_0} \exp(\alpha_0 t) + (2k+1)A_1 \right)^2} \quad (34)$$

$$A_h = \frac{2(k-1)^2}{(2k+1)^2}. \quad (35)$$

The statistics above demonstrate that as time (t) advances, both the spatial volume and average scale factor of the universe exhibit exponential growth, indicating the expansion of the universe. Furthermore, during the first epoch, which is when $t=0$, all values become finite. However, as t approaches infinity, they diverge. It is worth mentioning that when $k=1$, the model becomes shear-free and isotropic, as shown by the conditions $\sigma^2=0$ and $A_h=0$.

According to the HDE theory, for DE to be responsible for the current rapid expansion of the Universe, the total amount of vacuum energy contained inside a box of size $L \propto \lambda_3$ should not exceed the energy of a black hole of the same size, as determined by the Kaniadakis black hole entropy equation (Eq. (2)). Subsequently, an individual acquires

$$\Lambda^4 \equiv \rho_{khde} \propto \frac{S_{\mathcal{K}}}{\mathcal{L}^4} \quad (36)$$

for the vacuum energy ρ_{khde} . Now, taking the Hubble horizon of the universe as the IR cutoff (i.e., $L = \frac{1}{H} A = \frac{4\pi}{H^2}$),

$$\rho_{khde} = \frac{3C^2 H^4}{\mathcal{K}} \sinh \left(\frac{\pi \mathcal{K}}{H^2} \right) \quad (37)$$

where the constant C^2 is unknown, \mathcal{K} belongs to a set of real numbers, and $H = \frac{\dot{a}}{a}$ is the Hubble parameter. Now, it is clear that we have $\rho_{khde} \rightarrow \frac{3C^2 H^4}{\mathcal{K}}$ (the well-known Bekenstein entropy-based HDE) when $k \rightarrow 0$. Considering the pressureless fluid (with energy density ρ_m) and the dark energy candidate (with pressure p_{khde} and density ρ_{khde}).

The fractional energy densities of matter (Ω_m) and DE (Ω_{khde}) are given as

$$\Omega_m = \frac{\rho_m}{\rho_{cr}} = \frac{\rho_m}{3H^2} \quad \text{and} \quad \Omega_{khde} = \frac{\rho_{khde}}{\rho_{cr}} = \frac{C^2 H^2}{\mathcal{K}} \sinh \left(\frac{\pi \mathcal{K}}{H^2} \right), \quad (38)$$

ρ_{cr} is the critical energy density.

We are considering non-interacting DE and matter in this case. As a result, we have from Eq. (19) that both of these are conserved individually

$$\dot{\rho}_m + 3H\rho_m = 0, \quad (39)$$

$$\dot{\rho}_{khde} + 3H(1 + \omega_{khde})\rho_{khde} + \frac{6kH}{2k+1} \left(\frac{2}{A^2} + \frac{\alpha_0(k-1)\dot{3}H}{2k+1} \right) = 0. \quad (40)$$

Differentiating Eq. (37) concerning time, we obtain

$$\dot{\rho}_{khde} = \frac{\rho_{khde} \dot{H}}{H^2} \left(4H - \frac{2\pi \mathcal{K}}{H} \coth \left(\frac{\pi \mathcal{K}}{H^2} \right) \right). \quad (41)$$

Given Eqs. (33) and (41), from Eq. (40), we obtain the EoS parameter of KHDE as

$$\omega_{khde} = -1 - \frac{2\dot{H}}{3H^2} \left(2 - \frac{\pi \mathcal{K}}{H^2} \coth \left(\frac{\pi \mathcal{K}}{H^2} \right) \right) - \frac{2k}{3(2k+1)H^2 \Omega_{khde}} \left[\frac{2}{A^2} + \frac{3H\alpha_0(k-1)}{2k+1} \right] \quad (42)$$

where

$$\dot{H} = \frac{(2k+1)^2 A_0^2 \exp(2\alpha_0 t)}{3 \left(\frac{A_0(2k+1)}{\alpha_0} \exp(\alpha_0 t) + (2k+1)A_1 \right)^2} + \frac{(2k+1)A_0 \alpha_0 \exp(\alpha_0 t)}{3 \left(\frac{A_0(2k+1)}{\alpha_0} \exp(\alpha_0 t) + (2k+1)A_1 \right)}. \quad (43)$$

Here metric potential $A(t)$, Hubble parameter $H(t)$ and fractional energy density of KHDE Ω_{khde} are respectively given in Eqs. (29), (33) and (38).

3. COSMOLOGICAL PARAMETERS

In this section, we explore the expanding behaviour of the universe through well-known cosmological parameters like equation of state (EoS) ω_{khde} , squared sound speed v_s^2 , deceleration q parameters and cosmological planes such as $\omega_{khde} - \omega'_{khde}$, statefinders ($r - s$) and $r - q$ for the constructed anisotropic KHDE model.

EoS parameter

The equation of state parameter (ω) is often used to classify the different stages of the expanding universe. Specifically, the shift from decelerated to accelerated phases encompasses DE and radiation-dominated epochs. The equation of state (EoS) parameter, denoted by $\omega = \frac{p}{\rho}$, is defined as the ratio of pressure (p) to energy density (ρ) of the matter distribution. The decelerated and accelerated phases include the following periods:

- *Decelerated phase:* Cold dark matter or dust fluid $\omega = 0$, radiation era $0 < \omega < \frac{1}{3}$ and stiff fluid $\omega = 1$.
- *Accelerated phase:* Cosmological constant/vacuum era $\omega = -1$, quintessence $-1 < \omega < -\frac{1}{3}$, phantom era $\omega < -1$ and quintom era (combination of both quintessence and phantom).

The EoS parameter of KHDE with Hubble horizon cutoff is given in Eq. (42). In Fig. 1, we investigate the evolution of EoS parameter ω_{khde} in terms of redshift z for different values of \mathcal{C} . Fig. 1 shows that initially ω_{khde} starts from matter dominated era, varies in quintessence region $-1 < \omega_{khde} < -1/3$ and finally it becomes -1 , which means the model becomes Λ CDM model at late times.

Squared sound speed

The squared speed of the sound parameter is defined as

$$v_s^2 = \frac{\dot{p}_{khde}}{\dot{\rho}_{khde}} = \omega_{khde} + \frac{\rho_{khde}}{\dot{\rho}_{khde}} \dot{\omega}_{khde}. \tag{44}$$

This parameter is useful in discussing the stability of DE models depending upon its sign. The positive signature of v_s^2 determines a stable DE model otherwise the model becomes unstable.

Using energy density and EoS parameter given in the Eqs. (37) and (42) in the squared sound speed expression (v_s^2) Eq. (44), we analyze v_s^2 graphically for our model. Fig. 2 elaborates the plot of v_s^2 versus redshift z . Initially, the trajectories represent positive behaviour and negative at the present epoch and late times. Hence, this shows that our model is stable at the initial epoch and unstable at present and late times.

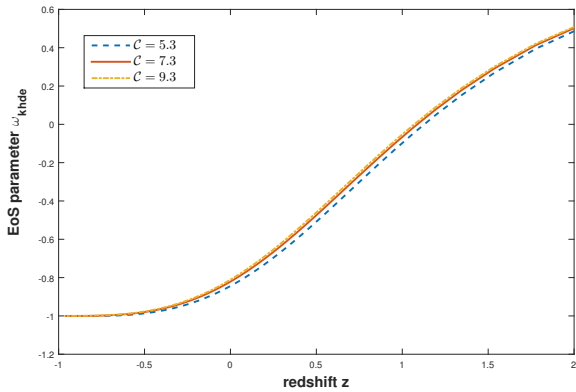


Figure 1. Plot of EoS parameter ω_{de} versus redshift z for $k = 0.98$, $A_1 = -0.04$, $\alpha_0 = 0.85$, $A_0 = 0.04$ and $\mathcal{K} = 0.01$.

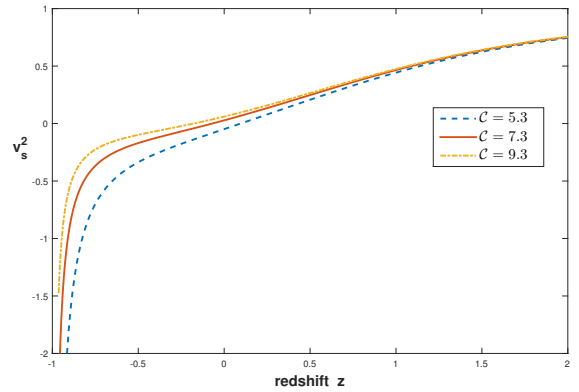


Figure 2. Plot of v_s^2 versus redshift z for $k = 0.98$, $A_1 = -0.04$, $\alpha_0 = 0.85$, $A_0 = 0.04$ and $\mathcal{K} = 0.01$.

$\omega_{khde} - \omega'_{khde}$ plane

We analyze the $\omega_{khde} - \omega'_{khde}$ plane, where ω'_{khde} represents the evolutionary mode of the equation of state parameter ω_{khde} , and the prime symbol indicates differentiation concerning the natural logarithm of the scale factor ' $\ln a$ '. Caldwell and Linder [67] have suggested using this framework to investigate the cosmic progression of the quintessence dark energy scenario. Furthermore, it has been noted that the $\omega_{khde} - \omega'_{khde}$ plane may be divided into two distinct regions: thawing ($\omega_{khde} < 0$, $\omega'_{khde} > 0$) and freezing ($\omega_{khde} < 0$, $\omega'_{khde} < 0$). The freezing zone demonstrates a more rapid period of cosmic expansion compared to the thawing region.

Figure 3 examines the relationship between the $\omega_{khde} - \omega'_{khde}$ plane and the KHDE model, specifically for various values of \mathcal{C} . Figure 3 illustrates that the $\omega_{khde} - \omega'_{khde}$ plane corresponds to the area where freezing occurs for all three parameter values. Contemporary cosmological measurements indicate that the freezing zone reveals a period of greater cosmic acceleration compared to the thawing region. Therefore, the $\omega_{khde} - \omega'_{khde}$ plane of our model demonstrates cosmic acceleration in the freezing area and aligns well with the facts.

Energy conditions

The investigation of energy conditions was began by the Raychaudhuri equations, which are essential in any examination of the alignment of null and time-like geodesics. The energy requirements are used to demonstrate other general theorems about the behavior of powerful gravitational fields. The energy situations often seen are as follows:

Dominant energy condition (DEC): $\rho_{de} \geq 0, \rho_{de} \pm p_{de} \geq 0$.

Strong energy conditions (SEC) : $\rho_{de} + p_{de} \geq 0, \rho_{de} + 3p_{de} \geq 0$,

Null energy conditions (NEC): $\rho_{de} + p_{de} \geq 0$,

Weak energy conditions (WEC): $\rho_{de} \geq 0, \rho_{de} + p_{de} \geq 0$,

Figure 4 illustrates the energy conditions of our KHDE model. There is an obvious violation of the NEC, leading to the model resulting in a Big Rip. Furthermore, it is seen that the WEC satisfies the condition $\rho_{de} \geq 0$. Furthermore, Figure 4 demonstrates that the DEC $\rho_{de} + p_{de}$ is not fulfilled. Furthermore, our model violates the SEC regulations, which are deemed suitable. This phenomenon, resulting from the universe's acceleration in its latter stages, aligns with current observational findings.

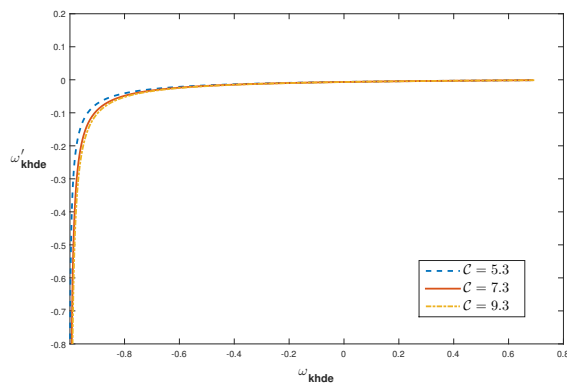


Figure 3. Plot of $\omega_{de} - \omega'_{de}$ plane for $k = 0.98$, $A_1 = -0.04$, $\alpha_0 = 0.85$, $A_0 = 0.04$ and $\mathcal{K} = 0.01$.

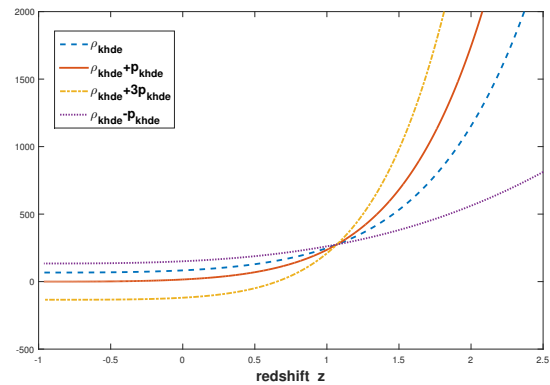


Figure 4. Plot of energy conditions versus redshift z for $k = 0.98$, $A_1 = -0.04$, $\alpha_0 = 0.85$, $A_0 = 0.04$, $\mathcal{C} = 9.3$ and $\mathcal{K} = 0.01$.

Deceleration parameter

The nature of the expansion of the universe can be estimated using the dimensionless cosmological parameter known as the deceleration parameter (DP). It defined as

$$q = -1 - \frac{\dot{H}}{H^2}. \quad (45)$$

For positive values of DP, the model decelerates in the standard way whereas for $q = 0$ the model expands at a constant rate. The model shows accelerated expansion for $-1 \leq q < 0$ and a super exponential expansion for $q < -1$. The deceleration parameter can be obtained as

$$q = -1 - \frac{3(2k+1)A_1\alpha_0}{(2k+1)\alpha_0 \exp(\alpha_0 t)}. \quad (46)$$

Figure 5 displays the relationship between the deceleration parameter q and the redshift z for different values of A_1 . It is important to highlight that the model demonstrates a seamless transition from the universe's initial decelerated phase to its present accelerated phase. Within the specified range of $0.5 < z < 0.85$, the universe transitioned from a state of deceleration to a state of acceleration. This aligns with previous findings in the field of cosmology [68, 69]. The transition redshift (z_t) from decelerating to accelerating expansion has been reported to be between 0.3 and 0.8, with a 95% confidence level. Additionally, it has been determined that the redshift for accelerating expansion (z_{acc}) is greater than 0.14 in the most conservative scenario.

Statefinder parameters

The dynamic expansion of the universe may be accurately characterized by the Hubble and deceleration parameters. Nevertheless, several dynamical dark energy models have identical parameter values at the current period. As a result, these factors were unsuccessful in determining the most suitable model among the several dynamical dark energy theories. Sahni et al. [70] developed a set of dimensionless cosmological parameters called statefinders, which are defined as follows:

$$r = \frac{\ddot{a}}{aH^3}, \quad s = \frac{r-1}{3(q-\frac{1}{2})}. \tag{47}$$

These statefinders establish a correspondence with the Λ CDM and CDM models for $(r, s) = (1, 0)$ and $(r, s) = (1, 1)$, respectively. If the trajectories of $r - s$ belong to the region $s > 0$ and $r < 1$, then the model belongs to the phantom and quintessence phases whereas the Chaplygin gas model appears for $r > 1$ with $s < 0$. The statefinders are obtained as

$$r = 10 + \frac{(A_0 \exp(\alpha_0 t) + A_1 \alpha_0)^2}{\alpha_0^2 \exp(2\alpha_0 t)}; \quad s = \frac{9 + \frac{(A_0 \exp(\alpha_0 t) + A_1 \alpha_0)^2}{\alpha_0^2 \exp(2\alpha_0 t)}}{3 \left(-\frac{3}{2} - \frac{3(2k+1)A_1 \alpha_0}{(2k+1)\alpha_0 \exp(\alpha_0 t)} \right)}. \tag{48}$$

Fig. 6 incorporates the trajectories of (r, s) parameters. It can be observed that the parameter ‘s’ is both positive and negative for all values of r . This implies that the KHDE model achieved a correspondence with the Chaplygin gas model, quintessence and phantom models. Also, the $r - s$ plane corresponds to Λ CDM limit at late times.

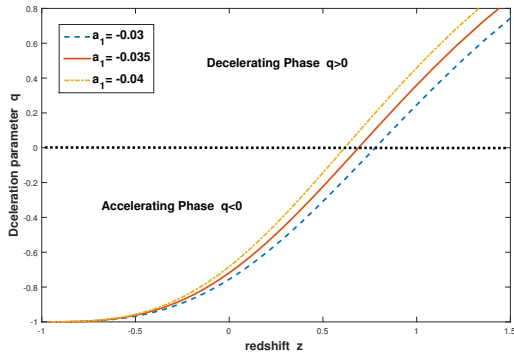


Figure 5. Plot of deceleration parameter q versus redshift z for $k = 0.98$, $A_1 = -0.04$ and $\alpha_0 = 0.85$.

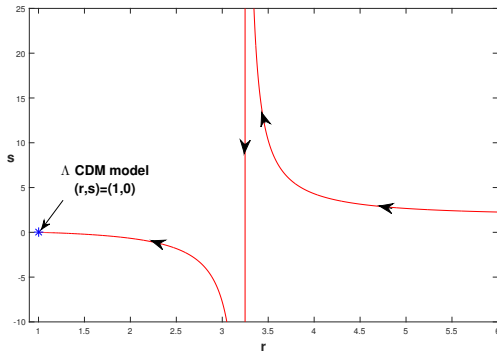


Figure 6. Plot of $r - s$ plane for $k = 0.98$, $A_1 = -0.04$ and $\alpha_0 = 0.85$.

$r - q$ plane

Figure 7 depicts the development of our model in the $r - q$ plane. The values $(r, q) = (1, 0.5)$ represent standard cold dark matter (SCDM) whereas $(r, q) = (1, -1)$ represents the steady state (SS) model. The Λ CDM model evolves along the dotted line (see Fig. 7) from a fixed point in the SCDM model to a fixed point in the SS model. At late times, our model comes close to the SS model. The $r - q$ trajectory of our model is found to be quite comparable to the DE models previously presented in the literature [71, 72]. In Fig. 7, we plot the trajectories in the $r - q$ plane. It can be observed from the figure that our KHDE model always approaches the study state model, i.e., $(r, q) = (1, -1)$ as Λ CDM model approach in the later epochs.

4. DISCUSSION AND CONCLUSION

This study investigates the Kaniadakis holographic dark energy within the context of anisotropic Bianchi type- V_{I_0} space-time in general relativity. In this case, we have regarded the Hubble horizon as the infrared cutoff. We have examined well-recognized cosmological parameters, including the equation of state (EoS), deceleration parameter, and squared speed of sound parameter. Additionally, we have explored cosmological planes such as the $\omega_{khde} - \omega'_{khde}$ plane, the statefinder $(r - s)$ plane, and the $r - q$ plane. Our findings have been condensed into the following summary:

- The EoS parameter ω_{khde} of the KHDE model initially starts from the matter-dominated era, varies in quintessence region $-1 < \omega_{khde} < -1/3$ and finally it becomes -1 , which means the model becomes Λ CDM

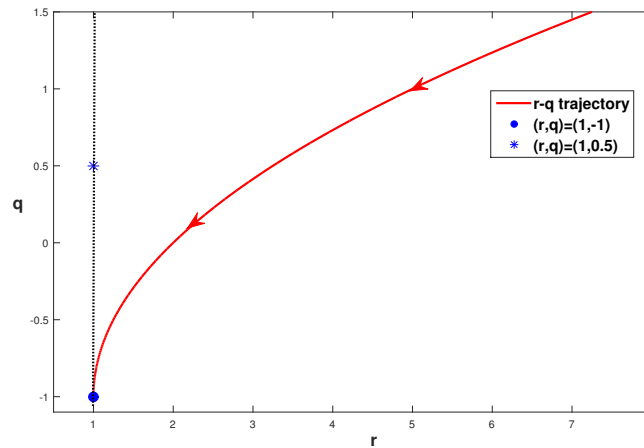


Figure 7. Plot of the $r - q$ plane for $k = 0.98$, $A_1 = -0.04$ and $\alpha_0 = 0.85$.

model at late times. We have made a comparison of our results with present Planck collaboration data (2018) [73] where the limits on the EoS parameter are given as

$$\begin{aligned}\omega_{khde} &= -1.56^{+0.60}_{-0.48} \text{ (Planck + TT + lowE)} \\ \omega_{khde} &= -1.58^{+0.52}_{-0.41} \text{ (Planck + TT, TE, EE + lowE)} \\ \omega_{khde} &= -1.57^{+0.50}_{-0.40} \text{ (Planck + TT, TE, EE + lowE + lensing)} \\ \omega_{khde} &= -1.04^{+0.10}_{-0.10} \text{ (Planck + TT, TE, EE + lowE + lensing + BAO)}.\end{aligned}$$

It can be seen that the results for the EoS parameter of our model are consistent with the Planck Collaboration data.

- The $\omega_{khde} - \omega'_{khde}$ plane (Fig. 3) depicts the area where freezing occurs for all three parameter values. Contemporary cosmological measurements indicate that the freezing zone reveals a period of greater cosmic acceleration compared to the thawing region. Therefore, the $\omega_{khde} - \omega'_{khde}$ plane of our model demonstrates cosmic acceleration in the freezing area and aligns well with the facts. The paths of the $\omega_{khde} - \omega'_{khde}$ plane, as predicted by our model, align with the observed data [74, 75]





$$\omega_{khde} = -1.13^{+0.24}_{-0.25}, \omega'_{khde} < 1.32 \text{ (Planck + WP + BAO)}.$$

- The squared sound speed trajectories exhibit positive behaviour initially and negative behaviour at the current epoch and late periods. Therefore, this demonstrates that our model is steady throughout the beginning period but becomes unsteady during the present and late times. The violation of the NEC leads to the occurrence of a Big Rip in the model. Furthermore, it is seen that the WEC satisfies the condition $\rho_{de} \geq 0$. Furthermore, the condition of the DEC $\rho_{de} + p_{de}$ is not met. Furthermore, our model violates the SEC regulations, which are deemed suitable. This phenomenon, resulting from the universe's acceleration in its latter stages, aligns with current observational findings.
- Our model demonstrates a smooth transition from the universe's initial decelerated phase to its present accelerated phase. Within the specified range of $0.5 < z < 0.85$, the universe transitioned from a state of deceleration to a state of acceleration. This aligns with previous findings in the field of cosmology [68, 69]. The present value of the deceleration parameter is ≈ -0.82 which is by the observational data (Capozziello et al. [76]) given as $q = -0.930 \pm 0.218$ ($BAO + Masers + TDSL + Pantheon + H_z$), $q = -1.2037 \pm 0.175$ ($BAO + Masers + TDSL + Pantheon + H_0 + H_z$). It can be observed from the $r - s$ plane that our model achieved a correspondence with the Chaplygin gas model, quintessence and phantom models. Also, the $r - s$ plane corresponds to Λ CDM limit at late times. It can be seen from the $r - q$ plane that our KHDE model always approaches the study state model, i.e., $(r, q) = (1, -1)$ as Λ CDM model approach in the later epochs.

Acknowledgments

Y. Aditya is thankful to the National Board for Higher Mathematics, Department of Atomic Energy, Govt. of India for its financial support under the grant No: 02011/8/2023 NBHM(R.P.)/R & D II/3073.

ORCID

 B. Ganeswara Rao, <https://orcid.org/0009-0007-4539-9130>;  Dipana Jyoti Mohanty, <https://orcid.org/0000-0002-1783-4090>;  Y. Aditya, <https://orcid.org/0000-0002-5468-9697>;  U.Y. Divya Prasanthi, <https://orcid.org/0009-0004-5397-050X>

REFERENCES

- [1] S. Perlmutter, et al., *Astrophys. J.* **517**, 565 (1999). <https://doi.org/10.1086/307221>
- [2] A.G. Riess, et al., *Astron. J.* **116**, 1009 (1998). <https://doi.org/10.1086/300499>
- [3] T. Koivisto, and D.F. Mota, *Phys. Rev. D*, **73**, 083502 (2006). <https://doi.org/10.1103/PhysRevD.73.083502>
- [4] E.J. Copeland, et al., *Int. J. Mod. Phys. D*, **15**, 1753 (2006). <https://doi.org/10.1142/S021827180600942X>
- [5] R.R. Caldwell, and M. Kamionkowski, *Ann. Rev. Nucl. Part. Sci.* **59**, 397 (2009). <https://doi.org/10.1146/annurev-nucl-010709-151330>
- [6] K. Bamba, et al., *Astrophys. Space Sci.* **342**, 155 (2012). <https://doi.org/10.1007/s10509-012-1181-8>
- [7] S. Nojiri, et al., *Phys. Rept.* **692**, 1 (2017). <https://doi.org/10.1016/j.physrep.2017.06.001>
- [8] B. Ratra, and P.J.E. Peebles, *Phys. Rev. D*, **37**, 3406 (1988). <https://doi.org/10.1103/PhysRevD.37.3406>
- [9] R.R. Caldwell, R. Dave, and P.J. Steinhardt, *Phys. Rev. Lett.* **80**, 1582 (1998). <https://doi.org/10.1103/PhysRevLett.80.1582>
- [10] T. Padmanabhan, *Phys. Rev. D*, **66**, 021301 (2002). <https://doi.org/10.1103/PhysRevD.66.021301>
- [11] C. Armendariz-Picon, V.F. Mukhanov, and P.J. Steinhardt, *Phys. Rev. Lett.* **85**, 4438 (2000). <https://doi.org/10.1103/PhysRevLett.85.4438>
- [12] J. Sadeghi, et al., *Int. J. Theor. Phys.* **55**, 81 (2016). <https://doi.org/10.1007/s10773-015-2635-x>
- [13] M. Li, *Phys. Lett. B*, **603**, 1 (2004). <https://doi.org/10.1016/j.physletb.2004.10.014>
- [14] L. Susskind, *J. Math. Phys.* **36**, 6377 (1995). <https://doi.org/10.1063/1.531249>
- [15] A. Cohen, and D. Kaplan, A. Nelson, *Phys. Rev. Lett.* **82**, 4971 (1999). <https://doi.org/10.1103/PhysRevLett.82.4971>
- [16] Z.K. Gao, et al., *Phys. Rev. D*, **74**, 127304 (2006). <https://doi.org/10.1103/PhysRevD.74.127304>
- [17] L.N. Granda, and A. Oliveros, *Phys. Lett. B*, **671**, 199 (2009). <https://doi.org/10.1016/j.physletb.2008.12.025>
- [18] H. Wei, and R.G. Cai, *Phys. Lett. B*, **660**, 113 (2008). <https://doi.org/10.1016/j.physletb.2007.12.030>
- [19] S. Nojiri, and S.D. Odintsov, *Gen. Rel. Grav.* **38**, 1285 (2006). <https://doi.org/10.1007/s10714-006-0301-6>
- [20] S. Nojiri, et al., *Phys. Lett. B*, **797**, 134829 (2019). <https://doi.org/10.1016/j.physletb.2019.134829>
- [21] M. Tavayef, A. Sheykhi, K. Bamba, and H. Moradpour, *Phys. Lett. B*, **781**, 195 (2018). <https://doi.org/10.1016/j.physletb.2018.04.001>
- [22] C. Tsallis, and L.J.L. Cirto, *Eur. Phys. J. C*, **73**, 2487 (2013). <https://doi.org/10.1140/epjc/s10052-013-2487-6>
- [23] A.S. Jahromi et al., *Phys. Lett. B*, **780**, 21 (2018). <https://doi.org/10.1016/j.physletb.2018.02.052>
- [24] H. Moradpour et al., *Eur. Phys. J. C*, **78**, 829 (2018). <https://doi.org/10.1140/epjc/s10052-018-6309-8>
- [25] D.R.K. Reddy, et al., *Astrophys Space Sci.* **361**, 356 (2016). <https://doi.org/10.1007/s10509-016-2938-2>
- [26] Y. Aditya, and D.R.K. Reddy, *Eur. Phys. J. C*, **78**, 619 (2018). <https://doi.org/10.1140/epjc/s10052-018-6074-8>
- [27] V.U.M. Rao, et al., *Results in Physics*, **10**, 469 (2018). <https://doi.org/10.1016/j.rinp.2018.06.027>
- [28] M.V. Santhi, et al., *Can. J. Phys*, **95**, 381 (2017). <https://doi.org/10.1139/cjp-2016-0781>
- [29] M.V. Santhi, et al., *Int. J. Theor. Phys.* **56**, 362 (2017). <https://doi.org/10.1007/s10773-016-3175-8>
- [30] K.D. Naidu, et al., *Eur. Phys. J. Plus*, **133**, 303 (2018). <https://doi.org/10.1140/epjp/i2018-12139-2>
- [31] Y. Aditya, et al., *Eur. Phys. J. C*, **79**, 1020 (2019). <https://doi.org/10.1140/epjc/s10052-019-7534-5>
- [32] S. Maity, U. Debnath, *Eur. Phys. J. Plus*, **134**, 514 (2019). <https://doi.org/10.1140/epjp/i2019-12884-6>
- [33] A. Iqbal, A. Jawad, *Physics of the Dark Universe*, **26**, 100349 (2019). <https://doi.org/10.1016/j.dark.2019.100349>
- [34] G. Kaniadakis, *Physica A: Stat. Mech. and its Appl.* **296**(3-4), 405 (2001). [https://doi.org/10.1016/S0378-4371\(01\)00184-4](https://doi.org/10.1016/S0378-4371(01)00184-4)
- [35] M. Masi, *Phys. Lett. A*, **338**, 217 (2005). <https://doi.org/10.1016/j.physleta.2005.01.094>
- [36] E.M. Abreu, et al., *EPL (Europhysics Letters)*, **124**, 30003 (2018). <https://doi.org/10.1209/0295-5075/124/30003>
- [37] H. Moradpour, et al. *Eur. Phys. J. C*, **80**, 1 (2020). <https://doi.org/10.1140/epjc/s10052-020-8307-x>



- [38] A. Jawad, and A.M. Sultan, Adv. High Energy Phys. **2021**, 5519028 (2021). <https://doi.org/10.1155/2021/5519028>
- [39] U.K. Sharma, et al., IJMPD, **31**, 2250013 (2022). <https://doi.org/10.1142/S0218271822500134>
- [40] N. Drepanou et al., ur. Phys. J. C, **82**, 449 (2022). <https://doi.org/10.1140/epjc/s10052-022-10415-9>
- [41] J. Sadeghi, et al., arXiv:2203.04375 (2022). <https://doi.org/10.48550/arXiv.2203.04375>
- [42] C.L. Bennett, et al., Astron. Astrophys. Suppl. Ser. **148**, 1 (2003). <https://doi.org/10.1086/377252>
- [43] O. Akarsu, and C.B. Kilinc, Astrophys. Space Sci. **326**, 315 (2010). <https://doi.org/10.1007/s10509-009-0254-9>
- [44] D.R.K. Reddy, et al., Can. J. Phys. **97**, 932 (2019). <https://doi.org/10.1139/cjp-2018-0403>
- [45] Y. Aditya, et al., Astrophys. Space Sci. **364**, 190 (2019). <https://doi.org/10.1007/s10509-019-3681-2>
- [46] Y. Aditya, and D.R.K. Reddy, Astrophys. Space Sci. **364**, 3 (2019). <https://doi.org/10.1007/s10509-018-3491-y>
- [47] K.D. Raju, et al., Astrophys. Space Sci. **365**, 45 (2020). <https://doi.org/10.1007/s10509-020-03753-1>
- [48] K.D. Raju, et al., Astrophys. Space Sci. **365**, 28 (2020). <https://doi.org/10.1007/s10509-020-3729-3>
- [49] Y. Aditya, et al., Ind. J. Phys. **95**, 383 (2021). <https://doi.org/10.1007/s12648-020-01722-6>
- [50] R.L. Naidu, et al., Astrophys. Space Sci. **365**, 91 (2020). <https://doi.org/10.1007/s10509-020-03796-4>
- [51] R.L. Naidu, et al., Ind. J. Phys. **85**, 101564 (2021). <https://doi.org/10.1016/j.newast.2020.101564>
- [52] K.D. Naidu, et al., Mod. Phys. A, **36**, 2150054 (2021). <https://dx.doi.org/10.1142/S0217732321500541>
- [53] Y. Aditya, et al., New Astr. **84**, 101504 (2021). <https://doi.org/10.1016/j.newast.2020.101504>
- [54] Y. Aditya, et al., Int. J. Mod. Phys. A, **37**, 2250107 (2022). <https://doi.org/10.1142/S0217751X2250107X>
- [55] M.P.V.V. Bhaskara Rao, et al., New Astr. **92**, 101733 (2022). <https://doi.org/10.1016/j.newast.2021.101733>
- [56] U.Y.D. Prasanthi, and Y. Aditya, Phys. Dark Univ. **31**, 100782 (2021). <https://doi.org/10.1016/j.dark.2021.100782>
- [57] U.Y.D. Prasanthi, and Y. Aditya, Results Phys. **17**, 103101 (2020). <https://doi.org/10.1016/j.rinp.2020.103101>
- [58] M.P.V.V. Bhaskara Rao, et al., Int. J. Mod. Phys. A, **36**, 2150260 (2021). <https://doi.org/10.1142/S0217751X21502602>
- [59] Y. Aditya, and U.Y.D. Prasanthi, Bulg. Astr. Journal, **38**, 52 (2023). <https://astro.bas.bg/AIJ/issues/n38/YAditya.pdf>
- [60] Y. Aditya, Bulg. Astr. Journal, **39**, 12 (2023). <https://astro.bas.bg/AIJ/issues/n39/YAditya.pdf>
- [61] C.B. Collins, et al., Gen. Relativ. Gravit. **12**, 805 (1980). <https://doi.org/10.1007/BF00763057>
- [62] O. Akarsu, and C.B. Kilinc, Gen. Relativ. Gravit. **42**, 119 (2010). <https://doi.org/10.1007/s10714-009-0821-y>
- [63] M. Sharif, and M. Zubair, Astrophys. Space Sci. **330**, 399 (2010). <https://doi.org/10.1007/s10509-010-0414-y>
- [64] M.V. Santhi, et al., Astrophys. Space Sci. **361**, 142 (2016). <https://doi.org/10.1007/s10509-016-2731-2>
- [65] M.V. Santhi, et al., Can. J. Phys. **95**, 179 (2017). <https://doi.org/10.1139/cjp-2016-0628>
- [66] Y. Aditya, and D.R.K. Reddy, Astrophys. Space Sci. **363**, 207 (2018). <https://doi.org/10.1007/s10509-018-3429-4>
- [67] R. Caldwell, and E.V. Linder, Phys. Rev. Lett. **95**, 141301 (2005). <https://doi.org/10.1103/PhysRevLett.95.141301>
- [68] S. Capozziello, et al., Phys. Rev. D, **90**, 044016 (2014). <https://doi.org/10.1103/PhysRevD.90.044016>
- [69] D. Muthukrishna, and D. Parkinson, JCAP, **11**, 052 (2016). <https://doi.org/10.1088/1475-7516/2016/11/052>
- [70] V. Sahni, et al., J. Exp. Theor. Phys. Lett. **77**, 201 (2003). <https://doi.org/10.1134/1.1574831>
- [71] Y. Aditya, et al., Int. J. Mod. Phys. A, **37**, 2250107 (2022). <https://doi.org/10.1142/S0217751X2250107X>
- [72] C.P. Singh, and P. Kumar, Astrophys. Space Sci. **361**, 157 (2016). <https://doi.org/10.1007/s10509-016-2740-1>
- [73] N. Aghanim, et al., [Plancks Collaboration] arXiv:1807.06209v2 (2018). <https://doi.org/10.48550/arXiv.1807.06209>
- [74] P.A.R. Ade, et al., Astrophys. **571**, A16 (2014). <https://doi.org/10.1051/0004-6361/201321591>
- [75] G.F. Hinshaw, et al., Astrophys. J. Suppl. **208**, 19 (2018). <https://doi.org/10.1088/0067-0049/208/2/19>
- [76] S. Capozziello, et al., MNRAS, **484**, 4484 (2019). <https://doi.org/10.1093/mnras/stz176>

КОСМОЛОГІЧНА ЕВОЛЮЦІЯ ГОЛОГРАФІЧНОЇ МОДЕЛІ ТЕМНОЇ ЕНЕРГІЇ
КАНІАДАКІСА ТИПУ БІАНКІ- $V I_0$ Б. Ганешвара Рао^{a,b}, Діпана Джіоті Моханті^b, Ю. Адитья^c, Ю.Й. Дів'я Прасанті^d^a Департамент математики Шрі G.C.S.R. Коледж, Раджам-532127, Індія^b Департамент математики, Університет GIET, Гунупур-765002, Індія^c Департамент математики, Технологічний інститут GMR, Раджам-532127, Індія^d Департамент статистики і математики, Коледж садівництва, д-р Y.S.R. Університет садівництва,
Парватіпур-535502, Індія

Метою цієї статті є побудова анізотропної та просторово однорідної голографічної моделі темної енергії Каніадакіса типу Біанкі $V I_0$ в загальній теорії відносності. Для цього ми розглядаємо обрії Хаббла як межу інфрачервоного випромінювання. Щоб отримати детермінований розв'язок рівнянь поля моделі, ми припускаємо зв'язок між метричними потенціалами, який призводить до експоненціального розв'язку та прискореного розширення. Щоб дослідити фізичну поведінку нашої моделі темної енергії, ми отримуємо деякі важливі космологічні параметри, такі як Хаббл, уповільнення, рівняння стану та вимірювач стану, а також $\omega_{k h d e} - \omega'_{k h d e}$, $r - s$ і $r - q$ площини. Ми також включили аналіз стабільності для моделі темної енергії через квадрат швидкості звуку. Помічено, що рівняння параметра стану показує модель Λ CDM у пізній час. Крім того, квадрат швидкості звуку дає стабільність моделі КНДЕ на початковій епосі, а модель є нестабільною на пізніх етапах. Діагностичні параметри вимірювача стану та параметри уповільнення демонструють плавний перехід Всесвіту від фази уповільнення до поточного прискореного розширення Всесвіту, а також відповідають моделі Λ CDM у пізні часи. Усі ці космологічні параметри підтверджують останні дані спостережень.

Ключові слова: модель темної енергії типу Bianchi- $V I_0$; загальна теорія відносності; космологія; голографічна темна енергія Каніадакіса

BARROW HOLOGRAPHIC DARK ENERGY MODEL IN BIANCHI TYPE-III UNIVERSE WITH QUINTESSENCE

 Chandra Rekha Mahanta,  Dibyajyoti Das*

Department of Mathematics, Gauhati University, Jalukbari, 781014, Assam, India

* *Corresponding Author e-mail: dasdibyajyoti07@gauhati.ac.in*

Received December 6, 2023; revised December 29, 2023; accepted January 8, 2024

In this paper, we study a spatially homogeneous and anisotropic Bianchi type-III universe containing cold dark matter and Barrow holographic dark energy within the framework of General Relativity. We assume the cold dark matter and Barrow holographic dark energy to be non-interacting and obtain exact solutions of the Einstein field equations by considering a hybrid expansion law and assuming that the expansion scalar is proportional to the shear scalar. We examine the physical and kinematical properties of the resulting model using parameters such as the Hubble parameter, the anisotropic parameter, the deceleration parameter, the equation of state parameter, the jerk parameter etc. We also examine whether the energy conditions are violated or validated. We find that the Null, Weak, and Dominant energy conditions are fulfilled, while the Strong Energy Condition is violated, which supports the accelerated expansion of the universe. The Statefinder diagnostics have been conducted based on recent cosmological observations. In addition, we reformulated the correspondence between quintessence scalar field and Barrow holographic dark energy model.

Keywords: *Cosmic acceleration; Barrow holographic dark energy; Bianchi type-III; Cold dark matter; Deceleration parameter; Equation of state parameter*

PACS: 98.80.-k, 98.80.Jk, 98.80.Es, 04.20.Jb

1. INTRODUCTION

The observational data from Supernovae Type Ia [1, 2] reveal that the universe is currently undergoing a phase of accelerated expansion and various other probes such as fluctuation of Cosmic Microwave Background Radiation (CMBR) [3], Sloan Digital Sky Survey (SDSS) [4], Wilkinson Microwave Anisotropy Probe (WMAP) [5], Large Scale Structure (LSS) [6], Baryonic Acoustic Oscillations [7], Gravitational Lensing [8], Chandra X-ray observatory [9] etc., strongly support the accelerated expansion of the universe at late times as well as the inflationary phase at the early stage of the universe. The observations demonstrate that the universe is dominated by some unusual cosmic fluid, namely the dark energy (DE), which is thought to be the driving force behind the ongoing expansion of the universe. According to standard cosmology, the dark energy exerts a huge negative pressure which makes up about three quarters of the total content of the universe.

In search of this mysterious dark energy various candidates are proposed in the literature including the cosmological constant Λ introduced by Albert Einstein in his field equations [10] which is the simplest and the most obvious theoretical candidate with the equation of state (EoS) parameter $\omega = -1$. However, there exist notable conceptual challenges that arise, including issues of fine-tuning and the cosmic coincidence problems [11]. So, to overcome these problems, several researchers have developed a variety of dynamically evolving scalar field models such as quintessence [12], k -essence [13], exotic fluid models like Chaplygin gas models [14], tachyon [15] etc.

An alternative solution to the puzzle of dark energy, called holographic dark energy (HDE), is also proposed in the literature which arises from a quantum gravitational principle called the Holographic Principle. The fundamental concept behind the Holographic Principle is that the quantity of possible configurations, known as degrees of freedom, that contribute to the entropy of a physical system is proportional to the surface area that surrounds the system, rather than its volume. G.'t Hooft [16] initially proposed this concept as an explanation for the thermodynamics of black hole physics. Subsequently, Fischler and Susskind [17] expanded upon this principle, applying it to the cosmological context by suggesting that the gravitational entropy flows through the past light-cone of that particular surface. To implement the holographic principle and formulate holographic dark energy, one utilizes the expression for black hole entropy. As a result, various versions of the theory can be derived by employing different entropy expressions. Li [18] investigated the dark energy model by considering the Holographic Principle with the choice of future event horizon as the IR cut-off which gives the desired scenario of an accelerating universe. Tsallis and Cirto in 2013 developed a holographic dark energy model namely Tsallis holographic dark energy (THDE) model by utilising the Tsallis generalized entropy $S_\delta = \gamma A^\delta$ where A is horizon area, γ is unknown parameter and δ is a non-additive parameter [19]. A new holographic

dark energy (NHDE) model is propose by considering the Granda and Oliveros cut-off [20] whose energy density is given by the the square of Hubble parameter and its time derivative. An another holographic dark energy model called Rényi holographic dark energy (RHDE) model was developed by using the Rényi entropy [21].

A noval black hole entropy relation has recently been proposed by Barrow [22] which emerges from the inclusion of quantum gravitational effects, potentially introducing complex and fractal characteristics to the area of a black hole, namely $S_B = \left(\frac{A}{A_{pl}}\right)^{1+\frac{\Delta}{2}}$, where A is the standard horizon area, A_{pl} is the Planck area and the exponent Δ with $0 \leq \Delta \leq 1$ quantifies the quantum-gravitational deformation. $\Delta = 0$ corresponds to the standard Bekenstein-Hawking entropy, i.e., the standard smooth structure while $\Delta = 1$ corresponds to the most intricate and fractal structure. The standard holographic dark energy is given by the inequality $\rho_{\text{HDE}}L^4 \leq S$, where L denotes horizon length, and under the imposition $S \propto A \propto L^2$ [23], the Barrow entropy will give the energy density of Barrow holographic dark energy (BHDE) as $\rho_{\text{BHDE}} = 3c^2M_p^2L^{\Delta-2}$, where c is a parameter and M_p is the Planck mass. Recently Saridakis [24] constructed the BHDE by applying the Barrow entropy instead of the usual Bekenstein-Hawking entropy. Srivastava and Sharma [25] also investigate the BHDE with Hubble horizon as IR cut-off for flat Friedmann-Lemaître-Robertson-Walker (FLRW) universe. Paul *et al.* [26] investigated Bianchi type-I universe in the presence of BHDE where they found that the new exponent plays an important role to identify the nature of the univese.

Even though the universe on a large scale appears to be homogeneous and isotropic, described well by the Friedmann-Lemaître-Robertson-Walker model, it is worth noting that there is no observational evidence that definitively rules out the existence of an anisotropic universe. Anisotropies might have been present in the early universe, as suggested by measurements of the anisotropy of the Cosmic Microwave Background (CMB). To better understand the dynamics of the evolving universe, spatially homogeneous and anisotropic Bianchi models are often considered, as they represent the simplest models with an anisotropic background and play a significant role in describing the large-scale behavior of the universe. Bianchi type models offer a way to include the influence of anisotropy, effectively connecting the homogeneous and isotropic FLRW models with the inhomogeneous and anisotropic models. Consequently, numerous researchers have explored spatially homogeneous and anisotropic Bianchi cosmological models in various contexts.

The cosmological constant Λ associated with the vacuum energy density provides crucial information about the universe’s large-scale behavior. A small value of Λ suggests that the observable universe is large and relatively flat. The inspiration to involve the cosmological constant Λ is that most DE models usually feature only a single component for DE. However, since the cold dark matter consists of more than one component, it may be possible that DE also consist of multiple components. Recently, a new DE model named Λ HDE has been proposed in which the DE contains two DE components namely the cosmological constant Λ and the holographic dark energy [?]. Therefore, in our present study, we consider the dark energy to be composed of two components: the cosmological constant Λ and BHDE.

In this paper, we consider a spatially homogeneous and anisotropic Bianchi type-III universe filled with pressureless cold dark matter and non-interacting Barrow holographic dark energy with IR cutoff as Hubble horizon $L = H^{-1}$. The paper is organised as follows: In section 2, we derive the modified Einstein field equations for the Bianchi type-III metric. In section 3, we obtain exact solutions of the field equations by considering a hybrid expansion law and assuming that the expansion scalar is proportional to the shear scalar. Additionally, various cosmologically significant parameters are taken into account. In section 4, we explore the physical and kinematical properties of the model and also analyze the energy conditions. In Section 5, we discuss the Statefinder diagnostics and analyze its implications. The correspondence between BHDE with quintessence scalar field is explained in Section 6. In section 7, we provide some concluding remarks on our findings.

2. THE METRIC AND FIELD EQUATIONS

We consider the spatially homogeneous and anisotropic Bianchi type-III space-time given by the metric

$$ds^2 = -dt^2 + A^2dx^2 + B^2e^{-2lx}dy^2 + C^2dz^2 \tag{1}$$

where A, B, C are the functions of the cosmic time t only and l is a positive constant. The Einstein modified field equations in natural unit are given by

$$R_{ij} - \frac{1}{2}Rg_{ij} + g_{ij}\Lambda = (T_{ij} + \bar{T}_{ij}) \tag{2}$$

where R_{ij} is the Ricci tensor, $R = g^{ij}R_{ij}$ is the Ricci scalar, g_{ij} is the metric tensor, Λ is the cosmological constant, T_{ij} and \bar{T}_{ij} are the energy momentum tensors of cold dark matter and Barrow HDE respectively. T_{ij} and \bar{T}_{ij} are defined by

$$T_{ij} = \rho_m u_i u_j \tag{3}$$

and

$$\bar{T}_{ij} = (\rho_{\text{BHDE}} + p_{\text{BHDE}})u_i u_j + g_{ij} p_{\text{BHDE}} \tag{4}$$

where ρ_m is the energy density of cold dark matter, and ρ_{BHDE} and p_{BHDE} are the energy density and pressure of the Barrow HDE respectively. The four velocity u_i satisfy $u_i u^i = -1$. Here, we consider the Barrow HDE density [24] given by

$$\rho_{\text{BHDE}} = DH^{2-\Delta} \tag{5}$$

where D is a constant and H is the Hubble parameter.

In comoving coordinate system, the Einstein field equations (2) with the help of equations (3) and (4) for the metric (1) lead to the following system of field equations:

$$\frac{\ddot{B}}{B} + \frac{\ddot{C}}{C} + \frac{\dot{B}\dot{C}}{BC} = -p_{\text{BHDE}} + \Lambda \tag{6}$$

$$\frac{\ddot{A}}{A} + \frac{\ddot{C}}{C} + \frac{\dot{A}\dot{C}}{AC} = -p_{\text{BHDE}} + \Lambda \tag{7}$$

$$\frac{\ddot{A}}{A} + \frac{\ddot{B}}{B} + \frac{\dot{A}\dot{B}}{AB} - \frac{l^2}{A^2} = -p_{\text{BHDE}} + \Lambda \tag{8}$$

$$\frac{\dot{A}\dot{B}}{AB} + \frac{\dot{A}\dot{C}}{AC} + \frac{\dot{B}\dot{C}}{BC} - \frac{l^2}{A^2} = \rho_m + \rho_{\text{BHDE}} + \Lambda \tag{9}$$

$$\frac{\dot{A}}{A} - \frac{\dot{B}}{B} = 0 \tag{10}$$

Here, an over dot (.) denotes differentiation with respect to the cosmic time t . On integrating, from equation (10), we obtain

$$B = mA \tag{11}$$

where m is a constant of integration.

Looking at the equation (11), the field equations (6)-(10) can be written as

$$\frac{\ddot{A}}{A} + \frac{\ddot{C}}{C} + \frac{\dot{A}\dot{C}}{AC} = -p_{\text{BHDE}} + \Lambda \tag{12}$$

$$2\frac{\ddot{A}}{A} + \left(\frac{\dot{A}}{A}\right)^2 - \frac{l^2}{A^2} = -p_{\text{BHDE}} + \Lambda \tag{13}$$

$$\left(\frac{\dot{A}}{A}\right)^2 + 2\frac{\dot{A}\dot{C}}{AC} - \frac{l^2}{A^2} = \rho_m + \rho_{\text{BHDE}} + \Lambda \tag{14}$$

The continuity equation is derived from the energy conservation law $(T^{ij} + \bar{T}^{ij})_{;j} = 0$ as

$$\dot{\rho}_m + \dot{\rho}_{\text{BHDE}} + 3H(\rho_m + \rho_{\text{BHDE}} + p_{\text{BHDE}}) = 0 \tag{15}$$

We assume the cold dark matter and Barrow HDE to be non-interacting, therefore they conserve independently as

$$\dot{\rho}_m + 3H\rho_m = 0 \tag{16}$$

and

$$\dot{\rho}_{\text{BHDE}} + 3H(\rho_{\text{BHDE}} + p_{\text{BHDE}}) = 0 \tag{17}$$

We now present some cosmological parameters which can be used to understand the evolution of the universe. For the given metric, the average scale factor a which parameterize the relative expansion of the universe, the spatial volume V and the mean Hubble parameter H which measures the rate of expansion of the universe are defined by

$$a = (ABC)^{\frac{1}{3}} \tag{18}$$

$$V = a^3 = ABC \tag{19}$$

$$H = \frac{1}{3}(H_1 + H_2 + H_3) \tag{20}$$

where $H_1 = \frac{\dot{A}}{A}$, $H_2 = \frac{\dot{B}}{B}$, $H_3 = \frac{\dot{C}}{C}$ are the directional Hubble parameters along the x, y, z directions respectively. The expansion scalar θ , the shear scalar σ , the average anisotropy parameter A_m are defined by

$$\theta = 3H = \frac{\dot{A}}{A} + \frac{\dot{B}}{B} + \frac{\dot{C}}{C} \tag{21}$$

$$\sigma^2 = \frac{1}{2} \left[\left(\frac{\dot{A}}{A} \right)^2 + \left(\frac{\dot{B}}{B} \right)^2 + \left(\frac{\dot{C}}{C} \right)^2 \right] - \frac{\theta^2}{6} \tag{22}$$

$$A_m = \frac{1}{3} \sum_{i=1}^3 \left(\frac{\Delta H_i}{H} \right)^2 \tag{23}$$

where $\Delta H_i = H_i - H$ ($i = 1, 2, 3$).

The expansion scalar θ measures the relative rate of expansion (or contraction) of the universe, the shear scalar θ gives the measure of the deformation of the cosmic structure caused by density fluctuation while the anisotropy parameter A_m measures the deviation from isotropy.

3. COSMOLOGICAL SOLUTIONS OF THE FIELD EQUATIONS

We have three independent field equations (12)-(14) with six unknowns $A, C, \rho_m, \rho_{\text{BHDE}}, p_{\text{BHDE}}$ and Λ together with the equation (5). So, to obtain an exact solution of the system, we need two additional constraints related to these parameters.

As a first constraint, we assume the expansion scalar θ to be proportional to the shear scalar σ which gives the relationship between the metric potentials as

$$C = A^k \tag{24}$$

where $k \neq 1$ is a positive constant.

Secondly, following the Akarsu *et al.* [28], we consider the average scale factor a to obey the hybrid expansion law given by

$$a(t) = a_0 t^\alpha e^{\beta(t-1)} \tag{25}$$

where α and β are non-negative constants. The relation (25) gives the power law for $\beta = 0$ and exponential law for $\alpha = 0$.

Then, from equations (11), (18) and (24), we get the directional scale factors as

$$A = m^{\frac{-1}{k+2}} \{a_0 t^\alpha e^{\beta(t-1)}\}^{\frac{3}{k+2}} \tag{26}$$

$$B = m^{\frac{k+1}{k+2}} \{a_0 t^\alpha e^{\beta(t-1)}\}^{\frac{3}{k+2}} \tag{27}$$

$$C = m^{\frac{-k}{k+2}} \{a_0 t^\alpha e^{\beta(t-1)}\}^{\frac{3k}{k+2}} \tag{28}$$

Therefore, the metric (1) becomes

$$ds^2 = -dt^2 + \{a_0 t^\alpha e^{\beta(t-1)}\}^{\frac{6}{k+2}} \left(m^{\frac{-2}{k+2}} dx^2 + m^{\frac{2(k+1)}{k+2}} e^{-2lx} dy^2 \right) + m^{\frac{-2k}{k+2}} \{a_0 t^\alpha e^{\beta(t-1)}\}^{\frac{6k}{k+2}} dz^2 \tag{29}$$

4. PHYSICAL AND KINEMATICAL PROPERTIES OF THE MODEL

For our model (29), the directional Hubble parameters H_1, H_2, H_3 and mean Hubble parameter H are obtained as

$$H_1 = H_2 = \frac{3}{k+2} \left(\beta + \frac{\alpha}{t} \right), \quad H_3 = \frac{3k}{k+2} \left(\beta + \frac{\alpha}{t} \right) \tag{30}$$

$$\therefore H = \left(\beta + \frac{\alpha}{t} \right) \tag{31}$$

The spatial volume V , the expansion scalar θ , the shear scalar σ and the average anisotropy parameter A_m of the model are obtained as

$$V = \{a_0 t^\alpha e^{\beta(t-1)}\}^3 \tag{32}$$

$$\theta = 3H = 3 \left(\beta + \frac{\alpha}{t} \right) \tag{33}$$

$$\sigma^2 = 3 \frac{(k-1)^2}{(k+2)^2} \left(\beta + \frac{\alpha}{t} \right)^2 \tag{34}$$

$$A_m = 2 \frac{(k-1)^2}{(k+2)^2} \tag{35}$$

From equations (31)-(35), we find that the spatial volume V is zero at the beginning of the universe. Therefore, our model starts with a Big Bang singularity. We plot the graph of scale factor a in figure 1. The Hubble parameter H , the expansion scalar θ , and the shear scalar σ are all diverse at $t = 0$ and decrease with an increase in cosmic time t up to a fixed limit. Figure 2 depicts the evolution of the Hubble parameter H over cosmic time t . The anisotropy parameter A_m and the shear scalar σ become nonzero constant for $k \neq 1$, so the model will remain anisotropic throughout the evolution of the universe. Both the parameters are equal to zero for $k = 1$. Therefore, the universe can become isotropic only when $k = 1$.

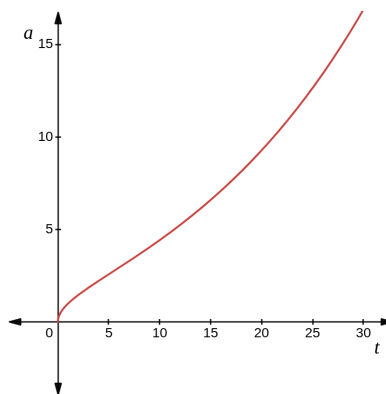


Figure 1. Evolution of the scale factor a versus cosmic time t for $\alpha = 0.49$ and $\beta = 0.04$

The deceleration parameter (q) is defined by

$$q = -\frac{a\ddot{a}}{\dot{a}^2} = -1 - \frac{\dot{H}}{H^2} \tag{36}$$

Using equation (25), the deceleration parameter q for our model is obtained as

$$q = -1 + \frac{\alpha}{(\beta t + \alpha)^2} \tag{37}$$

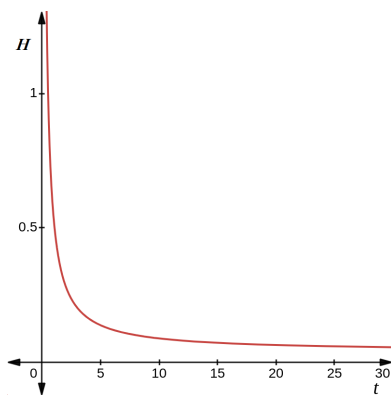


Figure 2. Evolution of the Hubble parameter H versus cosmic time t for $\alpha = 0.49$ and $\beta = 0.04$

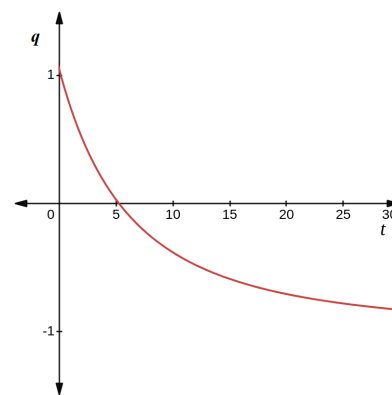


Figure 3. Evolution of the deceleration parameter q versus cosmic time t for $\alpha = 0.49$ and $\beta = 0.04$

The deceleration parameter q is a measure of whether the expansion of the universe is accelerating, decelerating or uniform. The expansion is accelerating for $q < 0$, decelerating for $q > 0$ and uniform for $q =$

0. Observations indicate that the universe is currently expanding at an accelerating rate, with a deceleration parameter in the range of $-1 \leq q < 0$.

From equation (37), it is clear that the universe evolves with variable deceleration parameter when both α and β are non zero. Figure 3 demonstrates the evolution of deceleration parameter q versus cosmic time t and shows that the deceleration parameter q is positive in the early universe but transition to negative at time $t = \frac{\sqrt{\alpha}-\alpha}{\beta}$ and $t = -\frac{(\sqrt{\alpha}+\alpha)}{\beta}$. Here, we do not consider the case $t = -\frac{(\sqrt{\alpha}+\alpha)}{\beta}$ as we consider our universe to begin at time $t = 0$ (in billion years). Hence, cosmic acceleration took place at the time $t = \frac{\sqrt{\alpha}-\alpha}{\beta}$, which implies that the parameter α falls within the range of $0 < \alpha < 1$. This transition marks the switch from early decelerating phase of the universe to its current accelerating phase. In this paper, we choose $\alpha = 0.49$ and $\beta = 0.04$ as these smaller values of α and β result in the universe's acceleration occurring around approximately 5.5 billion years, aligning with observational data. A relatively larger value of β would indicate acceleration happening much earlier in the evolution of the universe.

Using equations (31) and (25) in equation (16), to obtain the matter energy density ρ_m as

$$\rho_m = M\{a_0 t^\alpha e^{\beta(t-1)}\}^{-3} \tag{38}$$

where M is a constant.

Using equation (31) in equation (5), we obtain the Barrow HDE density ρ_{BHDE} as

$$\rho_{\text{BHDE}} = D \left(\beta + \frac{\alpha}{t} \right)^{2-\Delta} \tag{39}$$

From equations (38) and (39), we notice that both the energy densities are decreasing functions of cosmic time t . Figure 4 depicts the evolution of matter energy density ρ_m which demonstrates that it is high at early stage of the universe and tends to zero at late times. The BHDE density given by the equation (39) behaves like the standard HDE for $\Delta = 0$. The behavior of BHDE will differ from the standard one, depending on the Δ parameter, resulting to a distinct cosmological scenario. To understand the evolution of BHDE, we plot it against the cosmic time t in figure 5 for different values of Δ . From figure 5, we can see that for $\Delta = 0, 0.5$ and 1.5 , the BHDE density decrease with an increase of cosmic time t and tend to a constant value at late times. Whereas, for $\Delta = 2$, the BHDE density is constant throughout the evolution of the universe. In this scenario, the BHDE behaves like a cosmological constant and the model is referred as Λ CDM model. The physical implications of the decrease in energy densities suggest that the volume of the universe is increasing.

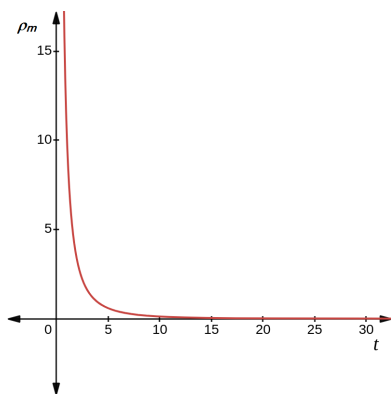


Figure 4. Evolution of matter energy density ρ_m versus cosmic time t for $M = 10, \alpha = 0.49, \beta = 0.04$ and $a_0 = 1$

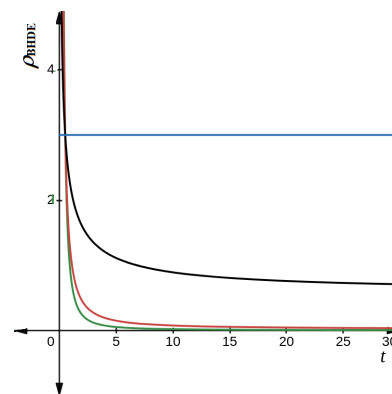


Figure 5. Evolution of BHDE density ρ_{BHDE} versus cosmic time t for $D = 3, \alpha = 0.49, \beta = 0.04$ and $\Delta = 0$ (green line), $\Delta = 0.5$ (red line), $\Delta = 1.5$ (black line), $\Delta = 2$ (blue line)

Using equations (39) and (31) in equation (17), we get pressure p_{BHDE} of the Barrow HDE as

$$p_{\text{BHDE}} = -D \left(\beta + \frac{\alpha}{t} \right)^{2-\Delta} + \frac{D\alpha(2-\Delta)}{3t^2} \left(\beta + \frac{\alpha}{t} \right)^{-\Delta} \tag{40}$$

Figure 6 displays the Barrow holographic dark energy pressure p_{BHDE} with respect to cosmic time t , as given by the equation (40). In case of $\Delta = 0$ and 0.5 , the pressure is positive in the initial stage and decreases

as cosmic time t increases and eventually become negative at late times. For $\Delta = 1.5$, the pressure p_{BHDE} is extremely negative at the beginning and rises gradually as cosmic time t increases until it reaches a certain constant value. However for $\Delta = 2$, the pressure is constantly negative in the entire evolution of the universe. This indicates that the universe is undergoing accelerated expansion for all the values of Δ , as the pressure remains negative throughout the evolution.

Using equations (26), (28) and (40) in equation (12), we obtain the expression for cosmological constant Λ as

$$\Lambda = \frac{9(k^2 + k + 1)}{(k + 2)^2} \left(\beta + \frac{\alpha}{t}\right)^2 - \frac{3\alpha(k + 1)}{t^2(k + 2)} - D \left(\beta + \frac{\alpha}{t}\right)^{2-\Delta} + \frac{D\alpha(2 - \Delta)}{3t^2} \left(\beta + \frac{\alpha}{t}\right)^{-\Delta} \tag{41}$$

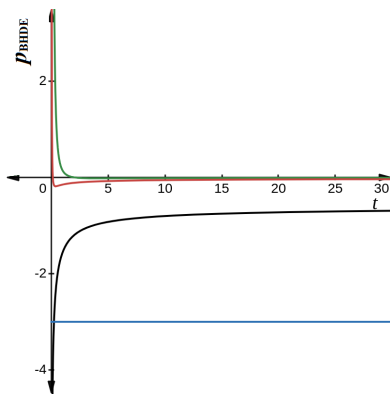


Figure 6. Evolution of BHDE pressure p_{BHDE} versus cosmic time t with $\alpha = 0.49$, $\beta = 0.04$, $D = 3$ and $\Delta = 0$ (green line), $\Delta = 0.5$ (red line), $\Delta = 1.5$ (black line), $\Delta = 2$ (blue line)

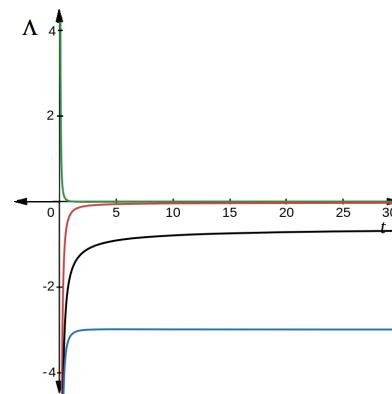


Figure 7. Evolution of cosmological constant Λ versus cosmic time t with $\alpha = 0.49$, $\beta = 0.04$, $D = 3$, $k = 0.1$ and $\Delta = 0$ (green line), $\Delta = 0.5$ (red line), $\Delta = 1.5$ (black line), $\Delta = 2$ (blue line)

Figure 7 illustrates the evolution of Λ with respect to cosmic time t for different value of Δ . From figure 7, we observe that Λ is positive but decreasing for $\Delta = 0$ and negative but increasing for $\Delta = 0.5, 1.5$ and 2 with cosmic time t . When Δ is set to 0 and 0.5 , the value of Λ approaches zero at the later stages of the universe. However, for $\Delta = 1.5$ and 2 , Λ remains at a constant negative value. Despite the negative value of Λ for $\Delta = 0.5, 1.5$, and 2 , it increases with cosmic time t . In both scenarios, the negative pressure at late times signifies the accelerated expansion of the universe. Biswa and Mazumdar [29] and Anjan *et al.* [30] have investigated cosmological models that feature a negative Λ . Currently, the determination of Λ is not only complicated, but it is also uncertain.

Using equations (39) and (40), the equation of state parameter (EoS parameter) ω_{BHDE} of Barrow HDE is obtained as

$$\omega_{\text{BHDE}} = \frac{p_{\text{BHDE}}}{\rho_{\text{BHDE}}} = -1 + \frac{\alpha(2 - \Delta)}{3t^2 \left(\beta + \frac{\alpha}{t}\right)^2} \tag{42}$$

Equation (42) implies that the EoS parameter ω_{BHDE} in our model is a strictly decreasing function of cosmic time t for $\Delta < 2$. Figure 8 depicts the variation of EoS parameter ω_{BHDE} with cosmic time t for different values of Δ . The figure displays that, for $\Delta = 0, 0.5$ and 1.5 , the EoS parameter ω_{BHDE} in our model varies in the quintessence region ($-1 < \omega_{\text{BHDE}} < -\frac{1}{3}$) after a particular point in time during its evolution. Additionally, we can note that the EoS parameter ω_{BHDE} converges to -1 at late times and eventually approach the Λ CDM ($\omega_{\text{BHDE}} = -1$) model in future. When $\Delta = 2$, the EoS parameter ω_{BHDE} remains constant at a value of -1 throughout its evolution. As previously mentioned, in this scenario, the Barrow holographic dark energy behaves like the cosmological constant. Considering all the cases of our model, we can conclude that the model will have a more accelerating effect at higher values of cosmic time t .

The density parameters are read as

$$\Omega_m = \frac{\rho_m}{3H^2}, \Omega_{\text{BHDE}} = \frac{\rho_{\text{BHDE}}}{3H^2}, \Omega_\sigma = \frac{\sigma^2}{3H^2}, \Omega_\Lambda = \frac{\Lambda}{3H^2}, \Omega_l = \frac{l^2}{3H^2 A^2}$$

where $\Omega_m, \Omega_{\text{BHDE}}, \Omega_\Lambda, \Omega_\sigma$ and Ω_l represent the dimensionless density parameters for matter, Barrow HDE, vacuum energy, shear anisotropy and l parameter respectively.

From equation (14), the total energy density parameter (Ω) is obtained as

$$\Omega \equiv \Omega_m + \Omega_{\text{BHDE}} + \Omega_\sigma + \Omega_\Lambda + \Omega_l = 1 \tag{43}$$

Therefore, equation (43) imply

$$\Omega = \frac{M}{3 \left(\beta + \frac{\alpha}{t}\right)^2 \{a_0 t^\alpha e^{\beta(t-1)}\}^3} + \frac{3(k^2 + k + 1)}{(k + 2)^2} - \frac{\alpha(k + 1)}{t^2(k + 2) \left(\beta + \frac{\alpha}{t}\right)^2} + \frac{D\alpha(2 - \Delta)}{9t^2 \left(\beta + \frac{\alpha}{t}\right)^{2+\Delta}} + \frac{(k - 1)^2}{(k + 2)^2} + \frac{m^{\frac{2}{k+2}} \times l^2}{3 \left(\beta + \frac{\alpha}{t}\right)^2 \{a_0 t^\alpha e^{\beta(t-1)}\}^{\frac{6}{k+2}}} = 1 \tag{44}$$

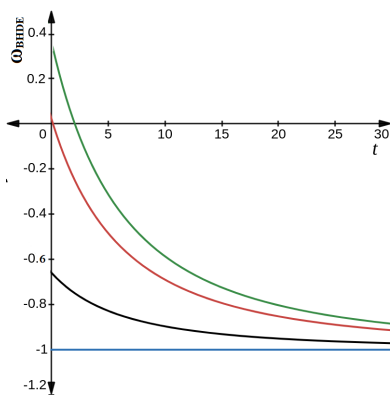


Figure 8. Evolution of EoS parameter ω_{BHDE} versus cosmic time t with $\alpha = 0.49, \beta = 0.04$ and $\Delta = 0$ (green line), $\Delta = 0.5$ (red line), $\Delta = 1.5$ (black line), $\Delta = 2$ (blue line)

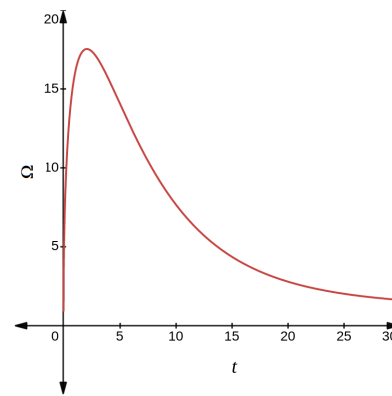


Figure 9. Evolution of overall density parameter Ω versus cosmic time t for $M = 10, \alpha = 0.49, \beta = 0.04, k = 0.1, \Delta = 0.5, l = 1, D = 3$ and $a_0 = 1$

The graph depicted in Figure 9 demonstrates how the total energy density Ω changes over cosmic time t . The total energy density parameter $\Omega > 1, \Omega = 1$ and $\Omega < 1$ represent the open, flat and closed universe respectively. As the figure indicates, the total density parameter Ω experiences a rapid increase during the early stages of the universe’s evolution, reaching a fixed point before beginning to decrease as time goes on. Eventually, the total density parameter Ω approaches 1 in later times, indicating that the universe becomes flat at late times.

4.1. Energy conditions:

Energy conditions are a set of theoretical inequalities that serve as linear combinations of energy density and pressure within the framework of general relativity. These conditions establish constraints on how matter and energy are distributed in spacetime. Energy conditions help to understand the behavior of gravity and derives many theorems within the classical general relativity such as the collapse of stars [31], the area increase theorem related to black holes [31], the positive mass theorem [32] etc. There are several energy conditions, among which the linear energy conditions are the null energy condition (NEC), the weak energy condition (WEC), the strong energy condition (SEC) and the dominant energy condition (DEC).

The standard energy conditions for T_{ij} , where T_{ij} is the energy-momentum tensor of perfect fluid are defined as:

- Null Energy Condition (NEC): For any null vector $k^i, T_{ij}k^i k^j \geq 0$. This implies the relation

$$\rho + p \geq 0$$

The NEC ensures that the pressure cannot be so negative that it dominates over the energy density of the universe. This means that as the energy density of the universe decreases, the pressure should become less negative with the universe’s expansion. Conversely, when the NEC is violated, it signifies that the pressure

becomes more negative compared to the energy density, leading to a more accelerating effect in the universe.

- Weak Energy Condition (WEC): For any timelike vector v^i , $T_{ij}v^iv^j \geq 0$ which leads to

$$\rho \geq 0 \quad \text{and} \quad \rho + p \geq 0$$

The WEC includes the NEC and adds the requirement that the energy density of the universe remains positive throughout its evolution. The violation of the WEC implies that either the energy density becomes negative, or the pressure overwhelms the energy density of the universe.

- Strong Energy Condition (SEC): For any timelike vector v^i , $T_{ij}v^iv^j + \frac{1}{2}T \geq 0$, where T is the trace of T_{ij} . This leads to the relation

$$\rho + 3p \geq 0 \quad \text{and} \quad \rho + p \geq 0$$

The SEC implies a positive deceleration parameter, which leads to a decelerating universe. However, if the SEC is violated, it signifies that the universe is undergoing an accelerated expansion phase.

- Dominant Energy Condition (DEC): For any timelike vector v^i , $T_{ij}v^iv^k \geq 0$ and $J_iJ^i \leq 0$ where $J^i = -T^i_jv^j$. This results in the following relation

$$\rho \geq 0 \quad \text{and} \quad \rho + p \geq 0 \quad \text{and} \quad \rho - p \geq 0$$

The DEC is the WEC with an extra condition that the pressure should not exceed the energy density of the universe. The DEC can be interpreted as stating that the energy density is always non-negative and should have dominance over pressure of the universe.

For our model,

$$\begin{aligned} \rho + p &= \frac{M}{\{a_0 t^\alpha e^{\beta(t-1)}\}^3} + \frac{D\alpha(2-\Delta)}{3t^2} \left(\beta + \frac{\alpha}{t}\right)^{-\Delta} \\ \rho - p &= \frac{M}{\{a_0 t^\alpha e^{\beta(t-1)}\}^3} + 2D \left(\beta + \frac{\alpha}{t}\right)^{2-\Delta} - \frac{D\alpha(2-\Delta)}{3t^2} \left(\beta + \frac{\alpha}{t}\right)^{-\Delta} \\ \rho + 3p &= \frac{M}{\{a_0 t^\alpha e^{\beta(t-1)}\}^3} - 2D \left(\beta + \frac{\alpha}{t}\right)^{2-\Delta} + \frac{D\alpha(2-\Delta)}{t^2} \left(\beta + \frac{\alpha}{t}\right)^{-\Delta} \end{aligned}$$

The above mentioned energy conditions are generally satisfied by the normal matter. However, the SEC is known to be violated in an accelerated expansion phase of the universe. Figure 10 shows a plot of the left side of the energy conditions, which indicates that in our model, initially, the NEC, WEC, SEC and DEC are all satisfied, but at late times, the SEC gets violated. The violation of the SEC results in the acceleration of the universe.

4.2. Jerk parameter (j):

The cosmic jerk parameter j is a measure of the acceleration of the universe, describing how quickly the rate of expansion is changing over cosmic time t . It is a dimensionless quantity defined as the third derivative of the scale factor a with respect to cosmic time t and provides an important information about the universe's expansion. A positive value of jerk parameter j signifies that the universe undergoes a transition from deceleration to acceleration in its expansion. For the popular Λ CDM model the value of jerk parameter j is equal to one.

Mathematically, the jerk parameter j is defined as

$$j = \frac{1}{aH^3} \frac{d^3a}{dt^3} \tag{45}$$

For our model, the jerk parameter j is obtained as

$$j = \frac{\beta^3 + \frac{3\alpha\beta^2}{t} + \frac{(3\alpha^2-3\alpha)\beta}{t^2} + \frac{\alpha^3-3\alpha^2+2\alpha}{t^3}}{\left(\beta + \frac{\alpha}{t}\right)^3} \tag{46}$$

The graph illustrating the jerk parameter j is displayed in figure 11. It is clear from the figure that the jerk parameter j remains positive throughout the universe's evolution, signifying that the rate of expansion of the universe is increasing. Additionally, in figure 11, it can be observed that the jerk parameter j converges to 1 at late times, indicating that the model behaves similar to the Λ CDM model.

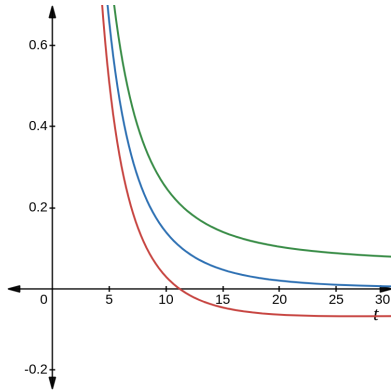


Figure 10. Graph of energy conditions versus cosmic time t for $M = 10$, $a_0 = 1$, $\alpha = 0.49$, $\beta = 0.04$, $D = 3$, $\Delta = 0.5$, $\rho + p$ (blue line), $\rho - p$ (green line) and $\rho + 3p$ (red line)

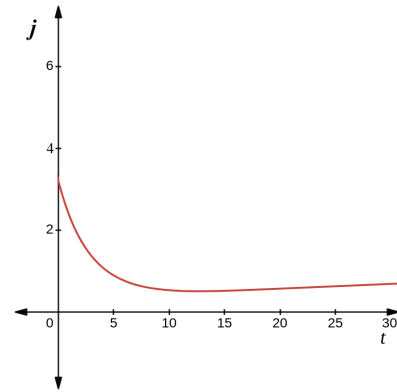


Figure 11. Evolution of jerk parameter j versus cosmic time t for $\alpha = 0.49$ and $\beta = 0.04$

4.3. Snap parameter (s):

The snap parameter s is a dimensionless quantity defined as the fourth order derivative of the scale factor a with respect to cosmic time t . It describes the rate of change of the acceleration of the universe's expansion and helps to understand the dynamics of the universe.

Mathematically, the snap parameter s is defined as

$$s = \frac{1}{aH^4} \frac{d^4 a}{dt^4} \tag{47}$$

For our model, the snap parameter s is obtained as

$$s = \frac{\beta^4 + \frac{4\alpha\beta^3}{t} + \frac{(6\alpha^2 - 6\alpha)\beta^2}{t^2} + \frac{(4\alpha^3 - 12\alpha^2 + 8\alpha)\beta}{t^3} + \frac{\alpha^4 - 6\alpha^3 + 11\alpha^2 - 6\alpha}{t^4}}{\left(\beta + \frac{\alpha}{t}\right)^4} \tag{48}$$

Figure 12 depicts the variation of the snap parameter s with respect to cosmic time t . The snap parameter s shows the increasing behavior. At $t \rightarrow 0$, it is negative and increases over cosmic time t . Eventually, the snap parameter s converges to 1 at late times. This suggests that the universe is experiencing a phase of accelerated expansion.

4.4. Lerk parameter (l):

The lerk parameter l is also a dimensionless quantity defined as the fifth order derivative of the scale factor a with respect to the cosmic time t .

Mathematically, the lerk parameter l is defined as

$$l = \frac{1}{aH^5} \frac{d^5 a}{dt^5} \tag{49}$$

For our model, the lerk parameter l is obtained as

$$l = \frac{\beta^5 + \frac{5\alpha\beta^4}{t} + \frac{(10\alpha^2 - 10\alpha)\beta^3}{t^2} + \frac{(10\alpha^3 - 30\alpha^2 + 20\alpha)\beta^2}{t^3} + \frac{(5\alpha^4 - 30\alpha^3 + 55\alpha^2 - 30\alpha)\beta}{t^4} + \frac{\alpha^5 - 10\alpha^4 + 35\alpha^3 - 50\alpha^2 + 24\alpha}{t^5}}{\left(\beta + \frac{\alpha}{t}\right)^5} \tag{50}$$

Figure 13 illustrates the variation of the lerk parameter l with respect to cosmic time t . The figure displays that the lerk parameter l has a high value at $t \rightarrow 0$ and gradually converges to 1 at late times.

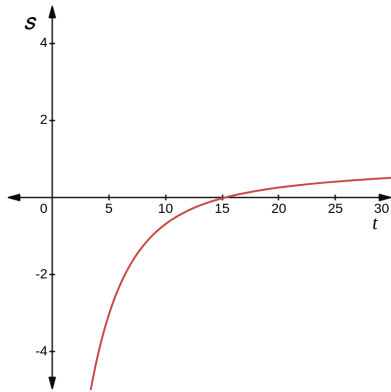


Figure 12. Evolution of snap parameter s versus cosmic time t for $\alpha = 0.49$ and $\beta = 0.04$

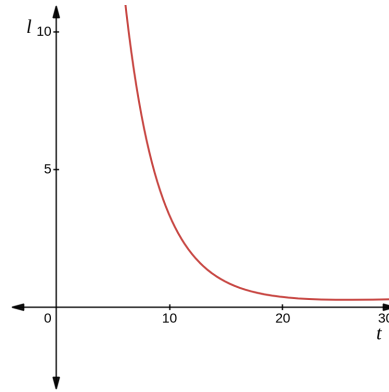


Figure 13. Evolution of lerk parameter l versus cosmic time t for $\alpha = 0.49$ and $\beta = 0.04$

4.5. Coincidence parameter (\bar{r}):

The parameter \bar{r} , known as the coincidence parameter, is defined as the ratio between two energy densities, i.e. $\bar{r} = \frac{\rho_{BHDE}}{\rho_m}$, of the universe. Current observations demand that the value of the coincidence parameter should either remain constant or change very slowly in response to the universe’s expansion. But the most simplest and widely accepted dark energy model, the Λ CDM model, is inconsistent with this observations. So, numerous alternative models are considered to avoid this coincidence problem. For our model, the coincidence parameter \bar{r} is obtained as

$$\bar{r} = \frac{\{a_0 t^\alpha e^{\beta(t-1)}\}^3 D(\beta + \frac{\alpha}{t})^{2-\Delta}}{M} \tag{51}$$

The variation of coincidence parameter \bar{r} versus cosmic time t is shown in figure 14. From figure, we observe that the value of \bar{r} increases rapidly at late times. So, the coincidence problem is not resolved in our model. Since, here we have considered the BHDE and dark matter to be non interacting, so, it will be interesting to see the behavior of coincidence parameter in case of interacting model. Thus, a specific form of interaction between BHDE and dark matter may make the ratio of their densities to remain relatively constant as the universe evolves.

5. STATEFINDER DIAGNOSTIC

To distinguish between various cosmological scenarios related to dark energy, it is essential to have a reliable and precise method to evaluate DE models. For this purpose Sahni *et al.* [33] introduced a diagnostic using the parameter pair $\{r, s\}$, commonly known as the Statefinder diagnostic. The pair is effective in distinguishing among various dark energy models, such as the cosmological constant, quintessence, the Chaplygin gas, braneworld models, and models involving interacting dark energy. The dimensionless Statefinder diagnostic is constructed by considering the scale factor a of the universe and its higher order derivative with respect to cosmic time t only. The parameter r represents the hierarchy of geometrical cosmological parameters, succeeding the Hubble parameter H and the deceleration parameter q . On the other hand, s is a parameter derived as a linear combination of q and r in a way that makes it independent of the density associated with dark energy.

The Statefinder diagnostic pair $\{r, s\}$ is defined as

$$r = \frac{1}{aH^3} \frac{d^3a}{dt^3} \quad \text{and} \quad s = \frac{r - 1}{3(q - \frac{1}{2})}, \quad \text{where } q \neq \frac{1}{2}$$

For our model,

$$r = \frac{\beta^3 + \frac{3\alpha\beta^2}{t} + \frac{(3\alpha^2 - 3\alpha)\beta}{t^2} + \frac{\alpha^3 - 3\alpha^2 + 2\alpha}{t^3}}{(\beta + \frac{\alpha}{t})^3} \tag{52}$$

$$s = \frac{-6\alpha\beta t - 6\alpha^2 + 4\alpha}{3(\beta t + \alpha)\{2\alpha - 3(\beta t + \alpha)^2\}} \tag{53}$$

The $r - s$ plane for these cosmological parameters for Λ CDM and standard CDM (SCDM) are $(1, 0)$ and $(1, 1)$ respectively. The quintessence DE epochs are given by the region $(r < 1, s > 0)$ whereas trajectories for Chaplygin gas lie in the range $(r > 1, s < 0)$. In our model, equations (52) and (53) indicate that the Statefinder diagnostic pair depend on the cosmic time t . As t approaches infinity, the diagnostic pair yields $r = 1$ and $s = 0$. The figure 15 also confirms that our model coincide with the Λ CDM model during later stages.

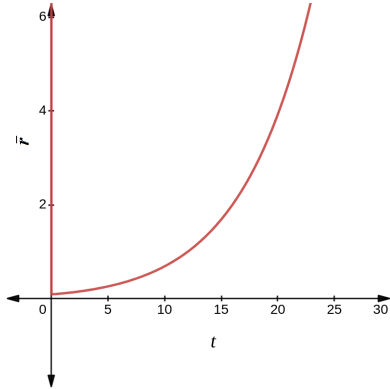


Figure 14. Evolution of coincidence parameter \bar{r} versus cosmic time t for $\alpha = 0.49$, $\beta = 0.04$, $M = 10$, $a_0 = 1$, $D = 3$ and $\Delta = 0.5$

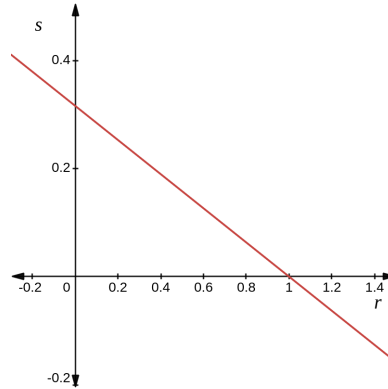


Figure 15. Evolution of the Statefinder parameters r versus s for $\alpha = 0.49$ and $\beta = 0.04$

6. CORRESPONDENCE BETWEEN THE BHDE MODEL AND QUINTESSENCE SCALAR FIELD MODEL

Quintessence is considered as one of the candidate of dark energy because it has the potential to explain the cosmic coincidence problem and can fit better with observational data compared to the cosmological constant. In order to get the accelerated expansion of the universe the EoS parameter for quintessence must be less than $-\frac{1}{3}$.

In this section, our focus is on investigating the correspondence between BHDE and the quintessence scalar field model. To establish the correspondence, we perform a comparison between the BHDE density and the energy density of the scalar field model. Additionally, we analyze the EoS parameter of BHDE in comparison to the EoS parameter of the scalar field.

The energy density and pressure of the quintessence scalar field model are given by

$$\rho_\phi = \frac{\dot{\phi}^2}{2} + V(\phi) \tag{54}$$

$$p_\phi = \frac{\dot{\phi}^2}{2} - V(\phi) \tag{55}$$

where ϕ is the scalar field and $V(\phi)$ is the potential of scalar field ϕ .

The EoS parameter for the scalar field is given by

$$\omega_\phi = \frac{p_\phi}{\rho_\phi} = \frac{\dot{\phi}^2 - 2V(\phi)}{\dot{\phi}^2 + 2V(\phi)} \tag{56}$$

Equations (54) and (55) gives

$$\dot{\phi}^2 = \rho_\phi + p_\phi \tag{57}$$

and

$$V(\phi) = \frac{\rho_\phi - p_\phi}{2} \tag{58}$$

Using equations (42) and (56), we get

$$-1 + \frac{\alpha(2 - \Delta)}{3t^2 \left(\beta + \frac{\alpha}{t}\right)^2} = \frac{\dot{\phi}^2 - 2V(\phi)}{\dot{\phi}^2 + 2V(\phi)} \tag{59}$$

By taking $\rho_\phi = \rho_{\text{BHDE}}$ and $p_\phi = p_{\text{BHDE}}$, we can calculate the kinetic energy $\dot{\phi}^2$ and the scalar potential $V(\phi)$ as

$$\dot{\phi}^2 = \frac{D\alpha(2 - \Delta)}{3t^2} \left(\beta + \frac{\alpha}{t}\right)^{-\Delta} \tag{60}$$

$$V(\phi) = D \left(\beta + \frac{\alpha}{t}\right)^{2-\Delta} - \frac{D\alpha(2 - \Delta)}{6t^2} \left(\beta + \frac{\alpha}{t}\right)^{-\Delta} \tag{61}$$

Thus, we have established the potential $V(\phi)$ and scalar field ϕ for the quintessence scalar field model that corresponds to the BHDE model. The kinetic energy $\dot{\phi}^2$ is plotted in the figure 16. The figure illustrates that the kinetic energy $\dot{\phi}^2$ decreases over cosmic time t and eventually diminishes at late times. Figure 17 depicts the scalar field potential $V(\phi)$ for the quintessence model. It can be seen that the potential $V(\phi)$ is also decreasing function of cosmic time t and tends toward a constant value at late times.

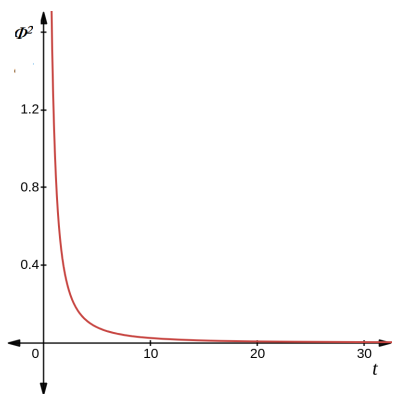


Figure 16. Evolution of kinetic energy $\dot{\phi}^2$ versus cosmic time t for $\alpha = 0.49$, $\beta = 0.04$, $D = 3$ and $\Delta = 0.5$

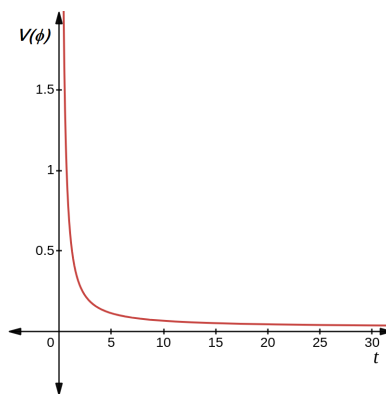


Figure 17. Evolution of the $V(\phi)$ versus t for $\alpha = 0.49$, $\beta = 0.04$, $D = 3$ and $\Delta = 0.5$



7. CONCLUSION

In this paper, we investigate a spatially homogeneous and anisotropic Bianchi type-III universe filled with pressureless cold dark matter and non-interacting Barrow holographic dark energy in the framework of Einstein’s General theory of Relativity. We obtain the exact solution of the Einstein field equations by choosing a hybrid expansion law and by assuming the expansion scalar to be proportional to the shear scalar. We investigate various cosmological parameters to discuss the physical and kinematical properties of the model and find that:

- At $t = 0$, the volume V of the universe vanish i.e. the universe starts with zero volume and tends to infinity at $t \rightarrow \infty$. So, the universe begins with a Big Bang singularity.
- The Hubble parameter H and the expansion scalar θ are decreasing functions of cosmic time t and $\frac{dH}{dt}$ and $\frac{d\theta}{dt}$ tend to 0 at $t \rightarrow \infty$.
- The shear scalar σ^2 diverges at $t = 0$ and converges to a constant value at $t \rightarrow \infty$.
- The anisotropy parameter is constant and not equal to zero unless $k = 1$ which implies that the universe remain anisotropic throughout the evolution. But, for $k = 1$ the anisotropy parameter, $A_m = 0$ and the universe become isotropic throughout the evolution.
- The matter energy density ρ_m and Barrow holographic dark energy density ρ_{BHDE} are decreasing functions of cosmic time t . The decrease of energy densities with an increase of cosmic time t leads to the volume expansion of the universe.
- The pressure of Barrow holographic dark energy p_{BHDE} is negative at late times which indicates the accelerated expansion of the universe.
- The EoS parameter ω_{BHDE} of Barrow holographic dark energy varies in quintessence region and tends to ΛCDM model at late times.

- The deceleration parameter q transits from its positive value in the early universe to -1 at late times. This transition shows the early decelerated phase to current accelerated phase of the universe.
- The total energy density parameter Ω converges to 1 as cosmic time $t \rightarrow \infty$. This suggests that the universe is approaching towards a flat universe at late times.
- The Null energy condition, the Weak energy condition and the Dominant energy condition are all satisfied but the Strong energy condition is violated at late times which supports the accelerated expansion of the universe.
- The cosmic jerk parameter j , the snap parameter s and the lerk parameter l all converges to 1 at late times. The convergence of j to at late times demonstrates that our model matches the Λ CDM model.
- The coincidence parameter \bar{r} is not constant in the univers's evolution. So, the coincidence problem is not resolved in our model.
- The Statefinder parameters pass through the point $(1, 0)$ which corresponds to the Λ CDM model.
- The correspondence between Barrow holographic dark energy model and quintessence scalar field model describe the accelerated phase of the expanding universe.

ORCID

 Chandra Rekha Mahanta, <https://orcid.org/0000-0002-8019-8824>;  Dibyajyoti Das, <https://orcid.org/0009-0007-0927-0903>

REFERENCES

- [1] A.G. Riess, *et al.*, "Observational evidence from supernovae for an accelerating universe and a cosmological constant," *The Astronomical Journal*, **116**, 1009-1038 (1998). <https://doi.org/10.1086/300499>
- [2] S. Perlmutter, *et al.*, "Measurements of Ω and Λ from 42 high-redshift supernovae," *The Astrophysical Journal*, **517**, 565-586 (1999). <https://doi.org/10.1086/307221>
- [3] D.N. Spergel, *et al.*, "First-year Wilkinson Microwave Anisotropy Probe (WMAP) observations: Determination of cosmological parameters," *Astrophys. J. Suppl. Ser.* **148**, 175-194 (2003). <https://doi.org/10.1086/377226>
- [4] U. Seljak, *et al.*, "Cosmological parameter analysis including SDSS Ly α forest and galaxy bias: constraints on the primordial spectrum of fluctuations, neutrino mass, and dark energy," *Phys. Rev. D*, **71**, 103515 (2005). <https://doi.org/10.1103/PhysRevD.71.103515>
- [5] C.L. Bennett, *et al.*, "First-Year *Wilkinson Microwave Anisotropy Probe (WMAP)* Observations: Preliminary Maps and Basic Results," *Astrophys. J. Suppl. Ser.* **148**, 1-27 (2003). <https://doi.org/10.1086/345346>
- [6] M. Tegmark, *et al.*, "Cosmological parameters from SDSS and WMAP," *Phys. Rev. D*, **69**, 103501, (2004). <https://doi.org/10.1103/PhysRevD.69.103501>
- [7] D.J. Eisenstein, *et al.*, "Detection of the Baryon Acoustic Peak in the Large-Scale correlation function of SDSS luminous red galaxies," *The Astronomical Journal*, **633**, 560-574 (2005). <https://doi.org/10.1086/466512>
- [8] C.R. Contaldi, C.R. Contaldi, H. Hoekstra, and A. Lewis, "Joint Cosmic Microwave Background and Weak Lensing Analysis: Constraints on Cosmological Parameters," *Phys. Rev. Lett.* **90**, 221303 (2003). <https://doi.org/10.1103/PhysRevLett.90.221303>
- [9] S.W. Allen, R.W. Schmidt, H. Ebeling, A.C. Fabian, and L. Van Speybroeck, "Constraints on dark energy from *Chandra* observations of the largest relaxed galaxy clusters," *Mon. Not. R. Astron. Soc.* **353**, 457-467 (2004). <https://doi.org/10.1111/j.1365-2966.2004.08080.x>
- [10] V. Sahni, and A. Starobinsky, "The Case for a Positive Cosmological Λ -term," *Int. J. Mod. Phys. D*, **9**, 373 (2000). <https://doi.org/10.1142/S0218271800000542>
- [11] S. Weinberg, "The cosmological constant problem," *Rev. Mod. Phys.* **61**, 1 (1989). <https://doi.org/10.1103/RevModPhys.61.1>
- [12] M. Sami, and T. Padmanabhan, "Viable cosmology with a scalar field coupled to the trace of the stress-tensor," *Phys. Rev. D*, **67**, 083509 (2003). <https://doi.org/10.1103/PhysRevD.67.083509>
- [13] T. Chiba, "Tracking K-essence," *Phys. Rev. D*, **66**, 063514 (2002). <https://doi.org/10.1103/PhysRevD.66.063514>
- [14] A. Kamenshchik, U. Moschella, and V. Pasquier, "An alternative to quintessence," *Phys. Lett. B*, **511**, 265-268 (2001). [https://doi.org/10.1016/S0370-2693\(01\)00571-8](https://doi.org/10.1016/S0370-2693(01)00571-8)
- [15] T. Padmanabhan, "Accelerated expansion of the universe driven by tachyonic matter," *Phys. Rev. D*, **66**, 021301 (2002). <https://doi.org/10.1103/PhysRevD.66.021301>
- [16] G. 't Hooft, "Dimensional reduction in quantum gravity, preprint (2009)," <https://doi.org/10.48550/arXiv.gr-qc/9310026>
- [17] W. Fischler, and L. Susskind, "Holography and cosmology," <https://doi.org/10.48550/arXiv.hep-th/9806039>
- [18] M. Li, "A model of holographic dark energy," *Phys. Lett. B*, **603**, 1-5 (2004). <https://doi.org/10.1016/j.physletb.2004.10.014>
- [19] C. Tsallis, and L.J.L. Cirto, "Black hole thermodynamical entropy," *Eur. Phys. J. C*, **73**, 2487 (2013). <https://doi.org/10.1140/epjc/s10052-013-2487-6>

- [20] L.N. Granda, and A. Oliveros, "Infrared cut-off proposal for the holographic density," Phys. Lett. B, **669**(5), 275-277 (2008). <https://doi.org/10.1016/j.physletb.2008.10.017>
- [21] H. Moradpour, *et al.*: "Thermodynamic approach to holographic dark energy and the Rényi entropy," Eur. Phys. J. C, **78**, 829 (2018). <https://doi.org/10.1140/epjc/s10052-018-6309-8>
- [22] J.D. Barrow, "The area of a rough black hole," Phys. Lett. B, **808**, 135643 (2020). <https://doi.org/10.1016/j.physletb.2020.135643>
- [23] S. Wang, Y. Wang, and M. Li, "Holographic dark energy," Phys. Rep., **696**, 1–57 (2017). <https://doi.org/10.1016/j.physrep.2017.06.003>
- [24] E.N. Saridakis, "Barrow holographic dark energy," Phys. Rev. D, **102**, 123525 (2020). <https://doi.org/10.1103/PhysRevD.102.123525>
- [25] S. Srivastava, and U.K. Sharma, "Barrow holographic dark energy with Hubble horizon as IR cutoff," Int. J. Geo. Methods in Mod. Phys. **18**, 2150014 (2021). <https://doi.org/10.1142/S0219887821500146>
- [26] B.C. Paul, *et al.*, "Bianchi-I anisotropic universe with Barrow holographic dark energy," Eur. Phys. J. C, **82**, 76 (2022). <https://doi.org/10.1140/epjc/s10052-022-10041-5>
- [27] Y. Hu, M. Li, N. Li, and Z. Zhang, "Holographic dark energy with cosmological constant," JCAP, **1508**, 012 (2015). <https://doi.org/10.1088/1475-7516/2015/08/012>
- [28] Ö. Akarsu, *et al.*, "Cosmology with hybrid expansion law: scalar field reconstruction of cosmic history and observational constraints," JCAP01, 022 (2014). <https://doi.org/10.1088/1475-7516/2014/01/022>
- [29] T. Biswas, and A. Mazumdar, "Inflation with a negative cosmological constant," Phys. Rev. D, **80**, 023519 (2009). <https://doi.org/10.1103/PhysRevD.80.023519>
- [30] A.A. Sen, S.A. Adil, and S. Sen, "Do cosmological observations allow a negative Λ ?" Mon. Not. of the Royal Astro. Society, **518**, 1 (2023). <https://doi.org/10.1093/mnras/stac2796>
- [31] S.W. Hawking, and G.F.R. Ellis, *The large scale structure of space-time*, (Cambridge, England, 1973)
- [32] R. Schoen, and S.T. Yau, "Positivity of the Total Mass of a General Space-Time," Phys. Rev. Lett. **43**, 1457 (1979). <https://doi.org/10.1103/PhysRevLett.43.1457>
- [33] V. Sahni, T.D. Saini, A.A. Starobinsky, and U. Alam, "Statefinder—a new geometrical diagnostic of dark energy," JETP Lett. **77**, 201-206 (2003). <https://doi.org/10.1134/1.1574831>

ГОЛОГРАФІЧНА МОДЕЛЬ ТЕМНОЇ ЕНЕРГІЇ БАРРОУ У ВСЕСВІТІ Б'ЯНКІ ТИПУ ІІІ З КВІНТЕСЕНЦІЄЮ





Чандра Рекха Маханта, Діб'яджоті Дас

^a Факультет математики, Університет Гаухаті, Джалукбарі, 781014, Ассам, Індія

У цій статті ми досліджуємо просторово однорідний і анізотропний Всесвіт Б'янкі типу ІІІ, що містить холодну темну матерію та голографічну темну енергію Барроу в рамках загальної теорії відносності. Ми припускаємо, що холодна темна матерія та голографічна темна енергія Барроу не взаємодіють, і отримуємо точні розв'язки рівнянь поля Ейнштейна, розглядаючи гібридний закон розширення та припускаючи, що скаляр розширення пропорційний скаляру зсуву. Ми перевіряємо фізичні та кінематичні властивості отриманої моделі, використовуючи такі параметри, як параметр Хаббла, параметр анізотропії, параметр уповільнення, параметр рівняння стану, параметр ривка тощо. Ми також перевіряємо, чи порушуються енергетичні умови або підтверджуються. Ми виявили, що умови нульової, слабкої та домінуючої енергії виконуються, тоді як умова сильної енергії порушена, що підтримує прискорене розширення Всесвіту. Діагностика Statefinder була проведена на основі останніх космологічних спостережень. Крім того, ми переформулювали відповідність між скалярним полем квінтесенції та голографічною моделлю темної енергії Барроу.

Ключові слова: космічне прискорення; голографічна темна енергія Барроу; Біанкі тип-ІІІ; холодна темна матерія; параметр уповільнення; рівняння параметра стану

REINTERPRETATION OF FRIEDMANN-ROBERTSON-WALKER UNIVERSE WITH VARIABLE GRAVITATIONAL AND COSMOLOGICAL TERM IN BOUNCING COSMOLOGY

 Asem Jotin Meitei^{a,*},  Kangujam Priyokumar Singh^a,  Syed Sabanam^a,  S. Kiranmala Chanu^b

^a Department of Mathematics, Manipur University, Canchipur, Imphal, 795003, Manipur, India

^b Department of Mathematics, Maharaja Bodhchandra College, Imphal, Manipur-795001, India

* Corresponding Author e-mail: jotinase@gmail.com

Received January 4, 2024; revised January 27, 2024; accepted February 17, 2024

This paper is devoted to investigate five dimensional homogeneous and isotropic FRW model with varying gravitational and cosmological constant with cosmic time. Exact solution of the Einstein field equations are obtained by using the equation of state $p = (\gamma - 1)\rho$ (gamma law), where γ which is an adiabatic parameter varies continuously as the universe expands. We obtained the solutions for different values of curvature $K = 0, 1, -1$ by using $a(t) = R_0(1 + \alpha^2 t^2)^n$, where α , n and R_0 are positive constants. Behaviour of the cosmological parameters are presented for different cases of the models. Physical interpretation of the derived model are presented in details. Interestingly the proposed model justified the current cosmological observations with dark energy.

Keywords: Five dimension; FRW metric; Cosmological term; Bouncing scale factor

PACS: 98.80.-K; 98.80Jk.

1. INTRODUCTION

The present universe is expanding with ever accelerating from the recent observational [1, 2, 3, 4] data on cosmic microwave background radiation (CMBR) and from WMAP data [5, 6]. Recent observations of type Ia supernovae (SNe Ia) at redshift $z < 1$ provide startling and puzzling evidence that the expansion of the universe at the present time appears to be accelerating, behavior attributed to “dark energy” with negative pressure [1, 2, 3, 7, 8, 9, 10, 11]. These observations strongly favour a significant and positive value of Λ . Some of the authors like [12, 13, 14] have studied the physics of the universe in higher dimensional space time.

Now-a-days peoples are more interested to study in higher dimensional space-time, since Einstein’s field equations in higher dimensions may have physical relevance as early as a time before the universe underwent compactification transitions. The solutions of Einstein field equations may have physical relevance in these higher dimensional space times. The phase transitions in the early universe can also lead to topological knots in the vacuum expectation value of a scalar field, which are concentrated in a small region, and by using a suitable scalar field we can prove that phase transitions can result in such objects. Therefore, to unify gravity and other interactions, it is more feasible to study higher dimensional space-time to solve cosmological problems. Also, it is well known that Friedmann-Robertson-Walker (FRW) spatially homogeneous and isotropic cosmological models are widely considered as good approximation of the present and early stages of the universe. FRW line element fits best with the cosmological principle and consistent with the present day observational data. At its early stage of evolution, study of five dimensional space-time is important because of the fact that cosmos might have had a higher dimensional era. In order to unify gravitation with electromagnetism, a five dimensional space-time geometry was first proposed by Kaluza [15] and Klein [16]. In the context of the Kaluza-Klein theories [15, 16, 17, 18] the study of higher dimensional cosmological models have obtained much importance. Many researchers have studied the problems in the field of higher dimensions. Appelquist et al. [18], Rahaman et al. [19] formulated higher dimensional spherically symmetric perfect fluid model in Lyra geometry. Samanta et al. [20] investigated five dimensional Bianchi type-1 string cosmological model in Lyra manifold.

In FRW type of homogeneous cosmological model, the dimensionality has a marked effect on the time temperature relation of the universe and our universe appears to cool more slowly in higher dimensional space time as suggested by Chatterjee [21]. In the recent years, cosmological model with a relic cosmological constant have received considerable attention among researchers for various reasons [22, 23, 24, 25, 26, 27]. We should realize that the existence of a nonzero cosmological constant in Einstein’s equations is a feature of deep and profound consequence. The recent observations indicate that $\Lambda \sim 10 - 55 \text{ cm}^2$ while particle physics prediction for Λ is greater than this value by a factor of order 10^{120} . This discrepancy is known as cosmological constant

problem. Ratra and Peebles[28], Dolgov [29, 30, 31], Sahni and Starobinsky [32], Padmanabhan [33] and Peebles [34] are the some of the researchers who recently studied on the cosmological constant “problem” and consequence on cosmology with a time-varying cosmological constant. For earlier reviews on this topic, we can referred to Zeldovich [35], Weinberg [36] and Carrol et al. [37].

G.S. Khadekar et.al.[38] discuss the big-bounce cosmological model by assuming the cosmological constant $\Lambda = \alpha\rho$ and $\Lambda = \beta H^2$, where α and β are the constant and ρ and H , are the energy density and Hubble parameter respectively by considering a class of five-dimensional cosmological model. Adhav K.S. et.al.[39] studied Bianchi type-III cosmological models in the presence of the bulk viscous fluid with varying Λ . Mukhopadhyay U. et. al.[40] discuss about the time variable and the accelerating universe in the Einstein’s field equations under the phenomenological assumption of $\Lambda = \alpha H^2$ for the full physical range of α . Shabani and Ziaie[42] studied about the classical bouncing behaviour of the Universe in terms of $f(R, T) = R + h(T)$ gravity theories. Minas et al. [43] examined the realization of bounces based on a modified gravity theory related to Finsler and Finsler-like geometries. Surendra and Kiranmala [44] studies the role of higher-dimensional FRW models with the framework of the particle creation in the context of variable cosmological and gravitational constants. Mahanta and Das [45] studied the spatially homogeneous and anisotropic Bianchi type-III universe filled with non interacting new holographic dark energy and cold dark matter with variable gravitational and cosmological constant terms. Further Agrawal et al.[46, 47, 48] developed a bouncing cosmology model with a suitable bouncing scale factor and studied its cosmic dynamics. Similarly, Singh et al.[49] studied the bouncing behaviour of the universe in modified gravity with higher-order curvature, finding that the extremal acceleration occurs at the bouncing point. And Zubair and Farooq[50] explore the bouncing models in the framework of 4D EGB with a flat, isotropic FRW universe.

Motivating from the above literatures here in this paper we investigate the spatially homogeneous and isotropic FRW universe in the context of variable cosmological and gravitational constants. We evaluate different cosmological parameters with the assumption that our universe is filled with distributions of matter. In sections 2.1-2.9, we have presented the solution of field equations and discussion for the cosmological parameters for the different values of curvature index parameters $K = 0, 1, -1$ and $\gamma = 1, \frac{4}{3}, 2$. In sec. 4 we also study the physical interpretation of the cosmological parameters in the context of solutions. Concluding remarks of the work is presented in sec. 5 .

2. FIELD EQUATIONS

Here we consider the five dimensional FRW metric[51, 52, 53] in the form

$$ds^2 = dt^2 - a^2(t) \left[\frac{dr^2}{(1 - Kr^2)} + r^2(d\theta^2 + \sin^2 \theta d\phi^2) + (1 - Kr^2)d\psi^2 \right] \tag{1}$$

where $a(t)$ is the scale factor $K = 0, -1$ or $+1$ is the curvature parameter for flat, open and closed universe respectively. The universe is assumed to be filled with distribution of matter represented by energy-momentum tensor of a perfect fluid

$$T_{\mu\nu} = (\rho + p)u_\mu v_\nu - pg_{\mu\nu}, \tag{2}$$

where ρ is the energy density of the cosmic matter, p is its pressure and u_μ is the five-velocity vector such that $u_\mu u^\mu = 1$. The Einstein field equations with time-dependent cosmological and gravitational constants is given by

$$R_{\mu\nu} - \frac{1}{2}g_{\mu\nu}R = 8\pi G(t)T_{\mu\nu} + \Lambda(t)g_{\mu\nu} \tag{3}$$

where $R_{\mu\nu}$ is the Ricci tensor, $G(t)$ and $\Lambda(t)$ being the variable gravitational and cosmological constants. The divergence of (3), taking into account the Bianchi identity, gives

$$(8\pi GT_{\mu\nu} + \Lambda g_{\mu\nu})^{;\nu} = 0. \tag{4}$$

Equation (3) and (4) may be considered as the fundamental equations of gravity with G and Λ coupling parameters. Using comoving coordinates

$$u_\nu = (1, 0, 0, 0, 0), \tag{5}$$

in (2) and with the line element (1), Einstein’s field equation (3), yields

$$8\pi G(t)\rho = \frac{6\dot{a}^2}{a^2} + \frac{6K}{a^2} - \Lambda(t), \tag{6}$$

$$8\pi G(t)p = -\frac{3\dot{a}}{a} - \frac{3\dot{a}^2}{a^2} - \frac{3K}{a^2} + \Lambda(t), \tag{7}$$

where dot denotes derivative w.r.t t' .

In uniform cosmology $G = G(t)$ and $\Lambda = \Lambda(t)$ so that the conservation (4) is given by

$$\dot{\rho} + 4(\rho + p)H = - \left(\frac{\dot{G}}{G}\rho + \frac{\dot{\Lambda}}{8\pi G} \right). \tag{8}$$

The usual energy momentum conservation relation $T^{\mu\nu}_{;\nu} = 0$ leads to

$$\dot{\rho} + 4(\rho + p)H = 0. \tag{9}$$

The field equations (6) - (7) can also be written as

$$\frac{3\ddot{a}}{a} = -4\pi G(t) \left[2p + \rho - \frac{\Lambda(t)}{8\pi G(t)} \right], \tag{10}$$

$$\frac{6\dot{a}^2}{a^2} = 8\pi G(t) \left[\rho + \frac{\Lambda(t)}{8\pi G(t)} \right]. \tag{11}$$

Equation (10) and (11) can be written in terms of the Hubble paramater $H = \frac{\dot{a}}{a}$ to give the below the equation respectively

$$\dot{H} + H^2 = -\frac{4\pi}{3}G(t)(2p + \rho) + \frac{\Lambda(t)}{6}, \tag{12}$$

$$H^2 = \frac{4\pi}{3}G(t)\rho + \frac{\Lambda(t)}{6} - \frac{K}{a^2}. \tag{13}$$

In order to solve the above field equations (9), (12) and (13) we used the bouncing scale factor as suggested by[41, 42, 50]

$$a(t) = R_0(1 + \alpha^2 t^2)^n, \tag{14}$$

where α , n and R_0 are positive constants.

The equation of state is

$$p = (\gamma - 1)\rho, \tag{15}$$

where γ is a constant ($1 \leq \gamma \leq 2$).

Using equations (14) and (15), equation (9) yields

$$\rho = \frac{C_1}{\{R_0(1 + \alpha^2 t^2)^n\}^{4\gamma}} \tag{16}$$

where C_1 is a arbitrary constant.

From eqn (15) and (16), the pressure is

$$p = \frac{(\gamma - 1)C_1}{\{R_0(1 + \alpha^2 t^2)^n\}^{4\gamma}} \tag{17}$$

From eqn (14), Hubble Paramater is

$$H = \frac{2n\alpha^2 t}{1 + \alpha^2 t^2}. \tag{18}$$

From eqn (12) and (13), we get

$$\dot{H} = -\frac{8\pi}{3}G(t)\rho\gamma + \frac{K}{a^2}. \tag{19}$$

Using eqns (14), (16) and eqn (18), eqn. (19) becomes

$$G(t) = \frac{3R_0^{4\gamma}(1 + \alpha^2 t^2)^{4n\gamma}}{8\pi\gamma C_1} \left[\frac{K}{R_0^2(1 + \alpha^2 t^2)^{2n}} - \frac{2\alpha^2 n(1 - \alpha^2 t^2)}{(1 + \alpha^2 t^2)^2} \right] \tag{20}$$

Using eqns. (14), (16), (18) and (20) eqn. (13) becomes

$$\Lambda(t) = \frac{3}{\gamma} \left[\frac{2\alpha^2 n(1 + \alpha^2(4\gamma n - 1)t^2)}{(1 + \alpha^2 t^2)^2} + \frac{(2\gamma - 1)K}{R_0(1 + \alpha^2 t^2)^{2n}} \right] \tag{21}$$

The deceleration parameter becomes

$$q = \frac{-1 + \alpha^2 t^2(1 - 2n)}{2\alpha^2 n t^2}. \tag{22}$$

Now we can prove to study for the different values of curvature parameters K and γ as under

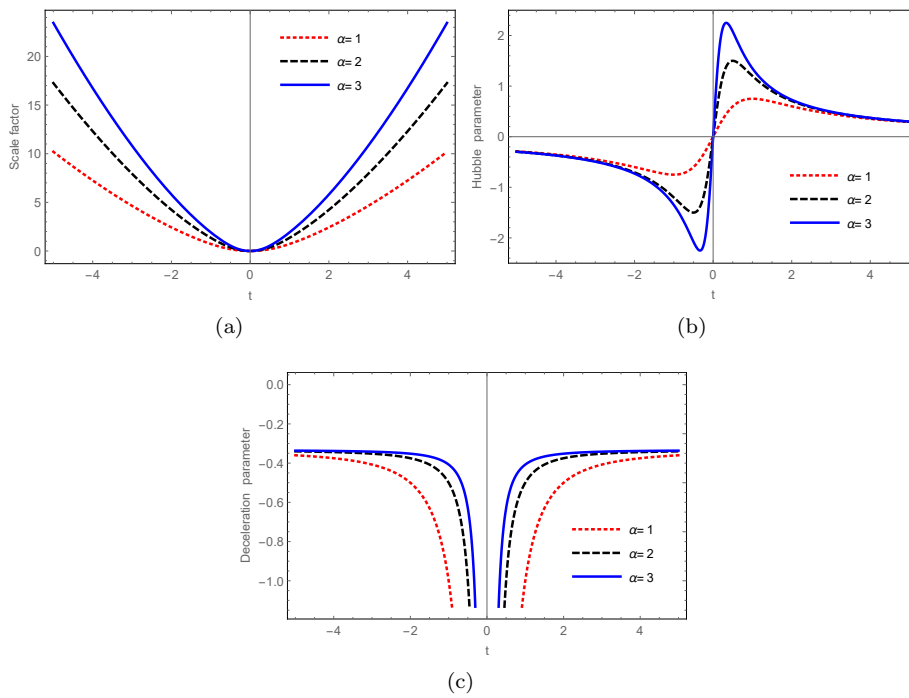


Figure 1. Behaviour of Scale factor $a(t)$, Hubble parameter $H(t)$ and Declaration parameter $q(t)$ against t for different values of α , $R_0 = 1$ and $n = \frac{3}{4}$.

2.1. When $K = 0$ (flat) and taking $\gamma = 1$ (Dust universe), we get

$$\begin{aligned} \rho &= \frac{C_1}{R_0^4(1 + \alpha^2 t^2)^{4n}}, \\ p &= 0 \\ G(t) &= \frac{3\alpha^2 n R_0^4}{4C_1 \pi} \cdot (-1 + \alpha^2 t^2)(1 + \alpha^2 t^2)^{-2+4n}, \\ \Lambda(t) &= \frac{1}{(1 + \alpha^2 t^2)^2} 6\alpha^2 n(1 + (-1 + 4n)\alpha^2 t^2). \end{aligned}$$

2.2. When $K = 0$ (flat) and taking $\gamma = \frac{4}{3}$ (Radiation universe)

$$\begin{aligned} \rho &= \frac{C_1}{R_0^{\frac{4}{3}}(1 + \alpha^2 t^2)^{\frac{16n}{3}}}, \\ p &= -\frac{2C_1}{3R_0^{\frac{4}{3}}(1 + \alpha^2 t^2)^{\frac{16n}{3}}}, \\ G(t) &= \frac{9\alpha^2 n(\alpha^2 t^2 - 1)(R_0(1 + \alpha^2 t^2)^n)^{\frac{16}{3}}}{16\pi C_1(1 + \alpha^2 t^2)^2}, \\ \Lambda(t) &= \frac{9\alpha^2 n}{2(1 + \alpha^2 t^2)^2} \left(1 + \left(-1 + \frac{16n}{3} \right) \alpha^2 t^2 \right). \end{aligned}$$

2.3. When $K = 0$ (flat) and taking $\gamma = 2$ (Zel'dovich universe)

$$\rho = \frac{C_1}{R_0^8(1 + \alpha^2 t^2)^{8n}},$$

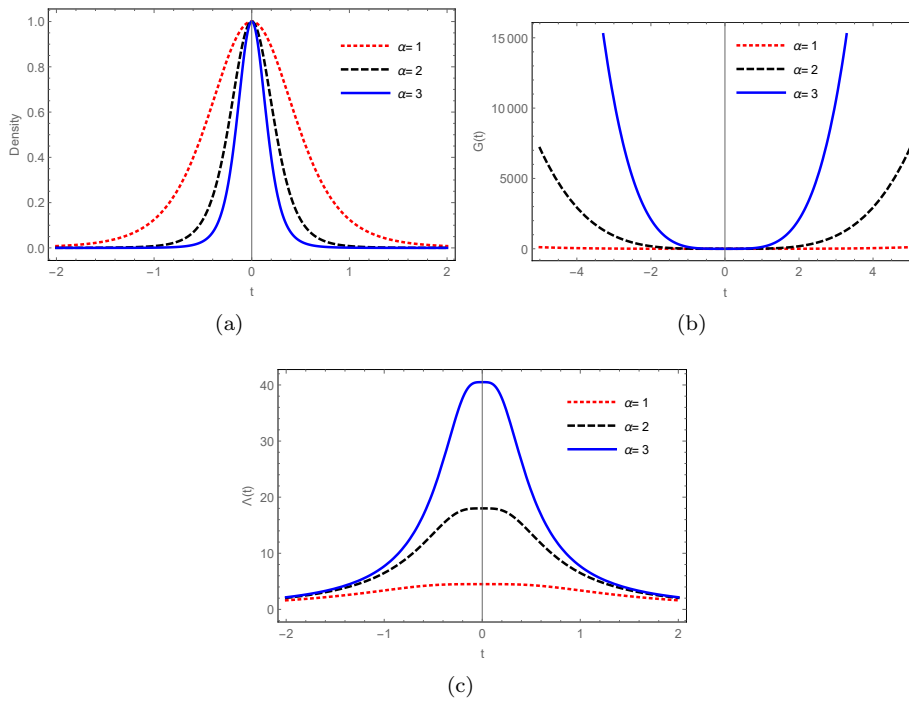


Figure 2. Plot (a) corresponds to the evolution of $\rho(t)$ against t , plot (b) corresponds to the behaviour of $G(t)$ against t , whereas plot (c) corresponds to the evolution of $\Lambda(t)$ against t for different values of α , $C_1 = R_0 = 1$ and $n = \frac{3}{4}$.

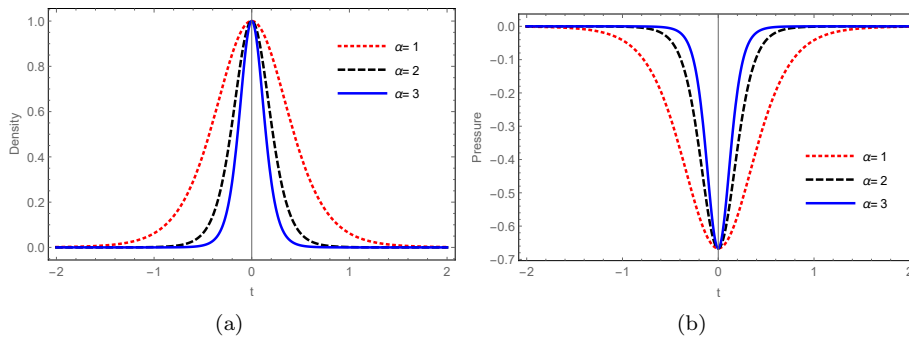


Figure 3. Plot (a) corresponds to the evolution of $\rho(t)$ against t whereas plot (b) corresponds to the behaviour of $p(t)$ against t for different values of α , $C_1 = R_0 = 1$ and $n = \frac{3}{4}$.

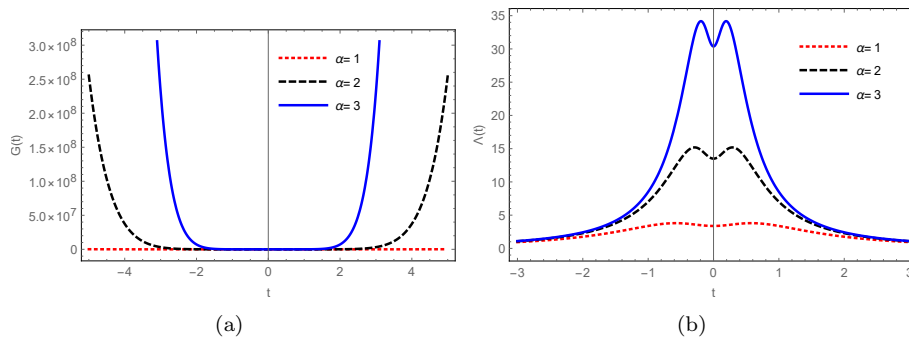


Figure 4. Plot (a) depicts to the behaviour of $G(t)$ against t , whereas plot (b) depicts to the evolution of $\Lambda(t)$ against t for different values of α , $C_1 = R_0 = 1$ and $n = \frac{3}{4}$.

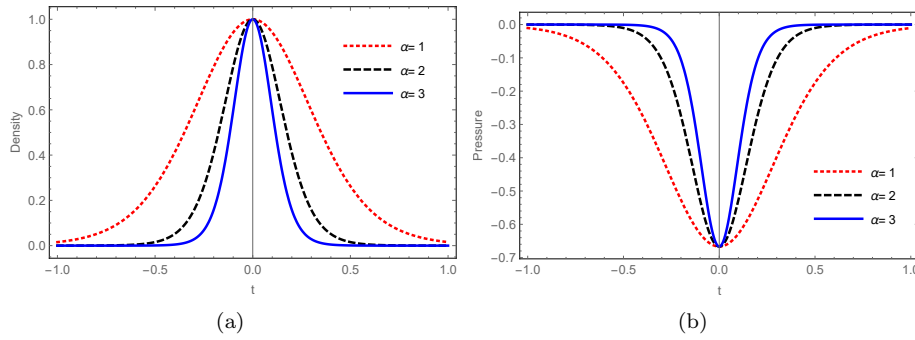


Figure 5. Plot (a) corresponds to the evolution of $\rho(t)$ against t and plot (b) corresponds to the behaviour of $p(t)$ against t for different values of α , $C_1 = R_0 = 1$ and $n = \frac{3}{4}$.

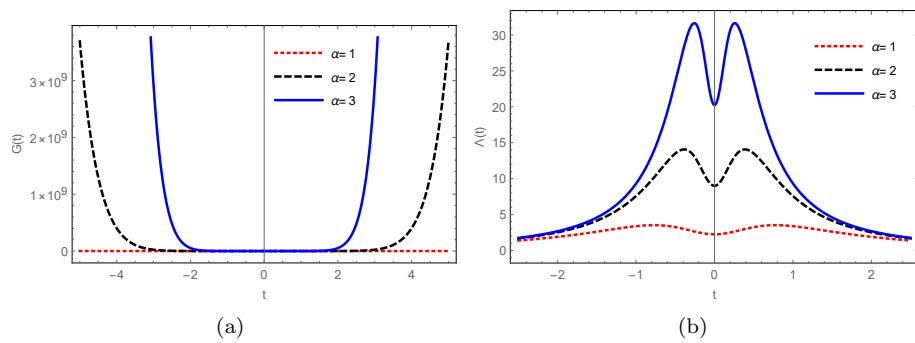


Figure 6. Plot (a) depicts to the behaviour of $G(t)$ versus t , whereas plot (b) depicts to the evolution of $\Lambda(t)$ versus t for different values of α , $C_1 = R_0 = 1$ and $n = \frac{3}{4}$.

$$p = \frac{C_1}{R_0^8(1 + \alpha^2 t^2)^{8n}},$$

$$G(t) = \frac{3\alpha^2 n R_0^8 (\alpha^2 t^2 - 1)(1 + \alpha^2 t^2)^{-2+8n}}{8\pi C_1},$$

$$\Lambda(t) = \frac{3\alpha^2 n}{(1 + \alpha^2 t^2)^2} (1 + \alpha^2 (-1 + 8n)\alpha^2 t^2).$$

2.4. When $K = 1$ (closed) and taking $\gamma = 1$ (Dust universe)

$$\rho = \frac{C_1}{R_0^4(1 + \alpha^2 t^2)^{4n}},$$

$$p = 0$$

$$G(t) = \frac{3R_0^4(1 + \alpha^2 t^2)^{4n}}{8\pi C_1} \left[\frac{1}{R_0(1 + \alpha^2 t^2)^{2n}} - \frac{2\alpha^2 n(1 - \alpha^2 t^2)}{(1 + \alpha^2 t^2)^2} \right]$$

$$\Lambda(t) = \frac{3}{R_0^2(1 + \alpha^2 t^2)^{2n}} + \frac{6\alpha^2 n(1 + (-1 + 4n)\alpha^2 t^2)}{(1 + \alpha^2 t^2)^2}.$$

2.5. When $K = 1$ (closed) and taking $\gamma = \frac{4}{3}$ (Radiation universe)

$$\rho = \frac{C_1}{R_0^{\frac{4}{3}}(1 + \alpha^2 t^2)^{\frac{16n}{3}}},$$

$$p = -\frac{2C_1}{3R_0^{\frac{4}{3}}(1 + \alpha^2 t^2)^{\frac{16n}{3}}},$$

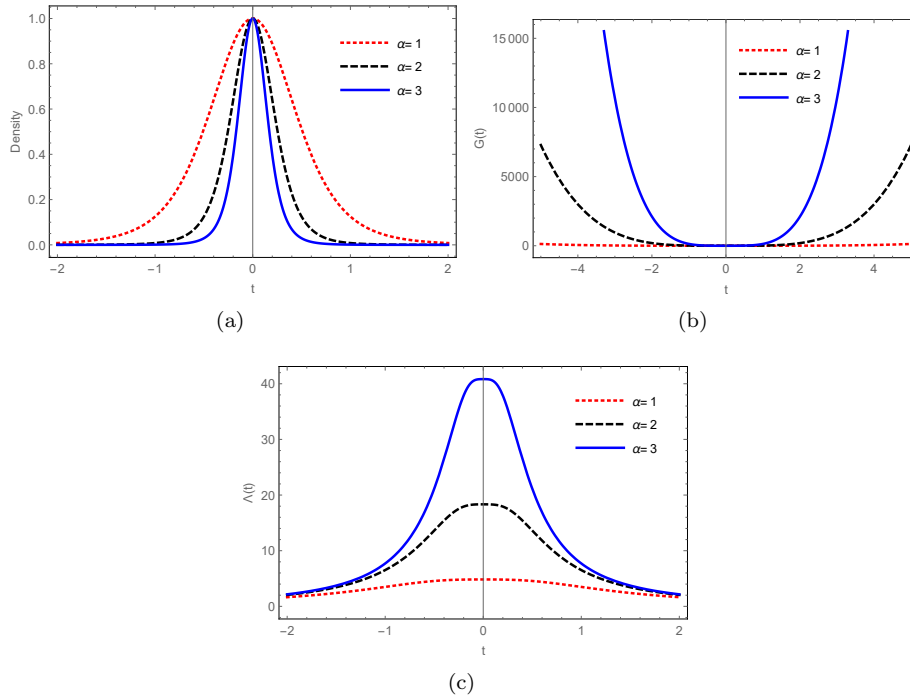


Figure 7. Plot (a) corresponds to the evolution of $\rho(t)$ versus t , (b) depicts to the behaviour of $G(t)$ against t , whereas plot (c) depicts to the evolution of $\Lambda(t)$ against t for different values of α , $C_1 = R_0 = 1$ and $n = \frac{3}{4}$.

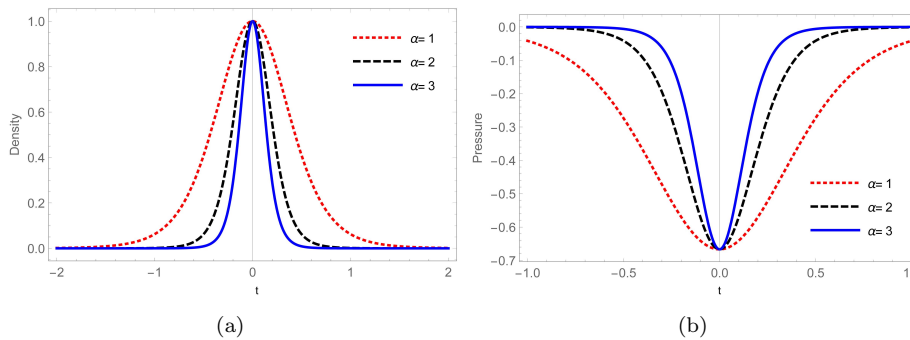


Figure 8. Plot (a) depicts to the behaviour of $\rho(t)$ against t , whereas plot (b) depicts to the evolution of $p(t)$ against t for different values of α , $C_1 = R_0 = 1$ and $n = \frac{3}{4}$.

$$G(t) = \frac{R_0^3(1 + \alpha^2 t^2)^{3n}}{2\pi C_1} \left[\frac{1}{R_0^2(1 + \alpha^2 t^2)^{2n}} - \frac{2\alpha^2 n(1 - \alpha^2 t^2)}{(1 + \alpha^2 t^2)^2} \right]$$

$$\Lambda(t) = \frac{2}{R_0^2(1 + \alpha^2 t^2)^{2n}} + \frac{8\alpha^2 n(1 + (-1 + 3n)\alpha^2 t^2)}{(1 + \alpha^2 t^2)^2}.$$

2.6. When $K = 1$ (closed) and taking $\gamma = 2$ (Zel'dovich universe)

$$\rho = \frac{C_1}{R_0^8(1 + \alpha^2 t^2)^{8n}},$$

$$p = \frac{C_1}{R_0^8(1 + \alpha^2 t^2)^{8n}},$$

$$G(t) = \frac{3R_0^8(1 + \alpha^2 t^2)^{8n}}{16\pi C_1} \left[\frac{1}{R_0^2(1 + \alpha^2 t^2)^{2n}} - \frac{2\alpha^2 n(1 - \alpha^2 t^2)}{(1 + \alpha^2 t^2)^2} \right]$$

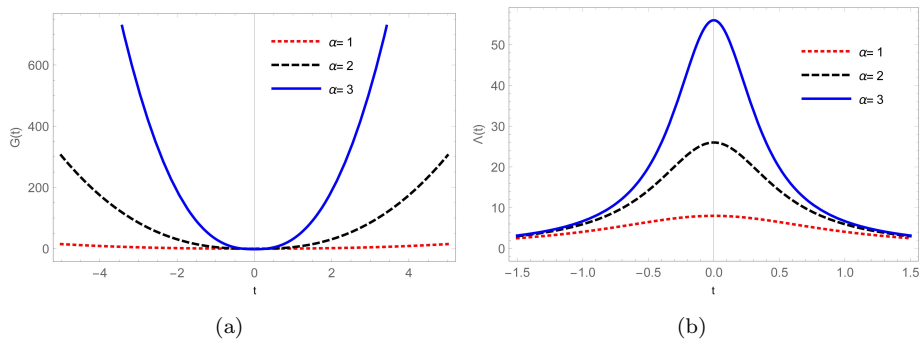


Figure 9. Plot (a) depicts to the behaviour of $G(t)$ versus t , whereas plot (b) depicts to the evolution of $\Lambda(t)$ versus t for different values of α , $C_1 = R_0 = 1$ and $n = \frac{3}{4}$.

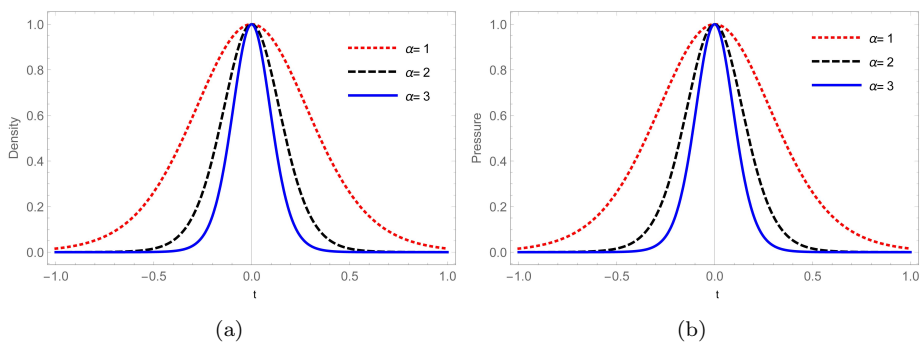


Figure 10. Plot (a) depicts to the behaviour of $\rho(t)$ against t , whereas plot (b) depicts to the evolution of $p(t)$ against t for different values of α , $C_1 = R_0 = 1$ and $n = \frac{3}{4}$.

$$\Lambda(t) = \frac{9}{2R_0^2(1 + \alpha^2 t^2)^{2n}} + \frac{3\alpha^2 n(1 + (-1 + 8n)\alpha^2 t^2)}{(1 + \alpha^2 t^2)^2}.$$

2.7. When $K = -1$ (open) and taking $\gamma = 1$ (Dust universe)

$$\rho = \frac{C_1}{R_0^4(1 + \alpha^2 t^2)^{4n}},$$

$$p = 0,$$

$$G(t) = \frac{3R_0^4(1 + \alpha^2 t^2)^{4n}}{8\pi C_1} \left[-\frac{1}{R_0^2(1 + \alpha^2 t^2)^{2n}} - \frac{2\alpha^2 n(1 - \alpha^2 t^2)}{(1 + \alpha^2 t^2)^2} \right]$$

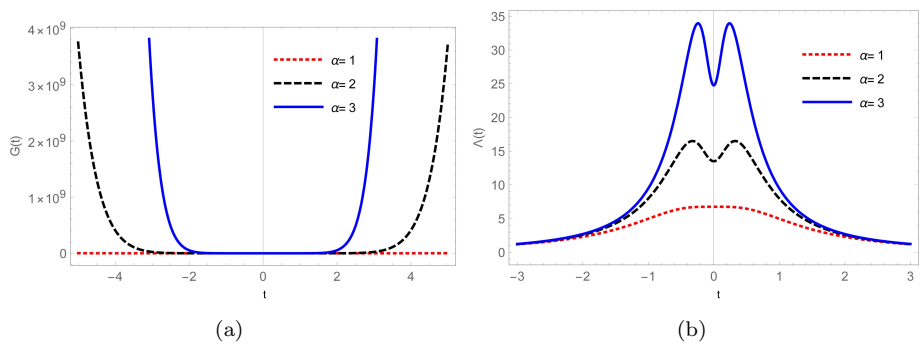


Figure 11. Plot (a) depicts to the behaviour of $G(t)$ against t , whereas plot (b) depicts to the evolution of $\Lambda(t)$ against t for different values of α , $C_1 = R_0 = 1$ and $n = \frac{3}{4}$.

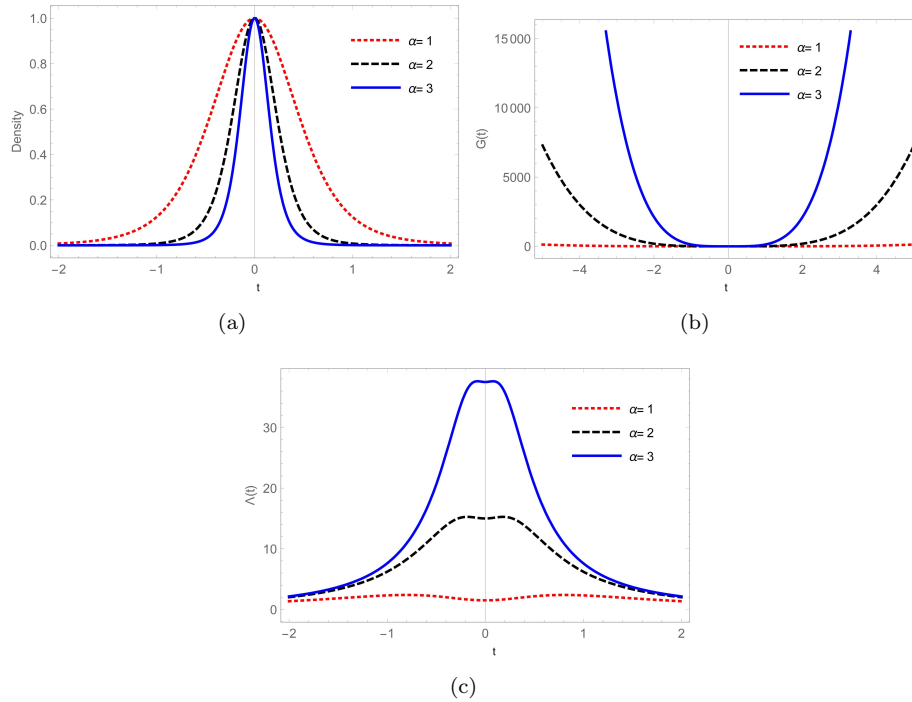


Figure 12. Plot (a) corresponds to the evolution of $\rho(t)$ versus t , plot (b) depicts to the behaviour of $G(t)$ against t , whereas plot (c) depicts to the evolution of $\Lambda(t)$ against t for different values of α , $C_1 = R_0 = 1$ and $n = \frac{3}{4}$.

$$\Lambda(t) = -\frac{3}{R_0^2(1 + \alpha^2 t^2)^{2n}} + \frac{6\alpha^2 n(1 + (-1 + 4n)\alpha^2 t^2)}{(1 + \alpha^2 t^2)^2}.$$

2.8. When $K = -1$ (open) and taking $\gamma = \frac{4}{3}$ (Radiation universe)

$$\begin{aligned} \rho &= \frac{C_1}{R_0^{\frac{4}{3}}(1 + \alpha^2 t^2)^{\frac{16n}{3}}}, \\ p &= -\frac{2C_1}{3R_0^{\frac{4}{3}}(1 + \alpha^2 t^2)^{\frac{16n}{3}}}, \\ G(t) &= \frac{9R_0^{\frac{16}{3}}(1 + \alpha^2 t^2)^{\frac{16n}{3}}}{32\pi C_1} \left[-\frac{1}{R_0^2(1 + \alpha^2 t^2)^{2n}} - \frac{2\alpha^2 n(1 - \alpha^2 t^2)}{(1 + \alpha^2 t^2)^2} \right] \\ \Lambda(t) &= \frac{3}{4} \left[-\frac{5}{R_0^2(1 + \alpha^2 t^2)^{2n}} + \frac{2\alpha^2 n(3 + (-3 + 16n)\alpha^2 t^2)}{(1 + \alpha^2 t^2)^2} \right]. \end{aligned}$$

2.9. When $K = -1$ (open) and taking $\gamma = 2$ (Zel'dovich universe)

$$\begin{aligned} \rho &= \frac{C_1}{R_0^8(1 + \alpha^2 t^2)^{8n}}, \\ p &= \frac{C_1}{R_0^8(1 + \alpha^2 t^2)^{8n}}, \\ G(t) &= \frac{3R_0^8 n \alpha^2 (-1 + \alpha^2 t^2)(1 + \alpha^2 t^2)^{-2+8n}}{8\pi C_1} - \frac{3R_0^6(1 + \alpha^2 t^2)^{6n}}{16\pi C_1} \\ \Lambda(t) &= \frac{3n\alpha^2(1 + (-1 + 8n)\alpha^2 t^2)}{(1 + \alpha^2 t^2)^2} - \frac{9}{2R_0^2(1 + \alpha^2 t^2)^{2n}}. \end{aligned}$$

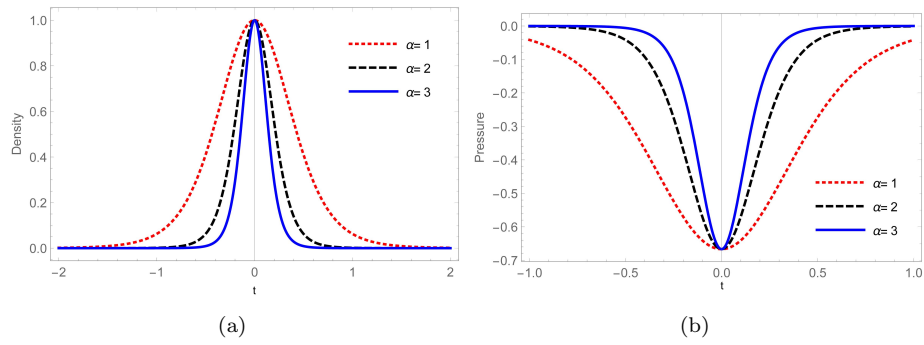


Figure 13. Plot (a) corresponds to the evolution of $\rho(t)$ versus t , plot (b) corresponds to the evolution of $p(t)$ against t for different values of α , $C_1 = R_0 = 1$ and $n = \frac{3}{4}$.

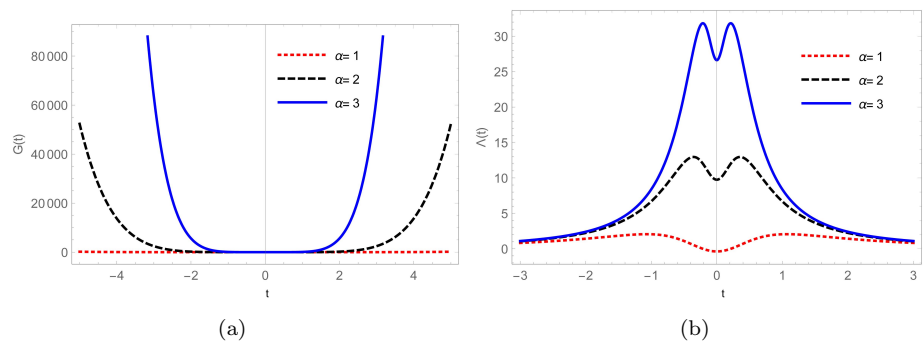


Figure 14. Plot (a) depicts to the behaviour of $G(t)$ against t , whereas plot (b) depicts to the evolution of $\Lambda(t)$ against t for different values of α , $C_1 = R_0 = 1$ and $n = \frac{3}{4}$.

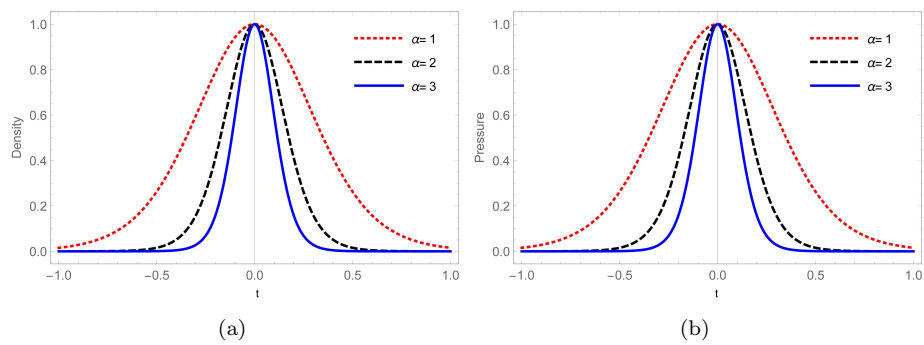


Figure 15. Plot (a) corresponds to the evolution of $\rho(t)$ versus t , plot (b) depicts to the evolution of $p(t)$ against t for different values of α , $C_1 = R_0 = 1$ and $n = \frac{3}{4}$.

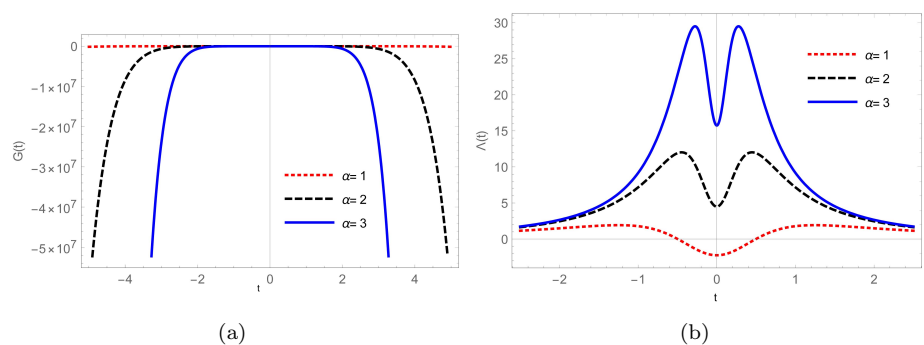


Figure 16. Plot (a) depicts to the behaviour of $G(t)$ against t , whereas plot (b) depicts to the behaviour of $\Lambda(t)$ against t for different values of α , $C_1 = R_0 = 1$ and $n = \frac{3}{4}$.

3. BEHAVIOUR OF BOUNCING COSMOLOGY

We will discuss matter bounce scenarios in FRW model in the present analysis. The study focuses on the dynamic of energy density ρ , pressure p , and the EoS parameter ω . In general, bouncing models meet the following conditions.

Bouncing models go through a contracting phase before bouncing, resulting in non-singular bounces i.e., the expansion of universe $a(t)$ decreases with time as $\dot{a}(t) < 0$. Thus, Hubble parameter $H = \frac{\dot{a}}{a} < 0$ represents contracting era of universe. As a result, Hubble parameter $H = 0$ disappears at bouncing point. EoS ω and deceleration parameter q are identical for homogeneous and flat FRW. The bounce point shows singular behaviour for both expressions.

Whenever $a(t)$ increases with increase in cosmic time t , this implies $\dot{a}(t) > 0$, which implies $H > 0$. When accelerating near the bouncing point ($\dot{H} > 0$), we can predict that the derivative of H will be positive. When an EoS parameter is bouncing, it evolves in phantom form. Different values of α , $R_0 = 1$ and $n = \frac{3}{4}$ can be used to measure the contribution of theory, while the bouncing parameter is used to measure the bouncing effects. We have also studied cosmological parameters, energy densities, pressures, cosmological parameters, and gravitational parameters in terms of cosmic time.

4. PHYSICAL INTERPRETATION

Fig 1(a) shows the behaviour of scale factor against cosmic time for different values of bouncing parameter α . Fig 1(b) of equation (18) shows the evolution of Hubble parameter, $H(t)$ becomes 0(zero) as $t \rightarrow 0$ and ∞ . Equation (22) suggests that the deceleration parameter versus time is plotted in Fig. 1(c), $q(t) \rightarrow -\infty$ at $t \rightarrow 0$ and q is negative quantities for sufficiently large values of t for different values of α , $R_0 = 1$ and $n = \frac{3}{4}$.

For different values of bouncing parameter, in the section 2.1 corresponds to fig.2 energy density becomes zero as t tends to infinity and at $t = 0$, $\rho = 1$ but for the flat universe the pressure is zero. The gravitational constant always increase when time increase whereas cosmological constant decreases when time increases and $G(t) \rightarrow 0$ when $t = 0$, but $\Lambda(t)$ is positive constant at $t = 0$. In fig. 3 and fig. 4 shows the dynamical behaviour of the section 2.2, energy density becomes zero as $t \rightarrow \infty$ and $\rho = 1$ when $t = 0$. The pressure is zero as $t \rightarrow \infty$ and $p = \frac{-2}{3}$ when $t = 0$. The gravitational constant always increase when time increase whereas cosmological constant decreases when time increases and $G(t) \rightarrow 0$ when $t = 0$, but $\Lambda(t)$ is positive constant at $t = 0$. In fig. 5 and fig. 6 shows the dynamical behaviour of the section 2.3, energy density becomes zero as $t \rightarrow \infty$ and $\rho = 1$ when $t = 0$. The pressure is zero as $t \rightarrow \infty$ and $p = \frac{-2}{3}$ when $t = 0$. The gravitational constant always increase when time increase whereas cosmological constant decreases when time increases and $G(t) \rightarrow 0$ when $t = 0$, but $\Lambda(t)$ is positive constant at $t = 0$.

For different values of α , $R_0 = 1$ and $n = \frac{3}{4}$, in the section 2.4 corresponds to fig.7 energy density becomes zero as t tends to infinity and at $t = 0$, $\rho = 1$ but for $K = 1$ (closed) and $\gamma = 1$ (Dust universe) the pressure is zero. The gravitational constant always increase when time increases whereas cosmological constant decreases when time increases and $G(t) \rightarrow 0$ when $t = 0$, but $\Lambda(t)$ is positive constant at $t = 0$. In fig. 8 and fig. 9 shows the dynamical behaviour of the section 2.5, energy density becomes zero as $t \rightarrow \infty$ and $\rho = 1$ when $t = 0$. The pressure is zero as $t \rightarrow \infty$ and $p = \frac{-2}{3}$ when $t = 0$. The gravitational constant always increases when time increases whereas cosmological constant also increases when time increases and $G(t) \rightarrow 0$ when $t = 0$, but $\Lambda(t)$ is positive constant at $t = 0$. In fig. 10 and fig. 11 shows the dynamical behaviour of the section 2.6, energy density becomes zero as $t \rightarrow \infty$ and $\rho = 1$ when $t = 0$. The pressure is also zero as $t \rightarrow \infty$ and $p = 1$ when $t = 0$. When time increases the gravitational constant always increases whereas cosmological constant decreases and $G(t) \rightarrow 0$ when $t = 0$, but $\Lambda(t)$ is positive constant at $t = 0$.

The graphical behaviour of cosmological parameter in the section 2.7 corresponds to fig.12 energy density becomes zero as $t \rightarrow \infty$ and $\rho = 1$ at $t = 0$ but for $K = -1$ (open) and $\gamma = 1$ (Dust universe) the pressure is zero. The gravitational constant always increase when time increase whereas cosmological constant decreases when time increases and $G(t) \rightarrow 0$ when $t = 0$, but $\Lambda(t)$ is constant at $t = 0$. In fig. 13 and fig. 14 shows the dynamical behaviour of the section 2.8, energy density becomes zero as $t \rightarrow \infty$ and $\rho = 1$ at $t = 0$. The pressure is zero as $t \rightarrow \infty$ and $p = \frac{-2}{3}$ at $t = 0$. The gravitational constant always increases when time increase whereas cosmological constant decreases when time increases and $G(t) \rightarrow 0$ when $t = 0$, but $\Lambda(t)$ is constant at $t = 0$. In fig. 15 and fig. 16 shows the dynamical evolution of the section 2.9, energy density becomes zero as $t \rightarrow \infty$ and $\rho = 1$ when $t = 0$. The pressure is zero as $t \rightarrow \infty$ and $p = 1$ when $t = 0$. The gravitational constant always increase when time increase whereas cosmological constant decreases when time increases and $G(t) \rightarrow 0$ when $t = 0$, but $\Lambda(t)$ is constant at $t = 0$.

5. CONCLUSION REMARKS

In the present contexts we attempt to reinterpret a mater bounce scenario with the framework of higher dimensional FRW model with variable G and Λ . Since now a days the study of bouncing cosmology becomes an interesting area to avoid the possible singularity occurring in the usual models under general theory of

relativity. Our proposed model can provide some useful scenario for the bouncing model. We have presented the different model for different stages of the universe by calculating the physical parameters of the models with the use of bouncing parameters. Analysing the Scale factor, Hubble parameter, deceleration parameter, energy density, pressure, gravitational and cosmological constant have been extensively investigated for different values of α , $R_0 = 1$ and $n = \frac{3}{4}$. In general, the behaviour near bounce is influenced by the bouncing parameter. It is emphasized by the bouncing scale factors that the cosmos undergoes a contraction, a bounce, and an accelerating phase at late times. The parameter H indicates the contracting phase ($H < 0$) before the bounce, and the expanding phase ($H > 0$) after the bounce at $t \approx 0$. In the decelerating phase of the universe, all deceleration parameter values are negative and indicate accelerated expansion.

In our model for different values of K and γ , all the behaviour of energy density increase before bounce and decrease after bounce but $\rho = 1$ at bouncing point $t = 0$. While the pressure profile is negative in the section 2.2, 2.3, 2.5 and 2.8, whereas $p = \frac{-2}{3}$ at bouncing point $t = 0$ which justifies the current cosmic expansion with dark energy. Although $p = 1$ at bouncing point $t = 0$, the pressure is positive in sections 2.6 and 2.9, also satisfied a contracting phase before the bounce and an expanding phase after the bounce. The choice of model parameters is strictly determined by the evolution of cosmological parameters and in particular, the conservation equation.

The constant G and Λ are allowed to depend on the cosmic time t . The gravitational constant G decreases before the bounce, and increases after the bounce and $G(t) = 0$ at $t = 0$ in all the sections 2.1 - 2.9. The cosmological term Λ increases before the bounce, and decreases after the bounce and $\Lambda(t) = constant$ at bouncing point $t = 0$ in all the sections 2.1 - 2.9. But in the case of $\alpha = 1$, of the section 2.7 - 2.9 cosmological term Λ is negative at bouncing point $t = 0$. In our research, we have found that the explosion of the universe at the early stages of its creation was only a consequence of the creation of matter. Thus, studying the early evolution of the universe requires understanding the implications of time varying Λ and G . And also we hope to shed some light on the real universe. In addition to providing insights into cosmological structure formation, this study could also provide insight into the formation of universe. Through this approach, higher dimensional space time allows the unified description of early evolution of the universe with variables G and Λ . Generally, the models are scalar expansion, non-shear, and isotropic. According to the above points, our proposed model provides good bouncing solutions with the parameters chosen.

6. CREDIT AUTHORSHIP CONTRIBUTION STATEMENT

Asem Jotin Meitei: Writing - original draft, Investigation, Data curation, Software, Visualization, review and editing. **Kangujam Priyokumar Singh:** Supervision, Resources, Methodology, Validation, Formal analysis. **Syed Sabanam:** Investigation, Data curation, Visualization and editing and **S. Kiranmala Devi:** Investigation, Data curation, Visualization, review and editing.

7. DECLARATION OF COMPETING INTEREST

There are no known competing financial interests or personal relationships that could have affected the authors' work reported in this paper.

8. DATA AVAILABILITY

In this published article, no data is available.

9. APPENDIX-I

The Einstein field equations with time dependent cosmological and gravitational terms is given by

$$R_{\mu\nu} - \frac{1}{2}g_{\mu\nu}R = 8\pi G(t)T_{\mu\nu} + \Lambda(t)g_{\mu\nu} \tag{23}$$

The Bianchi identities from eqn. (23) are given by

$$R^k_{\mu\nu i; j} + R^k_{\mu i j; \nu} + R^k_{\mu j \nu; i} = 0 \tag{24}$$

Apply antisymmetric property in the second term, we have

$$R^k_{\mu\nu i; j} - R^k_{\mu j i; \nu} + R^k_{\mu j \nu; i} = 0 \tag{25}$$

Contracting with respect to k and i , we get

$$R^k_{\mu\nu k; j} - R^k_{\mu j k; \nu} + R^k_{\mu j \nu; k} = 0 \tag{26}$$

But by the definition of Ricci tensor, we get

$$R^k_{\mu\nu k} = R_{\mu\nu} \text{ and } R^k_{\mu j k} = R_{\mu j}$$

From eqn. (26) gives

$$R_{\mu\nu;j} - R_{\mu j;\nu} + R_{\mu j\nu;k}^k = 0$$

Since derivatives of fundamental tensors are 0(zero), we can expressed the above equation as:

$$(g^{\mu j} R_{\mu\nu})_{;j} - (g^{\mu j} R_{\mu j})_{;\nu} + (g^{\mu j} R_{\mu\nu j}^k)_{;k} = 0$$

or

$$R_{\nu;j}^j - R_{;\nu} + R_{\nu;k}^k = 0$$

Changing the dummy indices j and k to μ , we obtain

$$R_{\nu;\mu}^\mu - R_{;\nu} + R_{\nu;\mu}^\mu = 0 \tag{27}$$

But

$$R_{;\nu} = \frac{\partial R}{\partial x^\nu} \frac{\delta}{\delta x^\mu} (\delta_\nu^\mu R) = (\delta_\nu^\mu R)_{;\mu}$$

Therefore eqn.(27) becomes

$$2R_{\nu;\mu}^\mu - (\delta_\nu^\mu R)_{;\mu} = 0$$

or

$$(R_\nu^\mu - \frac{1}{2}\delta_\nu^\mu R)_{;\mu} = 0$$

or

$$(R_{\mu\nu} - \frac{1}{2}g_{\mu\nu}R)^{;\mu} = 0$$

Hence eqn.(23) becomes

$$(8\pi G(t)T_{\mu\nu} + \Lambda(t)g_{\mu\nu})^{;\mu} = 0$$

10. APPENDIX-II

We have,

$$T_{\mu\nu} = (\rho + p)u_\mu u_\nu - p\delta_{\mu\nu}$$

Differentiation both side w.r.t. ν , we have

$$0 = [(\rho + p)u_\mu u_\nu - p\delta_{\mu\nu}]_{;\nu}$$

Multiplying both sides by u^μ , we have

$$\Rightarrow [(\rho + p)u_\mu u_\nu - p\delta_{\mu\nu}]_{;\nu} u^\mu = 0$$

$$\Rightarrow (\rho + p)_{;\nu} u_\mu u_\nu u^\mu + (\rho + p)(u_\mu u_\nu)_{;\nu} u^\mu - p_{;\nu} u^\mu = 0$$

$$\Rightarrow (\rho_{;\nu} + p_{;\nu})u_\nu + (\rho + p)(u_\nu)_{;\nu} - p_{;\nu} u^\mu = 0$$





$$\Rightarrow \rho_{;\nu} u_\nu + (\rho + p)[(u_\nu)_{;\nu} + u^\alpha \Gamma_{\alpha\nu,\nu}] = 0$$

$$\Rightarrow \dot{\rho} + 4(\rho + p)H = 0 \quad \because \Gamma_{12,2} = \Gamma_{13,3} = \Gamma_{14,4} = \Gamma_{15,5} = \frac{\dot{a}}{a} = H$$

Acknowledgments

Several desirable changes have been made to the manuscript as a result of the editor’s collaboration and the valuable suggestions of the referees. We would like to thank them for their time, effort, and expertise.

ORCID

 **Asem Jotin Meitei**, <https://orcid.org/0000-0003-3384-5264>;  **Kangujam Priyokumar Singh**, <https://orcid.org/0000-0002-8784-4091>;  **Syed Sabanam**, <https://orcid.org/0009-0002-3928-9924>;  **S. Kiranmala Chanu**, <https://orcid.org/0000-0001-9014-3811>

REFERENCES

- [1] S. Perlmutter, *et al.*, *Astrophys. J.* **483**, 565 (1997). <https://doi.org/10.1086/304265>
- [2] S. Perlmutter, *et al.*, *Nature*, **391**, 51 (1998). <https://doi.org/10.1038/34124>
- [3] A.G. Riess, *et al.*, *Astron. J.* **116**, 1009 (1998). <https://doi.org/10.1086/300499>
- [4] A. Balbi, *et al.*, *Astrophys. J.* **545**, L1 (2000). <https://doi.org/10.1086/317323>
- [5] D.N. Spergel, *et al.*, *Astrophys. J. Suppl.* **148**, 175 (2003). <https://doi.org/10.1086/377226>
- [6] D.N. Spergel, *et al.*, *Astrophys. J. Suppl.* **170**, 377 (2007). <https://doi.org/10.1086/513700>
- [7] S. Perlmutter, *et al.*, *Astrophys. J.* **517**, 565, astro-ph/9608192 (1999). <https://doi.org/10.1086/307221>
- [8] A.G. Riess, *PASP*, **112**, 1284 (2000). <https://doi.org/10.1086/316624>
- [9] P.M. Garnavich, *et al.*, *Astrophys. J.* **493**, L53, astro-ph/9710123 (1998). <https://doi.org/10.1086/311140>
- [10] P.M. Garnavich, *et al.*, *Astrophys. J.* **509**, 74, astro-ph/9806396 (1998). <https://doi.org/10.1086/306495>
- [11] B.P. Schmidt, *et al.*, *Astrophys. J.* **507**, 46, astro-ph/9805200 (1998). <https://doi.org/10.1086/306308>
- [12] P.G.O. Freund, *Nucl. Phys. B*, **209**, 146 (1982). [https://doi.org/10.1016/0550-3213\(82\)90106-7](https://doi.org/10.1016/0550-3213(82)90106-7)
- [13] D. Sahdev, *Phys. Lett. B*, **137**, 155 (1984). [https://doi.org/10.1016/0370-2693\(84\)90220-X](https://doi.org/10.1016/0370-2693(84)90220-X)
- [14] Q. Shafi, and C. Wetterich, *Phys. Lett. B*, **129**, 387 (1983). [https://doi.org/10.1016/0370-2693\(83\)90125-9](https://doi.org/10.1016/0370-2693(83)90125-9)
- [15] T. Kaluza, *Sitzungsber. Preuss. Akad. Wiss. Berlin, Phys. Math.* **K1**,, 966 (1921). <https://doi.org/10.48550/arXiv.1803.08616>
- [16] O. Klein, *Z. Phys.* **37**, 895 (1926). <http://dx.doi.org/10.1007/BF01397481>
- [17] H.C. Lee, *An Introduction to Kaluza-Klein Theories*, (World Scientific, Singapore, 1984).
- [18] T. Appelquist, A. Chodos, and P.G.O. Freund, *Modern Kaluza-Klein Theories*, (Addison-Wesley, Menlo Park, 1987).
- [19] F. Rahaman, S. Das, N. Begum, and M. Hossain, *Pramana J. Phys.* **61**, 153 (2003). <https://doi.org/10.1007/BF02704519>
- [20] G.C. Sanmanta, and S. Dedata, *J. Mod. Phys.* **3**, 180 (2012). <http://dx.doi.org/10.4236/jmp.2012.32024>
- [21] S. Chatterjee, *Astrophys. J.* **397**, 1 (1992). <https://adsabs.harvard.edu/full/1992ApJ...397...1C>
- [22] J.A. Frieman, and I. Waga, *Phys. Rev. D*, **57**, 4642 (1998). <https://doi.org/10.1103/PhysRevD.57.4642>
- [23] R. Carlberg, *et al.*, *Astrophys. J.* **462**, 32 (1996). <https://doi.org/10.1086/177125>
- [24] M. Özer, and M.O. Taha, *Nucl. Phys. B*, **287**, 776 (1987). [https://doi.org/10.1016/0550-3213\(87\)90128-3](https://doi.org/10.1016/0550-3213(87)90128-3)
- [25] K. Freese, *et al.*, *Nucl. Phys. B*, **287**, 797 (1987). [https://doi.org/10.1016/0550-3213\(87\)90129-5](https://doi.org/10.1016/0550-3213(87)90129-5)
- [26] J.C. Carvalho, *et al.*, *Phys. Rev. D*, **46**, 2404 (1992). <https://doi.org/10.1103/PhysRevD.46.2404>
- [27] V. Silverira, and L. Waga, *Phys. Rev. D*, **50**, 4890 (1994). <https://doi.org/10.1103/PhysRevD.50.4890>
- [28] B. Ratra, and P.J.E. Peebles, *Phys. Rev. D*, **37**, 3406 (1988). <https://doi.org/10.1103/PhysRevD.37.3406>
- [29] A.D. Dolgov, *The Very Early universe*, edited by G.W. Gibbons, S.W. Hawking, and S.T.C. Siklos, (Cambridge University Press, Cambridge, 1983).
- [30] A.D. Dolgov, M.V. Sazhin, and Y.B. Zeldovich, (Basics of Modern Cosmology, Editions Frontiers, Gif-sur-Yvette, 1990).
- [31] A.D. Dolgov, *Phys. Rev. D*, **55**, 5881 (1997). <https://doi.org/10.1103/PhysRevD.55.5881>
- [32] V. Sahni, and A. Starobinsky, *Int. J. Mod. Phys. D*, **09**(04), 373, astro-ph/9904398 (2000). <https://doi.org/10.1142/S0218271800000542>
- [33] T. Padmanabhan, *Phys. Rep.* **380**, 235, hep-th/0212290 (2003). [https://doi.org/10.1016/S0370-1573\(03\)00120-0](https://doi.org/10.1016/S0370-1573(03)00120-0)
- [34] P.J.E. Peebles, *Rev. Mod. Phys.* **75**, 599 astro-ph/0207347 (2003). <https://doi.org/10.1103/RevModPhys.75.559>
- [35] Y.B. Zeldovich, *Sov. Phys. Usp.* **11**, 381 (1968).
- [36] S. Weinberg, *Rev. Mod. Phys.* **61**, 1 (1989). <https://doi.org/10.1103/RevModPhys.61.1>
- [37] S.M. Carrol, *et al.*, *Ann. Rev. Astron. Astrophys.* **30**, 499 (1992). <https://doi.org/10.1146/annurev.aa.30.090192.002435>
- [38] G.S. Khadekar, *et al.*, *Asrtophys. Space Sci.* **310**, 141 (2007). <https://doi.org/10.1007/s10509-007-9489-5>
- [39] K.S. Adhav, *et al.*, *Bulg. J. Phys.* **34**, 260 (2007). https://www.bjp-bg.com/papers/bjp2007_4_260-272.pdf
- [40] U. Mukhopadhyay, *et al.*, *Int. J. Theor. Phys.* **50**, 752 (2011). <https://doi.org/10.1007/s10773-010-0611-z>
- [41] K.B. Vinod, and D. Archana, *Int. J. Geom. Methods Mod. Phys.* **17**, 2050203 (2020). <https://doi.org/10.1142/S0219887820502035>
- [42] H. Shabani, and A.H. Ziaie, *Eur. Phys. J. C.* **78**, 397 (2018). <https://doi.org/10.1140/epjc/s10052-018-5886-x>

- [43] G. Minas, *et al.*, Universe, **5**, 74 (2019). <https://doi.org/10.3390/universe5030074>
- [44] S.S. Singh, and S.K. Chanu, Brazilian Journal of Physics, **51**, 1364 (2021). <https://doi.org/10.1007/s13538-021-00955-y>
- [45] C.R. Mahanta, and M.P. Das, Adv. Math. Sci. Journal. **10**, 1691 (2021). <https://doi.org/10.37418/amsj.10.3.51>
- [46] A.S. Agrawal, *et al.*, Fortschr. Phys. **70**, 2100065 (2022). <https://doi.org/10.1002/prop.202100065>
- [47] A.S. Agrawal, *et al.*, Phys. Scr. **97**, 025002 (2022). [10.1088/1402-4896/ac49b2](https://doi.org/10.1088/1402-4896/ac49b2)
- [48] A.S. Agrawal, *et al.*, Eur. Phys. J. C, **83**, 113 (2023). <https://doi.org/10.1140/epjc/s10052-023-11266-8>
- [49] J.K. Singh, *et al.*, JHEP, **03**, 191 (2023). [https://doi.org/10.1007/JHEP03\(2023\)191](https://doi.org/10.1007/JHEP03(2023)191)
- [50] M. Zubair, and M. Farooq, Eur. Phys. J. C. **138**, 173 (2023). <https://doi.org/10.1140/epjp/s13360-023-03772-1>
- [51] M. Sharif, and F. Khanum, Gen. Relativ. Gravit. **43**, 2885 (2011). <https://doi.org/10.1007/s10714-011-1211-9>
- [52] D.R.K. Reddy, and G. Ramesh, Prespacetime Journal, **10**, 301 (2019). <https://www.prespacetime.com/index.php/pst/article/view/1633/1559>
- [53] R.L. Naidu, *et al.*, New Astronomy, **85**, 101564 (2021). <https://doi.org/10.1016/j.newast.2020.101564>

**ПЕРЕІНТЕРПРЕТАЦІЯ ВСЕСВІТУ ФРІДМАНА-РОБЕРТСОНА-ВОКЕРА
ЗІ ЗМІННИМ ГРАВІТАЦІЙНИМ ТА КОСМОЛОГІЧНИМ ЧЛЕНОМ
У КОСМОЛОГІЇ З ВІДСКОКОМ**

Асем Джотін Мейтей^а, Кангуджам Прійокумар Сінгх^а, Саед Сабанам^а, С. Кіранмала Чану^б




^а Факультет математики, Маніпурський університет, Канчіпур, Імфал, 795003, Маніпур, Індія

^б Факультет математики, коледж Мазараджа Бодхчандра, Імфал, Маніпур-795001, Індія

Ця стаття присвячена дослідженню п'ятивимірної однорідної та ізотропної моделі FRW зі зміною гравітаційної та космологічної постійної з космічним часом. Точний розв'язок рівнянь поля Ейнштейна отримується за допомогою рівняння стану $p = (\gamma - 1)\rho$ (гамма-закон), де γ , який є адиабатичним параметром, безперервно змінюється в міру розширення Всесвіту. Ми отримали рішення для різних значень кривизни $K = 0, 1, -1$, використовуючи $a(t) = R_0(1 + \alpha^2 t^2)^n$, де α , n і R_0 — додатні константи. Поведінка космологічних параметрів представлена для різних випадків моделей. Детально представлена фізична інтерпретація отриманої моделі. Цікаво, що запропонована модель виправдовує поточні космологічні спостереження темної енергії.

Ключові слова: *п'ятивимірний; FRW метрика; космологічний термін; масштабний коефіцієнт відскоку*

COSMIC ASPECTS OF SHARMA-MITTAL HOLOGRAPHIC DARK ENERGY MODEL IN BRANS-DICKE THEORY OF GRAVITY

 Y. Aditya^{a,*},  D. Tejeswararao^a,  U.Y. Divya Prasanthi^b

^aDepartment of Basic Science and Humanities, GMR Institute of Technology, Rajam-532127, India

^bDepartment of Statistics & Mathematics, College of Horticulture, Dr. Y.S.R. Horticultural University, Parvathipuram-535502, India

*Corresponding Author e-mail: aditya.y@gmrit.edu.in; yaditya2@gmail.com

Received January 1, 2024; revised January 25, 2024; accepted February 4, 2024

We investigate the cosmological scenario involving spatially homogeneous and anisotropic Bianchi type- VI_0 space-time in the context of the Sharma-Mittal holographic dark energy model within the framework of Brans-Dicke's theory of gravitation. In order to achieve this objective, the Hubble, deceleration, equation-of-state parameters have been discussed. The deceleration parameter (q) is used to measure the pace at which the expansion of the universe is accelerating. The equation-of-state parameter (ω_{smhde}) characterizes the quintessence and vacuum areas of the universe. All the parameters demonstrate consistent behaviour following the Planck 2018 data. We assess the dynamical stability by defining the squared speed of sound and examining its behaviour. In addition, the energy conditions and the variation of ω_{smhde} and ω'_{smhde} in the model indicate the present accelerating expansion of the universe.

Keywords: *Bianchi type- VI_0 model; Dark energy model; Brans-Dicke theory of gravity; Cosmology; Sharma-Mittal holographic dark energy*

PACS: 98.80.-k, 95.36.+x

1. INTRODUCTION

The phenomenon of accelerated expansion of the universe has been thoroughly demonstrated by several observations [1]-[3]. Studies imply that the universe is spatially flat and consists of two main components: dark energy (DE) with negative pressure, dust matter composed of cold dark matter (CDM) and baryons. To understand the nature of DE, it is necessary to determine whether it arises from a cosmological constant (Λ) or a dynamical model. The dynamical DE models may be distinguished from the cosmological constant by using the equation of state (EoS) parameter $\omega_{DE} = \frac{p_{DE}}{\rho_{DE}}$, where p_{DE} represents the pressure and ρ_{DE} represents the energy density of DE. Multiple possibilities for differential evolution have been suggested (Copeland et al. [4]). The data analysis of SNeIa demonstrates that these dynamical models are more consistent with the current understanding of the universe compared to Λ . An alternative approach involves altering the geometric component of the Einstein-Hilbert action, which is referred to as modified theories of gravity, to analyze the expansion phenomena. For a comprehensive examination of DE and modified theories of gravity, please refer to the sources cited as [5]-[7]. The developments in the exploration of black hole theory and string theory have led to the formulation of the holographic principle. This principle suggests that the number of possible configurations of a physical system should be limited as well as that this limitation should be determined by the system's surface area rather than its volume. Additionally, the holographic principle suggests that there should be a restriction on the system's lowest energy state.

The holographic DE (HDE) is a very intriguing dynamical concept that is founded upon the holographic principle. The validity of HDE has been evaluated and verified by many astronomical methodologies, including using the anthropic principle (Huang and Li [8]). Incorporating the holographic principle into cosmology allows for determining the maximum amount of entropy present in the universe. Li [9] put the following limit on the DE density, as stated by Cohen et al. [10]

$$\rho_{DE} = 3d^2 m_p^2 L^{-2}. \quad (1)$$

the symbol m_p represents the decreased Planck mass, $3d^2$ indicates a numerical constant, and L represents the IR-cutoff. Several types of IR-cutoff have been investigated in academic studies, including the Hubble horizon H^{-1} , event horizon, particle horizon, conformal universe age, Ricci scalar radius, and Granda-Oliveros cutoff [11]-[12]. The HDE models, using various infrared cutoffs, provide a modern understanding of the universe's acceleration. They additionally demonstrate that the transition redshift value, which marks the transfer from a previous deceleration phase ($q > 0$) to the current acceleration phase ($q < 0$), corresponds with contemporary

observable data. Nojiri and Odintsov [13] proposed a technique to merge the initial and final phases of the universe by using generalized HDE and phantom cosmology. They have now expanded this notion to what they refer to as HInflation [14]. Various formulations of entropy have been used in recent decades to construct and analyze cosmological models. Multiple innovative models of HDE have been developed, such as the Tsallis HDE [15, 16], the Sharma-Mittal HDE (SMHDE) [17], and the Renyi HDE model [18]. Numerous researchers have evaluated different cosmological models of new HDE models [19]- [30]. Jawad and Sultan [31], Sharma [32], and Drepanou et al. [33] have investigated SMHDE models within different gravitational theories. The researchers Sadeghi et al. [34] examined the dynamic formations of HDE within the framework of Brans-Dicke’s theory of gravity, using the Tsallis and Kaniadakis methodologies.

In the last few decades, universes that are both spatially homogeneous and anisotropic have attracted a lot of attention from theoretical cosmologists. According to Akarsu and Kilinc [35], the main empirical data from CMBR (Bennett et al. [36]) supports the idea that the universe is transitioning from a non-uniform to a uniform phase. Moreover, it is believed that the isotropic FRW model may not provide a complete and correct picture of matter in the early universe. It is essential to take into account anisotropic space-times to objectively evaluate cosmological models for their ability to attain the observed degree of homogeneity and isotropy. Because of its anisotropic character, researchers have given a lot of attention to homogeneous but not necessarily isotropic Bianchi type (BT) cosmological models. In the framework of anisotropic Bianchi type space-times, several renowned researchers have recently proposed fascinating cosmological models that include DE. several researchers (Ref. [37]-[49]) have looked at anisotropic cosmological models in various scenarios.

In this work, we take into account the BT- VI_0 universe filled with matter and SMHDE within the framework of Brans-Dicke’s theory of gravitation, motivated by the previously mentioned findings and discussion. This paper’s work is organized in the following way: Section-2 contains the BT- VI_0 metric and field equations of the model using anisotropic SMHDE fluid and matter. In addition, we constructed the SMHDE model and found the solutions to the field equations in section-3. Various cosmological parameters that constitute our model are presented in section-4. In the last section, we derive a few conclusions based on our results.

2. METRIC AND FIELD EQUATIONS

The Brans-Dicke [50] field equations in the presence of matter and DE are given by

$$R_{ij} - \frac{1}{2}Rg_{ij} = -8\pi\phi^{-1} (T_{ij} + \bar{T}_{ij}) - w\phi^{-2} \left(\phi_{,i}\phi_{,j} - \frac{1}{2}g_{ij}\phi_{,k}\phi^{,k} \right) - \phi^{-1} \left(\phi_{i;j} - g_{ij}\phi^{,k}_{;k} \right), \tag{2}$$

and

$$\phi^{,k}_{;k} = 8\pi (T + \bar{T}) (3 + 2w)^{-1}.$$

Also, the energy conservation equation is

$$\left(T^{ij} + \bar{T}^{ij} \right)_{;j} = 0. \tag{3}$$

The energy-momentum tensor for the matter and DE are respectively defined as

$$\bar{T}_{ij} = \rho_m u_i u_j, \quad T_{ij} = (\rho_{smhde} + p_{smhde})u_i u_j - p_{smhde}g_{ij}. \tag{4}$$

Here ρ_m, ρ_{smhde} are the energy densities of matter and the dark energy respectively. p_{smhde} is the pressure of the dark energy. In a comoving coordinate system, from equations (4), we get

$$T_1^1 = T_2^2 = T_3^3 = -p_{smhde}, T_4^4 = \rho_{smhde} \quad ; \quad \bar{T}_1^1 = \bar{T}_2^2 = \bar{T}_3^3 = 0, \bar{T}_4^4 = \rho_m \tag{5}$$

where ρ_m, ρ_{smhde} and p_{smhde} are the functions of cosmic time t only.

We consider the geometry of the universe as spatially homogeneous and anisotropic BT- VI_0 line element which can be written as

$$ds^2=dt^2 - A^2dx^2 - B^2e^{2x}dy^2 - C^2e^{-2x}dz^2, \tag{6}$$

where A, B and C are functions of cosmic time t only. The following are the some of physical parameters which are useful in finding the solution of field equations for the BT- VI_0 space-time given by Eq. (6). The average scale factor $a(t)$ and volume V of the BT- VI_0 space-time are defined as

$$V = [a(t)]^3 = ABC. \tag{7}$$

Anisotropic parameter A_h is given by

$$A_h = \frac{1}{3} \sum_{i=1}^3 \left(\frac{H_i - H}{H} \right)^2 \tag{8}$$

where $H_1 = \frac{\dot{A}}{A}$, $H_2 = \frac{\dot{B}}{B}$, $H_3 = \frac{\dot{C}}{C}$ are directional Hubble's parameters and $H = \frac{1}{3} \left(\frac{\dot{A}}{A} + \frac{\dot{B}}{B} + \frac{\dot{C}}{C} \right)$ is mean Hubble's parameter. Here and after an overhead dot denotes differentiation concerning cosmic time t . Expansion scalar (θ) and shear scalar (σ^2) are defined as

$$\theta = u_i^i = \frac{\dot{A}}{A} + \frac{\dot{B}}{B} + \frac{\dot{C}}{C} \quad (9)$$

$$\sigma^2 = \frac{1}{3} \left(\frac{\dot{A}^2}{A^2} + \frac{\dot{B}^2}{B^2} + \frac{\dot{C}^2}{C^2} - \frac{\dot{A}\dot{B}}{AB} - \frac{\dot{A}\dot{C}}{AC} - \frac{\dot{B}\dot{C}}{BC} \right) \quad (10)$$

where $u_i = (1, 0, 0, 0)$ is the four-velocity in the comoving coordinates. The deceleration parameter is given by

$$q = \frac{d}{dt} \left(\frac{1}{H} \right) - 1. \quad (11)$$

In the comoving coordinate system, with the help of (5), the field equations (2) for the metric (6) can be written as

$$\frac{\ddot{B}}{B} + \frac{\ddot{C}}{C} + \frac{\dot{B}\dot{C}}{BC} + \frac{1}{A^2} + \frac{w\dot{\phi}^2}{2\phi^2} + \frac{\dot{\phi}}{\phi} \left(\frac{\dot{B}}{B} + \frac{\dot{C}}{C} \right) + \frac{\ddot{\phi}}{\phi} = -8\pi \frac{\omega_{smhde} \rho_{smhde}}{\phi} \quad (12)$$

$$\frac{\ddot{A}}{A} + \frac{\ddot{C}}{C} + \frac{\dot{A}\dot{C}}{AC} - \frac{1}{A^2} + \frac{w\dot{\phi}^2}{2\phi^2} + \frac{\dot{\phi}}{\phi} \left(\frac{\dot{A}}{A} + \frac{\dot{C}}{C} \right) + \frac{\ddot{\phi}}{\phi} = -8\pi \frac{\omega_{smhde} \rho_{smhde}}{\phi} \quad (13)$$

$$\frac{\ddot{A}}{A} + \frac{\ddot{B}}{B} + \frac{\dot{A}\dot{B}}{AB} - \frac{1}{A^2} + \frac{w\dot{\phi}^2}{2\phi^2} + \frac{\dot{\phi}}{\phi} \left(\frac{\dot{A}}{A} + \frac{\dot{B}}{B} \right) + \frac{\ddot{\phi}}{\phi} = -8\pi \frac{\omega_{smhde} \rho_{smhde}}{\phi} \quad (14)$$

$$\frac{\dot{A}\dot{B}}{AB} + \frac{\dot{B}\dot{C}}{BC} + \frac{\dot{A}\dot{C}}{AC} - \frac{1}{A^2} - \frac{w\dot{\phi}^2}{2\phi^2} + \frac{\dot{\phi}}{\phi} \left(\frac{\dot{A}}{A} + \frac{\dot{B}}{B} + \frac{\dot{C}}{C} \right) = 8\pi \left(\frac{\rho_{smhde} + \rho_m}{\phi} \right) \quad (15)$$

$$\frac{\dot{B}}{B} - \frac{\dot{C}}{C} = 0 \quad (16)$$

$$\ddot{\phi} + \dot{\phi} \left(\frac{\dot{A}}{A} + \frac{\dot{B}}{B} + \frac{\dot{C}}{C} \right) = \frac{8\pi}{(3+2w)} (\rho_{smhde} - 3p_{smhde} + \rho_m). \quad (17)$$

Also the energy conservation equation (3) can be written as

$$\dot{\rho}_m + \left(\frac{\dot{A}}{A} + \frac{\dot{B}}{B} + \frac{\dot{C}}{C} \right) (\rho_m + \rho_{smhde} + p_{smhde}) + \dot{\rho}_{smhde} = 0 \quad (18)$$

where an overhead dot denotes differentiation with respect to time t and EoS parameter of DE is $\omega_{smhde} = \frac{p_{smhde}}{\rho_{smhde}}$. From (16) by taking the integrating constant as unity, we get

$$C = B \quad (19)$$

Using equation (19), the field equations (12) to (17) reduce to

$$2\frac{\ddot{B}}{B} + \frac{\dot{B}^2}{B^2} + \frac{1}{A^2} + \frac{w\dot{\phi}^2}{2\phi^2} + 2\frac{\dot{\phi}\dot{B}}{\phi B} + \frac{\ddot{\phi}}{\phi} = -8\pi \frac{\omega_{smhde} \rho_{smhde}}{\phi} \quad (20)$$

$$\frac{\ddot{A}}{A} + \frac{\ddot{B}}{B} + \frac{\dot{A}\dot{B}}{AB} - \frac{1}{A^2} + \frac{w\dot{\phi}^2}{2\phi^2} + \frac{\dot{\phi}}{\phi} \left(\frac{\dot{A}}{A} + \frac{\dot{B}}{B} \right) + \frac{\ddot{\phi}}{\phi} = -8\pi \frac{\omega_{smhde} \rho_{smhde}}{\phi} \quad (21)$$

$$2\frac{\dot{A}\dot{B}}{AB} + \frac{\dot{B}^2}{B^2} - \frac{1}{A^2} - \frac{w\dot{\phi}^2}{2\phi^2} + \frac{\dot{\phi}}{\phi} \left(\frac{\dot{A}}{A} + 2\frac{\dot{B}}{B} \right) = 8\pi \left(\frac{\rho_{smhde} + \rho_m}{\phi} \right) \quad (22)$$

$$\ddot{\phi} + \dot{\phi} \left(\frac{\dot{A}}{A} + 2\frac{\dot{B}}{B} \right) + = \frac{8\pi}{(3+2w)} (\rho_{smhde} - 3p_{smhde} + \rho_m). \quad (23)$$

3. MODEL AND COSMOLOGICAL PARAMETERS

The field equations (20)-(23) form a set of four distinct equations involving six variables: $A, B, \rho_{smhde}, \omega_{smhde}, \rho_m,$ and ϕ . To get a deterministic outcome for the nonlinear field equations in our model, we impose the following reasonable physical constraints. we consider the fact that expansion scalar θ is directly proportional to shear scalar σ which leads to a relation between the metric potentials as follows

$$B=A^k \tag{24}$$

k represents a positive constant that accounts for the anisotropy of space-time. Collins et al. [51] have determined that in a spatially homogeneous space-time, the normal congruence to the homogeneous expansion adheres to the constraint that the ratio of the shear stress (σ) to the Hubble parameter (H) remains constant.

In addition, it is common in the literature to employ a power-law relationship between scalar field ϕ and average scale factor $a(t)$ of the form (Johri and Sudharsan [52]; Johri and Desikan [53]) $\phi \propto [a(t)]^n$ where n denotes a power index. Many authors have looked into different aspects of this type of scalar field ϕ . Given the physical significance of preceding relationship, we employ the following assumption to reduce the mathematical complexity of the system

$$\phi(t) = \phi_0[a(t)]^n. \tag{25}$$

Using the relations (24) and (25) in Eqs. (20) and (21), we obtain the metric potentials as

$$A(t) = \sqrt{\frac{k_2 t^2}{4} - \frac{A_0}{k_2}}; \quad B(t) = C(t) = \left(\frac{k_2 t^2}{4} - \frac{A_0}{k_2}\right)^{\frac{k}{2}} \tag{26}$$

where $k_2 = \frac{2}{1-k}, n = \frac{3-6k}{2k+1}, A_0$ is an integrating constant. The scalar field of the model is

$$\phi(t) = \phi_0 \left(\frac{k_2 t^2}{4} - \frac{A_0}{k_2}\right)^{\frac{n(2k+1)}{6}}. \tag{27}$$

Now metric (6), with the help of metric potentials in Eq. (26), can be written as

$$ds^2 = dt^2 - \left(\frac{k_2 t^2}{4} - \frac{A_0}{k_2}\right) dx^2 - \left(\frac{k_2 t^2}{4} - \frac{A_0}{k_2}\right)^k (e^{2x} dy^2 + e^{-2x} dz^2). \tag{28}$$

Eq. (28) represents a spatially homogeneous and anisotropic BT- VI_0 SMHDE model within the framework of Brans-Dicke theory of gravitation with the following physical parameters. The average scale factor $a(t)$ and volume $V(t)$ of the model are, respectively, given by

$$V(t) = a(t)^3 = \left(\frac{k_2 t^2}{4} - \frac{A_0}{k_2}\right)^{\frac{2k+1}{2}}. \tag{29}$$

The average Hubble's parameter H and expansion scalar θ are obtained as

$$H = 3\theta = (2k + 1) k_2 t \left(3 k_2 t^2 - 12 \frac{A_0}{k_2}\right)^{-1}. \tag{30}$$

The shear scalar σ^2 and average anisotropic parameter A_h are given by

$$\sigma^2 = \frac{k_2^2(k-1)^2 t^2}{3 \left(k_2 t^2 - 4 \frac{A_0}{k_2}\right)^2}; \quad A_h = \frac{2(k-1)^2}{(2k+1)^2}. \tag{31}$$

From the above parameters it is observed that both the spatial volume and average scale factor of the universe exhibit the expansion of the universe. Furthermore, during the first epoch, which is when $t=0$, all values become finite. However, as t approaches infinity, they diverge. It is worth mentioning that when $k=1$, the model becomes shear-free and isotropic, as shown by the conditions $\sigma^2=0$ and $A_h=0$.

As a dynamical DE component, we assume Sharma-Mittal holographic DE. It is defined by (Sharma and Mittal [54]) and is formulated using Sharma-two-parametric Mittal's entropy

$$S_{SM} = \frac{1}{d_1} \left(\left(1 + \frac{\delta\kappa}{4}\right)^{\frac{d_1}{\delta}} - 1 \right), \tag{32}$$

where $\kappa = 4\pi L^2$ and L represents the IR cutoff. R and δ are two free parameters in this case. At the appropriate d_1 limits, Renyi and Tsallis entropies can be recovered. Sharma-Mittal entropy is transformed into Renyi entropy in the limit $d_1 \rightarrow 0$, and Tsallis entropy in the limit $d_1 \rightarrow 1 - \delta$. According to Cohen et al. [10], the relationship between the system entropy and the IR and UV cutoffs yields the energy density

$$\rho_{de} = \frac{3d_2^2 S_{SM}}{8\pi L^4}. \quad (33)$$

Using the above equation and the Hubble horizon cutoff $L = \frac{1}{H}$, we can calculate the energy density of the Sharma-Mittal HDE model (Jahromi et al. [17]) as follows:

$$\rho_{de} = \frac{3d_2^2 H^4}{8\pi d_1} \left(\left(1 + \frac{\delta\pi}{H^2} \right)^{\frac{d_1}{\delta}} - 1 \right), \quad (34)$$

where C^2 denotes the free parameter. Using Hubble parameter $H(t)$ in the above Eq. (34), we get the energy density of SMHDE of our model as

$$\rho_{de} = \frac{3d_2^2 ((2k+1)k_2 t)^4}{8\pi d_1 \left(3k_2 t^2 - 12\frac{A_0}{k_2} \right)^4} \left(\left(1 + \frac{\delta\pi \left(3k_2 t^2 - 12\frac{A_0}{k_2} \right)^2}{((2k+1)k_2 t)^2} \right)^{\frac{d_1}{\delta}} - 1 \right). \quad (35)$$

Using Eqs. (34), (27) and (26) in Eq. (15), we get the energy density of matter as

$$\begin{aligned} \rho_m = & \frac{\phi_0}{8\pi} \left(\frac{k_2 t^2}{4} - \frac{A_0}{k_2} \right)^{\frac{n(2k+1)}{6}} \left\{ \frac{2k_2^2 t^2 k}{\left(k_2 t^2 - 4\frac{A_0}{k_2} \right)^2} + \frac{k^2 k_2^2 t^2}{\left(k_2 t^2 - 4\frac{A_0}{k_2} \right)^2} - \left(\frac{k_2 t^2}{4} - \frac{A_0}{k_2} \right)^{-1} \right. \\ & \left. - \frac{wn^2 k_2^2 (2k+1)^2 t^2}{2 \left(3k_2 t^2 - 12\frac{A_0}{k_2} \right)^2} + nk_2 (2k+1)t \left(\frac{k_2 t + 2kk_2 t}{k_2 t^2 - 4\frac{A_0}{k_2}} \right) \left(3k_2 t^2 - 12\frac{A_0}{k_2} \right)^{-1} \right\} \\ & - \frac{3d_2^2 (2k+1)^4 k_2^4 t^4}{\left(3k_2 t^2 - 12\frac{A_0}{k_2} \right)^4 8\pi d_1} \left(\left(1 + \frac{\delta\pi}{(2k+1)^2 k_2^2 t^2} \left(3k_2 t^2 - 12\frac{A_0}{k_2} \right)^2 \right)^{\frac{d_1}{\delta}} - 1 \right). \quad (36) \end{aligned}$$

Using Eqs. (34), (27) and (26), from Eq. (20) and (21) we obtain the EoS parameter of SMHDE as

$$\begin{aligned} \omega_{smhde} = & -\frac{\phi_0 d_1}{3d_2^2 (2k+1)^4 k_2^4 t^4} \left(\frac{k_2 t^2}{4} - \frac{A_0}{k_2} \right)^{\frac{n(2k+1)}{6}} \left(3k_2 t^2 - 12\frac{A_0}{k_2} \right)^4 \left\{ \frac{3k^2 k_2^2 t^2}{\left(\frac{k_2 t^2}{4} - \frac{A_0}{k_2} \right)^2} \right. \\ & + \frac{3kk_2}{\left(k_2 t^2 - 4\frac{A_0}{k_2} \right)} + \frac{16(k^2 k_2^2 t^2 - kk_2^2 t^2) - k_2^2 t^2}{16 \left(\frac{k_2 t^2}{4} - \frac{A_0}{k_2} \right)^2} + \frac{k^2 k_2^2 t^2 + kk_2^2 t^2}{\left(k_2 t^2 - 4\frac{A_0}{k_2} \right)^2} + \frac{wn^2 k_2^2 (2k+1)^2 t^2}{\left(3k_2 t^2 - 12\frac{A_0}{k_2} \right)^2} \\ & + \frac{n^2 (2k+1)^2 k_2^2 t^2}{72 \left(\frac{k_2 t^2}{4} - \frac{A_0}{k_2} \right)^2} + \frac{2nk_2 (2k+1)}{\left(3k_2 t^2 - 12\frac{A_0}{k_2} \right)} - \frac{n(2k+1)k_2^2 t^2}{12 \left(\frac{k_2 t^2}{4} - \frac{A_0}{k_2} \right)^2} \\ & \left. + \left(\frac{(nk_2 (2k+1)t)(k_2 t + 3kk_2 t)}{3 \left(k_2 t^2 - 4\frac{A_0}{k_2} \right)^2} \right) \right\} \left(\left(1 + \frac{(2k+1)^{-2} \delta\pi}{\left(3k_2 t^2 - 12\frac{A_0}{k_2} \right)^{-2} k_2^2 t^2} \right)^{\frac{d_1}{\delta}} - 1 \right)^{-1}. \quad (37) \end{aligned}$$

4. PHYSICAL DISCUSSION

This section examines the expansion of the universe by analyzing cosmological parameters such as the scalar field, EoS ω_{smhde} , squared sound speed v_s^2 , deceleration q parameters, and the $\omega_{smhde} - \omega'_{smhde}$ plane for the anisotropic SMHDE model.

Scalar field: Figure 1 indicates the behavior of the scalar field in terms of cosmic time for various values

of parameter k . The scalar field exhibits a positive value and experiences a steady decline throughout its development. The decreasing nature of the scalar field indicates the increasing pattern of kinetic energy in this model. Furthermore, we have seen that when the parameter k increases, the scalar field decreases.

EoS parameter: The equation of state parameter (ω) is often used for classifying the many phases of the expanding universe. The EoS parameter, represented as $\omega = \frac{p}{\rho}$, is a measure of the relationship between pressure (p) and energy density (ρ) of a given matter distribution. The decelerated and accelerated phases consist of the following time intervals: Decelerated phases, such as those involving cold dark matter or dust fluid (ω is zero), indicating the radiation era for (ω is between 0 and 1/3), and the fluid is characterized as stiff for $\omega = 1$. Accelerating phase, such as the cosmic constant/vacuum period (ω is -1), which corresponds to the quintessence period (when $-1 < \omega < -1/3$), it is known as the phantom era ($\omega < -1$), indicating a quintom period characterized by the mixture of both quintessence and phantom components.

The EoS parameter of SMHDE with Hubble horizon cutoff is given in Eq. (37). In Fig. 2, we investigate the evolution of EoS parameter ω_{smhde} in terms of cosmic time t for different values of k . Fig. 2 shows that initially ω_{smhde} starts from DE era, varies in quintessence region $-1 < \omega_{smhde} < -1/3$ and phantom region $\omega_{smhde} < -1$. As the parameter k increases the EoS parameter of our model enters into phantom region.

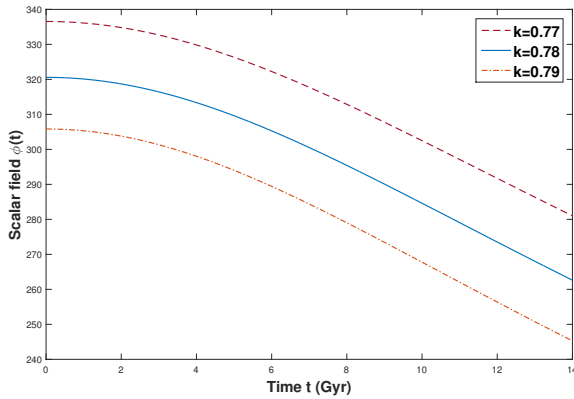


Figure 1. Plot of scalar field versus cosmic time t for $A_0 = -3900.69$ and $\phi_0 = 1750$.

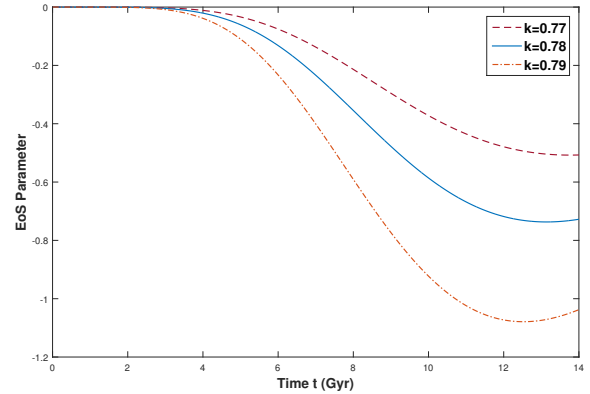


Figure 2. Plot of EoS parameter versus cosmic time t for $A_0 = -3900.69$, $\delta = 1.5$, $d_1 = 4.5$, $d_2 = 2.2$ and $\omega = 75000$.

Squared sound speed: The squared speed of the sound parameter is defined as

$$v_s^2 = \frac{\dot{p}_{smhde}}{\dot{\rho}_{smhde}} = \omega_{smhde} + \frac{\rho_{smhde}}{\dot{\rho}_{smhde}} \dot{\omega}_{smhde}. \quad (38)$$

The sign of this parameter is essential when considering the stability of DE models. The stability of the DE model is determined by the positive signature of v_s^2 . If the signature is negative, the model becomes unstable. By substituting the energy density and EoS parameter from equations (35) and (37) into the equation for squared sound speed (v_s^2) provided by equation (38), we do a graphical analysis of v_s^2 for our model. Figure 2 illustrates the relationship between the square of the velocity, denoted as v_s^2 , and the time t . The trajectories exhibit positive behaviour throughout the model's development. Therefore, this demonstrates the stability of our model.

$\omega_{smhde} - \omega'_{smhde}$ plane: We examine the $\omega_{smhde} - \omega'_{smhde}$ plane, where ω'_{smhde} represents the rate of change of the EoS parameter ω_{smhde} concerning the natural logarithm of the scale factor $\ln a$. Caldwell and Linder [55] propose using this framework to examine the cosmic evolution of the quintessence DE scenario. Moreover, it has been observed that the $\omega_{smhde} - \omega'_{smhde}$ plane can be separated into two distinct areas: thawing ($\omega_{smhde} < 0$, $\omega'_{smhde} > 0$) and freezing ($\omega_{smhde} < 0$, $\omega'_{smhde} < 0$). The freezing zone exhibits a more accelerated phase of cosmic expansion in comparison to the thawing area.

Figure 4 depicts the relationship between the $\omega_{smhde} - \omega'_{smhde}$ plane and various values of k . Figure 4 demonstrates that the $\omega_{smhde} - \omega'_{smhde}$ plane represents the area where freezing occurs, regardless of the specific parameter values. Modern cosmological data suggest that the freezing zone exhibits a phase of increased cosmic acceleration in contrast to the thawing area. Hence, the $\omega_{smhde} - \omega'_{smhde}$ plane of our model exhibits cosmic acceleration inside the freezing region.

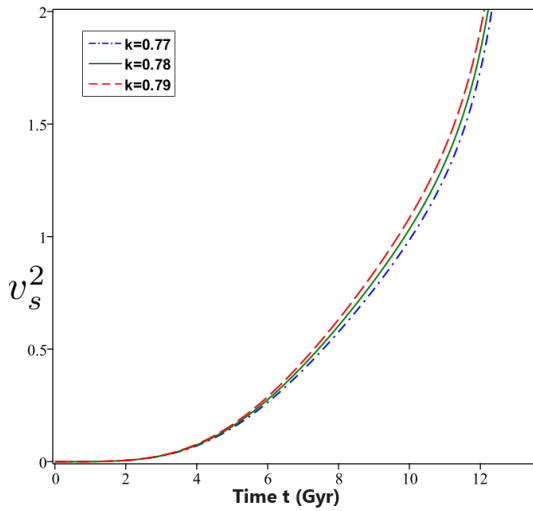


Figure 3. Plot of v_s^2 versus time t for $A_0 = -3900.69$, $\delta = 1.5$, $d_1 = 4.5$, $d_2 = 2.2$ and $\omega = 75000$.

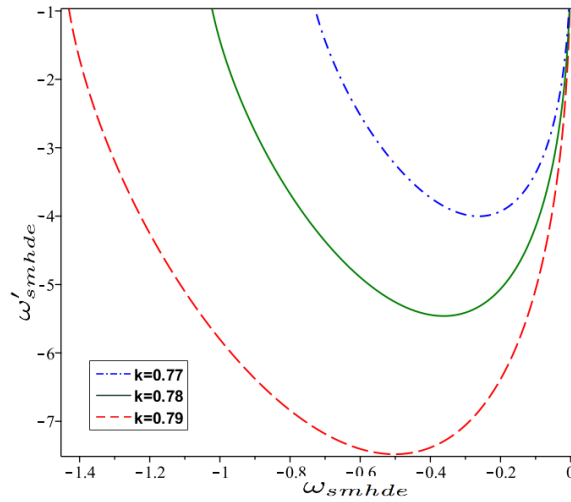


Figure 4. Plot of $\omega_{smhde} - \omega'_{smhde}$ for $A_0 = -3900.69$, $\delta = 1.5$, $d_1 = 4.5$, $d_2 = 2.2$ and $\omega = 75000$.

Energy conditions: The Raychaudhuri equations initiated the exploration of energy conditions, playing a crucial role in analyzing the alignment of null and time-like geodesics. The energy conditions are used to illustrate other universal principles about the dynamics of intense gravitational fields. The often observed energy conditions are as follows:

Dominant energy condition (DEC): $\rho_{smhde} \geq 0, \rho_{smhde} \pm p_{smhde} \geq 0$.

Strong energy conditions (SEC) : $\rho_{smhde} + p_{smhde} \geq 0, \rho_{smhde} + 3p_{smhde} \geq 0$,

Null energy conditions (NEC): $\rho_{smhde} + p_{smhde} \geq 0$,

Weak energy conditions (WEC): $\rho_{smhde} \geq 0, \rho_{smhde} + p_{smhde} \geq 0$,

Figure 5 illustrates the energy conditions of our SMHDE model. It is seen that the WEC satisfies the condition $\rho_{smhde} \geq 0$. Also, Fig. 5 demonstrates that the SEC $\rho_{smhde} + 3p_{smhde} \geq 0$ is not fulfilled. This phenomenon, resulting from the universe's acceleration in its latter stages, aligns with current observational findings.

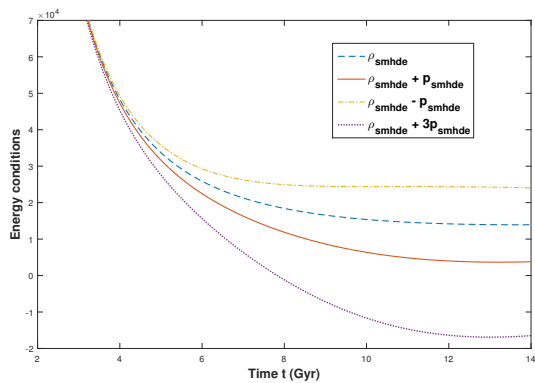


Figure 5. Plot of energy conditions versus cosmic time t for $A_0 = -3900.69$, $\delta = 1.5$, $d_1 = 4.5$, $d_2 = 2.2$ and $\omega = 75000$.

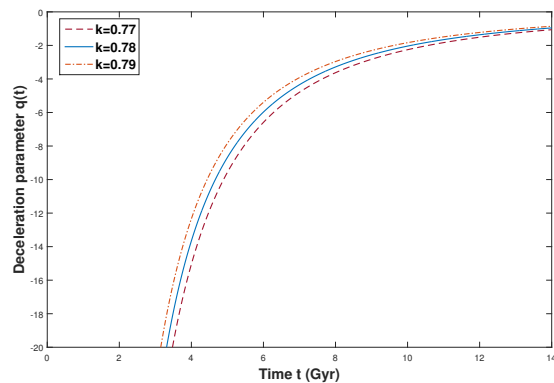


Figure 6. Plot of deceleration parameter versus cosmic time t for $A_0 = -3900.69$.

Deceleration parameter: The expansion of the universe may be determined by using the dimensionless cosmological parameter referred to as the deceleration parameter (DP). When DP has positive values, the model slows down in the usual manner. However, when q is equal to zero, the model grows at a consistent pace. The model demonstrates accelerated expansion when the value of q is between -1 and 0 , and a super-exponential expansion

when q is less than -1 . Using Eqs. (11) and (30), we get the deceleration parameter can be calculated as

$$q = \frac{3k_2^2 t^2 + 12A_0^2}{(2k+1)k_2^2 t^2} - 1. \quad (39)$$

Figure 5 displays the behavior of the deceleration parameter q in terms of cosmic time t for different values of k . It is important to mention that our model is accelerating throughout the evolution of the model and which is consistent with the recent observational data.

5. CONCLUSIONS




The accelerated expansion phenomenon of the universe has got much attraction with the passage of time. Upto now, many approaches have been adopted for explaining this phenomenon with variety of dynamical DE models and modified theories of gravity. Here, we reconsider the expansion phenomenon in the Brans-Dicke scenario leads to an accelerated universe. Thus, we have considered the Sharma-Mittal holographic dark energy within the context of anisotropic Bianchi type- $V I_0$ space-time in Brans-Dicke theory of gravitation. In this case, we have assumed the Hubble horizon as the infrared cutoff. We have examined well-recognized cosmological parameters, including the equation of state, deceleration, squared speed of sound parameters and $\omega_{smhde} - \omega'_{smhde}$ plane. Our findings have been condensed into the following summary:

The scalar field exhibits a positive value and experiences a steady decrease throughout its development. The decreasing nature of the scalar field indicates the increasing pattern of kinetic energy in this model. Furthermore, we have seen that when the parameter k increases, the scalar field decreases. The EoS parameter ω_{smhde} of the SMHDE model initially starts from the dark energy era and varies in quintessence region $-1 < \omega_{smhde} < -1/3$ and finally it becomes less than -1 , which means the model approaches phantom region at late times. We have made a comparison of our results with present Planck collaboration data [56] where the limits on the EoS parameter are given as $\omega_{de} = -1.56_{-0.48}^{+0.60}$ (Planck + TT + lowE), $\omega_{de} = -1.58_{-0.41}^{+0.52}$ (Planck + TT, TE, EE + lowE), $\omega_{de} = -1.57_{-0.40}^{+0.50}$ (Planck + TT, TE, EE + lowE + lensing), $\omega_{de} = -1.04_{-0.10}^{+0.10}$ (Planck + TT, TE, EE + lowE + lensing + BAO). It can be seen that the results for the EoS parameter of our model are consistent with the Planck Collaboration data. The $\omega_{smhde} - \omega'_{smhde}$ plane depicts the area where freezing occurs for all three parameter values. Modern cosmological measurements indicate that the freezing zone reveals a period of greater cosmic acceleration compared to the thawing region. Therefore, the $\omega_{smhde} - \omega'_{smhde}$ plane of our model demonstrates cosmic acceleration in the freezing area and aligns well with the facts. The paths of the $\omega_{smhde} - \omega'_{smhde}$ plane, as predicted by our model, align with the observed data [57, 58] $\omega_{smhde} = -1.13_{-0.25}^{+0.24}$, $\omega'_{smhde} < 1.32$ (Planck + WP + BAO). The squared sound speed trajectories exhibit positive behaviour throughout the evolution of the universe and hence our model is stable. Our model violates the SEC regulations and this phenomenon resulting from the universe's acceleration in its latter epochs aligns with current observational data. Our model demonstrates an accelerating expansion of the universe throughout the evolution of model.

Acknowledgments

Y. Aditya is thankful to the National Board for Higher Mathematics, Department of Atomic Energy, Govt. of India for its financial support under the grant No: 02011/8/2023 NBHM(R.P.)/R & D II/3073.

ORCID

 **Y. Aditya**, <https://orcid.org/0000-0002-5468-9697>;  **D. Tejeswararao**, <https://orcid.org/0000-0003-3508-346X>;  **U.Y. Divya Prasanthi**, <https://orcid.org/0009-0004-5397-050X>

REFERENCES

- [1] S. Perlmutter, et al., *Astrophys. J.* **517**, 565 (1999). <https://doi.org/10.1086/307221>
- [2] A.G. Riess, et al., *Astron. J.* **116**, 1009 (1998). <https://doi.org/10.1086/300499>
- [3] T. Koivisto, and D.F. Mota, *Phys. Rev. D*, **73**, 083502 (2006). <https://doi.org/10.1103/PhysRevD.73.083502>
- [4] E.J. Copeland, et al., *Int. J. Mod. Phys. D*, **15**, 1753 (2006). <https://doi.org/10.1142/S021827180600942X>
- [5] R.R. Caldwell, and M. Kamionkowski, *Ann. Rev. Nucl. Part. Sci.* **59**, 397 (2009). <https://doi.org/10.1146/annurev-nucl-010709-151330>
- [6] K. Bamba, et al., *Astrophys. Space Sci.* **342**, 155 (2012). <https://doi.org/10.1007/s10509-012-1181-8>
- [7] S. Nojiri, et al., *Phys. Rept.* **692**, 1 (2017). <https://doi.org/10.1016/j.physrep.2017.06.001>
- [8] Q.G. Huang, M. Li, *J. Cosmol. Astropart. Phys.* **3**, 1 (2005). <https://doi.org/10.1088/1475-7516/2004/08/013>
- [9] M. Li, *Phys. Lett. B*, **603**, 1 (2004). <https://doi.org/10.1016/j.physletb.2004.10.014>

- [10] A. Cohen, and D. Kaplan, A. Nelson, Phys. Rev. Lett. **82**, 4971 (1999). <https://doi.org/10.1103/PhysRevLett.82.4971>
- [11] L.N. Granda, and A. Oliveros, Phys. Lett. B, **671**, 199 (2009). <https://doi.org/10.1016/j.physletb.2008.12.025>
- [12] H. Wei, and R.G. Cai, Phys. Lett. B, **660**, 113 (2008). <https://doi.org/10.1016/j.physletb.2007.12.030>
- [13] S. Nojiri, and S.D. Odintsov, Gen. Rel. Grav. **38**, 1285 (2006). <https://doi.org/10.1007/s10714-006-0301-6>
- [14] S. Nojiri, et al., Phys. Lett. B, **797**, 134829 (2019). <https://doi.org/10.1016/j.physletb.2019.134829>
- [15] M. Tavayef, A. Sheykhi, K. Bamba, and H. Moradpour, Phys. Lett. B, **781**, 195 (2018). <https://doi.org/10.1016/j.physletb.2018.04.001>
- [16] C. Tsallis, and L.J.L. Cirto, Eur. Phys. J. C, **73**, 2487 (2013). <https://doi.org/10.1140/epjc/s10052-013-2487-6>
- [17] A.S. Jahromi et al., Phys. Lett. B, **780**, 21 (2018). <https://doi.org/10.1016/j.physletb.2018.02.052>
- [18] H. Moradpour et al., Eur. Phys. J. C, **78**, 829 (2018). <https://doi.org/10.1140/epjc/s10052-018-6309-8>
- [19] D.R.K. Reddy, et al., Astrophys Space Sci. **361**, 356 (2016). <https://doi.org/10.1007/s10509-016-2938-2>
- [20] Y. Aditya, and D.R.K. Reddy, Eur. Phys. J. C, **78**, 619 (2018). <https://doi.org/10.1140/epjc/s10052-018-6074-8>
- [21] V.U.M. Rao, et al., Results in Physics, **10**, 469 (2018). <https://doi.org/10.1016/j.rinp.2018.06.027>
- [22] M.V. Santhi, et al., Int. J. Theor. Phys. **56**, 362 (2017). <https://doi.org/10.1007/s10773-016-3175-8>
- [23] K.D. Naidu, et al., Eur. Phys. J. Plus, **133**, 303 (2018). <https://doi.org/10.1140/epjp/i2018-12139-2>
- [24] Y. Aditya, et al., Eur. Phys. J. C, **79**, 1020 (2019). <https://doi.org/10.1140/epjc/s10052-019-7534-5>
- [25] S. Maity, U. Debnath, Eur. Phys. J. Plus, **134**, 514 (2019). <https://doi.org/10.1140/epjp/i2019-12884-6>
- [26] A. Iqbal, A. Jawad, Physics of the Dark Universe, **26**, 100349 (2019). <https://doi.org/10.1016/j.dark.2019.100349>
- [27] G. Kaniadakis, Physica A: Stat. Mech. and its Appl. **296**(3-4), 405 (2001). [https://doi.org/10.1016/S0378-4371\(01\)00184-4](https://doi.org/10.1016/S0378-4371(01)00184-4)
- [28] M. Masi, Phys. Lett. A, **338**, 217 (2005). <https://doi.org/10.1016/j.physleta.2005.01.094>
- [29] E.M. Abreu, et al., EPL (Europhysics Letters), **124**, 30003 (2018). <https://doi.org/10.1209/0295-5075/124/30003>
- [30] H. Moradpour, et al. Eur. Phys. J. C, **80**, 1 (2020). <https://doi.org/10.1140/epjc/s10052-020-8307-x>
- [31] A. Jawad, and A.M. Sultan, Adv. High Energy Phys. **2021**, 5519028 (2021). <https://doi.org/10.1155/2021/5519028>
- [32] U.K. Sharma, et al., IJMPD, **31**, 2250013 (2022). <https://doi.org/10.1142/S0218271822500134>
- [33] N. Drepanou et al., Eur. Phys. J. C, **82**, 449 (2022). <https://doi.org/10.1140/epjc/s10052-022-10415-9>
- [34] J. Sadeghi, et al., arXiv:2203.04375 (2022). <https://doi.org/10.48550/arXiv.2203.04375>
- [35] O. Akarsu, and C.B. Kilinc, Astrophys. Space Sci. **326**, 315 (2010). <https://doi.org/10.1007/s10509-009-0254-9>
- [36] C.L. Bennett, et al., Astron. Astrophys. Suppl. Ser. **148**, 1 (2003). <https://doi.org/10.1086/377252>
- [37] D.R.K. Reddy, et al., Can. J. Phys. **97**, 932 (2019). <https://doi.org/10.1139/cjcp-2018-0403>
- [38] Y. Aditya, et al., Astrophys. Space Sci. **364**, 190 (2019). <https://doi.org/10.1007/s10509-019-3681-2>
- [39] Y. Aditya, and D.R.K. Reddy, Astrophys. Space Sci. **364**, 3 (2019). <https://doi.org/10.1007/s10509-018-3491-y>
- [40] Y. Aditya, et al., Ind. J. Phys. **95**, 383 (2021). <https://doi.org/10.1007/s12648-020-01722-6>
- [41] R.L. Naidu, et al., Astrophys. Space Sci. **365**, 91 (2020). <https://doi.org/10.1007/s10509-020-03796-4>
- [42] K.D. Naidu, et al., Mod. Phys. A, **36**, 2150054 (2021). <https://dx.doi.org/10.1142/S0217732321500541>
- [43] Y. Aditya, et al., New Astr. **84**, 101504 (2021). <https://doi.org/10.1016/j.newast.2020.101504>
- [44] Y. Aditya, et al., Int. J. Mod. Phys. A, **37**, 2250107 (2022). <https://doi.org/10.1142/S0217751X2250107X>
- [45] M.P.V.V. Bhaskara Rao, et al., New Astr. **92**, 101733 (2022). <https://doi.org/10.1016/j.newast.2021.101733>
- [46] U.Y.D. Prasanthi, and Y. Aditya, Phys. Dark Univ. **31**, 100782 (2021). <https://doi.org/10.1016/j.dark.2021.100782>
- [47] U.Y.D. Prasanthi, and Y. Aditya, Results Phys. **17**, 103101 (2020). <https://doi.org/10.1016/j.rinp.2020.103101>
- [48] Y. Aditya, and U.Y.D. Prasanthi, Bulg. Astr. Journal, **38**, 52 (2023). <https://astro.bas.bg/AIJ/issues/n38/YAditya.pdf>
- [49] Y. Aditya, Bulg. Astr. Journal, **39**, 12 (2023). <https://astro.bas.bg/AIJ/issues/n39/YAditya.pdf>
- [50] C.H. Brans, R.H. Dicke, Phys. Rev. **124**, 925 (1961). <https://doi.org/10.1103/PhysRev.124.925>
- [51] C.B. Collins, et al., Gen. Relativ. Gravit. **12**, 805 (1980). <https://doi.org/10.1007/BF00763057>

- [52] V.B. Johri, R. Sudharsan, Australian J. of Phys. **42(2)**, 215 – 222 (1989). <https://doi.org/10.1071/PH890215>
- [53] V.B. Johri, K. Desikan, Gen Relat Gravit **26**, 1217–1232 (1994). <http://dx.doi.org/10.1007/BF02106714>
- [54] B.D. Sharma, D.P. Mittal, J. Math. Sci. **10**, 28 (1975).
- [55] R. Caldwell, and E.V. Linder, Phys. Rev. Lett. **95**, 141301 (2005). <https://doi.org/10.1103/PhysRevLett.95.141301>
- [56] N. Aghanim, et al., [Plancks Collaboration] arXiv:1807.06209v2 (2018). <https://doi.org/10.48550/arXiv.1807.06209>
- [57] P.A.R. Ade, et al., Astrophys. **571**, A16 (2014). <https://doi.org/10.1051/0004-6361/201321591>
- [58] G.F. Hinshaw, et al., Astrophys. J. Suppl. **208**, 19 (2018). <https://doi.org/10.1088/0067-0049/208/2/19>

КОСМІЧНІ АСПЕКТИ ГОЛОГРАФІЧНОЇ МОДЕЛІ ТЕМНОЇ ЕНЕРГІЇ ШАРМА-МІТТАЛА В ТЕОРІЇ ГРАВІТАЦІЇ БРЕНСА-ДІККЕ

Ю. Адітья^a, Д. Теджешварарао^a, У.Ю. Дів'я Прасанті^b


^a Департамент фундаментальних та гуманітарних наук, Технологічний інститут GMR,
Раджам-532127, Індія

^b Факультет статистики та математики Коледжу садівництва, Університет рослинництва Dr. Y.S.R.,
Парватипурам-535502, Індія

Ми досліджуємо космологічний сценарій із просторово однорідним і анізотропним простором-часом типу Б'янкі VI_0 в контексті голографічної моделі темної енергії Шарма-Міттала в рамках теорії гравітації Бранса-Дікке. Для досягнення цієї мети обговорювалися Хаббл, уповільнення, параметри рівняння стану. Параметр уповільнення (q) використовується для вимірювання темпу, з яким прискорюється розширення Всесвіту. Параметр рівняння стану (ω_{smhde}) характеризує квінтесенцію та вакуумні області Всесвіту. Усі параметри демонструють узгоджену поведінку відповідно до даних Planck 2018. Ми оцінюємо динамічну стабільність, визначаючи квадрат швидкості звуку та досліджуючи його поведінку. Крім того, енергетичні умови та варіація ω_{smhde} і ω'_{smhde} у моделі вказують на поточне прискорене розширення Всесвіту.

Ключові слова: модель типу Bianchi- VI_0 ; модель темної енергії; теорія гравітації Бранса-Дікке; космологія; голографічна темна енергія Шарма-Міттала

SPECTRAL AND TEMPORAL PROPERTIES OF CXOUJ122956.7+075728 (ULX-1), AN ULTRALUMINOUS X-RAY SOURCE IN NGC 4472

 A. Seniorita Devi*

Department of Physics, Manipur University, Imphal, India

*Corresponding Author e-mail: senorita@manipuruniv.ac.in

Received January 1, 2024; revised January 26, 2024; accepted January 30, 2024

This report presents a comprehensive analysis of the spectral and temporal characteristics of a highly significant Ultraluminous X-ray Source (ULX) designated as CXOUJ122956.7+075728 (ULX-1) situated in the elliptical galaxy NGC 4472 within the Virgo cluster. ULX-1 exhibits a soft spectral state, featuring a cool accretion disk component with $kT_{in} \sim 0.15$ keV, accompanied by a power-law tail displaying a steep power-law photon index, $\Gamma \sim 2.8$. The spectral findings strongly support an estimated black hole mass of approximately $3.30 \times 10^3 M_{\odot}$ under an isotropic emission model, and around $1.47 \times 10^3 M_{\odot}$ in an extreme beaming scenario. Temporally, ULX-1 displays significant variability on time scales of 0.5, 1, and 2 ks, suggesting the possibility of instabilities within the accretion disk contributing to this behavior. However, despite this temporal variability, the power spectra analysis of this soft ULX reveals no signatures of pulsations, distinguishing it from certain pulsating ULXs (PULXs) typically associated with neutron stars. This absence of pulsations in ULX-1 further underscores its unique spectral and temporal characteristics within the broader context of ULX phenomena.

Keywords: *Accretion, Accretion disks; Galaxies: individual (NGC 4472); X-rays: binaries*

PACS: 97.10.Gz, 98.52.-b; 98.56.Ew, 95.85.Nv, 97.80.Jp

1. INTRODUCTION

Non-nuclear X-ray point sources exhibiting isotropic luminosity $\geq 10^{39}$ erg s⁻¹ in the (0.1 - 10.0) keV energy range are usually termed as Ultraluminous X-ray Sources (ULXs) [1]. Essentially, ULXs are accreting sources with X-ray luminosities surpassing the Eddington limit of a $10M_{\odot}$ black hole (BH) [2, 3]. The inferred high luminosity of ULXs have been modelled as due to - sub-Eddington accretion on to the Intermediate Mass Black Holes (IMBHs) [4, 5, 6]. Black Holes with masses in the range $M_{BH} \sim 10^2 - 10^5 M_{\odot}$ are termed as IMBHs. The formation process of IMBHs presented a challenge until the recent discovery of a binary black hole merger with a total mass of $M_{BH} \sim 150M_{\odot}$ [7], providing compelling evidence for the existence of IMBHs. This discovery has significantly contributed to our understanding of the potential formation mechanisms of Intermediate Mass Black Holes. The ULX model involving sub-Eddington accretion onto Intermediate Mass Black Holes (IMBHs) holds significant importance in elucidating the exceptionally high luminosities observed in certain ULXs, particularly those in very soft states such as CXOUJ132943.3+471135 of M51 [8], X-7 of NGC 6946 [9] etc.

In the last few decades advanced satellites like Chandra, XMM-Newton, NuSTAR etc. have enabled to catalogue around 1840 ULXs [10, 11]. Detailed spectral and temporal studies of these ULXs have revealed that majority of the ULXs are super-accretors. In this model, the very high luminosity of ULXs are being modelled as due to super-Eddington accretion on to stellar mass black holes or neutron stars [12, 13, 14, 15, 16, 17]. Example of super-Eddington accretor ULX include ULX NGC 1313 X-1 [18]. Indeed, recent studies have increasingly employed the model of super-Eddington accretion to explain the spectral and temporal properties of ULXs in terms of radiatively driven outflows/winds. Jithesh (2022) [19] extensively explored the physical characteristics of NGC 55 ULX1, an exceptionally super-soft and luminous ULX, by proposing a model based on supercritical radiatively driven outflowing winds to explain its unique features. Pinto et al. (2017) [20] & (2021) [21] has also reported the existence of outflowing wind in some ULXs.

In the past decade, a novel scenario has emerged with the discovery of pulsating ULXs (PULXs)- PULX in M82 [22], NGC 300 ULX-1 [23], NGC 1313 X-2 [24]; M 51 ULX-7 [25], ULX Swift J0243.6+6124 [26], M 81 X-6 [27] etc. PULXs are modeled as accreting systems where the compact object is a neutron star with a mass of approximately 1 - 2 M_{\odot} , accreting at extremely super-Eddington rates. Considering the scenarios above, the mass of compact objects within ULXs remains a topic of significant debate. While it's true that a significant portion of ULXs are categorized as super-accretors, the heterogeneity within this family is striking. ULXs exhibit diversity in terms of the compact objects they host, which can include Neutron Stars (NS), stellar-mass black holes, or even Intermediate Mass Black Holes (IMBHs), depending on the system.

Another important aspect to understand the physical nature of ULXs is its variability. The variability of Ultra-Luminous X-ray Sources (ULXs) spans a wide range of timescales, from kilo-seconds to weeks, and even extending to years. Notably, Krauss et al. (2005) [28] studied M74 X-1, an extremely variable ULX, displaying variations on very short timescales of approximately 1000 seconds, reminiscent of the behavior observed in the Galactic black hole system GRS 1915+105. Large amplitude variability on kilo-second timescales has been reported in many ULXs, potentially linked to spectral state transitions. The exploration of such variability in ULXs, whether on short or longer timescales, provides valuable insights into their dynamic behavior. These studies contribute to our understanding of the underlying processes governing ULXs and may unveil key features of their nature and evolution.

In this paper we present the detail spectral and temporal analysis of a very significant Ultraluminous X-ray source (ULX) named here as CXOUJ122956.7+075728 (ULX-1) in the elliptical galaxy NGC 4472 in the Virgo cluster. NGC 4472 is well known as a galaxy with hosting more than 200 X-ray sources, including even a good number (~ 80) of Low mass X-ray binaries (LMXBs) in Globular cluster [29]. Joseph et al. 2017 [29] has classified ULX-1 as a non Globular Cluster (GC) source. Here we adopt the distance to the galaxy NGC 4472 as 16 Mpc [30].

2. OBSERVATION AND DATA ANALYSIS

NGC 4472 have been observed by *Chandra* ACIS detector 17 times over a span of approximately 21 years, from 2000 to 2021. Notably, the source of interest, CXOUJ122956.7+075728 (referred to as ULX-1 hereafter), was prominently detected only during the year 2011 observation with Observation ID 12888, featuring an approximate exposure time of 160 ks. In the remaining observations, the positioning of the detectors did not provide proper coverage of ULX-1 in the field of view.. Consequently, the entirety of the presented work is based on the *Chandra* observation with ObsID 12888.

The reduction and analysis of the data were carried out by using Chandra Interactive Analysis of Observations (CIAO-4.16), along with its calibration data (CALDB 4.11.0) and Heasoft-6.32.1. Specific to the observation considered, the identification of problematic pixels was accomplished by configuring observation-specific bad pixel lists within the ardlb parameter file using the *acis_set_ardlib* tool.

The CIAO source detection tool, *Wavdetect*, was employed to identify X-ray sources from the level 2 event lists. The process involves two stages - *Wtransform* and *Wrecon*. In the first stage, *Wtransform*, putative source pixels were detected within the dataset using iterative correlation with "Mexican Hat" wavelet functions at different scales (1.0, 2.0, 4.0, 6.0, 8.0, and 16.0 pixels). Source pixels were identified based on the default value of the "sigthresh" parameter, set at approximately 10^{-6} . The second stage, *Wrecon*, utilized information obtained from *Wtransform* at each wavelet scale to generate a list of sources. In the source list, specifically, CXOUJ122956.7+075728 (ULX-1) was detected at RA $12^h29^m56.74^s$ and Dec. $+07^\circ57'27.77''$ with a total source count of ~ 556 . ULX-1 is found to be located at an off-nuclear distance $\approx 3.55'$. The source region is taken as a circular region with a radius of approximately 0.05 arcminutes, effectively encircling the source. The corresponding background region is chosen as a nearby source-free circular region. Using the CIAO tool *specextract* along with calibration data, the source and background spectra were extracted. The spectra were then grouped using the default setting of 15 counts per bin in *specextract*. Moreover, it is ensured that the source is not affected by pileup effects, given its count rate of approximately 2.96×10^{-03} counts s^{-1} . Also, for temporal analysis, using the CIAO tool *dmextract*, we have generated the background subtracted light curve of ULX-1 binned at 0.5, 1 and 2 ks.

3. SPECTRAL PROPERTIES OF CXOUJ122956.7+075728 (ULX-1)

In most cases, *Chandra* ULX spectra, due to low source count, are basically explained with simple empirical models such as powerlaw and multi-color disk blackbody. ULX-1, with a total source count ~ 556 , can be classified as possessing an averagely detailed *Chandra* spectrum. So, we first tried fitting the spectra of ULX-1 with simple models - an absorbed powerlaw model and then with an absorbed disk blackbody model separately. The XSPEC multiplicative model *phabs* was used as the absorption component. The spectra is all fitted in the energy range 0.3 - 8.0 keV. However neither of the two models could give a very good fit, as shown by the spectral parameters in Table 1. In both the cases, the fitting statistics were very poor with $\chi^2/\text{degrees of freedom (dof)} \approx 36.45/24$ for powerlaw model and $42.89/24$ for the absorbed disk blackbody model. So, neither of these two simple models (powerlaw or diskbb) could sufficiently represent the spectra of ULX-1.

Next, we tried the phenomenological two-component model i.e. the multi-color disk blackbody (*diskbb* in XSPEC) component added with a powerlaw (*pow* in XSPEC) component. This two-component model is frequently used to characterize the thermal emission originating from the accretion disc and the Comptonized emission emerging from either the hot corona or the inner accretion flow. *Phabs* was used as the absorption

component and the hydrogen column density (n_H) was set free to vary while fitting. Table 1 shows the model fitted spectral parameters. It is seen that this two-component model provides an improved fit as compared to the simple powerlaw or the disk blackbody. Rather, it gives a very good fit with $\chi^2/dof \approx 22.71/22$. The fitted spectra with this two component (diskbb + pow) model is shown in Figure 1.

Table 1. Spectral Properties of CXOUJ122956.7+075728 (ULX-1)

parameter	units	value
diskb blackbody (diskbb) model		
n_H	$(10^{22} \text{ cm}^{-2})$	$0.13^{+0.11}_{-0.08}$
kT_{in}	(keV)	$0.29^{+0.06}_{-0.06}$
$\log(L_{bol})$	(erg s^{-1})	$39.38^{+0.30}_{-0.19}$
χ^2/dof		42.89/24
powerlaw (pow) model		
n_H	$(10^{22} \text{ cm}^{-2})$	$0.45^{+0.18}_{-0.13}$
Γ		$4.76^{+1.14}_{-0.76}$
$\log(L_X)$	(erg s^{-1})	$40.05^{+0.68}_{-0.44}$
χ^2/dof		36.45/24
diskbb+pow model		
n_H	$(10^{22} \text{ cm}^{-2})$	0.43 ± 0.17
kT_{in}	(keV)	0.15 ± 0.04
Γ		2.82 ± 0.89
$\log(L_X)$	(erg s^{-1})	$39.84^{+0.10}_{-0.06}$
χ^2/dof		22.71/22

Consequently, we can accept that the spectra of ULX-1 can be well explained by this two-component model. It is found that ULX-1 have a soft component emission from the accretion disk with an inner disk temperature, $kT_{in} \sim 0.15$ keV, besides the spectra of ULX-1 is complimented with a powerlaw tail emission which might have arise due to inverse comptonization of soft seed photons in the hot corona near the inner accretion disk. Using the *cflux* model in XSPEC, we derived the unabsorbed flux. Then, using the distance to the source, $D \sim 16$ Mpc [30], we computed the unabsorbed luminosity (L_X) in the 0.3 - 8.0 keV range.

Analyzing the spectral parameters of ULX-1 in Table 1, it is evident that neither the single absorbed disk blackbody model nor the powerlaw model adequately explains the ULX-1 spectra. However, a preliminary examination of the parameters suggests that ULX-1 may indeed be in a soft spectral state, characterized by an inner disk temperature kT_{in} definitely less than 0.5 keV and a steep powerlaw photon index ($\Gamma \sim 4$). Additionally, individual estimations using these models indicate that ULX-1 is an exceptionally bright source, with an X-ray luminosity exceeding $10^{39} \text{ erg s}^{-1}$, firmly placing it in the high-soft state. This spectral state of ULX-1 is indeed confirmed from a more nuanced analysis employing a two-component model: a multicolor disk blackbody component combined with a powerlaw component. This model yields a robust fit, confirming that ULX-1 indeed exhibits a high-soft spectral state. The X-ray luminosity (L_X) is approximated to be $\sim 6.99 \times 10^{39} \text{ erg s}^{-1}$, and the spectral components include a cool disk with $kT_{in} \sim 0.15$ keV and a powerlaw tail characterized by a photon index $\Gamma \sim 2.82$. In analogy to the high-soft state of X-ray binaries, the presence of a low-temperature disk blackbody component in the ULX-1 spectra may be due to radiation from an accretion disk. In this scenario, the observed luminosity may be primarily attributed to emissions from a standard thin disk, extending up to the last innermost stable circular orbit (ISCO). Consequently, an

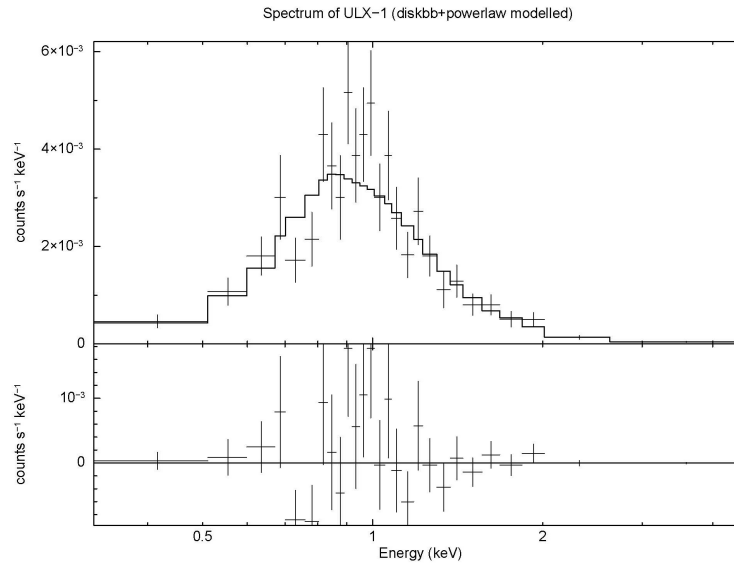


Figure 1. *Chandra* spectra of ULX-1 fitted with an absorbed (disk blackbody + powerlaw) model.

indirect estimation of the mass of the central compact object in ULXs can be derived from the disk blackbody component.

For the disk blackbody component, the inner disk radius from where the observed X-rays are emitted, is given by $R_{in} = (\sqrt{Normalisation} \times Distance_{10kpc}) / \sqrt{\cos \theta}$ km, where θ represents the viewing angle. Utilizing the normalization value obtained from the fit, the distance to the source, $D \approx 16$ Mpc and considering a viewing angle of $\cos \theta = 0.5$ [31], we can approximate the mass of the compact object. This estimation assumes that the inner disk radius R_{in} is situated at approximately 5 times the Schwarzschild radius ($R_{Sch} = 2GM/c^2$, where G is the Universal Gravitational Constant, M is the mass of the object, c is the speed of light in vacuum). Thus, for ULX-1 it is found that the mass of the central compact object is $\approx 3.30 \times 10^3 M_{\odot}$, which indeed correspond to the intermediate mass black hole range accreting at around 0.01 times the Eddington limit i.e $L/L_{Edd} = 0.01$. Referring to the work of King et al. (2001) [32], if we consider the emission to be anisotropic and beamed by a factor η , then R_{in} would be overestimated by a factor of $\eta^{1/2}$. Consequently, assuming maximum beaming with $\eta \sim 5$, as suggested by Misra and Sriram (2003) [33], the estimated black hole mass for ULX-1 is approximately $1.47 \times 10^3 M_{\odot}$; also falling within the range of intermediate mass black holes. Therefore, there is a high probability that ULX-1 in NGC 4472 is powered by an accreting intermediate mass black hole.

4. TEMPORAL PROPERTIES OF CXOUJ122956.7+075728 (ULX-1)

Ultra-Luminous X-ray Sources (ULXs) exhibit variability across a broad spectrum of time scales, ranging from a few kilo-seconds to weeks, and extending to periods spanning years. To examine the temporal variability of ULX-1 at the kilo-second time scale, we generated background-subtracted light curves for this source. These light curves were systematically binned over intervals of 0.5, 1 and 2 kilo-seconds, allowing for a detailed analysis of the source's temporal behavior over these specific time intervals. Figure 2 shows the light curve of ULX-1 in the specified time bins. The probability of a constant count rate during the observation is exceptionally low, with values less than 1.1×10^{-8} for 500 ks, 1.9×10^{-23} for 1000 ks, and 9.4×10^{-26} for 2000 ks binned light curves. Consequently, the likelihood of significant variability in the source exceeds 99% across all these time bins. This suggests that ULX-1 exhibits substantial amplitude variability on a kilo-second time scale. While the precise nature of such variability in Ultra-Luminous X-ray sources (ULXs) remains unclear, existing studies have explored various hypotheses, including potential beaming effects from a jet closely aligned with our line of sight [28] and large-scale instabilities within accretion disks.

In the case of ULX-1 in NGC 4472, its very soft spectra featuring a cool accretion disk component ($kT_{in} \sim 0.15$ keV) make it improbable for the variability to result from beaming effects associated with sub-Eddington accretors. Moreover, its likelihood of being powered by an Intermediate-Mass Black Hole (IMBH) with a mass around $10^3 M_{\odot}$ further diminishes this possibility. Therefore, it is suggested that the observed variability in ULX-1 may be attributed to substantial large-scale instabilities within the accretion disk, particularly within the detected time scales. However, it is essential to note that confirmation of any specific accretion disk instability model is pending further investigation.

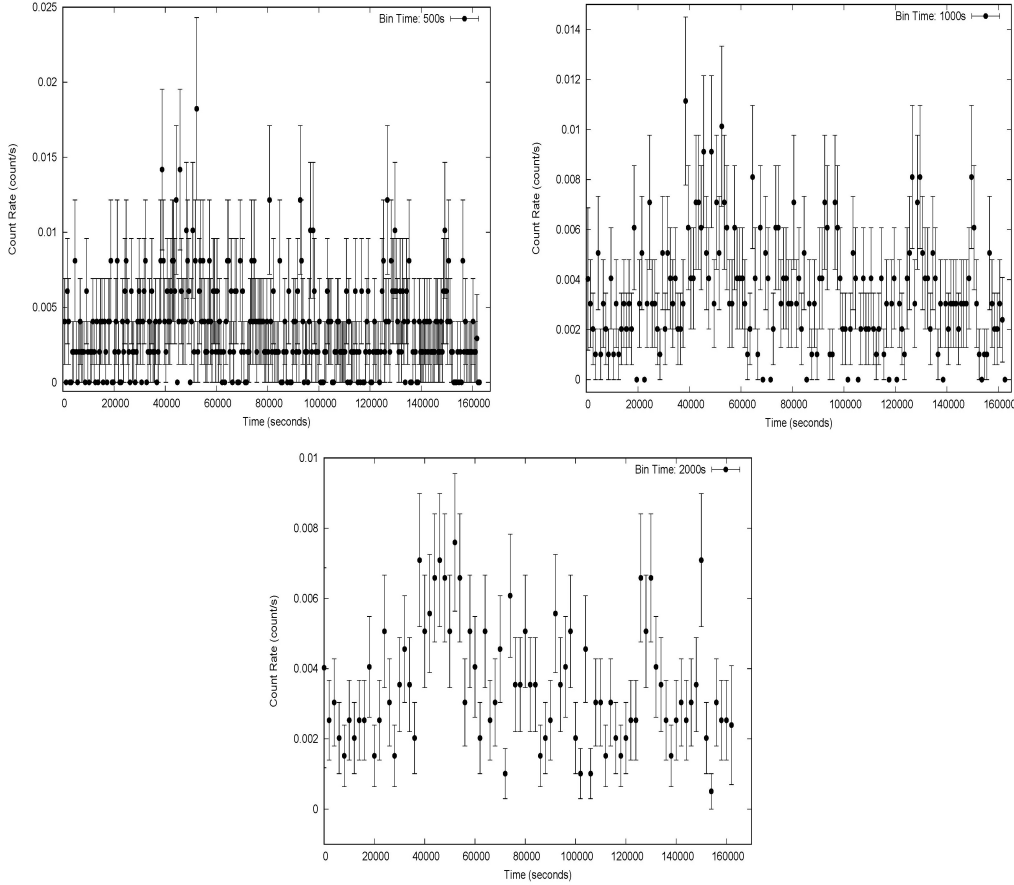


Figure 2. Lightcurve of ULX-1 binned at 0.5 ks, 1.0 ks & 2.0 ks

Again, to examine potential pulsations from the source, power spectra were generated using the FTOOL *powspec* within the 0.001 - 10 Hz frequency range. No pulsation signal was identified in the power spectra, diminishing the likelihood of ULX-1 being powered by a pulsating neutron star. It's crucial to note, however, that the limited timing capabilities of many sensitive X-ray instruments aboard satellites may have hindered the detection of the transient nature of pulsations in numerous variable sources. As a result, a more comprehensive future study, utilizing higher-quality data from alternative missions, could provide a clearer understanding of the genuine physical nature of this soft ULX, CXOUJ122956.7+075728 (ULX-1). Future observations and a detailed temporal study of this source are anticipated to contribute significantly to our understanding of the nature of this soft ULX.

5. SUMMARY AND CONCLUSION

We present the results of spectral and temporal analysis of the ULX - CXOUJ122956.7+075728 (ULX-1) in the elliptical galaxy NGC 4472 which is considered to be at a distance of around 16 Mpc. Even though *Chandra* has observed NGC 4472 many times in the last 21 years, the source of interest ULX-1 was significantly detected only in its observation of the year 2011 observation with Observation ID 12888. In this *Chandra* observation, ULX-1 was detected with an averagely detailed spectra with a source count ~ 556 . Initially, attempts were made to interpret ULX-1's spectrum using simple models, such as a single absorbed power-law or a single absorbed disk blackbody. However, both models yielded poor fit statistics. Subsequently, a two-component model, combining a standard thin disk model with a power-law component (diskbb + pow) in XSPEC, significantly improved the fit with $\chi^2/dof \approx 22.71/22$. This indicates that ULX-1's spectra are well-described by this two-component model, portraying a high-soft spectral state.

The derived spectral parameters reveal an X-ray luminosity (L_X) of approximately $6.99 \times 10^{39} \text{ erg s}^{-1}$, comprising a cool disk with $kT_{in} \sim 0.15$ keV and a power-law tail characterized by a photon index $\Gamma \sim 2.82$. The super soft spectra and the high luminosity suggests the presence of an Intermediate-Mass Black Hole (IMBH) with a mass estimate of $M_{BH} \sim 3.30 \times 10^3 M_{\odot}$ accreting at ~ 0.01 Eddington limit. Even in an extreme beaming scenario with a factor of $\eta \sim 5$, the estimated black hole mass remains relatively high at $M_{BH} \sim 1.47 \times 10^3 M_{\odot}$, supporting the likelihood of an IMBH rather than a stellar-mass black hole.

Additionally, investigations into the power spectra of ULX-1 ruled out pulsating neutron stars as a power source, and the observed significant variability in kilo-second time scales suggests potential instabilities in the accretion disk. However, a proper model of such accretion disk instability to explain the variability is pending further investigation. A comprehensive future study, leveraging higher-quality data from alternative missions, is needed for a deeper understanding of ULX-1's physical nature. Furthermore, ongoing observations and detailed temporal studies are expected to contribute significantly to unraveling the mysteries surrounding this soft ULX, CXOUJ122956.7+075728 (ULX-1).

Acknowledgments

The present work has used observational data from Chandra X-ray Center archive. The author expresses gratitude to the anonymous referee for their valuable suggestions, which have contributed to enhancing the quality of the paper.

ORCID

 A. Seniorita Devi, <https://orcid.org/0000-0001-9971-4262>

REFERENCES

- [1] P. Kaaret, H. Feng, and T. Roberts, "Ultraluminous X-ray sources," *Annu. Rev. Astron. Astrophys.* **55**, 303-341 (2017). <https://doi.org/10.1146/annurev-astro-091916-055259>.
- [2] J.M. Miller, A.C. Fabian, and M.C. Miller, "A Comparison of Intermediate-Mass Black Hole Candidate Ultraluminous X-Ray Sources and Stellar-Mass Black Holes," *ApJ*, **614**, L117 (2004). <https://doi.org/10.1086/425316>
- [3] M.C. Miller, and Colbert E.J.M., "Intermediate-mass black holes," *Int. J. Mod. Phys. D*, **13**(1), 1-64 (2004). <https://doi.org/10.1142/S0218271804004426>
- [4] E.J. Colbert, and R.F. Mushotzky, *Bulletin of the AAS*, **31**, 873 (1999).
- [5] O. Godet, B. Plazolles, T. Kawaguchi, J. Lasota, D. Barret, S. Farrell, V. Braito, et al., "Investigating slim disk solutions for HLX-1 in ESO 243-49," *Astrophys. J.* **752**, 34 (2012). <https://doi.org/10.1088/0004-637X/752/1/34>
- [6] A. Singha, and A. Devi, "Bimodal distribution of the hyperluminous X-ray sources," *Acta Astron.* **69**, 339-360 (2019). <https://doi.org/10.32023/0001-5237/69.4.3>
- [7] R. Abbott, et al., (LIGO Scientific Collaboration and Virgo Collaboration), "GW190521: A Binary Black Hole Merger with a Total Mass of 150 M_{\odot} ," *Phys. Rev. Lett.* **125**, 101102 (2020). <https://doi.org/10.1103/PhysRevLett.125.101102>
- [8] T. Sanatombi, A.S. Devi, and K.Y. Singh, "Spectral study of the Ultraluminous X-ray sources in M51 at different epochs of *Chandra* observation," *Chinese Journal of Physics*, **83**, 579-598 (2023). <https://doi.org/10.1016/j.cjph.2023.04.010>
- [9] A. Devi, R. Misra, K. Shanthi, and K. Singh, "The spectral and temporal properties of an ultraluminous X-ray source in NGC 6946," *Astrophys. J.* **682**, 218-222 (2008). <https://doi.org/10.1086/589710>
- [10] H.P. Earnshaw, T.P. Roberts, M.J. Middleton, D.J. Walton, and S. Mateoset, "A new, clean catalogue of extragalactic non-nuclear X-ray sources in nearby galaxies," *Mon. Not. R. Astron. Soc.* **483**, 5554-5573 (2019). <https://doi.org/10.1093/mnras/sty3403>
- [11] D.J. Walton, A.D.A. Mackenzie, H. Gully, N.R. Patel, T.P. Roberts, H.P. Earnshaw, and S. Mateos, "A multimission catalogue of ultraluminous X-ray source candidates," *MNRAS*, **509**(2), 1587-1604 (2022). <https://doi.org/10.1093/mnras/stab3001>
- [12] J. Gladstone, T. Roberts, and C. Done, "The ultraluminous state," *Mon. Not. R. Astron. Soc.* **397**, 1836-1851 (2009). <https://doi.org/10.1111/j.1365-2966.2009.15123.x>
- [13] M.J. Middleton, A.D. Sutton, T.P. Roberts, F.E. Jackson, and C. Done, "The missing link: a low-mass X-ray binary in M31 seen as an ultraluminous X-ray source," *MNRAS*, **420**, 2969 (2012). <https://doi.org/10.1111/j.1365-2966.2011.20145.x>
- [14] A. Sutton, T. Roberts, and M. Middleton, "The ultraluminous state revisited: Fractional variability and spectral shape as diagnostics of super-Eddington accretion," *Mon. Not. R. Astron. Soc.* **435**, 1758-1775 (2013). <https://doi.org/10.1093/mnras/stt1419>
- [15] E.S. Mukherjee, D.J. Walton, M. Bachetti, F.A. Harrison, D. Barret, E. Bellm, S.E. Boggs, F.E. Christensen, et al., "A Hard X-Ray Study of the Ultraluminous X-Ray source NGC 5204 X-1 with NuSTAR and XMM-NEWTON," *Astrophys. J.* **808**, 64 (2015). <https://doi.org/10.1088/0004-637X/808/1/64>
- [16] M. Middleton, L. Heil, F. Pintore, D. Walton, and T. Roberts, "A spectral-timing model for ULXs in the supercritical regime," *Mon. Not. R. Astron. Soc.* **447**, 3243-3263 (2015). <https://doi.org/10.1093/mnras/tu2644>

- [17] T. Ghosh, and V. Rana, "Super-Eddington accretion on to a stellar mass ultraluminous X-ray source NGC 4190 ULX1," MNRAS, **504**, 974–982 (2021). <https://doi.org/10.1093/mnras/stab774>
- [18] A. Gúrpide, O. Godet, F. Koliopanos, N. Webb, and J.F. Olive, "Long-term X-ray spectral evolution of ultraluminous X-ray sources: implications on the accretion flow geometry and the nature of the accretor," A&A, **649**, A104, (2021). <https://doi.org/10.1051/0004-6361/202039572>
- [19] V. Jithesh, "Spectral and temporal properties of ultra-luminous X-ray source NGC 55 ULX1," MNRAS, **509**, 5166–5178 (2022). <https://doi.org/10.1093/mnras/stab3307>
- [20] C. Pinto, W. Alston, R. Soria, M.J. Middleton, D.J. Walton, A.D. Sutton, A.C. Fabian, et al., "From ultraluminous X-ray sources to ultraluminous supersoft sources: NGC 55 ULX, the missing link," MNRAS, **468**(3), 2865–2883 (2017). <https://doi.org/10.1093/mnras/stx641>
- [21] C. Pinto, R. Soria, D. Walton, A. D’Ai, F. Pintore, P. Kosec, W.N. Alston, et al., "XMM-Newton campaign on the ultraluminous X-ray source NGC 247 ULX-1: outflows," Mon. Not. R. Astron. Soc. **505** 5058 (2021). <https://doi.org/10.1093/mnras/stab1648>
- [22] M. Bachetti, F. Harrison, D. Walton, B. Grefenstette, D. Chakrabarty, F. Fürst, D. Barret, A. Beloborodov, et al., "An ultraluminous X-ray source powered by an accreting neutron star," Nature, **514**, 202–212 (2014). <https://doi.org/10.1038/nature13791>
- [23] S. Carpano, F. Haberl, C. Maitra, and G. Vasilopoulos, "Discovery of pulsations from NGC 300 ULX1 and its fast period evolution," Mon. Not. R. Astron. Soc. **476**(1), L45–L49 (2018). <https://doi.org/10.1093/mnrasl/sly030>
- [24] R. Sathyaprakash, T.P. Roberts, D.J. Walton, F. Fuerst, M. Bachetti, C. Pinto, W.N. Alston, et al., "The discovery of weak coherent pulsations in the ultraluminous X-ray source NGC1313 X-2," Mon. Not. R. Astron. Soc. **488**, L35–L40 (2019). <https://doi.org/10.1093/mnrasl/slz086>
- [25] R. Castillo, G. Israel, A. Belfiore, F. Bernardini, P. Esposito, F. Pintore, A. De Luca, et al., "Discovery of a 2.8 s Pulsar in a 2 Day orbit high-mass X-ray binary powering the ultraluminous X-ray source ULX-7 in M51," Astrophys. J. **895**, 60 (2020). <https://doi.org/10.3847/1538-4357/ab8a44>
- [26] V. Doroshenko, et al., "First characterization of Swift J1845.7-0037 with Nustar," Astron. & Astroph. **634**, A89 (2020). <https://doi.org/10.1051/0004-6361/201937036>
- [27] V. Jithesh, C. Anjana, and R. Misra, "Broadband X-ray spectral study of ultraluminous X-ray source M81 X-6," MNRAS, **494**, 4026 (2020). <https://doi.org/10.1093/mnras/staa976>
- [28] M.I. Krauss, R.E. Kilgard, M.R. Garcia, T.P. Roberts, and A.H. Prestwich, "M74 X-1 (CXOU J013651.1+154547): An Extremely Variable Ultraluminous X-Ray Source," ApJ, **630**, 228 (2005). <https://doi.org/10.1086/431784>
- [29] T.D. Joseph, T.J. Maccarone, R.P. Kraft, and G.R. Sivakoffet, "A deeper look at the X-ray point source population of NGC 4472," MNRAS, **470**, 4133–4144 (2017). <https://doi.org/10.1093/mnras/stx1383>
- [30] L.M. Macri, J.P. Huchra, P.B. Stetson, N.A. Silbermann, W.L. Freedman, R.C. Kennicutt, J.R. Mould, et al., "The Extragalactic Distance Scale Key Project. XVIII. The Discovery of Cepheids and a New Distance to NGC 4535 Using the *Hubble Space Telescope*," ApJ, **521**, 155 (1999). <https://doi.org/10.1086/307541>
- [31] A. Devi, and K. Singh, "Discovery of an ultra-luminous X-ray source candidate, ULX (X-8) in NGC 3384 with *Chandra*," Astrophys. Space Sci. **354**, 535–540 (2014). <https://doi.org/10.1007/s10509-014-2091-8>
- [32] A.R. King, M.B. Davies, M.J. Ward, G. Fabbiano, and M. Elvis, "Ultraluminous X-ray Sources in External Galaxies," Astrophys. J. **552**, L109–L112 (2001). <https://doi.org/10.1086/320343>
- [33] R. Misra, and K. Sriram, "Flux enhancement in the inner region of a geometrically and optically thick accretion disk," Astrophys. J. **584**, 981–984 (2003). <https://doi.org/10.1086/345742>

СПЕКТРАЛЬНІ ТА ЧАСОВІ ВЛАСТИВОСТІ CXOUJ122956.7+075728 (ULX-1), НАДЯСКРАВОГО РЕНТГЕНІВСЬКОГО ДЖЕРЕЛА В NGC 4472




А. Сенорита Деві

Факультет фізики, Маніпурський університет, Імфал, Індія

У цьому дослідженні представлено комплексний аналіз спектральних і часових характеристик надзвичайно важливого надяскравого рентгенівського джерела (ULX), позначеного як CXOUJ122956.7+075728 (ULX-1), розташованого в еліптичній галактиці NGC 4472 у скупченні Діви. ULX-1 демонструє м'який спектральний стан із прохолодною компонентою акреційного диска з $kT_{in} \sim 0,15$ keV, що супроводжується хвостом степеневого закону, що відображає крутий степеневий фотонний індекс, $\Gamma \sim 2,8$. Спектральні результати переконливо підтверджують розрахункову масу чорної діри приблизно $3,30 \times 10^3 M_{\odot}$ за моделлю ізотропного випромінювання та близько $1,47 \times 10^3 M_{\odot}$ за сценарієм екстремального випромінювання. У часі ULX-1 демонструє значну мінливість на часових шкалах 0,5, 1 і 2 кс, що свідчить про можливість нестабільності всередині акреційного диска, що сприяє такій поведінці. Однак, незважаючи на таку часову мінливість, аналіз спектрів потужності цього м'якого ULX не виявляє ознак пульсацій, що відрізняє його від певних пульсуючих ULX (PULX), які зазвичай асоціюються з нейтронними зірками. Ця відсутність пульсацій в ULX-1 ще більше підкреслює його унікальні спектральні та часові характеристики в ширшому контексті явищ ULX.

Ключові слова: акреція, акреційні диски; галактики: індивідуальні (NGC 4472); рентгенівські промені: бінарні

PERFECT FLUID WITH HEAT FLOW IN $f(T)$ THEORY OF GRAVITY

 D.D. Pawar^{a*},  N.G. Ghungarwar^b,  P.S. Gaikwad^a

^a*School of Mathematical Sciences, SRTM University, Nanded-431606, Maharashtra, India*

^b*Shri D. M. Burungale Science and Arts College, Shegaon-444203, Maharashtra, India*

* *Corresponding Author e-mail: dypawar@yahoo.com*

Received December 19, 2023; revised February 4, 2024; accepted February 10, 2024

Bianchi Type-I cosmological models have been a subject of extensive research in cosmology due to their simplicity and relevance in understanding the dynamics of the early Universe. In this study, we investigate the dynamics of such models within the framework of $f(T)$ gravity, an alternative theory of gravity that extends teleparallel gravity by introducing a general function of the torsion scalar, T . We focus on the presence of a perfect fluid with heat flow in the cosmic medium. By solving the field equations of $f(T)$ gravity, we obtain exact solutions for the Bianchi Type-I cosmological models. These solutions provide valuable insights into the evolution of the Universe and how it is influenced by the modified gravity theory. Furthermore, we derive cosmological parameters in terms of redshift, offering a convenient way to interpret observational data and connect theoretical predictions to empirical measurements. Our findings not only contribute to a deeper understanding of the dynamics of Bianchi Type-I cosmological models but also provide a foundation for comparing $f(T)$ gravity with standard general relativity in the context of observational cosmology. This research paves the way for further exploration of alternative gravity theories and their implications for the early Universe's evolution and structure.

Keywords: $f(T)$ theory; Perfect fluid with heat flow; Bianchi type-I

PACS: 98.80.-k, 04.20.-q, 04.50.Kd

1. INTRODUCTION

The study of cosmological models has been instrumental in advancing our understanding of the evolution and structure of the Universe. In this context, Bianchi Type-I cosmological models have played a crucial role due to their inherent simplicity and applicability to various cosmological scenarios. These models assume a homogeneous and anisotropic distribution of matter and radiation in the early Universe, making them a valuable tool for investigating the dynamics of cosmic expansion.

Banerjee et al. [1] al. conducted investigations on Bianchi I cosmological models that incorporate a fluid possessing both bulk and shear viscosity. These studies reveal the evolving significance of shear viscosity and fluid density dynamics throughout the cosmic evolution. Sharif and Rani [2] have studied spatially homogeneous and anisotropic Bianchi type I universe in the context of $F(T)$ gravity. Beesham and Aroonkumar [3] studied Bianchi type I cosmological models with variable gravitational constants (G) and cosmological constants (Λ). Jacobs and Kenneth [4] Explored cosmologies of Bianchi type I with a uniform magnetic field. Sahoo and Sivakumar [5] examined LRS (Locally Rotationally Symmetric) Bianchi type-I cosmological models in $f(R, T)$ theory of gravity. Barrow [6] et al. analyzed the asymptotic stability of Bianchi type universes. Ashtekar [7] et al. Investigated loop quantum cosmology of Bianchi type I models. Akarsu [8] et al. explored LRS Bianchi type I models with anisotropic dark energy and constant deceleration parameters. Pawar [9] et al. investigated magnetized anisotropic dark energy by using Barber's self-creation theory. Saha [10] et al. investigated Bianchi type-I cosmology with scalar and spinor fields and they also Studied spinor fields in a Bianchi type-I universe, focusing on regular solutions. Jamil [11] et al. explored FRW and Bianchi type I cosmology of f -essence. Singh [12] et al. Explored Bianchi type-I cosmological models in Lyra's geometry. Singh [13] et al. analyzed Bianchi type-I cosmological models with variable G and Λ -term in general relativity. Arbab [14] has studied Bianchi type I viscous universe with variable G and Λ . Rodrigues [15] et al. have investigated Bianchi type-I, type-III, and Kantowski-Sachs solutions in $f(T)$ gravity. Shamir [16] has explored locally rotationally symmetric Bianchi type I cosmology in $f(R, T)$ gravity. Chirde [17] et al. Analyzed a Bianchi type I cosmological model with a perfect fluid and string in $f(T)$ theory of gravitation. Wanas [18] et al. have investigated Bianchi type I cosmological models in $f(T)$ gravitational theories. Fayaz [19] have studied $f(T)$ theories from holographic dark energy models within a Bianchi type I universe. Rodrigues [20] have explored locally rotationally symmetric Bianchi type-I cosmological models in $f(T)$ gravity, spanning from early to dark energy-dominated universes. Aslam [21] et al. have investigated Noether gauge symmetry for the Bianchi type I model in $f(T)$ gravity. Qazi [22] et al. have explored conformal vector fields of Bianchi type-I perfect fluid solutions in $f(T)$ gravity. Hasmani

Cite as: D.D. Pawar, N.G. Ghungarwar, P.S. Gaikwad, East Eur. J. Phys. 1, 102 (2024), <https://doi.org/10.26565/2312-4334-2024-1-08>

© D.D. Pawar, N.G. Ghungarwar, P.S. Gaikwad, 2024; CC BY 4.0 license

and Al-Haysah [23] have provided exact solutions for Bianchi type-I cosmological models in $f(R)$ Theory of Gravity. Shekh [24] et al. have explored an accelerating Bianchi type dark energy cosmological model with a cosmic string in $f(T)$ gravity. Koussour and Bennai [25] have conducted a stability analysis of anisotropic Bianchi type-I cosmological model in teleparallel gravity. Dawande [26] et al. have investigated LRS Bianchi Type-I Universe in $f(T)$ Theory of Gravity. Shukla [27] et al. have explored a Bianchi type-I cosmological model in a modified theory of gravity. Van den Hoogen [28] et al. investigated Bianchi type cosmological models in $f(T)$ tele-parallel gravity. Shamir [29] et al. have explored locally rotationally symmetric Bianchi type I cosmology in $f(R)$ gravity. Rodrigues [30] et al. analyzed anisotropic universe models in $f(T)$ gravity. Pawar [31] et al. have investigated LRS Bianchi type-I cosmological models in $f(Q, T)$ theory of gravity with observational constraints. Dagwal [32] has explored tilted two forms of dark energy in $f(T)$ theory of gravity. Solanke [33] et al. have studied an accelerating dark energy universe with LRS Bianchi type-I space-time. Pradhan [34] et al. have investigated Bianchi type I anisotropic magnetized cosmological models with varying Λ . General Relativity (GR), formulated by Albert Einstein, has long been the cornerstone of our understanding of gravitational interactions in the cosmos. However, in recent decades, alternative theories of gravity have gained attention, offering different perspectives on the gravitational field equations. One such alternative is $f(T)$ gravity [35], which extends the concept of teleparallel gravity by introducing a general function of the torsion scalar, T . Pawar et al.[36] have studied anisotropic behaviour of perfect fluid in fractal cosmology. $f(T)$ gravity has been explored as a viable alternative to GR, providing a framework to study the gravitational dynamics of the Universe beyond the confines of Einstein's theory.

In this research, we delve into the dynamics of Bianchi Type-I cosmological models within the framework of $f(T)$ gravity[37]. Our primary focus is on the inclusion of a perfect fluid with heat[38], which is crucial in understanding the thermodynamic aspects of the early Universe. By solving the field equations derived from $f(T)$ gravity, we aim to obtain exact solutions for the evolution of the Universe in the presence of these additional components. Pawar et al. [39]-[40] have studied several aspects of Bianchi Type-I with Two fluid axially symmetric cosmological models in $f(R, T)$ theory of gravitation and Tilted congruences with stiff fluid cosmological models.

Furthermore, one of the essential aspects of cosmological models is their ability to provide a connection between theoretical predictions and empirical observations. To facilitate this connection, we derive cosmological parameters that are expressed in terms of redshift, a key observational quantity. This approach enables us to relate our theoretical findings to astronomical data, enhancing the applicability and relevance of our research to the broader field of observational cosmology.

In summary, this research presents a comprehensive exploration of Bianchi Type-I cosmological models in $f(T)$ gravity, incorporating a perfect fluid with heat. The obtained solutions and derived cosmological parameters contribute to our understanding of the early Universe's dynamics and offer a bridge between theoretical predictions and observational data.

2. FIELD EQUATION

The line element for a flat, homogeneous and anisotropic LRS Bianchi type-I space time[41] is

$$ds^2 = dt^2 - A^2(t)dx^2 - B^2(t) [dy^2 + dz^2] \quad (1)$$

Here, t represents time, x is one spatial coordinate, and y and z are the other two spatial coordinates. The functions $A(t)$ and $B(t)$ are scale factors that describe the expansion or contraction of the space in the x and y - z directions, respectively.

We obtain the tetrad components as follows:

$$h_i^\mu = \text{diag}(1, A^{-1}, B^{-1}, B^{-1}) \quad (2)$$

The torsion scalar, denoted as “ T ,” is a scalar derived from the torsion tensor. It quantifies the deviation of the Weitzenböck connection from the Levi-Civita connection, which is used in general relativity. In simple terms, the torsion scalar reflects the inhomogeneity in the spacetime geometry due to torsion. The torsion scalar has the form

$$T = S_\rho^{\mu\nu} T_{\mu\nu}^\rho \quad (3)$$

The formulation of this theory's action involves extending and building upon the foundational principles of the Teleparallel Theory of Gravity.

$$I = \int e[f(T) + L_{\text{matter}}]d^4x \quad (4)$$

In this context, $f(T)$ signifies a function concerning with the torsion scalar T . Meanwhile, L_{matter} stands for the Lagrangian density associated with matter. Additionally, “ e ” corresponds to the determinant of the tetrad

field, which is intricately linked to the metric tensor through the relationship $e = \sqrt{-g}$. The non vanishing components of torsion tensor are defined as

$$T_{\mu\nu}^{\rho} = \Gamma_{\nu\mu}^{\rho} - \Gamma_{\mu\nu}^{\rho} = h_i^{\rho}(\partial_{\mu}h_{\nu}^i - \partial_{\nu}h_{\mu}^i) \tag{5}$$

The elements of the corresponding contorsion tensor are characterized by:

$$K_{\rho}^{\mu\nu} = -\frac{1}{2}(T_{\rho}^{\mu\nu} - T_{\rho}^{\nu\mu} - T_{\rho}^{\mu\nu}) \tag{6}$$

The determination of the elements of the tensor $S_{\rho}^{\mu\nu}$ is carried out in the following manner:

$$S_{\rho}^{\mu\nu} = \frac{1}{2}(K^{\mu\nu}_{\rho} + \delta_{\rho}^{\mu}T^{\theta\nu}_{\theta} - \delta_{\rho}^{\nu}T^{\theta\mu}_{\theta}) \tag{7}$$

By using above components we have computed the torsion scalar, “T,” as follows:

$$T = -2 \left(2 \frac{\dot{A}\dot{B}}{AB} + \frac{\dot{B}^2}{B^2} \right) \tag{8}$$

The derivation of the modified field equation in the teleparallel theory of gravity involves obtaining it through the variation of the action concerning the vierbein components, denoted as h_{μ}^i . This is expressed as:

$$S_{\mu}^{\nu\rho}\partial_{\rho}Tf_{TT} + [e^{-1}e^i_{\mu}\partial_{\rho}(ee^{\alpha}_i S_{\alpha}^{\nu\rho} + T_{\lambda\nu}^{\alpha}S_{\lambda\alpha}^{\nu})]f_T + \frac{1}{4}\delta_{\nu}^{\mu}f = 4\pi T_{\nu}^{\mu} \tag{9}$$

Where T_{μ}^{ν} is the energy momentum tensor, $f_T = \frac{df}{dT}$ and $f_{TT} = \frac{d^2f}{dT^2}$
 The energy momentum tensor for perfect fluid with heat flow [42] is

$$T_{ij} = (\rho + p)u_i u_j + pg_{ij} + h_i u_j + h_j u_i \tag{10}$$

where ρ is the energy density, p is thermodynamic pressure, h_i is heat flow vector. The field equation corresponding to metric (1) are obtained by

$$f + 4f_T \left[\frac{\dot{B}^2}{B^2} + 2\frac{\dot{A}\dot{B}}{AB} \right] = -16\pi\rho \tag{11}$$

$$f + 4f_T \left[\frac{\ddot{B}}{B} + \frac{\dot{B}^2}{B^2} + \frac{\dot{A}\dot{B}}{AB} \right] + 4\frac{\dot{B}}{B}\dot{T}f_{TT} = 16\pi p \tag{12}$$

$$f + 2f_T \left[\frac{\ddot{A}}{A} + \frac{\ddot{B}}{B} + \frac{\dot{B}^2}{B^2} + 3\frac{\dot{A}\dot{B}}{AB} \right] + 2 \left(\frac{\dot{A}}{A} + \frac{\dot{B}}{B}\dot{T}f_{TT} \right) = 16\pi p \tag{13}$$

The crucial parameters in cosmological observations include the mean scale factor a , mean Hubble parameter H , scalar expansion θ , deceleration parameter q , shear scalar σ^2 , and mean anisotropic parameter A_m . These quantities, derived from metric (1), are expressed as:

$$a = (AB^2)^{1/3} \tag{14}$$

$$H = \frac{1}{3} \left(\frac{\dot{A}}{A} + 2\frac{\dot{B}}{B} \right) \tag{15}$$

$$\theta = \frac{\dot{A}}{A} + 2\frac{\dot{B}}{B} \tag{16}$$

$$q = -\frac{a\ddot{a}}{\dot{a}^2} = \frac{d}{dt} \left(\frac{1}{H} - 1 \right) \tag{17}$$

$$A_m = \frac{2}{9H^2} \left(\frac{\dot{A}}{A} - \frac{\dot{B}}{B} \right)^2 \tag{18}$$

3. SOLUTION OF FIELD EQUATION

Solving field equations (11), (12) and (13) we obtain

$$A(t) = \{(3 + 2m)(c_1t + c_2)\}^{\frac{m}{3+2m}} \tag{19}$$

and

$$B(t) = \{(3 + 2m)(c_1t + c_2)\}^{\frac{1}{3+2m}} \tag{20}$$

using equations (19) and (20) we get

$$T = \frac{-2(1 + 2m)}{(3 + 2m)^2 \cdot (c_1t + c_2)^2} \tag{21}$$

$$f = -4K \frac{(1 + 2m)}{(5 + 3m)} (3 + 2m)^{\frac{2+m}{3+2m}} c_1^2 (c_1t + c_2)^{-\frac{5+3m}{3+2m}} \tag{22}$$

$$\rho = \frac{K}{4\pi} \frac{(1 + 2m)(2 + m)}{(5 + 3m)} c_1^2 ((3 + 2m)(c_1t + c_2))^{-\frac{5+3m}{3+2m}} \tag{23}$$

$$p = \frac{K}{4\pi} \frac{(1 + 2m)}{(5 + 3m)} (3 + 2m)^{\frac{2+m}{3+2m}} c_1^2 (c_1t + c_2)^{-\frac{5+3m}{3+2m}} \tag{24}$$

The formulas for the Hubble parameter H , scalar expansion θ , shear scalar σ , and the mean anisotropic parameter A_m are obtained as follows:

$$\theta = 3H = c_1 \frac{2 + m}{3 + 2m} (c_1t + c_2)^{-1} \tag{25}$$

$$\sigma^2 = \frac{1}{3} \left(\frac{m - 1}{3 + 2m} \right)^2 c_1^2 (c_1t + c_2)^{-2} \tag{26}$$

$$A_m = \frac{2m^2 - 4m + 2}{(m + 2)^2} \tag{27}$$

The value of the deceleration parameter is found to be

$$q = \frac{5m + 7}{m + 2} \tag{28}$$

which is constant.

By using $1 + z = \frac{a_0}{a}$ we get above physical parameters in terms of redshift z .

The torsion scalar is a geometric quantity associated with theories of gravity that incorporate torsion in addition to curvature. In the context of general relativity (which does not include torsion), the torsion tensor is assumed to be zero. However, in alternative theories of gravity, such as the Einstein-Cartan theory, torsion is considered. We have obtained torsion scalar in terms of redshift.

$$T = \frac{-2(1 + 2m)}{(3 + 2m)^2} c_1^3 \frac{(1 + z)^{\frac{3+2m}{m+2}}}{(3 + 2m)} \tag{29}$$

Figure 1 illustrates the correlation between the torsion scalar T and the redshift z across various constant m values in cosmological observations. The torsion scalar T , measuring spacetime geometry deviation from standard general relativity due to torsion, consistently exhibits negative values across all z and m , indicating a departure from general relativity. Redshift z , serving as a gauge of universe expansion and object distance, increases as the torsion scalar T decreases, suggesting a more pronounced deviation from general relativity in earlier cosmic epochs. Moreover, the value of m influences both the slope and magnitude of the torsion scalar T depicted in the figure, with higher m values corresponding to steeper slopes and smaller magnitudes of T .

$$f = \frac{-4K(1 + 2m)}{(5 + 3m)(3 + 2m)} (1 + z)^{-3 \frac{(5+3m)}{m+2}} \tag{30}$$

The relationship between pressure (P) and redshift (z) in cosmology is characterized by the equation of state parameter (ω). In the early universe dominated by radiation, ω is $\frac{1}{3}$, indicating positive pressure. As non-relativistic matter becomes dominant, ω for matter is 0, representing zero pressure. Dark energy, with a constant $\omega < 0$, contributes a negative pressure and is associated with the observed accelerated expansion of the universe.

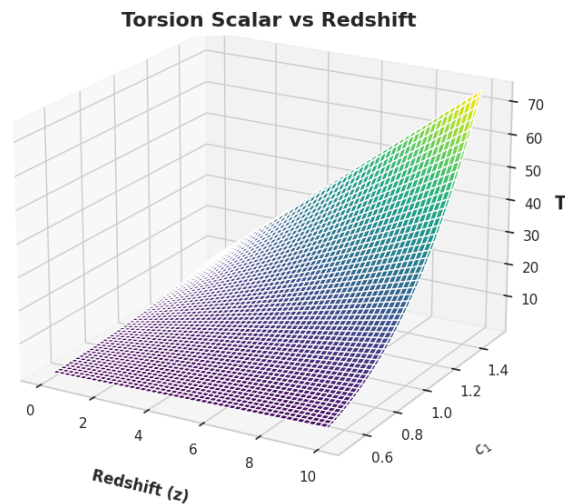


Figure 1. Torsion Scalar vs Redshift for $m = -1, 0.5 < c_1 < 1.5$

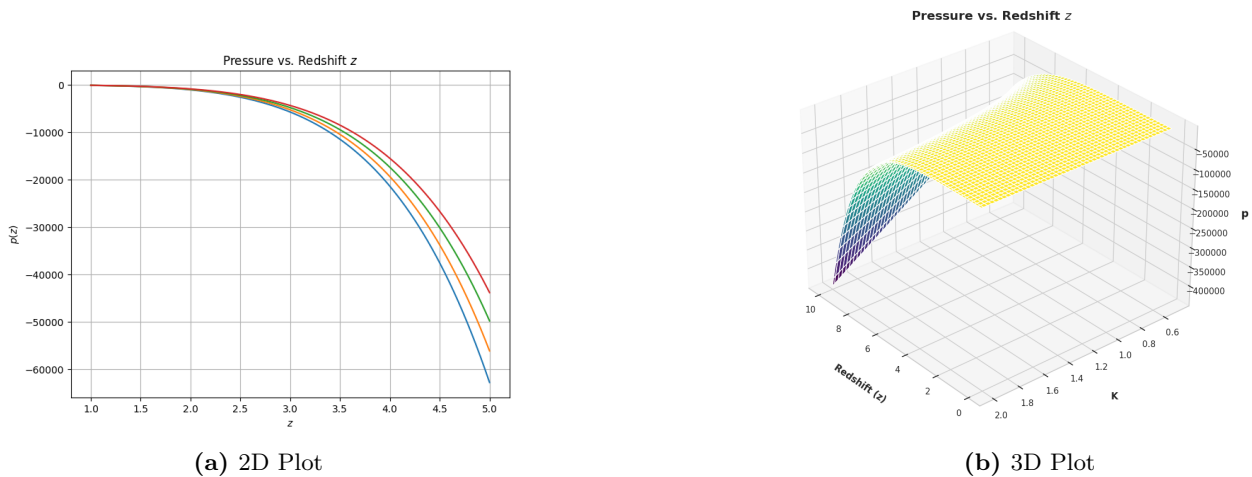


Figure 2. The plot of pressure vs cosmic redshift z

The pressure is calculated as follows:

$$p = \frac{K}{4\pi} \frac{(1 + 2m)(2 + m)}{(5 + 3m)} (3 + 2m)(1 + z)^{\frac{3(5+3m)}{m+2}} \tag{31}$$

In Figure 2, pressure is plotted against cosmic redshift z for different values of m , a constant in the Bianchi type-I cosmological model relating the expansion scalar and shear scalar. Pressure consistently exhibits negativity across all m and z values, indicative of a tension-like effect associated with dark energy, presumed to fuel the universe’s accelerated expansion. With increasing redshift, pressure diminishes, reflecting a rise in dark energy density over time and its eventual dominance over matter and radiation in the late universe. Notably, smaller values of m correspond to more negative pressure, suggesting a heightened repulsive gravitational effect, where the anisotropy of the Bianchi type-I model enhances the impact of dark energy.

The relationship between energy density and redshift is influenced by the contributions from radiation, matter, dark energy, and possibly other components, and it is described by the evolving scale factor in the Friedmann equations of cosmology. Here we have obtained the energy density in terms of redshift for perfect fluid.

$$\rho = \frac{K}{4\pi} \frac{(1 + 2m)(2 + m)}{(5 + 3m)} (1 + z)^{-\frac{3(5+3m)}{m+2}} \tag{32}$$

From Figure 3 we observed that the density of the universe is positive and decreases with increasing redshift. Additionally, the density of the universe is higher for lower values of m , indicating a stronger influence

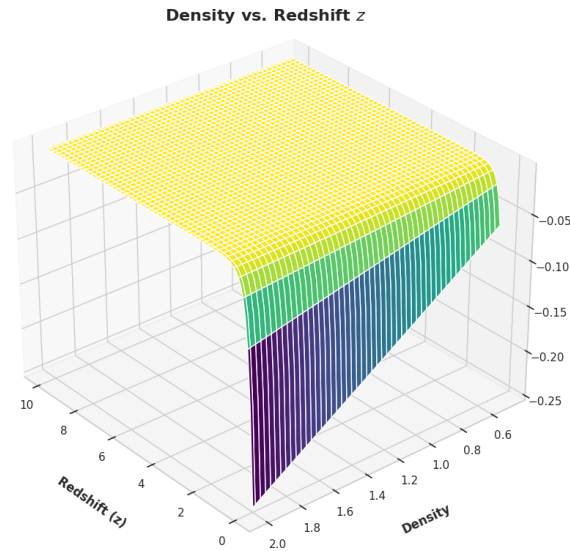


Figure 3. Density vs Redshift for $m = -1$

of matter on the cosmic expansion. Moreover, the density of the universe approaches zero as the redshift approaches infinity, implying a negligible contribution of matter in the early universe.

The equation of state parameter, typically denoted by ω , relates the pressure (p) to the energy density (ρ) of a substance. It's defined as $\omega = \frac{p}{\rho}$. The equation of state parameter (ω) characterizes the relationship between pressure and energy density in the universe. In the early universe, dominated by radiation, ω is $1/3$. As non-relativistic matter becomes dominant, ω for matter is 0 , and for dark energy, assumed constant, ω is < 0 . The evolution of ω with redshift reflects the changing contributions of different cosmic components to the energy density over cosmic time. We have calculated the equation of state parameter in terms of redshift as follows:

$$\omega = (3 + 2m)(1 + z)^{\frac{6(5+3m)}{m+2}} \tag{33}$$

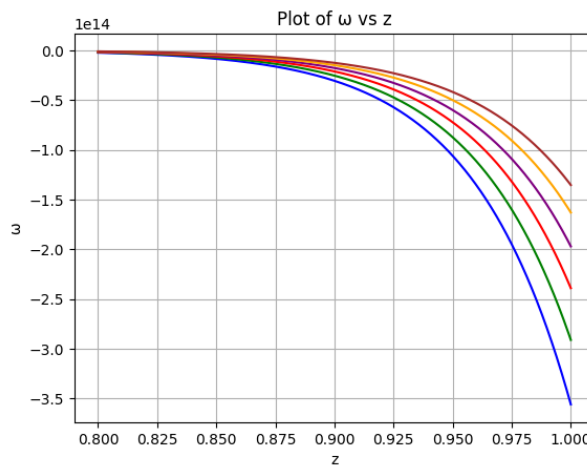


Figure 4. Equation of state parameter vs redshift

In Figure 4, we see how a parameter called the equation of state ω changes as the redshift z varies for different values of m . This parameter helps us understand the relationship between pressure and energy density in the universe. Some important points from Figure 4 include: all the curves have negative values for ω , indicating negative pressure, which is often associated with dark energy driving the universe's accelerated expansion; as the redshift increases, indicating earlier times in the universe, the negative pressure becomes stronger, suggesting that dark energy played a bigger role in the early universe; and the shape of the curves varies depending on the value of m , which reflects how the universe is structured (its anisotropy), indicating that the equation of state depends on the universe's structure.

The relationship between the Hubble parameter (H) and redshift (z) is often expressed in the context of the Friedmann-Lemaître-Robertson-Walker (FLRW) metric, which describes the expanding universe in cosmology. The Hubble parameter is related to the rate of expansion of the universe.

Hubble parameter H is calculated as:

$$H = \frac{2 + m}{3} (1 + z)^{\frac{3(3+2m)}{m+2}} \tag{34}$$

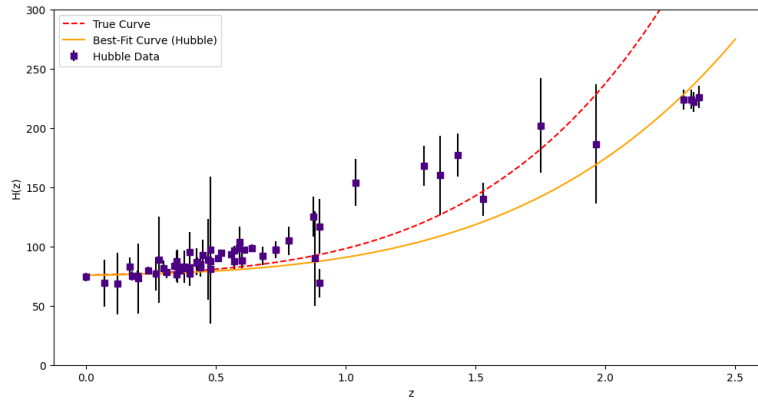


Figure 5. The plot of Hubble parameter vs Redshift along with Hubble Data-Set

In Figure 5, we observe how the universe expands over time. It shows that as we look back in time, the universe expanded more slowly, measured by something called the Hubble parameter H at different redshifts z . The graph also indicates that the Hubble parameter is influenced by a constant called “ m ,” which affects how the universe expands in a the model. Additionally, the graph compares theoretical expectations with real observations from telescopes like the Hubble Space Telescope and the Sloan Digital Sky Survey, and they seem to match up quite well, considering the uncertainties.

4. DISCUSSION AND CONCLUSION

Redshift in cosmology refers to the phenomenon where the light from distant galaxies or celestial objects appears to be shifted towards longer wavelengths, moving towards the red end of the electromagnetic spectrum. This is primarily due to the expansion of the universe.

As the universe expands, the space between galaxies also expands, causing the wavelengths of light emitted by these galaxies to stretch. This stretching of light results in a shift towards longer wavelengths, which is observed as a redshift. The greater the distance to a galaxy, the higher its redshift. Redshift is a crucial tool for astronomers in measuring the distances to and the velocities of objects in the universe.

In terms of redshift, as the universe expands, the effects of dark energy become more pronounced. If the pressure associated with dark energy remains negative, it can counteract the attractive force of gravity, leading to an accelerated expansion. This is consistent with the observations of distant supernovae and other cosmological data. The behavior of the universe is influenced when w is negative:

- **Accelerated Expansion:** The negative pressure associated with dark energy leads to an accelerated expansion of the universe. This is in contrast to matter, which has positive pressure and tends to slow down the expansion due to gravitational attraction.
- **Dominance at Late Times:** As the universe expands, the effects of dark energy become more pronounced over time. In the current epoch of the universe, dark energy is believed to be the dominant component, driving the observed acceleration.
- **Redshift of Distant Objects:** The acceleration of the universe affects the redshift of distant galaxies. Observationally, distant supernovae and other cosmological probes indicate that the rate of expansion is increasing with time.

The effect of the Hubble parameter on the universe can be summarized as follows:

- **Expansion Rate:** The Hubble parameter at a given redshift, $H(z)$, indicates the rate at which the universe is expanding at that particular cosmic time. A higher value of $H(z)$ implies a faster rate of expansion.

- **Historical Expansion:** Observing the Hubble parameter at different redshifts allows us to study the historical expansion of the universe. By looking at more distant objects, corresponding to higher redshifts, we are effectively looking back in time.
- **Cosmic Acceleration:** Changes in the Hubble parameter with redshift can provide insights into the cosmic acceleration. In a universe dominated by dark energy, the Hubble parameter may not decrease as much with increasing redshift as in a universe without dark energy.
- **Critical Density Determination:** The Hubble parameter is related to the critical density of the universe (ρ_{crit}). Understanding its behavior with redshift helps in determining the overall energy content and fate of the universe.

In this research, we explore the characteristics of the Bianchi type-I space-time within the framework of $f(T)$ gravity theory, where T represents the torsion scalar. The model is constructed based on specific assumptions. The first assumption posits a proportional relationship between the expansion scalar θ and the shear scalar σ , leading to the expression $A = B^m$, where A and B are metric coefficients, and m is a real constant. The second assumption sets equal pressure components in the x , y , and z directions, governed by an equation of state $p = \omega\rho$. Additionally, a power-law relation between F and the scale factor B is employed to derive the exact solution of the field equations.

Several key cosmological parameters, including the torsion scalar T pressure p , density ρ , equation of state parameter ω Hubble parameter H in terms of cosmic time t and redshift z . The behaviour of the graph of the pressure vs redshift shows that the pressure is negative and constatly decreasing for the various values of $m = -1.03, -1.05, -1.07, -1.09$. If the pressure is negative (which corresponds to a situation where the substance has a tension-like effect rather than compressive), it can have significant implications for the evolution of the universe. A substance with negative pressure is often referred to as "exotic" or "dark energy."

The most well-known example of dark energy is the cosmological constant (Λ) associated with the vacuum of space. A negative pressure is a key component of dark energy because it's believed to be responsible for the observed accelerated expansion of the universe. The graph of density vs redshift we have plotted in 3D which shows that the density is positive. A positive density in terms of redshift typically refers to the energy density of matter in the universe. In cosmology, matter can have positive density, and its effects are often associated with the deceleration of the universe's expansion.

The pressure and density with the redshift shows the singularity at $m = -2$. Notably, the equation of state parameter ω shows the the negative behaviour and graph decreases rapidly for the values of $m = -2.201, -2.203, -2.205, -2.207, -2.209, -2.211$. When the equation of state parameter (w) in terms of redshift is negative, it implies that the substance in question has a negative pressure. This scenario is often associated with dark energy, which is believed to be responsible for the observed accelerated expansion of the universe.

The equation of state parameter is defined as $w = \frac{p}{\rho}$, where p is the pressure and ρ is the energy density. For dark energy, the negative pressure contributes to a repulsive gravitational effect, counteracting the attractive force of gravity caused by matter.

The Hubble parameter H plotted vs redshift z . The graph shows the values of Hubble parameter in the range of standard dataset which supports the current observational data.

The Hubble parameter in terms of redshift is a crucial observational quantity that informs us about the current state and past history of the universe's expansion. Studying its behavior with redshift provides valuable information about the underlying cosmological model and the influence of various components like matter, radiation, and dark energy on the evolution of the cosmos.

ORCID

📧 D.D. Pawar, <https://orcid.org/0000-0001-8986-5243>; 📧 N.G. Ghungarwar, <https://orcid.org/0009-0004-2292-1537>; 📧 P.S. Gaikwad, <https://orcid.org/0009-0001-2443-8969>

REFERENCES

- [1] A. Banerjee, S.B. Duttachoudhury, and A.K. Sanyal, "Bianchi type I cosmological model with a viscous fluid," Journal of mathematical physics, **26**(11), 3010-3015 (1985). <https://doi.org/10.1063/1.526676>
- [2] M. Sharif, and S. Rani. "F(T) models within bianchi type-i universe," Modern Physics Letters A, **26**(22), 1657-1671 (2011). <https://doi.org/10.1142/S0217732311036127>
- [3] A. Beesham, "Bianchi type I cosmological models with variable G and A," General relativity and gravitation, **26**, 159-165 (1994). <http://dx.doi.org/10.1007/BF02105151>
- [4] K.C. Jacobs, "Cosmologies of Bianchi type I with a uniform magnetic field," Astrophysical Journal, **155**, 379-155 (1969). <https://doi.org/10.1086/149875>
- [5] P.K. Sahoo, and M. Sivakumar, "LRS Bianchi type-I cosmological model in f(R,T) theory of gravity with $\Lambda(T)$," Astrophysics and Space Science, **357**, 60 (2015). <https://doi.org/10.1007/s10509-015-2264-0>

- [6] J.D. Barrow, and D.H. Sonoda, "Asymptotic stability of Bianchi type universes," *Physics Reports*, **139**(1), 1-49 (1986). [https://doi.org/10.1016/0370-1573\(86\)90025-6](https://doi.org/10.1016/0370-1573(86)90025-6)
- [7] A. Ashtekar, and E. Wilson-Ewing, "Loop quantum cosmology of Bianchi type I models," *Physical Review D*, **79**(8), 083535 (2009). <https://doi.org/10.1103/PhysRevD.79.083535>
- [8] Ö. Akarsu, and C.B. Kilinç. "LRS Bianchi type I models with anisotropic dark energy and constant deceleration parameter," *General Relativity and Gravitation*, **42**, 119-140 (2010). <https://doi.org/10.1007/s10714-009-0821-y>
- [9] D. D. Pawar, Y. S. Solanke, "Magnetized Anisotropic Dark Energy Models in Barber's Second Self-Creation Theory", *Advances in High Energy Physics*, **2014**, Article ID 859638, 9 pages, 2014. <https://doi.org/10.1155/2014/859638>
- [10] B. Saha, and T. Boyadjiev, "Bianchi type-I cosmology with scalar and spinor fields," *Physical Review D*, **69**(12), 124010 (2004). <https://doi.org/10.1103/PhysRevD.69.124010>
- [11] M. Jamil, D. Momeni, N.S. Serikbayev, and R. Myrzakulov, "FRW and Bianchi type I cosmology of f-essence," *Astrophysics and Space Science*, **339**, 37-43 (2012). <https://doi.org/10.1007/s10509-011-0964-7>
- [12] T. Singh, and G.P. Singh, "Bianchi type-I cosmological models in Lyra's geometry," *Journal of Mathematical Physics*, **32**(9), 2456-2458 (1991). <https://doi.org/10.1063/1.529495>
- [13] J.P. Singh, A. Pradhan, and A.K. Singh, "Bianchi type-I cosmological models with variable G and Λ -term in general relativity," *Astrophysics and Space Science*, **314**, 83-88 (2008). <https://doi.org/10.1007/s10509-008-9742-6>
- [14] Arbab, Arbab I. "Bianchi type I viscous universe with variable G and Λ ," *General Relativity and Gravitation*, **30**(9), 1401-1405 (1998). <https://doi.org/10.1023/A:1018856625508>
- [15] M.E. Rodrigues, A.V. Kpadonou, F. Rahaman, P.J. Oliveira, and M. J. S. Houndjo "Bianchi type-I, type-III and Kantowski-Sachs solutions in f (T) gravity," *Astrophysics and Space Science*, **357**, 129 (2015). <https://doi.org/10.1007/s10509-015-2358-8>
- [16] M.F. Shamir, "Locally rotationally symmetric Bianchi type I cosmology in f(R,T) gravity," *The European Physical Journal C*, **75**(8), 354 (2015). <https://doi.org/10.1140/epjc/s10052-015-3582-7>
- [17] V.R. Chirde, S.P. Hatkar, and S.D. Katore, "Bianchi type I cosmological model with perfect fluid and string in f(T) theory of gravitation," *International Journal of Modern Physics D*, **29**(08), 2050054 (2020). <https://doi.org/10.1142/S0218271820500546>
- [18] M.I. Wanas, G.G.L. Nashed, and O.A. Ibrahim, "Bianchi type I in f(T) gravitational theories," *Chinese Physics B*, **25**(5), 050401 (2016). <https://doi.org/10.1088/1674-1056/25/5/050401>
- [19] V. Fayaz, H. Hossienkhani, A. Pasqua, M. Amirabadi, and M. Ganji "f(T) theories from holographic dark energy models within Bianchi type I universe," *The European Physical Journal Plus*, **130**, 28 (2015). <https://doi.org/10.1140/epjp/i2015-15028-2>
- [20] M.E. Rodrigues, I.G. Salako, M.J.S. Houndjo, and J. Tossa, "Locally rotationally symmetric Bianchi type-I cosmological model in f (T) gravity: from early to dark energy dominated universe," *International Journal of Modern Physics D*, **23**(01), 1450004 (2014). <https://doi.org/10.1142/S0218271814500047>
- [21] M.E. Rodrigues, I.G. Salako, M.J.S. Houndjo, and J. Tossa, "Locally rotationally symmetric Bianchi type-I cosmological model in f (T) gravity: from early to dark energy dominated universe," *International Journal of Modern Physics D*, **23**(01), 1450004 (2014). <https://doi.org/10.1142/S0218271814500047>
- [22] S. Qazi, F. Hussain, and G. Shabbir, "Exploring conformal vector fields of Bianchi type-I perfect fluid solutions in f(T) gravity," *International Journal of Geometric Methods in Modern Physics*, **18**(10), 2150161 (2021). <https://doi.org/10.1142/S0219887821501619>
- [23] A.H. Hasmani, and A.M. Al-Haysah, "Exact solutions for bianchi type-I cosmological models in f (R) Theory of Gravity," *Applications and Applied Mathematics: An International Journal (AAM)*, **141**(1), 334-348 (2019). <https://digitalcommons.pvamu.edu/aam/vol14/iss1/22>
- [24] S.H. Shekh, and V.R. Chirde, "Accelerating Bianchi type dark energy cosmological model with cosmic string in f (T) gravity," *Astrophysics and Space Science*, **365**(3), 60 (2020). <https://doi.org/10.1007/s10509-020-03772-y>
- [25] M. Koussour, and M. Bennai, "Stability analysis of anisotropic Bianchi type-I cosmological model in teleparallel gravity," *Classical and Quantum Gravity*, **39**(10), 105001 (2022). <https://doi.org/10.1088/1361-6382/ac61ad>
- [26] M.V. Dawande, K.S. Adhav, and S.S. Nerkar, "LRS Bianchi Type-I Universe in F (T) Theory of Gravity," *Advances in Astrophysics*, **2**(2), 117-125 (2017). <https://dx.doi.org/10.22606/adap.2017.22006>
- [27] B.K. Shukla, V. Mishra, S.N. Shukla, and A. Singh, "Bianchi type-I Cosmological model in modified theory of gravity," (2022).
- [28] R.J. van den Hoogen, A.A. Coley, and D.D. McNutt, "Bianchi type cosmological models in f (T) tele-parallel gravity," *Journal of Cosmology and Astroparticle Physics*, **2023**(10), 042 (2023). <https://doi.org/10.1088/1475-7516/2023/10/042>
- [29] Shamir, M. Farasat, and Z. Raza, "Locally rotationally symmetric Bianchi type I cosmology in f (R) gravity," *Canadian Journal of Physics*, **93**(1), 37-42 (2015). <https://doi.org/10.1139/cjp-2014-0338>
- [30] M.E. Rodrigues, et al. "Anisotropic universe models in f (T) gravity," *Physical Review D*, **86**(10), 104059 (2012). <https://doi.org/10.1103/PhysRevD.86.104059>

- [31] Y.S. Solanke, A.P. Kale, D.D. Pawar, and V.J. Dagwal "LRS Bianchi type-I cosmological model in $f(Q, T)$ theory of gravity with observational constraints," International Journal of Geometric Methods in Modern Physics, **20**(12), 2350212 (2023). <https://doi.org/10.1142/S0219887823502122>
- [32] V.J. Dagwal, "Tilted two forms of dark energy in $f(T)$ theory of gravity," Indian Journal of Physics, (2023). <https://doi.org/10.1007/s12648-023-02879-6>
- [33] Y.S. Solanke, D.D. Pawar, and V.J. Dagwal, "Accelerating dark energy universe with LRS Bianchi type-I spacetime," International Journal of Geometric Methods in Modern Physics, **18**(04), 2150062 (2021). <https://doi.org/10.1142/S0219887821500626>
- [34] A. Pradhan, and O.P. Pandey, "Bianchi type I anisotropic magnetized cosmological models with varying Λ ," International Journal of Modern Physics D, **12**(07), 1299-1314 (2003). <https://doi.org/10.1142/S0218271803003761>
- [35] V.J. Dagwal, and D.D. Pawar, "Two-fluid sources in $F(T)$ theory of gravity," Modern Physics Letters A, **35**(04), 1950357 (2020). <https://doi.org/10.1142/S0217732319503577>
- [36] D.D. Pawar, D.K. Raut, and W.D. Patil, "Anisotropic behavior of perfect fluid in fractal cosmology," New Astronomy, **100**, 101999 (2023). <https://doi.org/10.1016/j.newast.2022.101999>
- [37] V.J. Dagwal, and D.D. Pawar, "Tilted cosmological models in $f(T)$ theory of gravity," Indian Journal of Physics, **95**(9), 1923-1931 (2021). <https://doi.org/10.1007/s12648-020-01830-3>
- [38] D.D. Pawar, R.V. Mapari, and J.L. Pawade, "Perfect fluid and heat flow in $f(R, T)$ theory," Pramana, **95**(1), 10 (2021). <https://doi.org/10.1007/s12043-020-02058-w>
- [39] D.D. Pawar, V.J. Dagwal, and P.K. Agrawal, "Two fluid axially symmetric cosmological models in $f(R, T)$ theory of gravitation," Malaya Journal of Matematik, **4**(01), 111-118 (2016). https://www.malayajournal.org/articles/MJM16_14.pdf
- [40] V.J. Dagwal, and D.D. Pawar, "Tilted congruences with stiff fluid cosmological models," Indian Journal of Physics, **94**(11), 1861-1867 (2020). <https://doi.org/10.1007/s12648-019-01625-1>
- [41] C.R. Mahanta, and N. Sarma, "Bianchi Type-III Cosmological Model in $f(R, T)$ Theory of Gravity with $\Lambda(T)$," International Journal of Mathematical Archive-6 (12), 40-46 (2015). <http://www.ijma.info/index.php/ijma/article/view/3968/2400>
- [42] A. Pradhan, A.K. Singh, and D.S. Chouhan, "Accelerating Bianchi type-V cosmology with perfect fluid and heat flow in Saez-Ballester theory," International Journal of Theoretical Physics, **52**(1), 266-278 (2013). <https://doi.org/10.1007/s10773-012-1329-x>

ІДЕАЛЬНА РІДИНА З ТЕПЛОВИМ ПОТОКОМ У $f(T)$ ТЕОРІЇ ГРАВІТАЦІЇ

Д.Д. Павар^а, Н.Г. Гунгарвар^б, Р.С. Гайквад^а

^а Школа математичних наук, Університет SRTM, Нандед - 431606, Махараштра, Індія

^б Коледж науки та мистецтв Шрі Д.М. Бурунгале, Шегаон-444203, Махараштра, Індія

Космологічні моделі Б'янкі типу I були предметом інтенсивних досліджень у космології через їхню простоту та актуальність для розуміння динаміки раннього Всесвіту. У цьому дослідженні ми досліджуємо динаміку таких моделей у рамках $f(T)$ гравітації, альтернативної теорії гравітації, яка розширює телепаралельну гравітацію шляхом введення загальної функції торсійного скаляра T . Ми акцентуємо увагу на наявності в космічному середовищі ідеальної рідини з тепловим потоком. Розв'язуючи рівняння поля гравітації $f(T)$, ми отримуємо точні розв'язки для космологічних моделей Б'янкі типу I. Ці рішення дають цінну інформацію про еволюцію Всесвіту та про те, як на неї впливає модифікована теорія гравітації. Крім того, ми виводимо космологічні параметри в термінах червоного зсуву, пропонуємо зручний спосіб інтерпретації даних спостережень і зв'язування теоретичних прогнозів з емпіричними вимірюваннями. Наші висновки не лише сприяють глибшому розумінню динаміки космологічних моделей Б'янкі типу I, але й створюють основу для порівняння $f(T)$ гравітації зі стандартною загальною теорією відносності в контексті спостережної космології. Це дослідження прокладає шлях для подальшого вивчення альтернативних теорій гравітації та їхнього впливу на еволюцію та структуру раннього Всесвіту.

Ключові слова: теорія $f(T)$; ідеальна рідина з тепловим потоком; Б'янкі типу I